DESIGN, SYNTHESIS and CHARACTERIZATION of BIOINSPIRED NANOMATERIALS for ENGINEERING and BIOMEDICINE

A DISSERTATION SUBMITTED TO
MATERIALS SCIENCE AND NANOTECHNOLOGY PROGRAM
OF THE GRADUATE SCHOOL OF ENGINEERING AND SCIENCE
OF BILKENT UNIVERSITY
IN PARTIAL FULFILLMENT OF THE REQUIREMENTS
FOR THE DEGREE OF
DOCTOR OF PHILOSOPHY

By

HAKAN CEYLAN

August, 2014

I certify that I have read this thesis and that in my opinion it is fully adequate, in scope and in quality, as a thesis of the degree of Doctor of Philosophy.

…….

Asst. Prof. Dr. Ayşe Begüm Tekinay (Advisor)

I certify that I have read this thesis and that in my opinion it is fully adequate, in scope and in quality, as a thesis of the degree of Doctor of Philosophy.

…….

Assoc. Prof. Dr. Mustafa Özgür Güler (Co-Advisor)

I certify that I have read this thesis and that in my opinion it is fully adequate, in scope and in quality, as a thesis of the degree of Doctor of Philosophy.

…….

Prof. Dr. Engin Umut Akkaya

I certify that I have read this thesis and that in my opinion it is fully adequate, in scope and in quality, as a thesis of the degree of Doctor of Philosophy.

…….

Prof. Dr. Halil İbrahim Ünal

I certify that I have read this thesis and that in my opinion it is fully adequate, in scope and in quality, as a thesis of the degree of Doctor of Philosophy.

…….

Asst. Prof. Dr. Ali Osmay Güre

I certify that I have read this thesis and that in my opinion it is fully adequate, in scope and in quality, as a thesis of the degree of Doctor of Philosophy.

…….

Assoc. Prof. Dr. Hüseyin Özkan

Approved for the Graduate School of Engineering and Science:

…….

Prof. Dr. Levent Onural

Director of the Graduate School of Engineering and Science

ABSTRACT

DESIGN, SYNTHESIS and CHARACTERIZATION of BIOINSPIRED NANOMATERIALS for ENGINEERING and BIOMEDICINE

Hakan Ceylan
PhD in Materials Science and Nanotechnology
Supervisor: Ayşe Begüm Tekinay, PhD
Co-Supervisor: Mustafa Özgür Güler, PhD
August, 2014

Nature is an inspirational school for materials scientists. Natural selection process puts a massive pressure on biological organisms giving rise to effective strategies for fabricating materials, which generally outperform their man-made counterparts. Mimicking physical and chemical features of biological materials can greatly aid in overcoming existing design constraints of engineering and medicine. In this dissertation, a reductionist, bottom-up approach is demonstrated to recapitulate biological functionalities in fully-synthetic hybrid constructs. For material design, the potential of short, rationally-designed peptides for programmed organization into nanostructured materials is explored. The resulting nano-ordered materials exhibit multifunctional and adaptive properties, which can be tailored by the information within monomeric peptide sequences as well as the emerging properties upon their self-assembly. In light of these, design, synthesis and characterization of the prototypes of nanostructured functional materials are described in the context of regenerative medicine and biomineralization.

Keywords: Bioinspired Materials, Functional Self-Assembly, Biomaterials, Surface Functionalization, Biomineralization

ÖZET

BİYOLOJİK SİSTEMLERDEN ESİNLENEREK PROGRAMLANAN NANO YAPILI MALZEMELERİN MÜHENDİSLİK ve BİYOMEDİKAL UYGULAMALAR İÇİN TASARIMI, SENTEZİ ve KARAKTERİZASYONU

Hakan Ceylan
Malzeme Bilimi ve Nanoteknoloji, Doktora
Tez Danışmanı: Dr. Ayşe Begüm Tekinay
Eş Danışman: Dr. Mustafa Özgür Güler
Ağustos, 2014

Malzeme bilimi araştırmacıları için doğa ilham verici bir okuldur. Canlı organizmalar, doğal seçilim eleklerinden başarıyla geçmelerini sağlayacak işlevsel olarak çok iyi organize olmuş malzemeler geliştirerek varlıklarını sürdürmektedir. Bu yönüyle biyolojik malzemeler benzer koşullar için yapay olarak üretilenlerden çok daha başarılı bir performans sergiler. Bu nedenle biyolojik malzemelerdeki fiziksel veya kimyasal etkenlerin yapay malzemelerde yeniden ortaya çıkartılması ile hâlihazırda endüstri ve tıp alanlarında karşılaşılan birçok zorluğun aşılabileceği değerlendirilmektedir. Bu tezde minimalist bir yaklaşım kullanarak, aşağıdan-yukarı fabrikasyon yöntemiyle geliştirilen hibrit yapılarda biyolojik malzemelerin işlevsel özellikleri taklit edilmektedir. Yapı malzemesi olarak, mantıksal olarak tasarlanan kısa sentetik peptit dizinlerinin programlı olarak organizasyonu (kendiliğinden toplanması) değerlendirilmiştir. Elde edilen nano-yapılı malzemelerin dinamik ve

işlevsel özellikleri peptitleri oluşturan aminoasitlerin dizilimi ve toplanma sonrası ortaya çıkan yeni durum ile kontrol edilebilmektedir. Bu perspektifle, biyolojik malzemelerden esinlenerek geliştirilen, yenileyici tıp ve biyomineralizasyon alt başlıklarında uygulanan prototiplerin tasarımı, sentez ve karakterizasyonu incelenmektedir.

Anahtar kelimeler: Doğadan Esinlenerek Geliştirilen Malzemeler, İşlevsel Süpramoleküler Nanoyapılar, Biyomalzemeler, İşlevsel Yüzeyler, Biyomineralizasyon

Acknowledgements

I would like to express my gratitude to my advisors, Prof. Tekinay and Prof. Güler for their guidance and support to my research. Their encouragement helped me develop a trans-disciplinary understanding, which I can carry with me throughout my research career.

I would like to acknowledge the PhD scholarship from TÜBİTAK (The Scientific and Research Council of Turkey) BIDEB 2211-A. I would also like to thank for two international conference supports (in the form of 2224-A) as well as the generous support for the 61st Lindau Nobel Laureate Meeting. TÜBİTAK has a very special place in my academic development.

This thesis simply would not have been possible by the endless devotion and exceptional support of Şeyma Özkan. She is truly a remarkable person. Her encouraging liveliness kept me motivated all the time. She is the unseen hero behind this work. Therefore, I would like to dedicate this thesis to her as my tribute.

I would like to express my most sincere thanks to Samet Kocabey, Seher Yaylacı and Hilal Ünal Gülsüner for their companionship in this long marathon. Their support has always kept me motivated. Their friendship deserves all compliments.

I would like to express my special thanks to Samet Kocabey, Hilal Ünal Gülsüner, Cağla-Özgit Akgün and Ruslan Garifullin for their fruitful collaboration. Together, we pursued interesting scientific questions, which we managed to publish in high quality journals. Another special thanks to Ayşegül Tombuloğlu who taught

me many tools and techniques, which significantly eased my adaptation to the laboratory in my first year. I have never forgotten her kindness.

I would also like to thank Handan Acar, Melis Göktaş, Gülistan Tansık, Gülcihan Gülseren, Melike Sever, Berna Şentürk, Ceren Garip, Nuray Gündüz, Elif Arslan, Elif Ergül, Yasin Tümtaş, Öncay Yaşa, Ahmet Emin Topal, Alper Devrim Özkan and Mevhibe Yakut for creating such a warm working environment. My special thanks to Zeynep Ergül Ülger and Zeynep Erdoğan not only for their immense technical help, but also for their sincere friendship for all these years. It was wonderful to work with them.

I would like to thank Prof. Salim Çıracı for supporting my participation to a truly inspirational organization, the 3rd "Global Challenges- Opportunities for Nanotechnology Workshop". It significantly contributed to my understanding of science and technology as productive means to address the growing complexity of global problems.

I would like to take this opportunity to give my tribute in memory of Prof. İhsan Doğramacı, the founder of Bilkent University. Bilkent University has been my home with all the unforgettable memories for the past nine years, including my undergraduate education. Prof. Doğramacı's endless pursuit of reaching perfection opened wide avenues in my endeavors.

Finally, I would like to express my most sincere gratitude to my family who always supported me with their endless love to become who I am now. I am proud of them. I work for day and night to elevate their name and honor.

CONTENTS

LIST OF FIGURES

LIST OF TABLES

ABBREVIATIONS

ALD	**:**	Atomic layer deposition
ALP	**:**	Alkaline phosphatase
ATR-FTIR	**:**	Attenuated total reflectance-Fourier transform infrared spectrometry
BMP-2	**:**	Bone morphogenetic protein-2
BSA	**:**	Bovine serum albumin
CD	**:**	Circular dichroism
DCM	**:**	Dichloromethane
DMF	**:**	N, N-Dimethylformamide
DMEM	**:**	Dulbecco's modified Eagle's medium
Dopa	**:**	3,4-Dihydroxy-L-phenylalanine
ECM	**:**	The extracellular matrix
EdU	**:**	5-ethynyl-2'-deoxyuridine
EDS	**:**	Energy-dispersive x-ray spectrometry
ESI	**:**	Electrospray ionization
FBS	**:**	Fetal bovine serum
FCS	**:**	Fetal calf serum
GAG	**:**	Glycosaminoglycan
HAp	**:**	Hydroxyapatite
HEPES	**:**	2-[4-(2-hydroxyethyl)piperazin-1-yl] ethanesulfonic acid
HGF	**:**	Human gingival fibroblast
hMSC	**:**	Human mesenchymal stem cell
HPLC	**:**	High performance liquid chromatography
EDTA	**:**	Ethylenediaminetetraacetic acid

HUVEC	**:**	Human umbilical vein endothelial cell
LC-MS	**:**	Liquid chromatography-mass spectrometry
MTT	**:**	3-(4,5-dimethylthiazol-2-yl)-2,5-diphenyltetrazolium bromide
PA	**:**	Peptide amphiphile
PBS	**:**	Phosphate-buffered saline
Q-TOF	**:**	Quadrupole time of flight
SAED	**:**	Selected area electron diffraction
SBF	**:**	Simulated body fluid
SDS	**:**	Sodium dodecyl sulfate
SEM (Microscopy)	**:**	Scanning electron microscope
SEM (Statistics)	**:**	Standard error of the mean
STEM	**:**	Scanning transmission electron microscope
TIS	**:**	Triisopropylsilane
TCP	**:**	Tissue culture plate
TEM	**:**	Transmission electron microscope
TFA	**:**	Trifluoroacetic acid
TRITC	**:**	Tetramethylrhodamine
XRD	**:**	X-ray diffraction
XPS	**:**	X-ray photoelectron spectrometry
TGA	**:**	Thermogravimetric analysis

CHAPTER 1

1 Introduction: Concepts in Bioinspired Nanomaterial Design

This work is partially described in the following publication:

Ceylan H., Tekinay, A. B., Guler, M. O. Biological and Biomimetic Adhesives: Challenges and Opportunities, *the Royal Society of Chemistry*, 103-116, 2013.

Materials scientists are looking to nature in awe. Biological organisms develop highly sophisticated materials in tremendous diversity. Driven by the stringent natural selection process, physical or chemical demands occurring in a particular environment are met by elegant biological constructions having various components assembled following a distinct pattern.[1] Hierarchical organization of material from nano- up-to- millimeter level is also highly economical in amount. These properties of biological materials inspire for novel technologies and more efficient engineering principles, as the performance of them outperform their man-made counterparts. This enterprise requires a multi-disciplinary approach, integrating chemistry, biology and materials science. This dissertation aims at developing new bioinspired design strategies for materials used in biomedical, environmental and industrial applications. However, one-to-one imitation of highly sophisticated biological materials is almost impossible and may even be inadequate depending on the type of the application. Therefore, here we followed a reductionist approach to reconstruct minimally

functional physical and/or chemical units of biological materials in a nanostructured backbone material. Such a strategy has an immediate advantage of larger scale production of the functional material through chemical synthesis. Besides, combination of different functionalities from different sources in one construct can enable design of hybrid materials that can be used at a wider scope with higher efficiency. Well-controlled chemistry and composition of the final material also provide robustness, i.e., less batch-to-batch variations, which are hardly controlled in dynamically evolving biological systems. Finally, nanostructured presentation of functional cues enables steric control over the molecular-level interactions. As the backbone material, we investigate the utility of rationally designed, short peptides, which can assemble into large macromolecular structures through noncovalent interactions. In the rest of this introductory chapter (Chapter 1), we mainly concentrate on the fundamentals of bioinspired nanomaterial design by first explaining sources of inspiration on the focus of this dissertation. Then, we provide an overview of supramolecular engineering concepts for material design. This design framework is then applied in the context of developing underwater adhesives as functional interfaces for cardiovascular and bone implants (Chapters 2, 3 and 4), selective microenvironments for competitive cell behavior in the context of guided tissue regeneration (Chapter 2 and 3), mechanically robust supramolecular hydrogels with self-healing and adaptive properties (Chapter 5), nano-templated atomic-layer mineralization semiconductor metal oxides (Chapter 6) and modular peptide design for one-step synthesis and functionalization of gold nanoparticles (Chapter 7). In Chapter 8, we provide an overview of the bio-inspired material design with a future perspective.

1.1 Sources of Inspiration

1.1.1 Underwater adhesion: Analogy between marine environment and mammalian tissues

Underwater adhesion is a daunting task for organisms living in the seashores. Irregularities in salinity, abrasive wearing of the ocean waves, microbial invasions, and sharp thermal fluctuations create an environment of harsh extremes. On the other hand, continuous supply of nutrients moved from the ocean to the living zone of the organisms through the tides sustains an ecosystem inhabited by unique organisms, some of which exhibit exceptional adaptive characteristics for adhesion under highly unstable conditions. Adhesion strategies of different organisms living in these zones, such as sandcastle worm, adult barnacles and their larvae (the cyprid), and mussels have been under close examination by researchers in recent years with the purpose of translating their adhesive technology into synthetic platforms for industrial and medical applications.[2-11] A natural underwater adhesive is usually synthesized and secreted onto the substrate with low initial viscosity followed by curing of the glue over the course of minutes to hours into its final hardened structure. An impressive feature of these adhesives is that they require little or no surface preparation prior to secretion.[12] This capability is desirable in man-made adhesives which, so far, are incapable of functioning on highly solvated surfaces. Highly polar water molecules, dissolved ions and organic contaminants interact both with the surface and the adhesive molecules, interfering with the adhesion process (Figure 1.1).

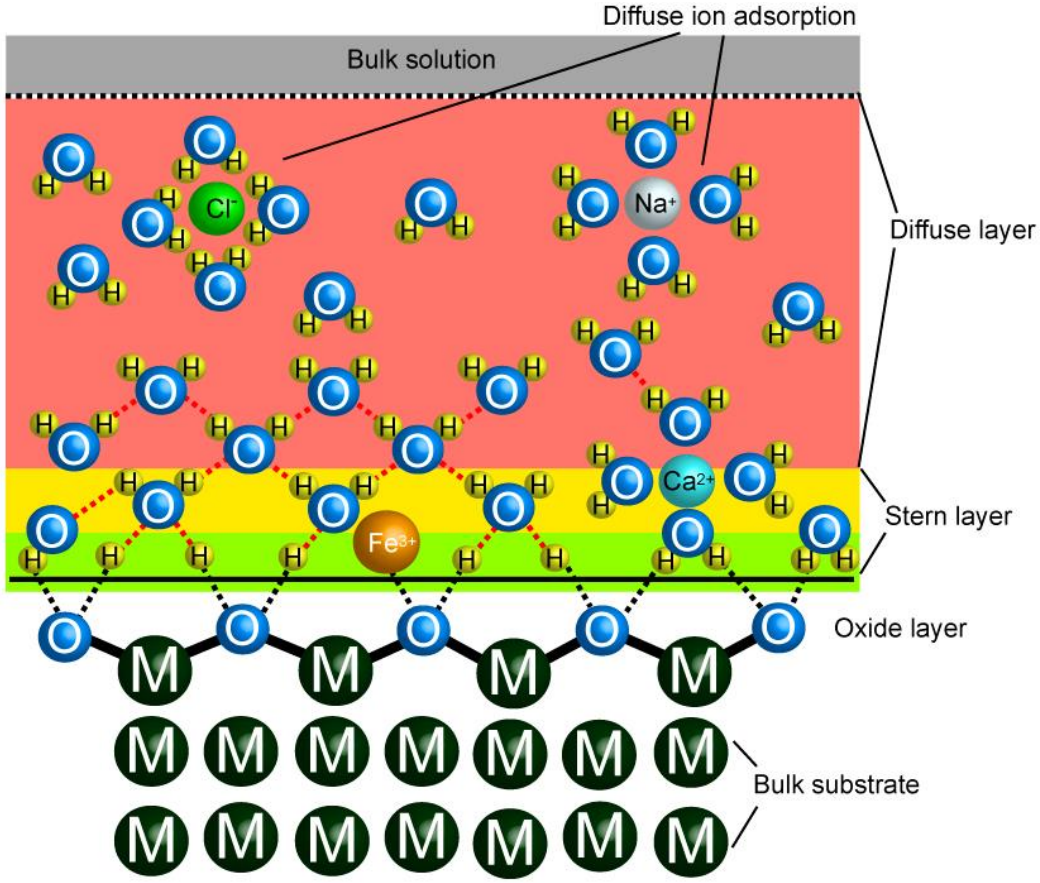

Figure 1.1 Interaction of water molecules and dissolved ions with surface. Highly polar water molecules, dissolved ions and organic contaminants interact both with the surface and the adhesive molecules, interfering with the adhesion process.

The nature of biofunctional interface, separating an inert biomedical device from the native tissue while integrating the material into the body, is of utmost importance for the long-term efficiency of tissue regeneration. In order to achieve this, strong and biologically safe underwater synthetic adhesives, which can modulate cellular activities through biologically active signals, are required.[13-15] The mainstream research in this field has largely concentrated on creating artificial cellular microenvironments by mimicking the architecture and biology of the native extracellular matrix. Toward this purpose, various polymers and self-assembled nanofibers of peptidic structures have been engineered to present desired biofunctional ligands to interfere with cellular signaling. On the other hand, immobilization of such materials onto a substrate has remained an unresolved issue. Physical and chemical conditions in the applications where these adhesives are normally used, both resemble the conditions in the intertidal zone. For example, the mechanical abrasiveness in load-bearing tissues, such as bone and cartilage, the high shear force experienced in blood vessels and the high ionic strength and polyionic environment of bodily fluids create a challenging environment for adhesives to operate efficiently. Therefore, natural underwater adhesives provide a plethora of inspiration towards developing biologically safe and reliable synthetic adhesives for medical applications.

Underwater adhesion of mussels, particularly *Mytulis edulis* and *Mytulis californianus*, has drawn escalating interest in biomimetics research.[16, 17] In their natural habitat these sessile (non-motile) organisms cling themselves to underwater solid surfaces (e.g., rocks, wood, etc.) in the intertidal zones. The adhesion capacity of mussels encompasses virtually all types of surfaces, including metals, alloys,

metal oxides, organic surfaces, and plastics, even polytetrafluoroethylene (TEFLON®).[18, 19] Due to their extensive adhesion capacity, fouling of mussels on ship hulls and coastal infrastructure has been a growing economic concern. There is no man-made glue that can bind to such a broad variety of surfaces. The adhesion strength of mussels is one of the strongest known in natural underwater adhesives.[16] In order to achieve this, mussels produce a special polyphenolic glue containing hierarchically organized proteins, known as mussel adhesive proteins (mfps), with varying content of 3,4-dihydroxy-L-phenylalanine (Dopa) residues (Figure 1.2 and Table 1.1). Spatial and temporal evolution of this phenolic residue within the wet glue precursor is believed to play an indispensible role in mussel adhesion and cohesion. The mussel adhesive unit is called a byssal thread, or byssus in plural, and contains three main functional and biochemical components: a stem embedded in the soft tissues of the mussel, a hard and flexible thread-like extension (byssal thread), and an adhesive plaque (Figure 1.2).[17, 20] The whole structure is composed of different proteins called mfps. Up to now, six major proteins have been isolated and identified with different highly organized functions in adhesion process (mfp-1 to mfp-6).

The catechol side chain of Dopa can be involved in a variety of physical and chemical reaction mechanisms. For example, catechols can form exceptionally stable complexes with metals and metal oxides, thereby mediating adhesion to these surfaces. Lee *et al.* measured the dissociation force of a single tethered Dopa molecule from TiO_2 using single-molecule atomic force microscopy (AFM).[21] The dissociation force of the single Dopa-TiO_2 bond (~800 pN) is about half of a covalent bond (~2000 pN) and much higher than the dissociation force of hydrogen

bonds that hold the DNA double helix intact (10-20 pN).[21-23] In spite of the high bond strength, Dopa binding to TiO_2 surface is completely reversible with thousands of break/reformation series.[21] Catechol groups in mfps can also undergo covalent reactions that contribute significantly to the cohesive and water-resistant characters of the mussel glue.[24, 25] Under the basic conditions of seawater (pH ~8.5), catechol is oxidized to highly reactive quinone and semiquinone species that further react with each other to covalently cross-link (cure) the mfps.[19, 25] Further, Dopa-quinone was reported to covalently react with primary amine and sulfhydryl groups.[21, 26]

A byssal thread is composed of an extensible inner core and a hard outer shell (the cuticle).[27] Typically, hardness of the cuticle is roughly five times higher than the hardness of inner core proteins.[20] The inner core is formed by extracellular matrix proteins, with a central collagen core flanked by silk and elastin-like domains.[28] Because of the spatial distribution of the silk- and elastin-collagen complexes in the thread, the distal portion (closer to the substrate) is typically an order of magnitude more rigid than the proximal (closer to the mussel) portion. However, the distal and proximal portions are extensible up to 109% and 200%, respectively, without breaking apart.[29-31] The cuticle consists of densely packed granules, 0.8 μm in diameter, constituting ~50% of the cuticle volume.[27] mfp-1 is a 108 kDa structural protein containing a unique repetitive decapeptide, and it coats the entire adhesion plaque and the distal portion of the byssus.[32] Recent evidence suggests that the granules in the cuticle are formed by mfp-1 proteins densely cross-linked by ferric iron ions. mfp-1 can form reversible bis-$Fe(Dopa)_2$ and tris-$Fe(Dopa)_3$ complexes with iron ions in alkaline sea water.[20]

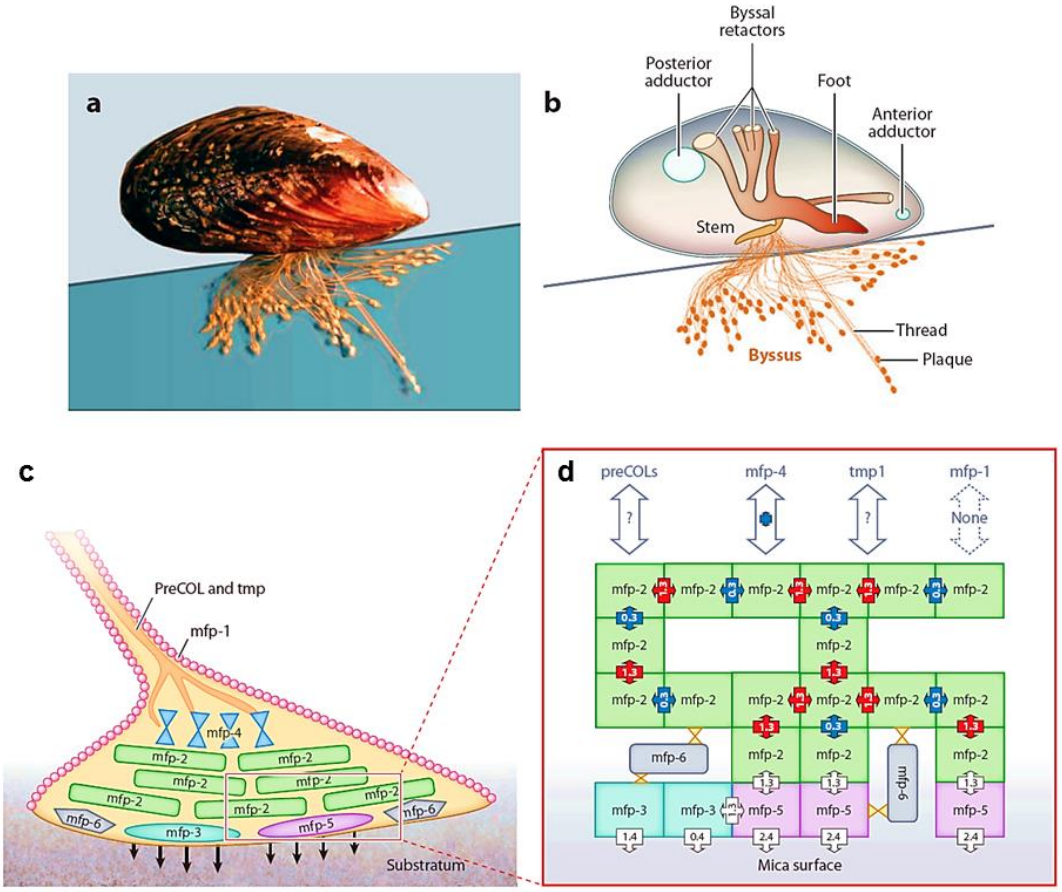

Figure 1.2 Mussel adhesion strategy inspires synthetic adhesives that can operate under water. (a) A typical mussel with its adhesive byssi. (b) A mussel adhesive organ consisting of a stem embedded in the soft tissues, a hard and flexible thread-like extension (byssal thread), and an adhesive plaque. (c, d) The thread and the adhesive pad consist of a number of proteins hierarchically assembled to maintain mechanical rigidity as well as facilitate surface adhesion (Reproduced from Ref. 17 with permission from Royal Society of Chemistry).

Table 1.1 *Molecular weight and Dopa content of mussel adhesive proteins.*[8, 33-36]

Proteins	Isolated species†	Molecular weight (kDa)	Dopa content (mol %)
mfp-1	Me/Mc	108/90	10-15
mfp-2	Me	46	3
mfp-3	Me	6	21
mfp-4	Mc	93	2
mfp-5	Me	9	27-30
mfp-6	Mc	11	4

† Species are *Mytilus edulis* (Me) and *Mytilis californianus* (Mc).

These complexes have very high stability constants (log K_s ~37-40), implying that iron ions are a critical element of mussel adhesion that endows the cuticle with both hardness and self-healing ability after fracture.[37] Holten-Anderson *et al.* showed that removal of iron ions largely inhibits self-healing of Dopa-conjugated polymer and supramolecular networks.[38] Despite its high stiffness, the cuticle is highly extensible, with ultimate tensile strain around 70%.[39] Deformations up to this point are prevented from propagating by densely cross-linked granules, whereas micro tears that are formed during deformation are mended by a rapid healing process.[20, 39] Adhesive plaques establish adhesion of the animal to the surface.[8, 40] Proteins that are in direct contact with the substrate (mfp-3 and mfp-5) have the highest Dopa content, highlighting the significance of this phenolic residue for adhesion (Table 1.1). mfp-3 and mfp-5 both contain a high number of cationic arginine and lysine residues, respectively.[17, 33] The ε-amine group of lysine is reactive with oxidized catechol (quinone), which may entail cross-linking in the mussel glue.[26]

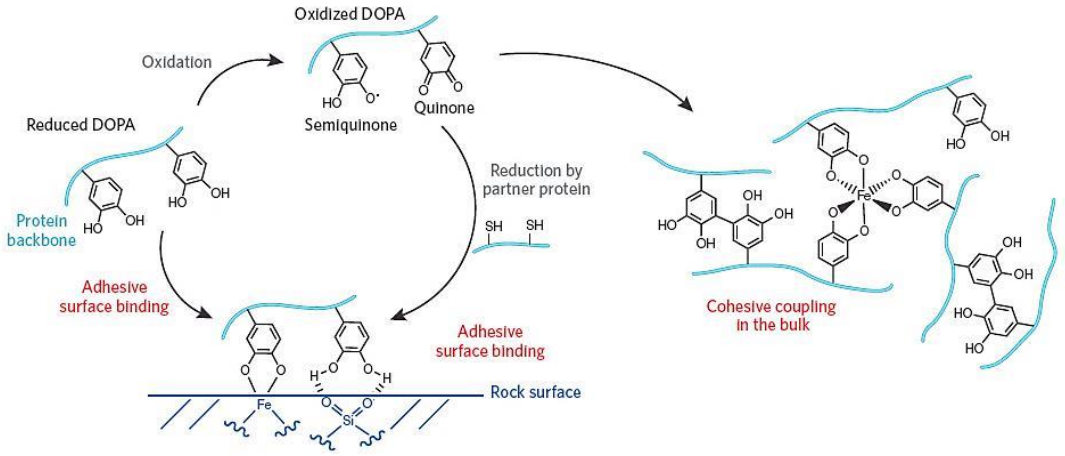

Figure 1.3 Mussel glue: Adhesion and curing mechanisms (Reproduced from Ref. 41 with permission from Nature Publishing Group).

However, *ex vivo* studies of mussel proteins and Dopa-containing peptides have not yet confirmed such reactivity.[42, 43] The current view is that the excess positive charge forms columbic interactions with surfaces that mussels bind to in their native environment, such as rocks that are rich in negatively charged silicates and aluminates.[44-46] mfp-5 is also enriched in serine and phosphoserine residues, whose roles remain unknown.[6] Although, mfp-3 and mfp-5 are more enriched with Dopa, the bulk of the adhesive plaque largely consists of mfp-1, mfp-2, and mfp-4. mfp-2 is known to be resistant to proteolysis and is thought to act as the stabilizer of byssus cement.[40] This protein contains a large number of cysteine residues. mfp-4, on the other hand, is thought to serve as a bridge in the thread-plaque junction by linking the core collagen fibers of the distal byssus to plaque proteins, and has high levels of histidine, arginine, and lysine.[47, 48] mfp-6, which was discovered in *Mytilus californianus*, has surprisingly low Dopa (4%) and high cysteine content (11%).[35] Zhao and Waite reported the presence of 5-S-Cysteinyl Dopa, a cysteine-Dopa adduct. Therefore, this protein is believed to provide a cohesive link between the surface-coupling proteins (mfp-3 and mfp-5) and the bulk plaque proteins (mfp-2 and mfp-4).[35] A very recent report, however, attributed a more fundamental role to this protein by suggesting that mfp-6 prevents auto-oxidation of Dopa to quinone in mfp-3 before adhering onto substrate.[49] Quinone formation dramatically reduces the adhesion capacity onto TiO_2 and mica surfaces, by about 80%.[21, 50] Thiol group on side chain of cysteine residues in mfp-6 successfully maintain Dopa by coupling oxidation of thiols to reduction of quinones.

Despite the high underwater adhesive performance of the mussel glue, the inimitable complexity and the hierarchical organization of its constituent proteins restricted the

practical use of this material. Even isolation of the individual mfps is a demanding task due to their labour-intensive and inefficient production yield. For instance, approximately 10,000 mussels are required to extract only 1 g of mfp-1; and the purity of this extract is not reliable due to high batch-to-batch variation.[51] In order to produce this protein at large scale, *E. coli* and *S. cerevisiae* have been used,[52-54] however, attempts to produce functional mfps failed mainly due to codon bias and small expression quantity.[53-55] Although there has been partial success in the expression of mfp-1 repetitive sequences in *S. cerevisiae*[53] and *E. coli*[54, 55] using synthetic gene constructs, their adhesion profiles were found to be poor. In another study, Choi *et al.* took a recombinant approach by fusing domains of mfp-1 and mfp-5 with functional groups of extracellular matrix proteins, such as RGD and YIGSR in order to create cell-friendly coatings.[56]

However, mfp production through recombinant production is still an unresolved challenge due to lack of the post-transcriptional modifications, including formation of Dopa by hydroxylation of Tyr residues. Limitations of obtaining high-purity and functional mfps led to alternative biomimetic approaches. Conjugation of Dopa, or the catechol group, to synthetic platforms has been the most widely recognized strategy. Dopa is chosen because not only can it adhere to a wide variety of substrates underwater, but also it has a very simple chemical structure, which can be easily grafted onto synthetic systems.[25, 57, 58] Use of a synthetic backbone with well-defined chemistry, onto which Dopa can be attached, offers a more reliable platform with minimum batch-to-batch variation compared to natural adhesive proteins. Moreover, biomimetic reconstitution of mussel adhesives on synthetic platforms with additional functionalities provides a wider range of applications and development

strategies of novel hybrid materials with superior performance. Using this approach, catechol-conjugated poly(ethylene glycol) (PEG) was synthesized to obtain anti-fouling surfaces.[59-61] Likewise, catechol-functionalized chitosan/pluronic thermo-responsive and injectable hydrogels were utilized as tissue adhesives.[62] Using poly(dopamine methacrylamide-comethoxyethyl acrylate), a reversible dry/wet adhesive platform was developed by Lee *et al.* through combining mussel-mimetic Dopa adhesion with gecko-mimetic polydimethyl siloxane pillars.[63] Dopa-modified polymers were used to functionalize not only bulk surfaces, but also surfaces of nanoparticles. For instance, binding of methoxy poly(ethylene glycol), which was grafted to hyper-branched polyethylenimine and polyDopa, onto hydrophobic nanoparticles provided stabilization in harsh biological environments.[64] Oxidation-mediated grafting of catechols conferred redox activity to chitosan films.[65] These films were characterized to be poor in direct electron transfer, whereas electrons can readily flow through soluble mediators. As a result of this interaction, catechol-modified chitosan films exhibited amplification, partial rectification, and switching capabilities, thereby holding promise for sensor development. At basic pH, dopamine undergoes an oxidation-triggered auto-polymerization reaction in water. Hong *et al.* revealed that both noncovalent assembly and covalent polymerization contribute to polydopamine formation.[66] Virtually any type of surface, regardless of its chemistry, can be coated with polydopamine by simply dipping it into dopamine solution at pH ~8.5. Moreover, polydopamine coating thickness is proportional to the time of immersion and the chemical properties of this coating allow secondary modifications through coupling to nucleophilies.[19, 26] Ryu *et al.* demonstrated that the polydopamine coating provides a general route for bone-like hydroxyapatite

crystallization on a surface.[67] Wei *et al.* functionalized superparamagnetic iron oxide nanoparticles (SPIONs) with a dopamine sulfonate ligand to provide nanoparticles stability in water against pH and salinity changes in addition to enabling further functionalization with streptavidin or a maleimide dye.[68] Very recently, Kang *et al.* demonstrated a one-step surface functionalization strategy by mixing dopamine with a diverse range of organic and inorganic species and dipping the substrate into this mixture.[69]

In summary, biomimetic materials field has emerged as a converging discipline to reconstitute adaptive characteristics of biological systems in synthetic platforms to solve structural and functional problems in engineering, materials science, and medicine. A high performance adhesive, stable in aqueous and saline environments but with surface versatility and environmental compatibility will find a broad range of applications in industry and medicine. Although natural underwater adhesives exhibit exceptional performance under highly abrasive conditions, the high cost of obtaining adhesives from their original natural sources promotes alternative biomimetic solutions. Because of the simplicity of catechol that allows easy grafting to synthetic materials and the versatility of substrates it could bind to, mussel-inspired surface functionalization has become a prevalent strategy. Due to its general biocompatibility and water-resistant character, the main application area of mussel-mimetic materials has been medical applications. Unique underwater adaptations of other aquatic organisms also offer potential opportunities and novel inspirations for the purpose of developing advanced functional materials. Improving their efficiency and conditions under which synthetic adhesives operate is a continuing venture to meet the ever-changing demands of industry. This process is highly analogous to the

evolution of natural adhesives under the force of natural selection in order to meet the ever-changing conditions of the environment.

1.1.2 The extracellular matrix: Learning from nature for biomaterial design

In most OECD countries, the population is ageing, which requires efficient treatment strategies for diseases related to tissue and organ malfunctions.[70] Regenerative medicine is a translational research branch that aims at supporting tissue's own healing process by providing them with appropriate physical and chemical cues. At the molecular level, these cues imitate the native extracellular matrix (ECM) by directly interacting with cell-surface receptors to guide adhesion, proliferation, migration and differentiation processes. In a native tissue, the ECM is a dense biomolecular network that surrounds cells, providing them with mechanical and bio-regulatory supports to form an organized, functional tissue (Figure 1.4). Almost every cell in the body is exposed to the ECM components.[71] Osteocytes in bone, for example, are surrounded by a three-dimensional, mineralized composite matrix. Instead, the endothelial cells are exposed to two-dimensional basement membrane, which confers cell polarity. Even cells in the blood stream interact with soluble ECM proteins, such as fibronectin.[72] The interaction between cells and the ECM is highly dynamic and reciprocal. Cells embedded in the ECM are able to remodel its microenvironment through enzymatic and non-enzymatic activities, depending on the type and the physiological state of the tissue. For example, the bone remodeling process, i.e., formation vs. resorption of inorganic bone composite, is under well-adjusted control of osteoblasts and osteoclasts.

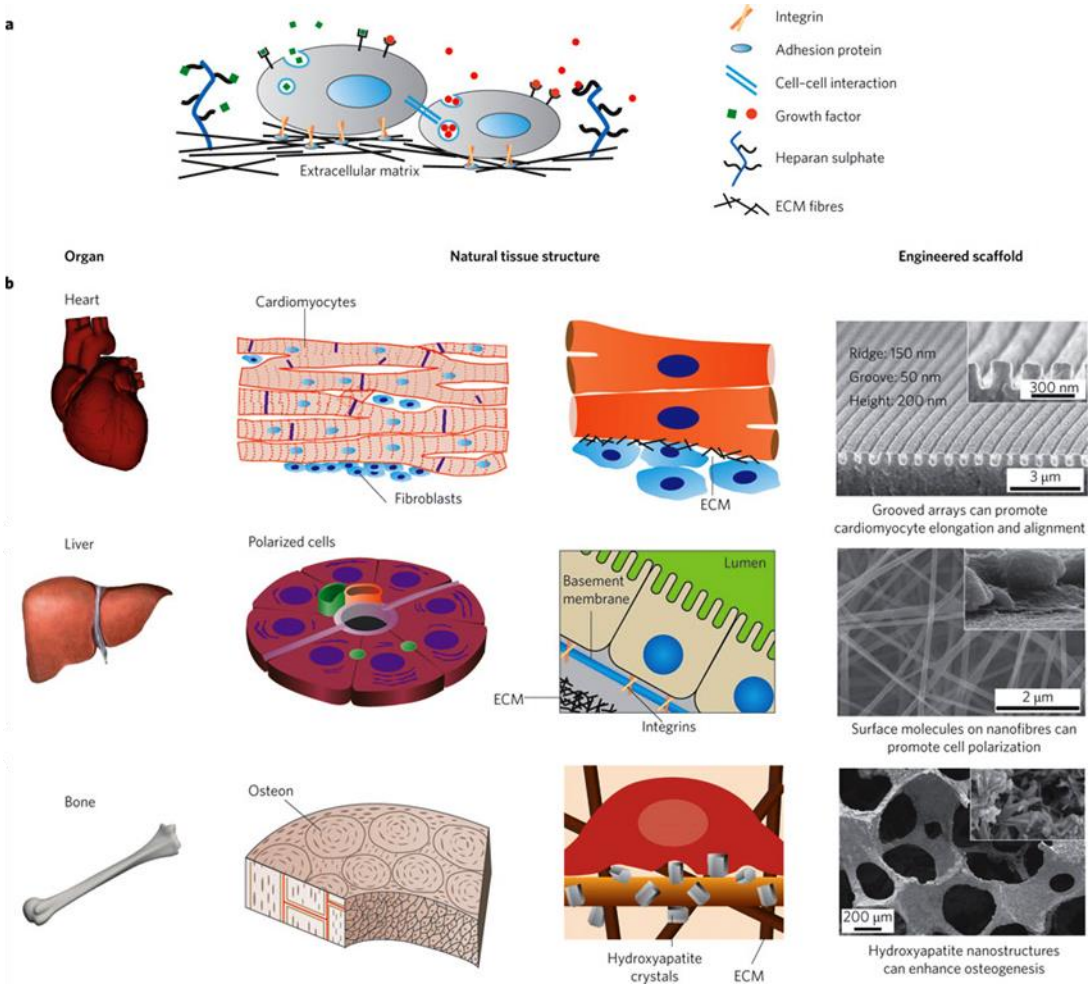

Figure 1.4 ECM provides a physical and bioactive support to the cells forming a functional tissue and organ. (a) Cell-cell, cell-ECM and soluble factor-cell interactions collectively define the cell fate. Growth factors can be sequestered in the ECM to regulate its bioactivity. (b) Hierarchically organized heart, liver and bone tissues show that ECM can take distinct nano- and micro-scale architectures that meet the physiological function. Consequently, a synthetic scaffold or cell support can be designed to mimic functionalities of the natural tissue to mimic the native microenvironment of the cells. Scanning electron micrographs of the synthetically engineered scaffolds are shown on the right hand side (Reproduced from Ref. 73 with permission from Nature Publishing Group).

Composition and structural organization of the ECM is also heterogeneous, varying within and between tissues (Figure 1.4).[74] A typical example of the ECM of cardiac muscle tissue require elongated and aligned cell bundles that create an anisotropic syncytium.[73] Therefore, aligned surface topography is a suitable biomimetic support for cardiac tissue engineering because they guide cardiomyocytes to align (Figure 1.4).

The ECM is mainly composed of two classes of biomacromolecules: fibrous proteins and glycosaminoglycans (GAGs).[74] Fibrous ECM proteins, including collagen, elastin and fibronectin, constitute the structural backbone of the ECM. These proteins also contain a number of binding sites for cells and other ECM proteins. Collagens are the most abundant fibrous proteins in the ECM, forming up to 30% of the total protein mass of a multicellular animal.[74] 28 different types of collagens have been identified in vertebrates.[75] The majority of the collagens form a triple helix, which then further assemble into fiber or network, thereby constituting the unique architecture of the ECM in a tissue.[74] In the connective tissues, for example, fibrous collagens form the backbone of the interstitial tissue. On the other hand, network collagens are incorporated into the basal membrane structure. Collagen type I is the major fibrous collagen in bone, cornea, dermis, tendon and connective tissues. Synthesis and supramolecular organization of this collagen is well-understood from nano- to meso-scales, thereby providing a rich source of information for developing various biomimetic systems.[76] Collagen type I is assembled into a triple helix via two α1 chains and one α2 chain. α chains are comprised from uniquely repetitive trimeric sequences. A glycine residue is required at the third position of each trimer in the form of X-Y-Gly where X is usually proline and Y is usually hydroxyproline.[75] The

presence of glycine residue enables rotational freedom for helix formation. Proline and hydroxyproline residues cause kink formation, which confers steric stability for the formation of triple helix. At the flanking regions of each α chain, there are non-collagenous, i.e., non X-Y-G, regions which contain binding sites for cells and other ECM proteins (Figure 1.6).[75] Preparation of functional helical collagen type I requires a number of post-translational modifications, such as hydroxylation of proline and lysine residues, glycosylation of lysine, as well as the cleavage of N- and C- terminal of the chains.[75] For mechanical strength, the collagen fibers form bundles on the order of microns to centimeters.[76] These bundles are then covalently cross-linked between lysine residues of the constituent collagen molecules by lysyl oxidase.[77] This enzyme catalyzes aldehyde formation from amines, which further react with other aldehydes or with unmodified lysine residues to establish intermolecular covalent linkages. The degree of cross-linking can tune the mechanical properties of the ECM and hence the tissue. This provides one further level of regulation over the biological properties of the tissue.[76] As such, mechanical properties have been shown to drastically regulate various cellular behaviors, such as adhesion and differentiation.[78-80]

Fibronectin is a multi-adhesive, fibrous ECM protein, which is secreted as a dimer linked by two disulfide bonds at the C-terminal of each chain (Figure 1.6). Each chain is 60-70 nm in length, 2-3 nm in thickness. Fibronectin mediates cell adhesion to the ECM proteins through its binding sites for collagen, heparin, and several cell-surface integrin receptors. There are over 20 isoforms of fibronectin that are generated by alternative splicing. A typical fibronectin contains repetitive sequences organized to form in three distinct domains (type I, II, or III domains).

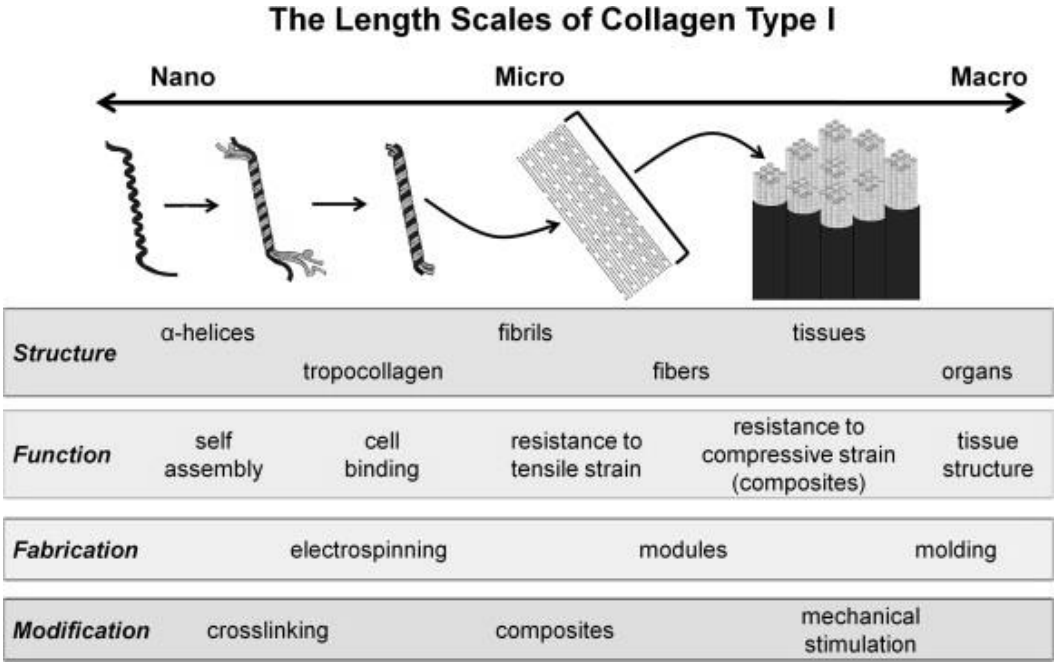

Figure 1.5 Hierarchical assembly of collagen type I from nano- to meso-scales. The assembly mechanism of this protein is a source of inspiration for synthetic fibrous architectures, which finds a wide range of applications in regenerative medicine and biomineralization (Reproduced from Ref. 76 with permission from John Wiley & Sons, Inc.).

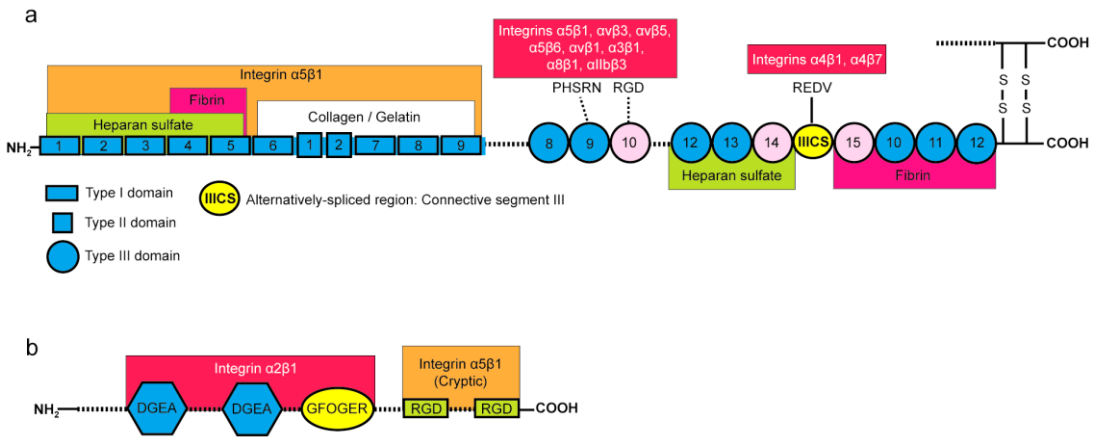

Figure 1.6 Schematic domains in fibronectin and collagen type I alpha 1. Both fibronectin (a) and collagen (b) contain a number of binding sites. Only one chain of the dimeric fibronectin is shown. Both chains have very similar sequences.[81] Bioactive sequences on the ECM proteins inspire for developing biomimetic platforms to regulate cellular behaviors, including adhesion, proliferation, migration and differentiation.

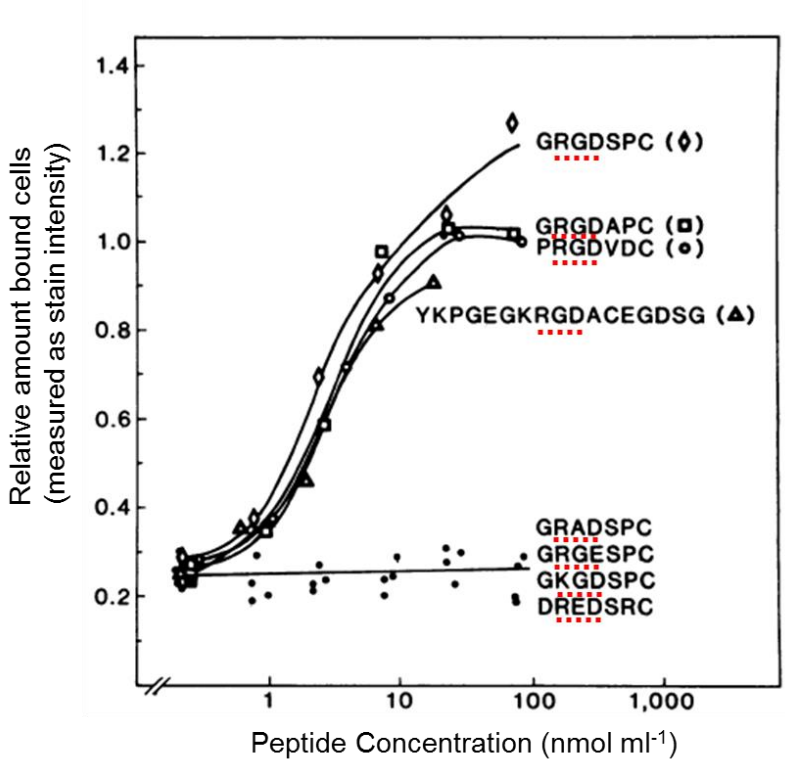

Figure 1.7 Adhesion of normal rat kidney cells to fibronectin-mimetic short peptides. The synthetic peptides were investigated for their ability to promote the attachment cells by immobilizing peptides to polystyrene culture dish. The conservative substitutions of lysine for arginine, alanine for glycine, or glutamic acid for aspartic acid each resulted in abolition of the cell attachment-promoting activity characteristic of the natural sequence. In this sense, a minimal bioactive sequence can function to mimic the bioactivity of intact fibronectin protein (Reproduced from Ref. 82 with permission from the National Academy of Sciences of the U.S.A.).

Type III domain contains binding sites for integrins, such as the sequence Arg-Gly-Asp (RGD), which appears as a minimal sequence required for recognition by integrin receptors. In this sense, RGD can mimic the biological function of fibronectin protein despite the fact that its affinity for integrins is substantially less than that of intact fibronectin. Nonetheless, the bioactivity of this short peptide sequence and others found in both fibronectin and other ECM proteins is valuable in many dimensions. First, the ability of a short peptide sequence to mimic the function of the native ECM protein motivates for large scale production through chemical synthesis at considerably lower cost. Second, batch-to-batch variations in extracted natural ECM proteins can be eliminated with the synthetic, chemically well-defined materials. Besides, natural materials always have the risk of pathogen transmission and immunogenicity, all of which are dramatically reduced by the synthetic peptides. Presenting bioactive ligands on synthetic systems can also allow steric (geometric) control to understand of how cells recognize and respond to physical and chemical signals in their microenvironment. This will pave the way of designing more efficient synthetic supports, and hence well-defined platforms for next generation biomaterials.

The initial interaction between a cell and the ECM is towards establishing adhesion and spreading. A major route for cell-ECM interaction is mediated by integrins. Integrins are heterodimer transmembrane receptors containing α and β subunits. Following binding to an ECM ligand, integrins cluster into large focal adhesion complexes.[83] Focal adhesion complex is connected to the actin cytoskeleton via vinculin proteins.[84] Consequently, this complex can couple outside mechanical stress to the intracellular tension. This tension has a large impact on cell adhesion,

spreading and migration.[72] On the other hand, a focal adhesion complex can transmit a signal from the ECM into the intracellular transduction machinery, which ultimately lead to changes in gene expression.[85] The combination of integrin subunits determines which ECM components that cell can bind to.[86] For example, major collagen receptors are integrin α1β1 and α2β1.[87] Integrin α1β1 is particularly expressed by smooth muscle cells while α2β1 integrin is abundant in epithelial cells and platelets. Nonetheless, an integrin can bear affinities for the same ECM ligand in different tissue microenvironments. For example, α2β1 mediates cell adhesion to both fibrillar and basement membrane collagens. Many other cell types, including osteoblasts, chondrocytes and endothelial cells can express both of the receptors. Additionally, integrin-mediated signaling intersects with growth factor-mediated signaling through various levels of cross-talk.

GAGs are highly polar, linear polysaccharides, which fill the extracellular space in the form of hydrogels. Depending on the molecular composition and the molecular weight, GAGs carry out wide variety of functions, including mechanical buffering, growth factor bioactivity, cell proliferation and differentiation. GAGs are found with distinct compositional and steric configurations.[88] Each GAG consists of unique disaccharide repeats along with its chain length. GAGs, including chondroitin sulfate, heparin, heparan sulfate, dermatan sulfate and keratin sulfate bear dense sulfate and carboxylate groups, which can be attributed for the anionic character of these macromolecules. However, the negative charge density and position varies significantly within the disaccharide units. Hyaluronic acid is not sulfated and hence is the GAG with the least negative charge density.

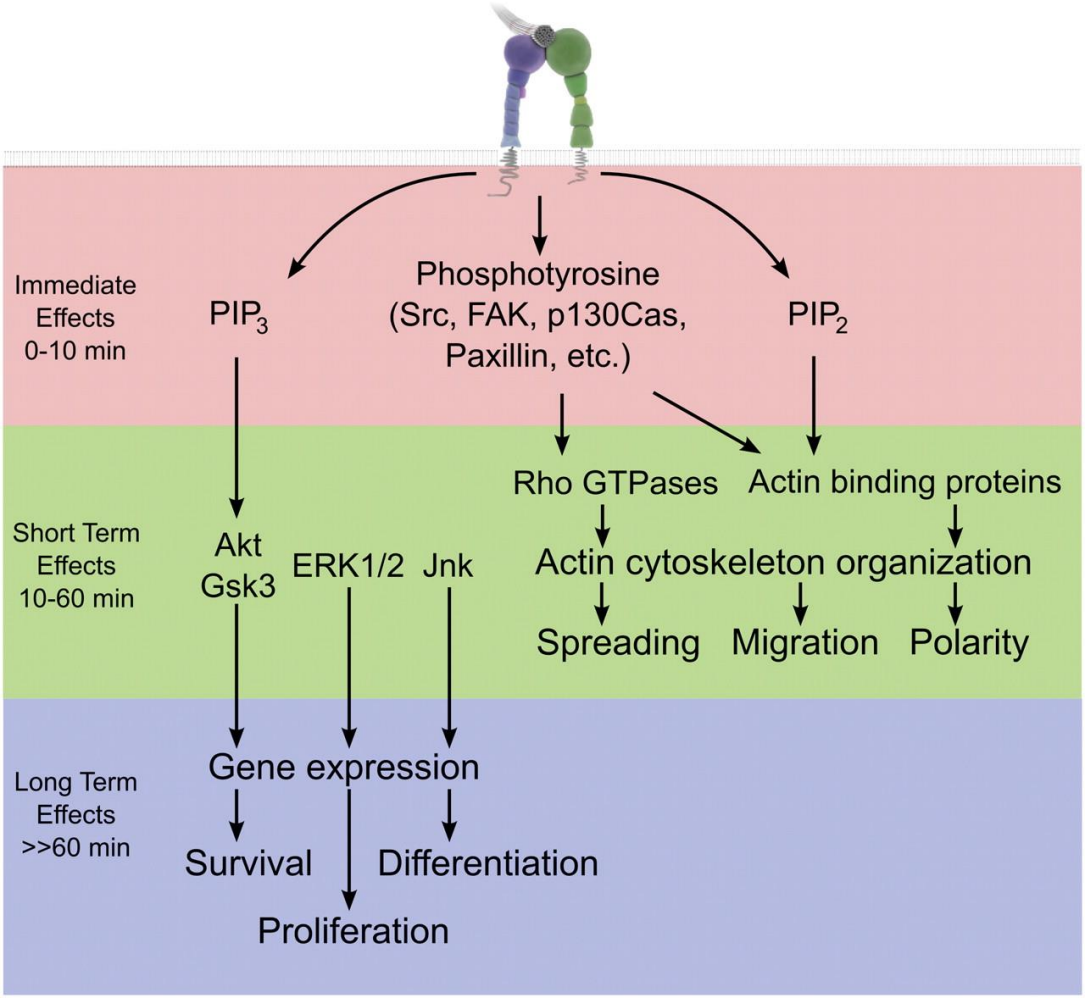

Figure 1.8 Integrin activation and its time-based downstream signaling. In the first 0-10 min, lipid kinase activity is upregulated to elevate secondary messengers. Within several minutes, these immediate effects lead to the activation of signaling pathways for reorganization of the actin cytoskeleton. In the long term, integrin activation leads to activation of proliferation and differentiation pathways, which control the cell and tissue fate (Reproduced from Ref. 86 with permission from Cold Spring Harbor Laboratory Press).

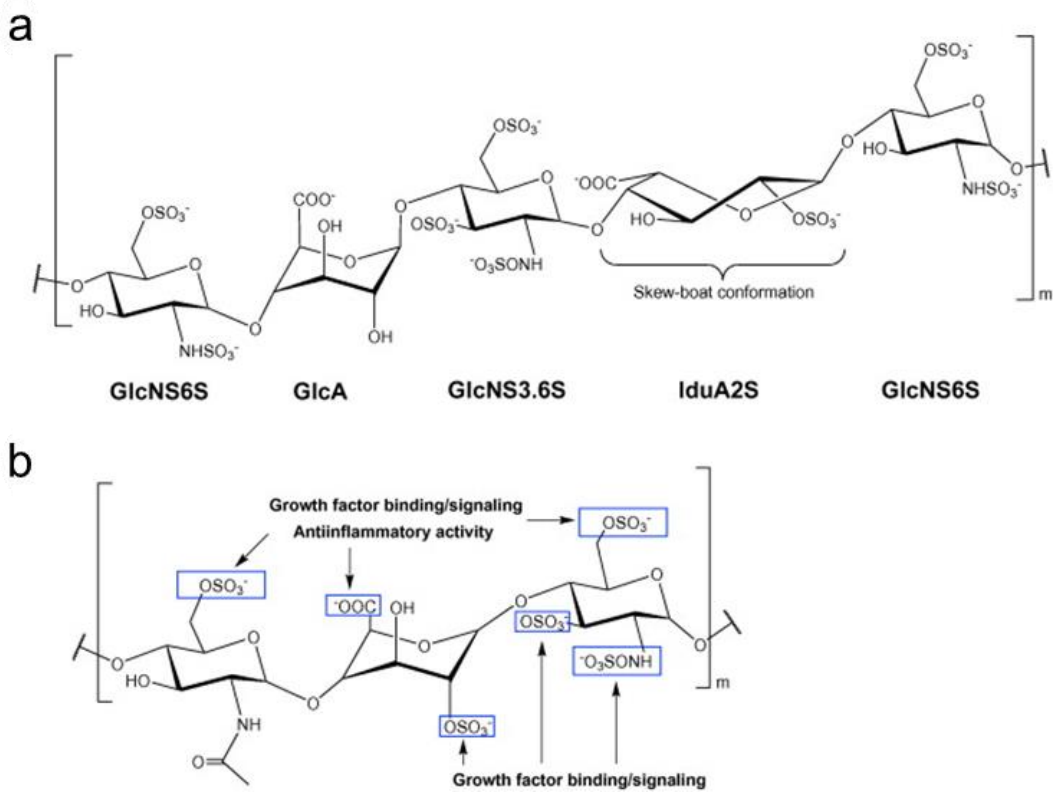

Figure 1.9 Steric conformation and functional groups are inspirational sites to mimic the biological function of GAGs. (a) A specific pentasaccharide binding sequence on heparin for anti-thrombin III. (b) Important binding sites for growth factors to a heparin/heparan sulfate. Blue boxes label the position of the sulfate groups critical in growth factor binding (Reproduced from Ref. 88 with permission from Elsevier).

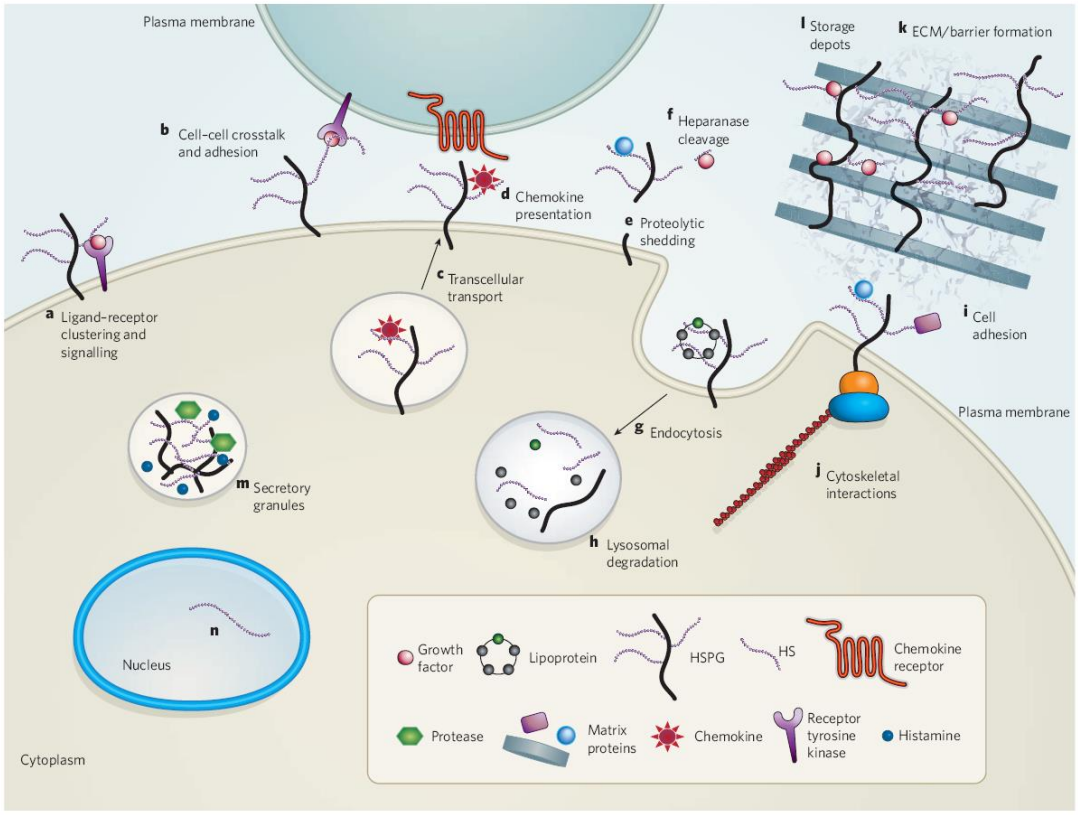

Figure 1.10 Heparan sulfate proteoglycans carry out a number of biological functions. (a, b) Heparan sulfate can act as co-receptors for growth factors and hence modulate their bioactivity. (c, d) They can also transport and modulate chemokine bioactivity by presenting them at the cell surface. (d-f) Proteolytic cleavage can liberate growth factors to modulate their bioactivity at longer distances. (g, h) Cell-surface heparan sulfates can also be internalized by endocytosis and recycled back to the cell surface. (i, j) Heparan sulfate proteoglycans can facilitate the cell adhesion to the extracellular matrix by forming a linkage between cytoskeleton and the ECM. (k, l) Heparan sulfate proteoglycans form growth factor depots and facilitate their later release following degradation (Reproduced from Ref. 89 with permission from Nature Publishing Group).

GAGs are found either as covalently attached to proteoglycans (e.g. heparan sulfate) or as independent macromolecules (e.g. hyaluronic acid). Many growth factors have been reported to bind to heparin and to heparan sulfate proteoglycans, such as fibroblast growth factors (FGFs) and vascular endothelial growth factors (VEGFs). Their interaction with the growth factors might be either sequence specific through certain binding domains or non-specific (Figure 1.9).[88] Because these macromolecules are negatively-charged, positively-charged growth factors are attracted through electrostatic interactions.[90] As a result, heparan sulfate proteoglycans act as a reservoir of growth factors by establishing stable gradients in the ECM. Such gradients of growth factors play important roles in developmental patterning and tissue heterogeneity. This binding can affect the growth factor bioactivity in two ways. First, heparan sulfate act as a cofactor of growth factor signaling, i.e., growth factor is simultaneously bind to heparan sulfate and its receptor (Figure 1.10). For example, binding of FGF to its receptor depends on its binding to heparan sulfate.[89] In an alternative mechanism, growth factors can act after being released from the ECM through degradation of ECM proteins or GAGs. With this mechanism in action, GAGs can be seen as localized reservoirs for soluble growth factors that are released as soluble ligands (Figure 1.10).[89]

In conclusion, a complex variety of parameters create an array of interactions between cells and the ECM to orchestrate responses that have essential roles in tissue morphogenesis, homeostasis and repair.[74] Such bio-regulatory parameters constitute a useful source of inspiration for guiding cellular behavior towards efficient tissue regeneration. Reconstitution of artificial microenvironments that direct cellular activities in a controlled way can provide cells with certain biofunctional cues that

guide cellular behaviors (e.g. adhesion, morphogenesis, viability, proliferation, migration and differentiation) for proper functioning of the regenerating tissue.

1.2 Bioinspired Design Strategies: From Supramolecular Chemistry to Hybrid Materials

Living organisms are extremely sophisticated to be completely imitated. Organization of biological materials require both spatial (structural) and temporal (dynamic) control for the maximum functional efficiency. Despite the emergence of minimalist design principles that enables functional biomimetic material design, the ultimate efficiency of such a system is always limited by the lack a dynamic control over the system. To overcome that limitation, we need better strategies for complex material design and for structural mimicry of the biological materials. Supramolecular chemistry is a rapidly growing field of research studying complex molecular assemblies resulting from weak intermolecular forces.[91] As opposed to traditional organic material synthesis, which requires covalent bond formation, synthesis of supramolecular species requires formation of noncovalent interactions, such as dispersion forces, hydrogen bond, and hydrophobic interactions. Biological systems rely heavily on such assemblies with highly stereospecific processes, such as multi-protein complexes, receptor-ligand interactions, complete viral assembly, and so forth.[1, 91] Although individual strength of such forces are significantly below to that of a covalent bond, a number of them can together hold a supramolecular species intact with an exceptional stability, as nicely exemplified in the formation of amyloid plaques in Alzheimer's disease.[92, 93]

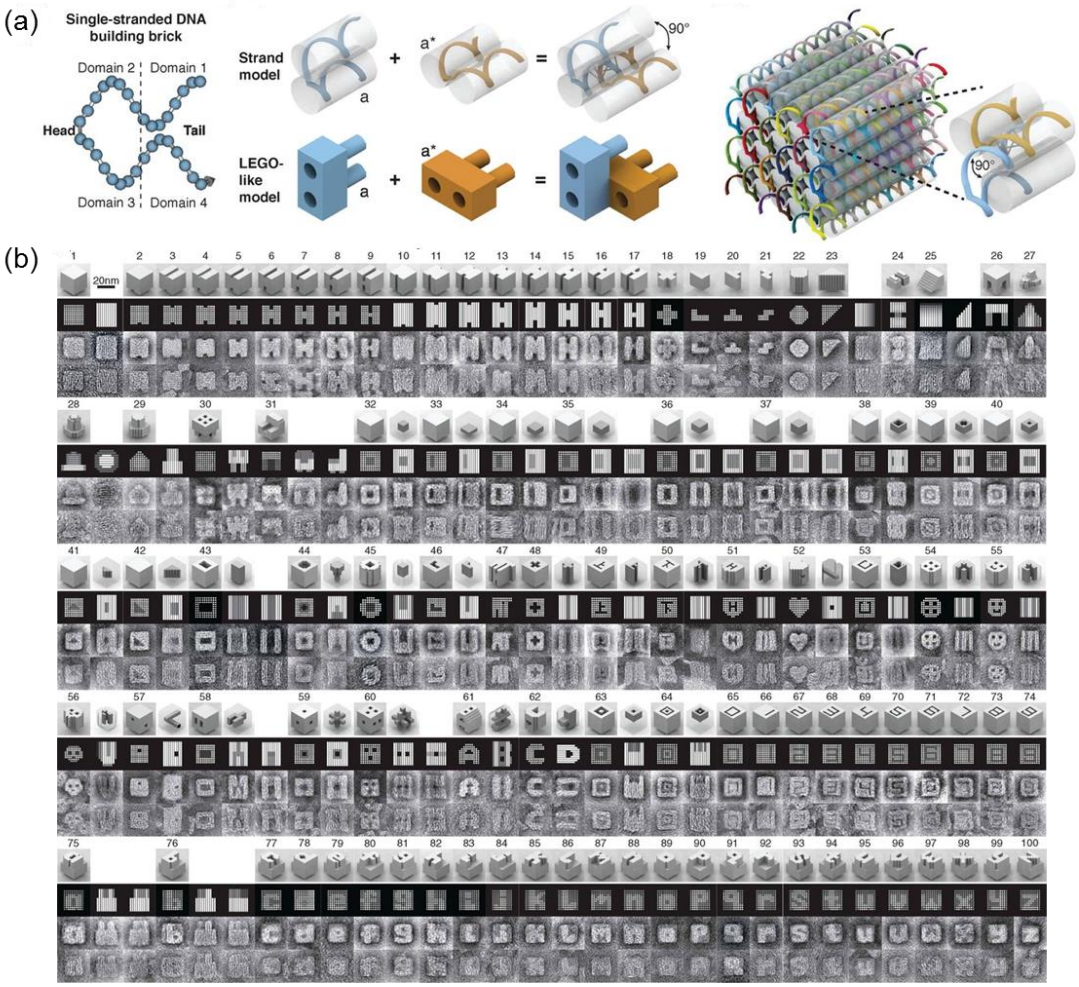

Figure 1.11 Sequence-specific information of DNA provides a vast source for programmable supramolecular materials. (a) DNA strands can be designed to share complementary domains which form larger LEGO-like bricks. (b) Bricks can be further used as the building blocks to form more complex three-dimensional structures with cavities (Reproduced from Ref. 94 with permission from American Association for the Advancement of Science).

In a typical supramolecular design, building blocks carry the stereospecific information, which drives the directional assembly of its components from a simple aggregation of a condensed matter to highly organized system with increasing complexity. Self-assembling building blocks that organize into well-defined supramolecular architectures can also be regarded as a programmed system. Therefore, understanding, inducing and directing the self-assembly process is key to building complex materials.[95]

DNA origami is a prime example of this endeavor. As the ultimate information carrier of life in the form of Watson-Crick pairing of nucleic acids, programmed assembly of DNA strands can be exploited to obtain intricate structures with remarkable spatial and temporal control (Figure 1.11).[94, 96] Thus, the degree of information encrypted in the system determines the overall complexity of a material.

Supramolecular polymers have recently opened a whole new avenue to introduce the supramolecular design principles into the polymer world. A supramolecular polymer can be synthesized by the directional, noncovalent assembly of monomers into one-dimensional high-aspect-ratio nanofibers.[97] Therefore, an intrinsic advantage of a supramolecular polymer is their dynamic ability of depolymerization under mild conditions. This feature is commonly exploited by the living systems. For example, dynamic assembly-disassembly of long cytoskeletal structures is vital for a number of cell functions.[97] Besides, noncovalent linkages can easily reform even at room temperature and atmospheric pressure, thereby imparting a self-healing character to supramolecular polymers. Aida *et al.* proposes two mechanisms for supramolecular polymerization: random-coil supramolecular polymers and ordered supramolecular polymers.[97]

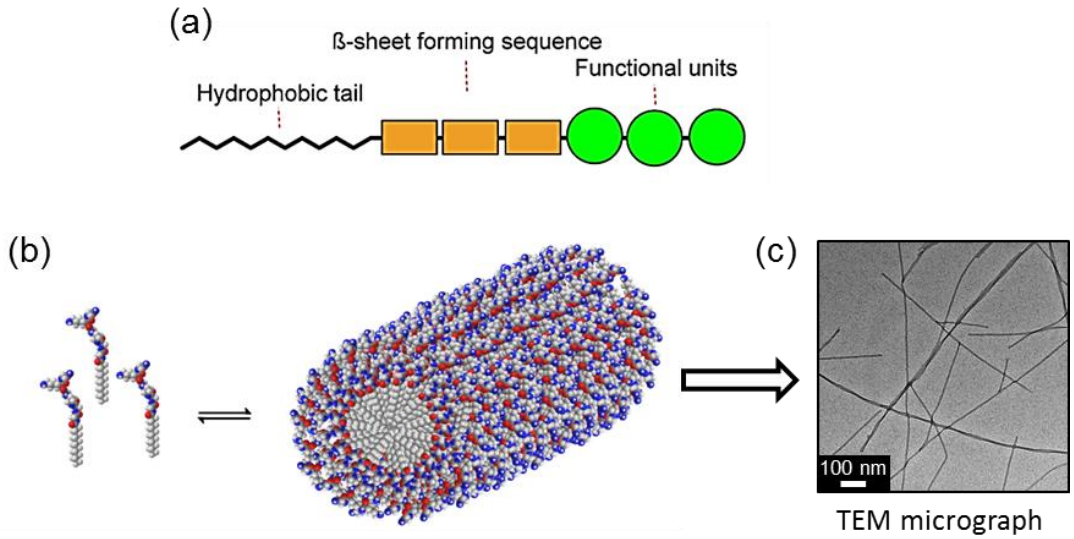

Figure 1.12 Rationally-designed modular peptide amphiphiles can dynamically assemble into long one-dimensional nanofibers. (a) Schematic of the modular design of a peptide amphiphile with basic domains of hydrophobic tail, β-sheet producing unit and the functional units. (b) (Left) Stimuli-responsive, reversible assembly of monomeric peptide amphiphiles into ultra-high-aspect-ratio nanofibers. (Right) TEM micrograph of peptide nanofibers stained with osmium tetroxide.

In random-coil supramolecular polymers, there is no long-range internal order. Typically an isodesmic supramolecular polymerization is analogous to the stepwise growth mechanism of traditional polymers. The resulting polymers are characterized by their high polydispersity. In ordered supramolecular polymers, a stable (or metastable in the observed time interval) nanostructure is formed with a high degree of internal order.

One important example of type of material is self-assembled peptide nanofibers.[98] Self-assembled peptide-based materials have attracted a special attention because of their inherent biocompatibility and chemical versatility.[99-103] For regenerative medicine applications, self-assembled peptides can be designed to form one-dimensional nanofibers imitating the ECM in both two- and three- dimensions.[99, 102, 104-109] Peptide amphiphiles are among these self-assembling peptide systems (Figure 1.12). A typical peptide amphiphile structure contains several modular units that carry information for self-assembly into one-dimensional nanofibers.[57, 58, 106] A hydrophobic segment covalently attached to the end of a peptide chain forces packing of PA monomers into micellar assemblies. In water, the hydrophobic segment is buried inside the nanofiber exposing hydrophilic part to the outer environment. Hydrophobic amino acids having high β-sheet making propensity, such as Val or Leu, are conjugated next to the hydrophobic segment of the PA structure. The amide backbone of this part facilitates β-sheet secondary structure through hydrogen bonds in the direction of nanofiber elongation. Diameter of a typical peptide amphiphile nanofiber is ~10 nm with a mesh size of the entangled network in the range of 5-200 nm.[98, 110] Modifying the amino-acid sequence in the modular units of peptide amphiphiles drastically affect the shape of the final supramolecular

structure and their ability to form three-dimensional networks.[111-113] Because of the design principle, PA nanofibers can display bioinstructive ligands in a multivalent fashion to support adhesion, proliferation, and differentiation of various cell types, including bone, cartilage, endothelial, and nerve cells as well as their progenitors.[109, 114-116]

CHAPTER 2

2 Selective Adhesion and Growth of Vascular Endothelial Cells on Bioactive Peptide Nanofiber Functionalized Stainless Steel Surface

This work is partially described in the following publication:

Ceylan H., Tekinay, A. B., Guler, M. O., *Biomaterials* 32(34), 8797–8805, 2011.

2.1 Objective

Metal-based implants such as stents are the most preferred treatment methods for coronary artery disease. However, impaired endothelialization on the luminal surface of the stents is a major limitation occasionally leading to catastrophic consequences in the long term. Coating the stent surface with relevant bioactive molecules is considered to aid in recovery of endothelium around the wound site. However, this strategy remains challenging due to restrictions in availability of proper bioactive signals that will selectively promote growth of endothelium and the lack of convenience for immobilization of such signaling molecules on the metal surface. In this study, we developed self-assembled peptide nanofibers that mimic the native endothelium extracellular matrix and that are securely immobilized on stainless steel surface through mussel-inspired adhesion mechanism. We synthesized Dopa-conjugated peptide amphiphile and REDV-conjugated peptide amphiphile that are

self-assembled at physiological pH. We report that Dopa conjugation enabled nanofiber coating on stainless steel surface, which is the most widely used backbone of the current stents. REDV functionalization provided selective growth of endothelial cells on the stainless steel surface. Our results revealed that adhesion, spreading, viability and proliferation rate of vascular endothelial cells are remarkably enhanced on peptide nanofiber coated stainless steel surface compared to uncoated surface. On the other hand, although vascular smooth muscle cells exhibited comparable adhesion and spreading profile on peptide nanofibers, their viability and proliferation significantly decreased. Our design strategy for surface bio-functionalization created a favorable microenvironment to promote endothelial cell growth on stainless steel surface, thereby providing an efficient platform for bioactive stent development for long term treatment of cardiovascular diseases.

2.2 Introduction

The World Health Organization describes cardiovascular diseases as number one cause of death globally. Currently, stent implantation is the most widely used method of performing coronary intervention because of its immediate success in preventing acute vessel closure and elastic recoil following balloon angioplasty.[117] However, in the long term, the risks of restenosis and in-stent thrombosis limit the ultimate success and ubiquitous use of this technology.[118-121] In order to improve the effectiveness of stents and to overcome the challenges associated with their use, a number of optimization strategies have been employed. Conventional drug-eluting stents and biodegradable stents are among these efforts. Drug eluting stent technologies slowly release anti-proliferative drugs to inhibit the proliferation of

smooth muscle cells and they have been a breakthrough strategy to reduce the rate of in-stent restenosis.[122, 123] Nevertheless, since anti-proliferative role of the drugs delay endothelialization, blood is exposed to the stent struts and/or to the surface coating, markedly increasing the propensity of thrombosis.[124, 125] Delayed or impaired endothelialization also limits the long-term success against restenosis.[125, 126]

Endothelial cells are responsible for proper functioning of the coronary arteries, tightly controlling the migration and proliferation of smooth muscle cells, and inhibiting platelet activation inside the blood. Rapid recovery of endothelium at the coronary intervention site is, therefore, considered to be a critical factor in the healing process of the arterial walls. For this reason, an optimal cardiovascular therapy should target selective growth of endothelium on the stent surface, rather than ubiquitously blocking the growth of all residual cells by administering a number of toxins within the arteries. For this purpose, mimicking the native tissue properties to promote re-formation of endothelium will be the most advantageous strategy to succeed in the long-term treatment of cardiovascular diseases. The conventional stent technologies largely lack this bio-functionality for selective promotion of endothelial growth.

In the present study, we developed a bioactive stent coating that provides endothelial cells selective advantages in adhesion, spreading, viability and proliferation on stainless steel surface, which is the most widely used backbone material of the coronary stents. Our coating design is composed of three basic components that are equally critical for optimal functionalization of the metal surface in order to promote endothelialization. First component is a bioactive element that mediates endothelial cell specific adhesion, spreading and growth. For this purpose, we utilized a peptide

amphiphile (PA) molecule with REDV sequence derived from the alternatively-spliced IIICS-5 fibronectin domain. The REDV epitope is recognized by α4β1 integrins and had been reported to selectively promote endothelial cell adhesion and spreading over smooth muscle cells and platelets.[127, 128] Second component includes a Dopa molecule which is a biocompatible biological adhesive element for efficient immobilization of bioactive molecules on metal surfaces. Dopa (3,4-dihydroxyphenyl-l-alanine) is highly enriched in mussel-adhesive system to attach the mussel body onto almost any kind of inorganic or organic surface by forming strong hydrogen bonds with hydrophilic surfaces and very strong complexes with metal ions and metal oxides.[19, 21, 129, 130] Despite strong and noncovalent adhesive character, Dopa adhesion is fully reversible.[21] With such unique properties, Dopa-mediated adhesion system offers outstanding potential in surface functionalization of metals with a wide variety of biological molecules. The third component, peptide amphiphile nanofibers, is the backbone platform that will mimic the native extracellular matrix in terms of structure and biology by presenting the bioactive REDV signal, with an optimal geometry and ligand density. By bringing together the architecture and function of extracellular matrix, self-assembled PA nanofibers sustain cell–matrix interactions at the molecular level with end results including cellular adhesion, spreading, proliferation and differentiation.[102, 106, 131] In addition, PA nanofiber scaffolds can provide both instructive cues and mechanical support to the developing tissue.[102, 106, 132] Therefore, we designed and synthesized two self-assembling PA molecules; one functionalized with REDV peptide sequence and the other with a Dopa residue (Figure 2.1). Upon their self-assembly, catechol groups of Dopa residues on the nanofibers formed surface adsorption, while REDV signals

mediated endothelial cell specific bioactivity. We analyzed adsorption of PA nanofibers and characterized surface properties of the nanofibrous network adsorbed on stainless steel surface. *In vitro* adhesion, spreading, viability and proliferation of vascular endothelial and smooth muscle cells on the nanofibers coated on stainless steel surface were characterized. We further investigated platelet attachment on the nanofibers coated on stainless steel surface.

2.3 Results and Discussion

2.3.1 Synthesis of PA molecules and characterization of their self-assembly into nanofibers

REDV-PA and Dopa-PA molecules were designed (Figure 2.1a) and synthesized for functionalization of stainless steel surfaces. REDV-PA was designed to enhance endothelial cell specific activity, including adhesion, spreading, survival and proliferation. Under flow conditions in blood, growing endothelium will feel resistance to attach to the struts of the stent or to the polymer coatings, where anti-proliferative toxin release might double the difficulty. The advantage of REDV over other popular binding sequences, such as RGD or YIGSR, is the selectivity of this ligand toward endothelial cells.[127, 128] Unlike REDV, other bio-adhesive sequences also attract platelets.[133] The rationale behind Dopa incorporation into the PA design was to immobilize REDV-conjugated fibers on the implant surface. In order to assess the specific function of Dopa and REDV, K-PA and E-PA, respectively, were synthesized (Figure 2.2). REDV-PA and Dopa-PA molecules were mixed at 1:3 ratios, respectively, to form a homogenous nanofibrous network, where all the charges are balanced.

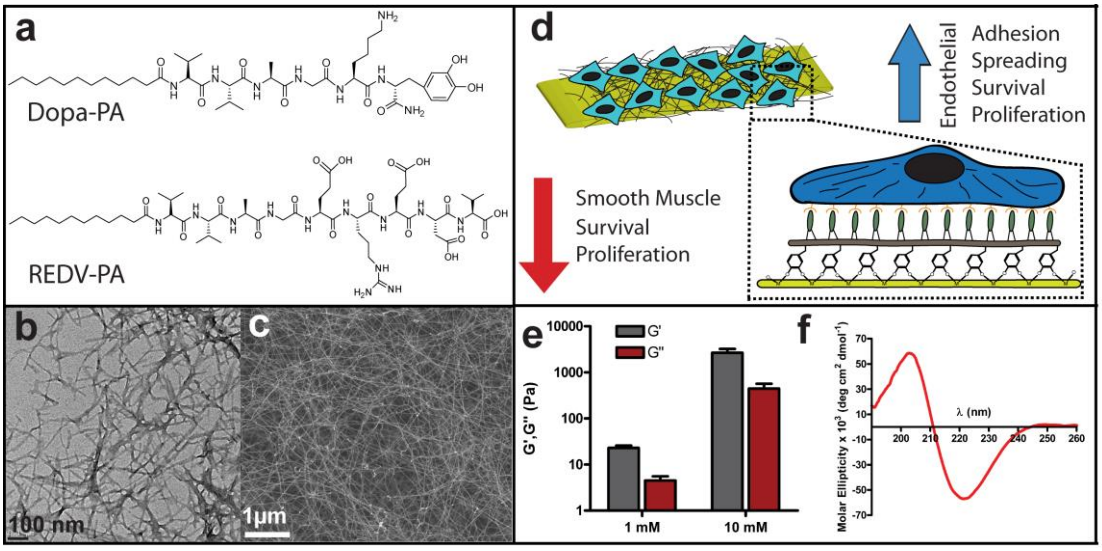

Figure 2.1 Design and self-assembly of REDV-PA and Dopa-PA molecules. (a) Chemical sketch of the molecules. (b) TEM and (c) SEM images revealed the nanofibrous network that mimic the native matrix architecture. (d) Schematic representation of REDV-PA/Dopa-PA network, which is designed to functionalize stainless steel surface to support endothelial cell adhesion, spreading, viability and proliferation. (e) Circular dichroism results revealed formation of β-sheet structure, which drives nanofiber formation upon mixing Dopa-PA and REDV-PA at physiological pH. (f) Rheology results showed gelation as a result of nanofibrous network formation by Dopa-PA and REDV-PA at pH 7.

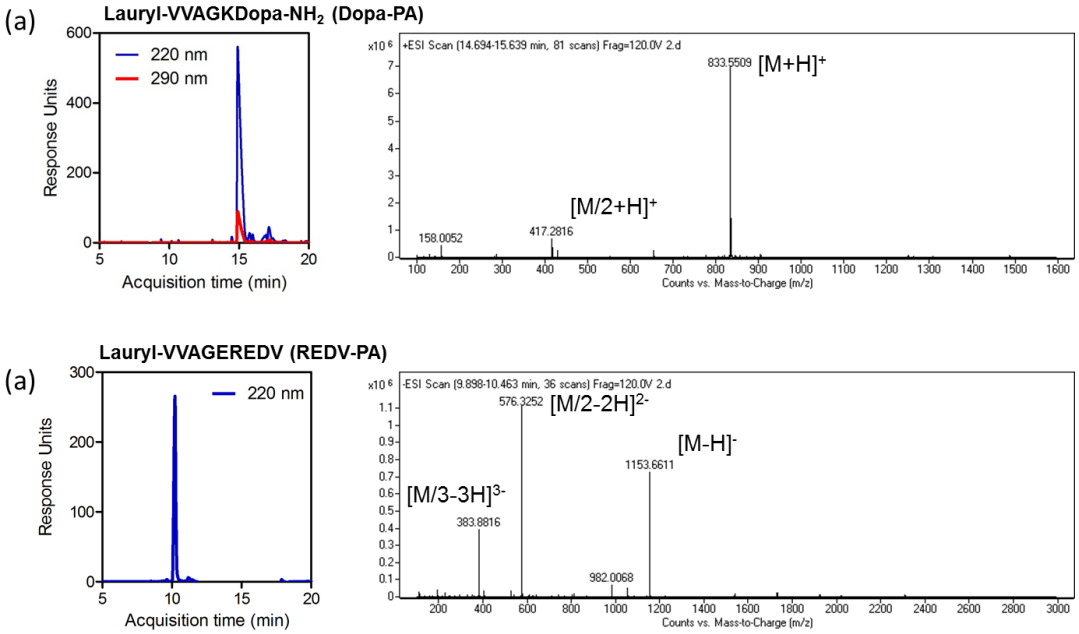

Figure 2.2 Liquid chromatography-mass spectrometry (LC-MS) analysis of the synthesized PAs. The purities of the crude products were analyzed according to the optical density at 220 nm.

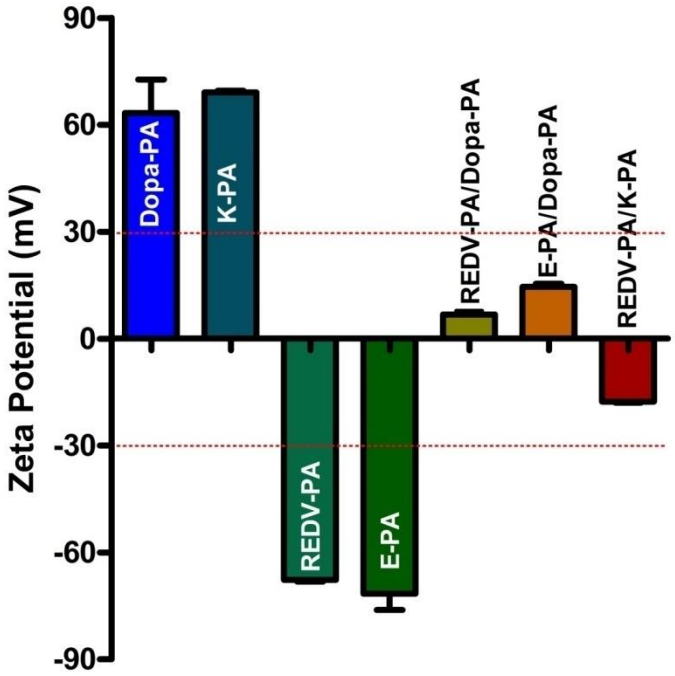

Figure 2.3 Zeta potentials of individual PA molecules and their mixtures at pH 7.4. REDV-PA and Dopa-PA were mixed at 1:3 ratio, respectively, to form REDV-PA/Dopa-PA nanofibers. E-PA and Dopa-PA were mixed at 1:2 ratio, respectively, to form E-PA/Dopa-PA nanofibers. K-PA and REDV-PA were mixed to form REDV-PA/K-PA nanofibers. All PA molecules become unstable upon mixing at physiological pH, indicating homogenous mixing of oppositely charged PA molecules into PA nanofibers.

Niece et al. previously showed that two oppositely charged PA molecules attract each other via electrostatic interactions and thus can be homogenously mixed to form heterogeneous peptide nanofibers at physiological pH.[134] To support homogenous mixing of REDV-PA and Dopa-PA into heterogeneous nanofibers, we employed circular dichroism (CD) technique. CD results revealed that when Dopa-PA and REDV-PA are in solution, their β-sheet forming capacity is limited based on the magnitude of molar ellipticity (Figure 2.1e). However, upon mixing, their combined capacity of β-sheet formation becomes much greater than the sum of the individual fibers. This showed that emerging salt bridges between oppositely charged PA molecules stabilize them to drive nanofiber formation. Zeta potential measurements supported self-assembly process as mixing two oppositely charged PA molecules reduced the stability of the mixture between −30/+30 mV (Figure 2.3). Transmission electron microscopy (TEM) and scanning electron microscopy (SEM) images revealed the porous and nano-scale architecture formed by REDV-PA/Dopa-PA that recapitulated the structure of native extracellular matrix (Figure 2.1b, c). Rheology measurements indicated formation of a hydrogel (G′>G″) at both 1 mM and 10 mM concentrations of PA mixtures even within 10 min at pH 7.4 (Figure 2.1f). This result further confirmed the formation of a scaffold formed by the self-assembled REDV-PA/Dopa-PA nanofibers at physiological pH.

2.3.2 Adsorption analysis and surface characterizations of the nanofibers on stainless steel surface

Adsorption of REDV-PA/Dopa-PA nanofibers onto stainless steel surface was primarily inspected by XPS, FT-IR, and SEM techniques. The primary reason for

choosing stainless steel for adsorption study is that most of the currently available coronary stents are made out of stainless steel, primarily due to its exceptional biocompatibility.[135] The complete suppression of photoelectron peaks of iron (Fe 2p) and chromium (Cr 2p) from the stainless steel surface and the emergence of a new nitrogen (N 1s) peak along with increased carbon (C 1s) peak after the washing were considered as evidence for the permanent adsorption of REDV-PA/Dopa-PA nanofibers (Figure 2.4a). In order to verify that the adsorption was mainly Dopa-mediated, but not due to simple electrostatic interactions between PA nanofibers and the steel surface, we formed peptide nanofibers by mixing REDV-PA and K-PA molecules at pH 7.4 at 1:3 ratios, respectively. In this construct, the nanofibers were functionalized with bioactive REDV peptide, but did not contain Dopa residue. Under the same washing conditions, REDV-PA/K-PA poorly attached onto the steel surface and did not form a peptide layer. These observations emphasize the critical role of Dopa in adhesion of nanofibers onto the stainless steel surface for convenient surface functionalization. Using SEM, we further characterized and confirmed the adsorbent species in REDV-PA/Dopa-PA samples on stainless steel surface to be PA nanofibers (Figure 2.4b). FT-IR spectrum of adsorbed REDV-PA/Dopa-PA nanofibers on stainless steel was found to be similar to the FT-IR spectrum of previously reported Mefp-1 protein adsorbed on ZnSe surfaces.[129] From this spectrum, amide I, amide II and Dopa-specific peaks were assigned (Figure 2.4c). FT-IR spectra in the range of 980 and 1760 cm^{-1} for PA nanofibers adsorbed on stainless steel surface provided information to characterize the presence of Dopa on adsorbed PA nanofibers. In peptide structures, amide I is the most intense absorption band, which is characterized by absorption in the range of 1600-1700 cm^{-1}.

Absorption at this range is governed by the stretching vibrations of the carbonyl (C=O) and amide (C-N) groups. The exact localization of the band center is related to the secondary order of the structure. In our experiment, the amide I band was found to be centered to 1639 cm^{-1}.[129] Absorption at this wavenumber had been previously reported to indicate β-sheet-rich secondary order. This observation is consistent with the self-assembly-driven nanofiber formation by means of beta sheets between adjacent micelles and with the results of circular dichroism measurements (Figure 2.4c). Amide II is characterized by absorption in the range of 1490 to 1600 cm^{-1}; 1540 cm^{-1} in our construct [129, 136]. It mainly derives from N-H bending and C-N stretching vibrations. The difference in position of the amide II band is believed to result from differences in experimental conditions.[129] Absorption around the band centered at 1455 cm^{-1} is expected for the vibration of substituted aromatics.[137] In previous studies, similar bands were characterized for adsorbed mefp-1 protein in this region and were attributed to the presence of Dopa.[129, 136, 137] The band centered at 1382 cm^{-1} is due to the alkane -C-H bending that is found in peptide backbone.[138] The band that is centered at 1236 cm^{-1} was previously associated with C-O stretching vibrations of the catecholic side chains of Dopa. [129, 138, 139] The broad band spanning 960 and 1120 cm^{-1} is reported to arise from the carboxylic and phenolic residues, probably due to the presence of E-PA and Dopa-PA.[129] Change in the surface hydrophilicity due to the adsorbing peptide layer was investigated by contact angle measurements. The contact angle of the bare stainless steel surface was measured to be 86.0 ± 1° (Figure 2.4d). The peptide layer radically decreased the contact angle value below 10° (Figure 2.4e).

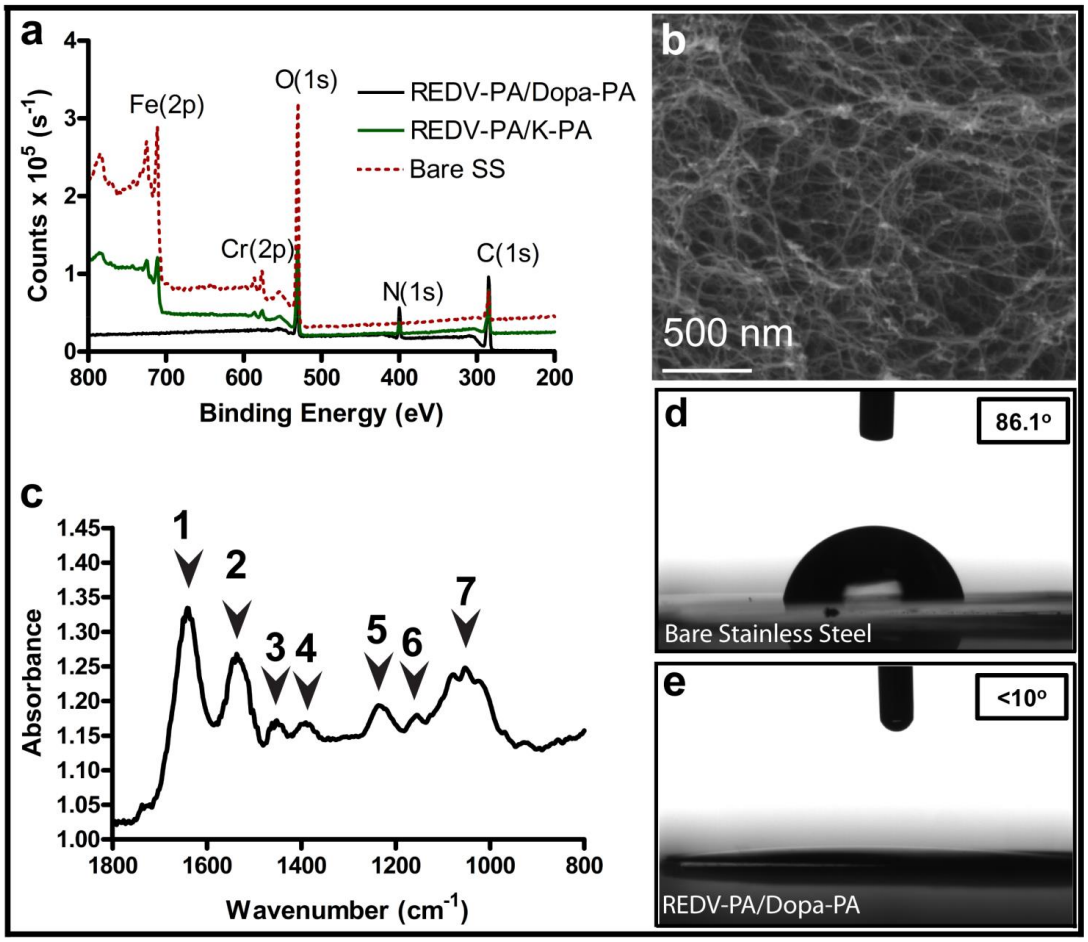

Figure 2.4 Adsorption of REDV-PA/Dopa-PA nanofibers on stainless steel surface. (a) XPS spectra of REDV-PA/Dopa-PA, REDV-PA/K-PA adsorbed and bare stainless steel surfaces. (b) SEM micrographs acquired on the REDV-PA/Dopa-PA-adsorbed steel surface. (c) FT-IR spectra acquired on REDV-PA/Dopa-PA adsorbed surface. (d, e) Contact angles on bare and REDV-PA/Dopa-PA adsorbed stainless steel surfaces.

This can be explained by the highly porous and hydrophilic surface characteristics manifested by the outer surfaces of adsorbent PA nanofibers.

2.3.3 Characterization of the cellular responses on peptide nanofibers

Adhesion and spreading are the first events of cellular response to a substrate. REDV is an endothelial cell specific adhesive ligand found in the alternatively-spliced IIICS-5 domain of human plasma fibronectin.[127, 128] This epitope was reported to mediate cell adhesion and spreading through α4β1 integrin in endothelial cells, but not in smooth muscle cells and fibroblasts.[127, 128] By functionalizing PA nanofibers with this ligand, we aimed to create a microenvironment that imitates native matrix but selectively favors endothelium growth. For these reasons, the ability of PA nanofibers to functionally mimic native extracellular matrix was evaluated by analyzing first early adhesion and spreading of vascular cells on REDV-PA/Dopa-PA coated steel surfaces. Early adhesion and spreading experiments were carried out under serum-free conditions in order to avoid the interference of soluble ECM proteins found in the serum, to the observed behavior. Similarly, any unbound PA nanofibers were removed from the coated surface by PBS washing in order to prevent their interference into biological activity when they are in solution. In addition, the interference of endogenous proteins was minimized with a pre-treatment of BSA and cyclohexamide, a known translation inhibitor. Our results indicate that adhesion of HUVECs on REDV-PA/Dopa-PA coated surface was increased more than 7 folds compared to bare steel surface at 2 h (Figure 2.5a, c, d). Similar trends were observed on coated glass and tissue culture plate surfaces (Figure 2.6a).

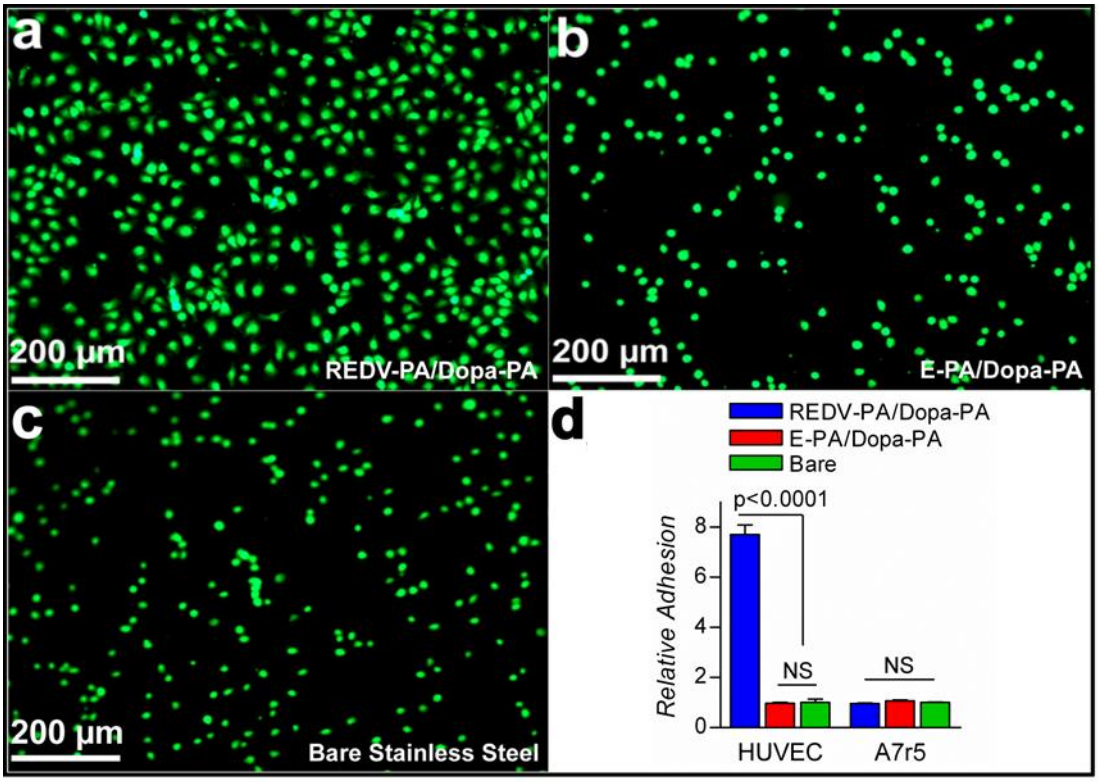

Figure 2.5 Representative calcein-AM stained fluorescent images of HUVECs attached on the stainless steel surfaces. (a) HUVECs on REDV-PA/Dopa-PA nanofibers, (b) E-PA/Dopa-PA nanofibers, (c) bare steel surface at 2 h. (d) Relative adhesion of HUVECs and A7r5 smooth muscle cells on REDV-PA/Dopa-PA and E-PA/Dopa-PA coated surfaces with respect to the bare stainless steel surface at 2 h. NS: Non-significant.

Despite such noteworthy increase in adhesion of HUVECs on REDV-functionalized PA nanofibers, there was no significant difference in adhesion of A7r5 vascular smooth muscle cells at 2 h on PA coated or uncoated stainless steel (Figure 2.5d) and glass (Figure 2.6c) surfaces. Moreover, a relatively slight (~0.2 fold) decrease in adhesion of these cells was observed on tissue culture plate surfaces when coated with REDV-PA/Dopa-PA nanofibers at 2 h. The selective bias of REDV-PA/Dopa-PA nanofibers toward endothelial cells in adhesion strength shows the critical role of REDV within this construct. To further verify this, we synthesized a negatively-charged PA molecule, E-PA, which can self-assemble with Dopa-PA but lacked REDV signal. E-PA was mixed with Dopa-PA at 1:2 ratios, to balance the charges and thus to drive nanofiber formation. The adhered number of HUVECs on E-PA/Dopa-PA coated stainless steel surface was reduced to a level comparable to the bare steel surface (Figure 2.5b, c, d). In addition, adhered number of A7r5 cells was found to be insignificant between REDV-PA/Dopa-PA and E-PA/Dopa-PA coated steel surfaces (Figure 2.5d). This crashing drop in the number of adhered HUVECs in the absence of REDV further underlies the crucial bioactivity and, more importantly, selectivity provided by this ligand in cell adhesion. By exploiting the sensitivity of HUVECs on REDV-PA/Dopa-PA, we qualitatively addressed the homogeneity of the REDV-PA/Dopa-PA coating and the reproducibility of the ligand density. In parallel to the adhesion behavior, HUVECs showed improved spreading morphology on REDV-PA/Dopa-PA coated steel surfaces at 2 h than on bare stainless steel surface and on E-PA/Dopa-PA nanofibers (Figure 2.7a–i). HUVECs gained their native morphology on REDV-PA/Dopa-PA within 2 h with an average cell diameter of 61.8 ± 1.19 μm.

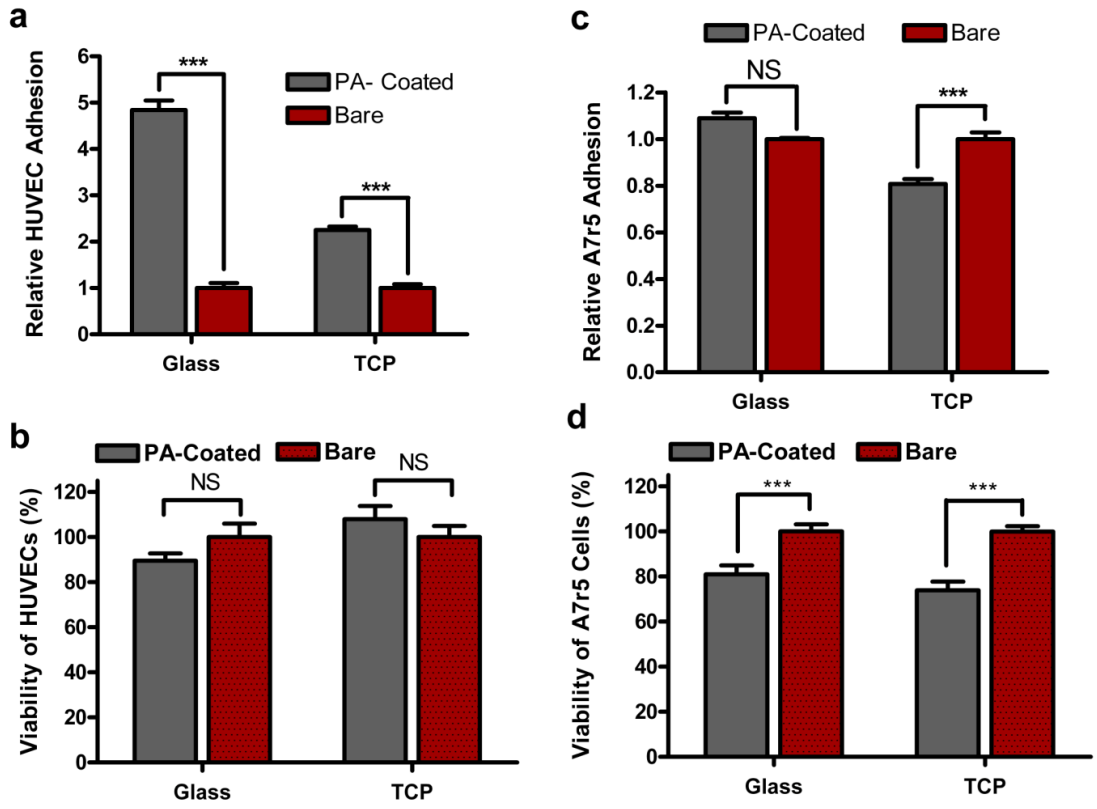

Figure 2.6 Adhesion and viability of HUVECs and A7r5 cells on REDV-PA/Dopa-PA-coated glass and tissue culture plate (TCP) surfaces. HUVECs adhered onto the PA-coated glass and TCP surfaces significantly more than bare surfaces (a). The same adhesion trend shown on different surfaces, when taken together with the adhesion profile shown in Figure 2.5, is consistent with the hypothesis of selectively enhanced endothelial cell adhesion on REDV-PA/Dopa-PA nanofibers. HUVECs were shown to be viable on REDV-PA/Dopa-PA coated on glass and TCP surfaces (c), while A7r5 cells demonstrated decreased viability (d). ** $P < 0.0001$, NS: Non-significant.

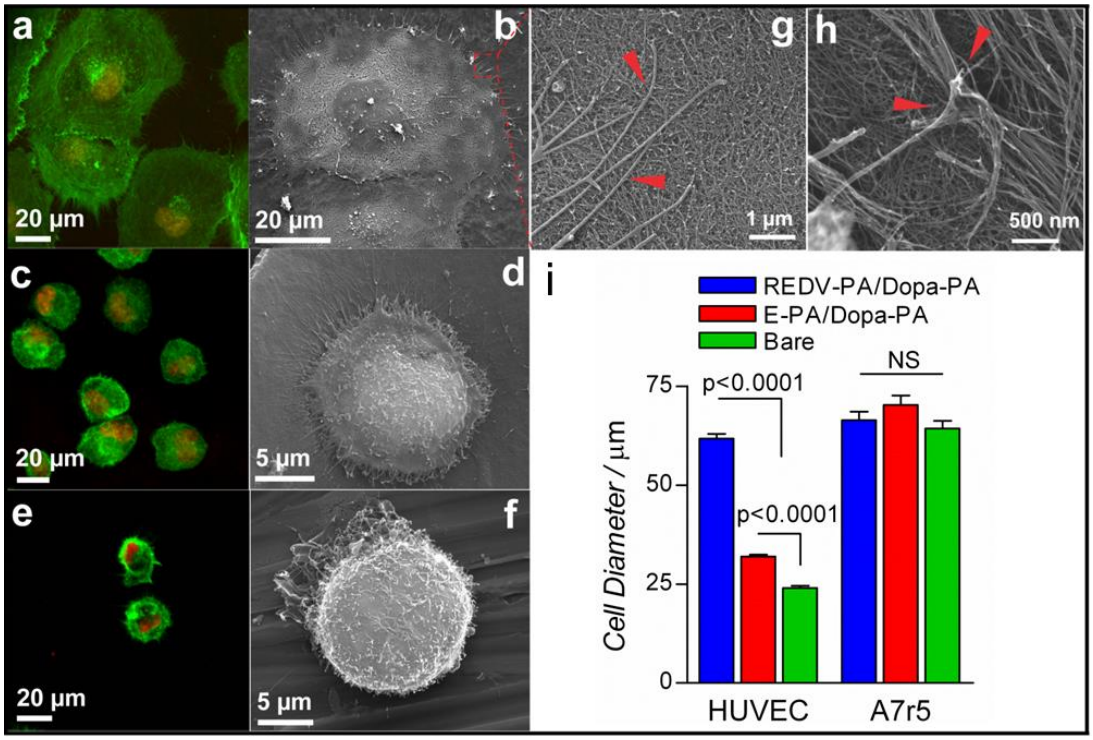

Figure 2.7 Spreading of vascular cells on REDV-PA/Dopa-PA, E-PA/Dopa-PA coated and bare stainless steel surfaces. (a, b) HUVECs spread over REDV-PA/Dopa-PA to gain their native morphologies within 2 h even in the absence of serum. On the other hands, HUVECs slightly spread on E-PA/Dopa-PA (c, d) and retained their rounded shape on stainless steel surface (b, d). (g) HUVECs formed dynamic interactions with their surrounding REDV-PA/Dopa-PA nanofibers. By this way, REDV-PA/Dopa-PA networks imitate the native extracellular matrix; HUVECs extend protrusions on the matrix within 2 h (as shown by red arrows) and exert force (h) to pull the network. a, c and e are confocal images. Green regions indicate filamentous actin stained by Phalloidin-TRITC, while red regions indicate the nucleus stained by TO-PRO®-3 iodide. (b, d, f, g and h) SEM micrographs. NS: Non-significant.

Their average cell area is almost 6 folds higher than HUVECs seeded on bare steel surface and nearly 3.5 folds higher than seeded on E-PA/Dopa-PA. HUVECs seeded on E-PA/Dopa-PA nanofibers had an average diameter of 31.9 ± 0.48 μm (nearly 1.7 folds of increase in cell area compared to the bare steel surface), again, highlighting the significance of REDV ligand for early spreading of endothelial cells on stainless steel surface. On the other hand, there was no significant difference in the average cell diameter of A7r5 cells seeded on neither REDV-PA/Dopa-PA nor on E-PA/Dopa-PA relative to bare metal surface. Overall, we demonstrate that REDV sequence on REDV-PA/Dopa-PA nanofiber network functions as a selective bioactive domain for endothelial cells by increasing their adhesion strength and spreading onto the stainless steel surface, two vital factors in the way of forming a monolayer inside the stent surface for functional regeneration.

After analyzing early adhesion and spreading of cells on REDV-PA/Dopa-PA coated stainless steel surface, we sought to investigate the morphology, viability and proliferation of the vascular cells in the long term. Biocompatibility of surface coating in the long term period is an important parameter to evaluate the use of this coating. In this respect, HUVECs were observed to maintain their native morphology by forming actin stress fibers on REDV-PA/Dopa-PA coated stainless steel surface at 24 and 72 h (Figure 2.8a, b, d, e). The viability of HUVECs at 24 h was found to be comparable on REDV-PA/Dopa-PA and E-PA/Dopa-PA coated and bare stainless steel surfaces (Figure 2.8c). This result was also in agreement with viability of these cells on coated glass and tissue culture plates (Figure 2.6b). Surprisingly, the viability of vascular smooth muscle cells was found to decrease sharply on both REDV-PA/Dopa-PA and E-PA/Dopa-PA coated surfaces with respect to bare steel

surface. Viable A7r5 cell number decreased to 66 ± 2.3% on REDV-PA/Dopa-PA coated stainless steel surface with respect to bare stainless steel surface. This result was parallel on glass and tissue culture plate surfaces with 80.9 ± 3.9% and 73.9 ± 3.8% viability, respectively (Figure 2.6d). It seems, however, that muscle cell viability was not caused by REDV epitope as cells behaved similarly on both E-PA/Dopa-PA and REDV-PA/Dopa-PA at 24 h. Overall, this trend of decrease in viability of smooth muscle cells on coated surfaces strengthens the idea that this coating provides an unfavorable environment for this cell type. On the other hand, increased adhesion and spreading of HUVECs with long term viability on REDV-PA/Dopa-PA coating favors endothelialization over the stainless steel surface. The adaptive and viable microenvironment provided by REDV-PA/Dopa-PA nanofibers also imparted a selective advantage for HUVECs to proliferate at a higher rate in the long term. Proliferation of HUVECs on this surface was found to increase by 16.9 ± 5.2% after 72 h compared to bare metal surface (Figure 2.8f). This increase was also observed in E-PA/Dopa-PA coated steel surface with 18.3 ± 5.4%, revealing that REDV might not be responsible for the increased proliferation. The increase in proliferation of HUVECs might be due to the adaptive microenvironment provided by the nano-scale matrix through surface topography, hydrophilicity, and structure that mimics natural matrix. On REDV-PA/Dopa-PA, HUVECs attached and spread readily, thereby gaining a competitive advantage in this biomimetic microenvironment for proliferation to form a monolayer on the metal surface. In addition, PA coating on stainless steel increases hydrophilicity (Figure 2.4d, e) of the surface, which may dramatically influence the growth of these cells on this coating. The growth of HUVECs was previously shown to increase on nano-scale rough

surfaces.[140] Proliferation rates of vascular smooth muscle cells were also in a similar trend with viability results. Relative rate of proliferation of A7r5 cells on REDV-PA/Dopa-PA coated metal surface was found to be 45.5 ± 2.8% of cells cultivated on bare metal and 50.0 ± 1.3% on E-PA/Dopa-PA coated steel surface of cells cultivated on bare surface (Figure 2.8f). Despite the fact that muscle cells attached at comparable rates and spread in similar morphology on PA coated and bare metal surfaces, the viability and proliferation of these cells remarkably decreased at 24 h and 72 h. We also noticed that REDV signal might not be the key determinant for the differences in viability of HUVECs and A7r5 cells. We implicated that the lowered proliferation rates of A7r5 and A10 smooth muscle cells were the result of the unfavorable conditions that also cause lowered viability of these cells on the peptide nanofibers. Apart from potential receptor-mediated interactions, the physical and chemical factors including surface chemistry, topography, hydrophilicity and structural and mechanical properties of the nanofibrous network, provided by peptide nanofibers, collectively, are determining factors for the long term viability and proliferation of cells.[141-143]

2.3.4 Platelet adhesion on PA nanofibers

Another major limitation of currently available vascular grafts is the risk of progression of late thrombosis. Since the main orientation of this study is to promote endothelialization on the stent surface, the recovery of endothelium is believed to regulate platelet activity inside the stent. However, it is still vital to evaluate the platelet attachment onto the bare stent coating because attachment of platelets at the implant site has been associated with thrombosis and subsequent restenosis.[144] We tested the attachment of platelets on PA coated stainless steel surfaces under static

conditions at 2 h (Figure 2.9). The number of platelets adhered on REDV-PA/Dopa-PA coated stainless steel surface was found to be 6.6 ± 0.87 folds higher with respect to bare stainless steel. However, relative adhesion of platelets on collagen I-coated surface was 70.5 ± 5.83 folds with respect to the bare surface, showing that adhesion of platelets on collagen I was more than 10 folds higher than PA network. It was also noticed that there was no significant difference in attached platelet density between REDV-PA/Dopa-PA and E-PA/Dopa-PA, thereby indicating that REDV sequence by itself has no inhibition effect on platelet binding. REDV-PA/Dopa-PA network presents a promising feature in terms of relatively low platelet adhesion. Notably, rapid recovery of endothelial monolayer inside the stent surface will successfully prevent platelet binding and activation. In addition, peptide amphiphiles are known to be biodegradable owing to their peptide nature. It is believed that as the growing monolayer of endothelial cells synthesizes their native matrix, the PA coating will be degraded without leaving any known toxic degradation products. This feature of peptide nanofibers also encouraged us to conjugate REDV and Dopa residues on these nanostructures. Also, under *in vivo* shear conditions the coating might be worn off over time despite the anticorrosive feature of Dopa. However, these issues must be addressed in a separate discussion.

2.4 Conclusion

We developed a peptide-based self-assembled nanofibrous coating functionalized with fibronectin-derived endothelial cell specific adhesion signal, REDV, and mussel-adhesive protein inspired, Dopa residue.

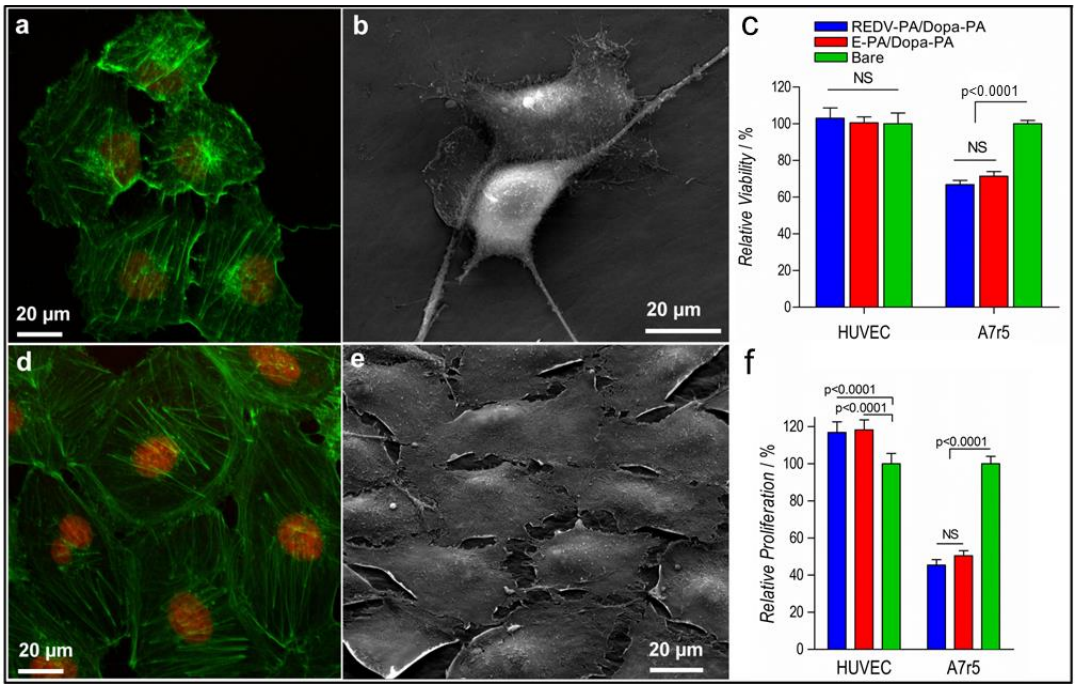

Figure 2.8 Cellular morphology, viability and proliferation at 24 h and 72 h. (a, b, d, e) HUVECs obtained their native morphology and formed filamentous actin-based stress fibers after 24 and 72 h on REDV-PA/Dopa-PA network. (c) HUVECs were completely viable on both PA surfaces compared to the bare steel surface. On the other hand, A7r5 cells showed decreased viability on both PA coated steel surfaces compared to the bare steel surface. (f) HUVECs demonstrated enhanced proliferation on both PA coated surfaces while the proliferation of A7r5 cells decreased profoundly on the PA networks. (a, d) are confocal images. Green regions indicate filamentous actin stained by Phalloidin-TRITC, while red regions indicate the nucleus stained by TO-PRO®-3 iodide. (b, e) are SEM micrographs. NS: Non-significant.

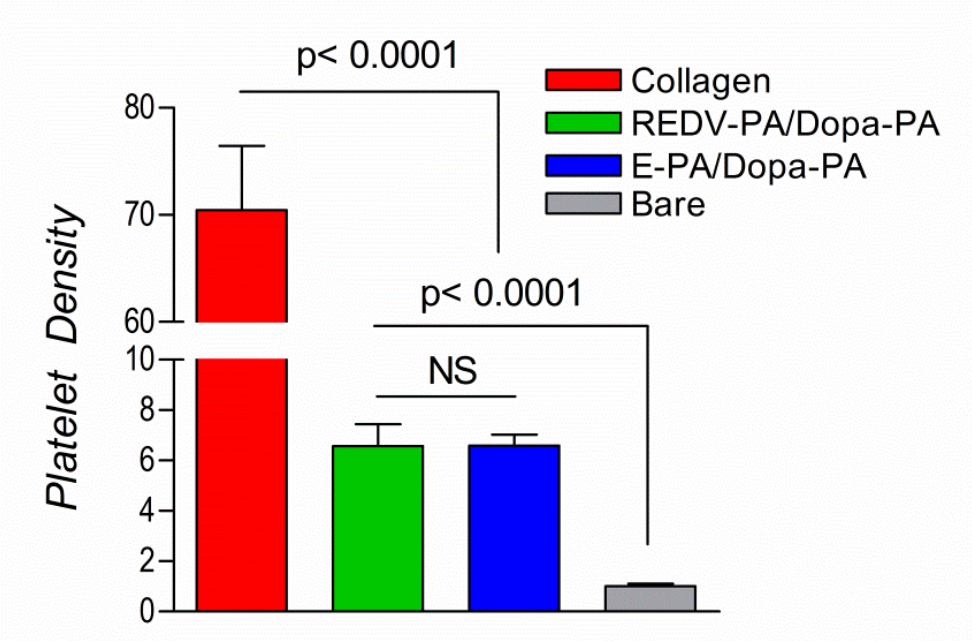

Figure 2.9 Relative attachment of platelets. Relative platelet density is normalized to bare stainless steel surface at 2 h. NS: Non-significant.

Functionalization of stainless steel surfaces with these bioactive molecules provided a native endothelium extracellular matrix-mimetic microenvironment that selectively promotes endothelial cell adhesion, spreading and proliferation. Strikingly, the results showed that the viability of vascular smooth muscle cells significantly decreased on the PA nanofibers. In addition, platelet attachment to the PA matrix in comparison to collagen I was found be significantly lower. These results show that our material provides a promising approach for future clinical use as a bioactive coating for cardiovascular stents. Overall, our findings suggest that this peptide-based bioactive matrix can address major obstacles of contemporary stent technology by combining a biocompatible and convenient surface coating technology with integrin-mediated bioactivity that promote selective endothelialization on the stainless steel surface. These results provide vast opportunities for functionalization of currently used vascular grafts and coronary stents. The long-term success of stent implantation depends on the recovery of endothelium on the luminal surface of the stent. Endothelial cells carry out an indispensable mission in the proper functioning of the arteries and have a tight control over smooth muscle cell proliferation and platelet activity. Thus a treatment strategy to promote endothelialization around the wound site would prevent long term complications like restenosis and thrombosis.

2.5 Experimental Section

2.5.1 Materials

9-Fluorenylmethoxycarbonyl (Fmoc) and other protected amino acids, lauric acid, [4-[α-(2′,4′-dimethoxyphenyl) Fmoc-amino methyl] phenoxy] acetomidonorleucyl-MBHA resin (Rink amide MBHA resin), 2-(1H-Benzotriazol-1-yl)-1,1,3,3-

tetramethyluroniumhexafluorophosphate (HBTU) and diisopropylethylamine (DIEA) were purchased from Merck and ABCR. 100–200 mesh Wang resin was purchased from NovaBiochem and valine was loaded onto it for Fmoc-Val-Wang resin. Stainless steel, cover glass (15 mm Φ) and tissue culture plates (24-well) were purchased from Small Parts, Deckglaser, and BD, respectively. All other chemicals and materials used in this study were analytical grade and obtained from Invitrogen, Fisher, Merck, Alfa Aesar, and Sigma–Aldrich.

2.5.2 Synthesis and characterization of peptide amphiphiles (PA)

Functionalized PA molecules were synthesized manually by standard solid phase Fmoc peptide synthesis chemistry. REDV-PA (C12-VVAGEREDV) and E-PA (C12-VVAGE) were synthesized on Fmoc-Val-Wang and Fmoc-Glu-Wang resins, respectively. Dopa-PA (C12-VVAGKDopa-NH_2) and K-PA (C12-VVAGK-NH_2) were synthesized on Rink amide resins. Amino acid couplings were performed with 2 equivalents of amino acids activated with 1.95 equivalents of HBTU, and 3 equivalents of DIEA for 1 equivalent of starting resin. Coupling time for each amino acid was 2 h. Lauric acid addition was performed similarly to amino acid coupling except that coupling time was 4 h. Fmoc removal was performed with 20% piperidine/dimethylformamide (DMF) solution for 20 min. 10% acetic anhydride/DMF solution was used to permanently acetylate the unreacted amine groups after each coupling step. DMF and dichloromethane (DCM) were used as washing solvents. Cleavage of protecting groups and peptide molecules from the resin was carried out by 95% trifluoroacetic acid-containing cleavage cocktail (95% TFA, 2.5% water, 2.5% triisopropylsilane) for 3 h. Excess TFA removal was carried

out by rotary evaporation. PAs in the remaining solution were precipitated in ice-cold diethyl ether overnight. The precipitate was collected next day by centrifugation and dissolved in ultra-pure water. This solution was frozen at −80 °C for 4 h and then lyophilized for one week. Synthesis of PAs were characterized by Agilent 6530 quadrupole time of flight (Q-TOF) mass spectrometry with electrospray ionization (ESI) source equipped with reverse-phase analytical high performance liquid chromatography (HPLC) with Zorbax Extend-C18 2.1 × 50 mm column for basic conditions and Zorbax SB-C8 4.6 × 100 mm column for acidic conditions. An optimized gradient of 0.1% formic acid/water and 0.1% formic acid/acetonitrile for acidic conditions and 0.1% ammonium hydroxide/water and 0.1% ammonium hydroxide/acetonitrile for basic conditions were used as mobile phase for analytical HPLC, respectively. A reverse-phase preparative-HPLC (Agilent 1200 series) system was employed for purification of REDV-PA by using Zorbax Extend-C18 21.2 × 150 mm column. Residual TFA was removed from positively-charged Dopa-PA by 0.1% HCl treatment. All lyophilized PA samples were reconstituted in 20 mM HEPES buffer at pH 7.4 for further use.

2.5.3 Self-assembled nanofibrous network formation

Nanofibers were formed by mixing negatively-charged REDV-PA and positively-charged Dopa-PA at pH 7.4 at 1:3 ratio, respectively. For Dopa control, REDV-PA and K-PA were mixed to form REDV-PA/K-PA nanofibers at pH 7.4 at 1:3 ratio, respectively. For REDV control, E-PA and Dopa-PA were mixed to form E-PA/Dopa-PA nanofibers at pH 7.4 at 1:2 ratio, respectively. These ratios were used to balance the charges on mixing PA molecules.

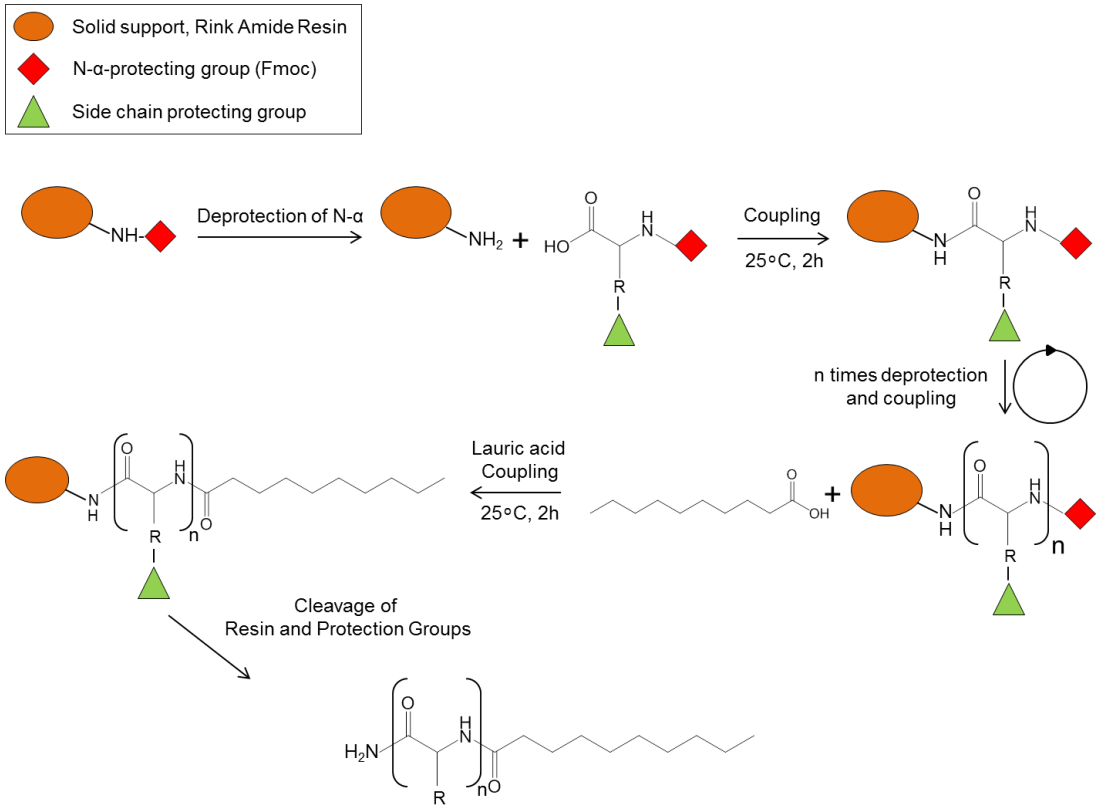

Figure 2.10 Synthesis route of a typical peptide amphiphile using solid phase peptide synthesis. This synthesis relies on subsequent removal of a base-labile protecting group from the N-terminus for coupling with an activated ester. After the completion of coupling steps, acid-labile resin linker and the side chain protections can be removed with TFA-containing cleavage cocktails.

To visualize nanofibers and the resulting network formation, scanning electron microscopy (SEM) and transmission electron microscopy (TEM) were employed. SEM samples were prepared on cleaned stainless steel surface by mixing 1 mM REDV-PA and Dopa-PA at 1:3 ratio, respectively. Following 10 min of gelation, the hydrogel was dehydrated in gradually increasing concentrations of ethanol solutions. The dehydrated hydrogel was dried with a Tourismis Autosamdri®-815B critical-point-drier to preserve the network structure. The dried samples were coated with 3 nm Au/Pd and visualized under high vacuum with a FEI Quanta 200 FEG scanning electron microscope equipped with ETD detector. TEM images were acquired with FEI Tecnai G2 F30 TEM at 300 kV. Samples for TEM were prepared by mixing 1 mM REDV-PA and Dopa-PA at 1:3 ratio, respectively, on a 200-mesh carbon TEM grid for 3 min followed by 2 wt% uranyl-acetate staining for 1 min and drying immediately under nitrogen gas. Formation of network structure at pH 7.4 was also validated by using oscillatory rheology. An Anton Paar Physica RM301 Rheometer operating with a 25 mm parallel plate configuration was used to probe the viscoelastic properties of the PA networks. Samples of both 1 mM REDV-PA and Dopa-PA or 10 mM REDV-PA and Dopa-PA were mixed on the lower stage of the rheometer at 1:3 ratio, respectively, and allowed for gelation for 10 min before the measurements. A gap distance of 0.5 mm was used with 10 rad/s angular frequency and 0.1% shear strain. To investigate the secondary structure of PA nanofibers, circular dichroism (CD) spectra of 1 x 10^{-5} M REDV-PA, 3 x 10^{-5} M Dopa-PA and their mixture at these concentrations at pH 7.4 were measured at room temperature from 260 nm to 190 nm with 0.1 nm data interval and 500 nm/min scanning speed. The results were converted to and represented as the mean residue ellipticity, θ. Zeta

potential measurements were performed with a Malvern Zeta-ZS Zetasizer using individual PA solutions or their mixture at ratios and 1 x 10^{-6} concentrations indicated above.

2.5.4 Adsorption analysis and surface characterization of PA nanofibers on stainless steel

The adsorption behavior of PA nanofibers on stainless steel surface was assessed by X-ray photoelectron spectroscopy (XPS), attenuated total internal reflectance Fourier transform infrared spectroscopy (ATR-FT-IR), contact angle measurements, and SEM 1 mM REDV-PA and Dopa-PA (or REDV-PA/K-PA nanofibers were formed as a control for Dopa activity) solutions were mixed on cleaned stainless steel surface at 1:3 ratio, respectively. In order to prevent solvent evaporation and thus to ensure adsorption in the presence of water, the samples were kept in a humidified environment for 24 h at room temperature. The substrates were then rinsed in water for half an hour with agitation, and dried at 37 °C for a further period of 24 h. In order to characterize the chemical composition and the molecular structure of the film formed on the surface upon drying; XPS and FT-IR spectra were acquired on the surface. A Thermo Scientific XPS spectrometer with Al-K_α monochromatic (100–400 eV range) X-ray source and ultra-high vacuum (~10^{-9} Torr) was employed to identify the chemical composition of the surface. The spectra were acquired from at least three random locations on the surface. VORTEX 70 Fourier transform infrared spectrometer equipped with liquid nitrogen-cooled MCT detector was utilized to identify the FT-IR spectrum of the surface by using a germanium ATR objective. The spectrum range was between 4000 and 400 cm^{-1}. The spectra were

acquired from at least three different locations on the surface. The change in the surface hydrophilicity was probed by an OCA 30 Data physics contact angle meter to measure the static water contact angles on the stainless steel surface before and after adsorbed PA nanofibers. 4 μL water droplets were used with Laplace–Young fitting for contact angle measurements. Adsorbed peptide nanofibers on stainless steel were visualized using SEM Samples were prepared by dehydrating the coating after the washing in gradually increasing concentrations of ethanol solutions. The dehydrated sample was dried with a Tourismis Autosamdri®-815B critical-point-drier. The dried samples were coated with 3 nm Au/Pd and visualized under high vacuum with a FEI Quanta 200 FEG scanning electron microscope equipped with ETD detector.

2.5.5 PA-coated surface preparation for in vitro characterizations

In order to elucidate the impact of functionalized PA nanofibers on vascular cells, cleaned stainless steel, glass and tissue culture plates were prepared by coating with PA nanofibers. Stainless steel surfaces were cleaned by using ultrasonic cleaning in acetone, ethanol and ultra-pure water, for 1 h each, sequentially. The cleaned surfaces were kept in a vacuum oven at 90 °C for 4 h to completely evaporate the residual water. Glass and tissue culture plate surfaces were used as received. Stainless steel, glass and tissue culture plate surfaces were coated with PA nanofibers by drop-casting method. 1 mM REDV-PA and 1 mM Dopa-PA solutions were mixed on the surfaces at 1:3 ratio, respectively. The coated surfaces were first air-dried in a chemical hood overnight. The substrates were further dried at 37 °C for 24 h. Sterilization of the coated substrates was carried out by UV irradiation for 2–3 h. All coated surfaces were washed with PBS for ~15 min prior to the experiments.

2.5.6 Cell culturing and maintenance

Adhesion, spreading, viability and proliferation behaviors of vascular cells on REDV-PA/Dopa-PA nanofibers were characterized by using human umbilical vein endothelial cells (HUVECs), A7r5 rat aortic smooth muscle cells (ATCC® Cat# CRL-1444™) and A10 rat aortic smooth muscle cells (ATCC® Cat# CRL-1476™). HUVECs were donated by Yeditepe University, Istanbul, Turkey. HUVECs were purified as described and characterized by staining with CD34, CD31, and CD90 surface markers.[145] These cells were found to be positive for CD31 and CD34 but negative for CD90. HUVECs and A10 cells were cultured in 75 cm^2 polystyrene cell culture flasks with 10% fetal bovine serum (FBS), 2 mM L-glutamine and 1% penicillin/streptomycin containing Dulbecco's modified eagle medium (DMEM). A7r5 cells were grown in 10% fetal calf serum (FCS), 2 mM L-glutamine and 1% penicillin/streptomycin containing DMEM. All *in vitro* experiments and passaging were carried out at cell confluence between 80 to 90% using trypsin/EDTA chemistry. Cells were diluted 1:2 and 1:3 for splitting.

2.5.7 Adhesion, spreading and cytoskeleton analyses of vascular cells on PA-coated surfaces

Early adhesion of HUVEC, A7r5 and A10 cells were analyzed on PA-coated stainless steel surfaces after 2 h of incubation. PA-coated glass and tissue culture plate surfaces were also used to evaluate the adhesion of the cells on different surfaces. Prior to adhesion experiments, HUVEC, A10 and A7r5 cells were incubated with serum-free DMEM medium supplemented with 4 mg mL^{-1} BSA and 50 μg mL^{-1} cyclohexamide for 1 h at standard cell culture conditions (37 °C, 5%

CO2 and 95% humidity). Then the cells were seeded onto the surfaces with serum-free DMEM at densities of 3×10^4, 1.5×10^4, and 1.5×10^4 cells/cm^2, respectively. The cells were incubated at standard cell culture conditions for 2 h. After 2 h, the unbound cells were washed away with PBS, and the remaining bound cells were stained with 1 μM calcein-AM (Invitrogen). Relative cell adhesions were quantified by counting the number of cells on different locations (at least 4 different locations per surface, i.e., at least 36 photographs per type of surface, such as "REDV-PA/Dopa-PA coated stainless steel surface", were acquired) of the surface using a fluorescent microscope. The total number of cells was averaged for each type of surface (i.e., coated stainless steel, bare glass, etc) and normalized to bare surfaces to evaluate the relative cell adhesion. Spreading and cytoskeletal organization of vascular cells were analyzed on PA coated stainless steel surface at 2 h, 24 h and 72 h. Samples to be analyzed at 2 h were prepared similarly to cell adhesion experiment. Preparation of the sample to be analyzed at 24 h was the same as the sample for the viability assay and preparation of the sample to be analyzed at 72 h was the same as the sample for the proliferation assay except that no EdU was added into the medium. After these time intervals, i.e. 2 h, 24 h and 72 h later, cells were fixed with 3.7% formaldehyde for 15 min and permeabilized in 0.1% Triton X-100 for 10 min. Filamentous actins were stained with TRITC-conjugated phalloidin and the cell nuclei were stained with TO-PRO®-3 iodide. The samples were analyzed with Zeiss LSM 510 confocal microscope. Cell spreading was quantified by measuring cell diameters on the equipment's software, ZEN 2008. HUVEC-matrix interactions were investigated using scanning electron microscopy. HUVECs were seeded on PA coated stainless steel surface in the same manner described in the sample preparation

for the cell adhesion experiments. Following 2 h incubation, HUVECs were fixed with 2% gluteraldehyde and 4% osmium tetroxide solutions at room temperature for 1 h each, sequentially. The samples were then dehydrated in increasing concentrations of ethanol and dried with Tourismis Autosamdri®-815B critical point drier to preserve cellular and nanofibrous structures. The samples were coated with 4 nm Au/Pd and analyzed by using FEI Quanta 200 FEG scanning electron microscope equipped with ETD detector under high vacuum.

2.5.8 Viability and proliferation of vascular cells on PA nanofibers

Viability and proliferation of HUVEC, A7r5, and A10 cells were analyzed on PA-coated stainless steel surface at 24 h and 72 h, respectively. Coated glass and tissue culture plate surfaces were also used to evaluate the viability of the cells on different surfaces. Cells were seeded onto PA coated stainless steel, glass and tissue culture plate surfaces with DMEM media supplemented with 10% FBS (for HUVECs and A10 cells) or 10% FCS (for A7r5 cells), 2 mM L-glutamine, and 1% penicillin/streptomycin at densities of 1.5×10^4, 0.75×10^4 and 0.75×10^4 cells/cm^2, respectively. Cells were incubated at standard tissue culture conditions for 24 h. After 24 h, cells were washed with and then stained with 1 μM calcein-AM. Viability of the cells on PA coated surfaces was quantified by counting the number of live cells in images taken with a fluorescence microscope. The total count of live cells was normalized to bare surfaces to evaluate the relative viability. In order to evaluate cell proliferation on PA coated stainless steel, Click-iT™ EdU assay was utilized. Vascular cells were incubated with a nucleoside analog of thymine, EdU (5-ethynyl-2′-deoxyuridine), in their cell culture media. EdU incorporates in DNA during the

synthesis phase (S phase) of the cell cycle and thus enables direct quantification of proliferation. HUVEC, A10, and A7r5 cells were seeded on the steel surfaces with DMEM media supplemented with 10% FBS (for HUVECs and A10 cells) or 10% FCS (for A7r5 cells), 2 mM L-glutamine, and 1% penicillin/streptomycin, at a density of 5×10^3 cells/cm^2. Bare stainless steel surface served as a negative control. After the initial 8 h incubation upon seeding, cell medium was replaced with 10 μM EdU-containing DMEM media supplemented with 10% FBS (HUVECs and A10 cells) or 10% FCS (A7r5 cells), 2 mM L-glutamine, and 1% penicillin/streptomycin. Cells were incubated at standard cell culture conditions for another 72 h. Cells were then fixed with 4% formaldehyde, permeabilized in 5% Triton X-100 and treated with Alexaflour-488 conjugated azide in accordance with the recommendation of the supplier. Proliferation rates of the cells were quantified upon the staining of nuclei. Using a fluorescent microscope, the average counts of stained cell nuclei were used to evaluate the relative rates of proliferation.

2.5.9 Platelet adhesion on PA nanofibers

The protocol used to evaluate platelet adhesion on PA coated stainless steel surface was derived from a previous report.[131] Whole blood from a healthy volunteer was collected into BD Vacutainer® EDTA K2E tubes and then mixed with Quinacrine dihydrochloride to label platelets. Collagen I-coated stainless steel surface served as positive control and the bare metal surface served as negative control. 2.5 mg mL^{-1} collagen I prepared in 3% glacial acetic acid was coated on stainless steel surface in the same manner described in PA coating. Blood samples were incubated on each surface for 2 h at 37 °C. Platelet attachment was quantified by acquiring 5 random

images on each surface at 10X magnification by using a fluorescent microscope. Average numbers of adhered platelets were used to evaluate the relative attachment of platelets onto the surfaces.

2.5.10 Statistical analysis

Unless otherwise indicated, all the quantitative results were expressed as mean ± standard error of means (SEM). All *in vitro* experiments were quantified with at least 4 replicates and with at least 3 independent repeats. All surface characterizations were carried out with at least 3 independent repeats. Statistical analyses were carried out by either one-way analysis of variance (ANOVA) or Student's t-test. A *P* value less than 0.05 was considered statistically significant.

CHAPTER 3

3 Surface-Adhesive and Osteogenic Self-Assembled Peptide Nanofibers for Bioinspired Functionalization of Titanium Surfaces

This work is partially described in the following publication:

Ceylan H., Kocabey S., Tekinay, A. B., Guler, M. O., *Soft Matter* 8, 3929-3932, 2012.

3.1 Objective

Mechanical properties and biological inertness of titanium provide potential in orthopedic and dental implants. However, integration of titanium-based implants into the existing tissue is a major problem. Herein, we demonstrate biofunctionalization of titanium surfaces through a mussel-inspired adhesion mechanism conjugated to self-assembled peptide nanofibers in order to overcome biocompatibility issues. A Dopa conjugated peptide nanofiber coating was used along with bioactive peptide sequences for osteogenic activity to enhance osseointegration of medical grade titanium surface, Ti6Al4V alloy. Dopa-mediated immobilization of osteogenic peptide nanofibers on titanium surfaces created an osteoconductive interface between osteoblast-like cells and inhibited adhesion and viability of soft tissue forming fibroblasts compared to the uncoated titanium substrate. This biofunctionalization

strategy can be extended into other surface immobilization systems owing to the versatile adhesive properties of Dopa and the ease of ligand conjugation to peptide amphiphile molecules.

3.2 Introduction

Titanium-based materials have been widely used as orthopedic and dental implants because of their mechanical properties and biological inertness.[146, 147] A major concern with titanium implants is integration into the existing tissue. When bone cells cannot adhere to the surface of the implanted material, the implant cannot be integrated and will eventually detach from the body in the long term. Guiding cellular behaviors (e.g. adhesion, morphogenesis, viability, proliferation, migration and differentiation) has been a critical concern for enhancing osseointegration. In order to overcome tissue integration problems, most of the past and current research has concentrated on modification of bone implants' surface properties by increasing roughness and altering surface chemistry, mostly coating the surface with an oxide layer or immobilizing hydroxyapatite.[141, 147-151] On the other hand, modification of implant surfaces with biologically active species (e.g. triggering cellular signaling and cues to mimic extracellular matrix) has recently emerged as a promising approach to enhance osseointegration.[105, 148, 152-155] The extracellular matrix (ECM) constituents regulate cellular behaviors in natural cellular microenvironment by providing cells with spatially and temporally controlled bioactive signals.

The ability of self-assembled peptide amphiphile nanofibers to mimic ECM has attracted intensive interest in recent years. Such biodegradable nanoscale matrices created by these nanofibers have similar structural and mechanical properties to the

native ECM. The flexibility in their molecular design allows conjugation of a wide range of bioactive sequences, which are efficiently presented to the cells to promote cellular adhesion, proliferation and differentiation both in *in vitro* and *in vivo* environments.[73, 102, 105, 106, 154] These characteristics are solely controlled through the design of the building blocks that form the nanofibers.[57, 102, 148, 154, 156] We recently reported a novel biointerface that mediates endothelial cell-selective adhesion and survival on a stainless steel surface. The peptide nanofibers were used to mimic the adhesion strategy of mussels and were conveniently immobilized onto the stainless steel surface along with a fibronectin-derived endothelial cell-specific adhesion epitope, REDV.[57] A similar approach can be exploited to promote osteogenic activity on titanium implants, since promoting osteoblast adhesion and survival on titanium in a selective manner is a challenging task. Rapid and selective adhesion and growth of osteoblasts on implant surfaces are critical because delayed healing can cause fibroblast-mediated scar tissue formation leading to tissue softening around the implant and requirement for further revision surgeries.[157-160] The KRSR peptide epitope found in the heparin binding protein in the ECM is known to bind to transmembrane proteoglycans and observed to promote selective adhesion of osteoblasts, while inhibiting the adhesion of fibroblasts.[161-163]

Although novel soft bioactive interface materials enhancing biocompatibility and durability of the implant is an emerging choice, most of the available materials suffer from insufficient stability in the aqueous environment. Functionalization of the implant surface such as biotin–streptavidin and nitriloacetic acid–histidine interactions, provide a reversible adhesion platform under controlled conditions, however these techniques are weak in terms of adhesion strength and require surface

preparation prior to immobilization. Covalent attachment techniques including N-hydroxysuccinimide (NHS)–ethyl (dimethylaminopropyl) carbodiimide (EDC) coupling, ensure strong surface binding and thus offer a wider range of applications. Nevertheless, in addition to the persisting need for surface preparation, these systems are generally susceptible to hydrolysis, that lowers the efficiency of immobilization, and their degradation products may cause biocompatibility issues.[26, 164, 165]

To overcome disadvantages of the currently available adhesive methods for medical applications, a sessile organism, mussel, offers a valuable strategy that allows adhesion to inorganic and organic surfaces in the presence of water. Mussels adhere to surfaces via special adhesive proteins that are highly enriched with 3,4-dihydroxy-L-phenylalanine (Dopa), which forms strong bonds with hydrophilic surfaces and complexes with metal ions and metal oxides.[19] Thus, conjugating Dopa to synthetic materials has attracted growing attention not only because it can operate under aqueous conditions without requiring any surface preparation but also because it is fully biocompatible.[19, 26, 67] In terms of adhesion strength, Dopa adhesion displays a covalent character whilst it is resistant to hydrolysis and is fully reversible.[26, 166] Lee et al. measured the dissociation force between Dopa and TiO_2 as 805 pN, which is beginning to approach the dissociation force of a typical carbon–silicon covalent bond (2000 pN) and is much higher than the dissociation force of hydrogen bonds that hold the DNA double helix intact (10–20 pN), indicating the strength of the adhesion formed between Dopa and TiO_2.[21, 22]

In this work, we investigated one-step immobilization of bone ECM–mimetic self-assembled peptide nanofibers on titanium surfaces exploiting mussel adhesion chemistry. For this purpose, we used medical grade titanium alloy, Ti6Al4V, which

is denoted here simply as titanium substrate for clarity. We designed and synthesized a peptide amphiphile (PA) molecule covalently conjugated to Dopa (Lauryl-VVAGE-Dopa-NH_2) for titanium surface functionalization and another PA molecule conjugated to a heparin-binding adhesion peptide sequence, KRSR (Lauryl-VVAGKRSR-NH_2) to promote osteogenic activity (Figure 3.1). These molecules self-assemble to form a nanofibrous network at physiological pH. In order to investigate the benefit of Dopa residues on the PA molecule, a PA molecule (E-PA) without the Dopa residue (Lauryl-VVAGE) was also synthesized. The utility of the KRSR peptide in the PA construct was also tested by using a PA molecule (K-PA) that lacked the KRSR sequence but retained the rest of the peptide sequence (Lauryl-VVAGK-NH_2) We exploited mussel adhesion chemistry along with osteogenic signals on titanium surfaces in order to selectively promote adhesion, viability and osteogenic activity of osteoblast-like Saos2 cells and to inhibit adhesion and growth of osteolytic gingival fibroblasts.[167]

3.3 Results and Discussion

3.3.1 Synthesis, characterization and self-assembly of peptide amphiphiles

The KRSR peptide functionalized PA (KRSR-PA) and Dopa conjugated PA (Dopa-PA) molecules were synthesized by using a solid-phase peptide synthesis method. Electrostatic stabilization triggered self-assembly of oppositely charged KRSR-PA and Dopa-PA molecules at pH 7.4 into growing nanofibers that elongate via β-sheets formed in the direction of elongation.[134] We visualized the nanofibrous and porous network formed following the self-assembly of KRSR-PA and Dopa-PA using scanning electron microscopy (SEM) (Figure 3.2a) and scanning transmission

electron microscopy (STEM) (Figure 3.2b). We performed circular dichroism analysis (Figure 3.2e) to characterize KRSR-PA/Dopa-PA nanofibers and homogenous distribution of the building blocks within the nanofibers. Neither Dopa-PA nor KRSR-PA formed an organized structure by themselves in solution at pH 7.4. However, upon mixing, they predominantly formed β-sheet structures within seconds, indicating β-sheet-driven nanofiber formation. Rheology measurements of the KRSR-PA and Dopa-PA mixture further confirmed formation of a gel at pH 7.4 that is stabilized by the physical entanglements of nanofibers, a reminiscent feature of native ECM (Figure 3.2c) The self-assembly process was further verified by using zeta potential measurements, as mixing two oppositely charged PA molecules brought the charge of the system up to zero at pH 7.4 (Figure 3.2d).

3.3.2 Surface adhesive osteoinductive nanofibers

Osteoconductive modification of the titanium surface is crucial when long-term contact between the implant surface and surrounding cells is required. For this purpose, the binding of the KRSR-PA/Dopa-PA nanofibers on the titanium surface was investigated in the presence of water using X-ray photoelectron spectroscopy (XPS). The coated titanium surfaces were analyzed with XPS after washing. The complete suppression of a photoelectron signal from the titanium substrate and the emergence of a strong nitrogen signal along with increased carbon signal after washing were considered as evidence for the permanent adsorption of KRSR-PA/Dopa-PA nanofibers and the formation of a peptide surface coating (Figure 3.3a). To study the role of Dopa in the surface adhesion mechanism, we tested KRSR-PA/E-PA nanofibers under identical conditions.

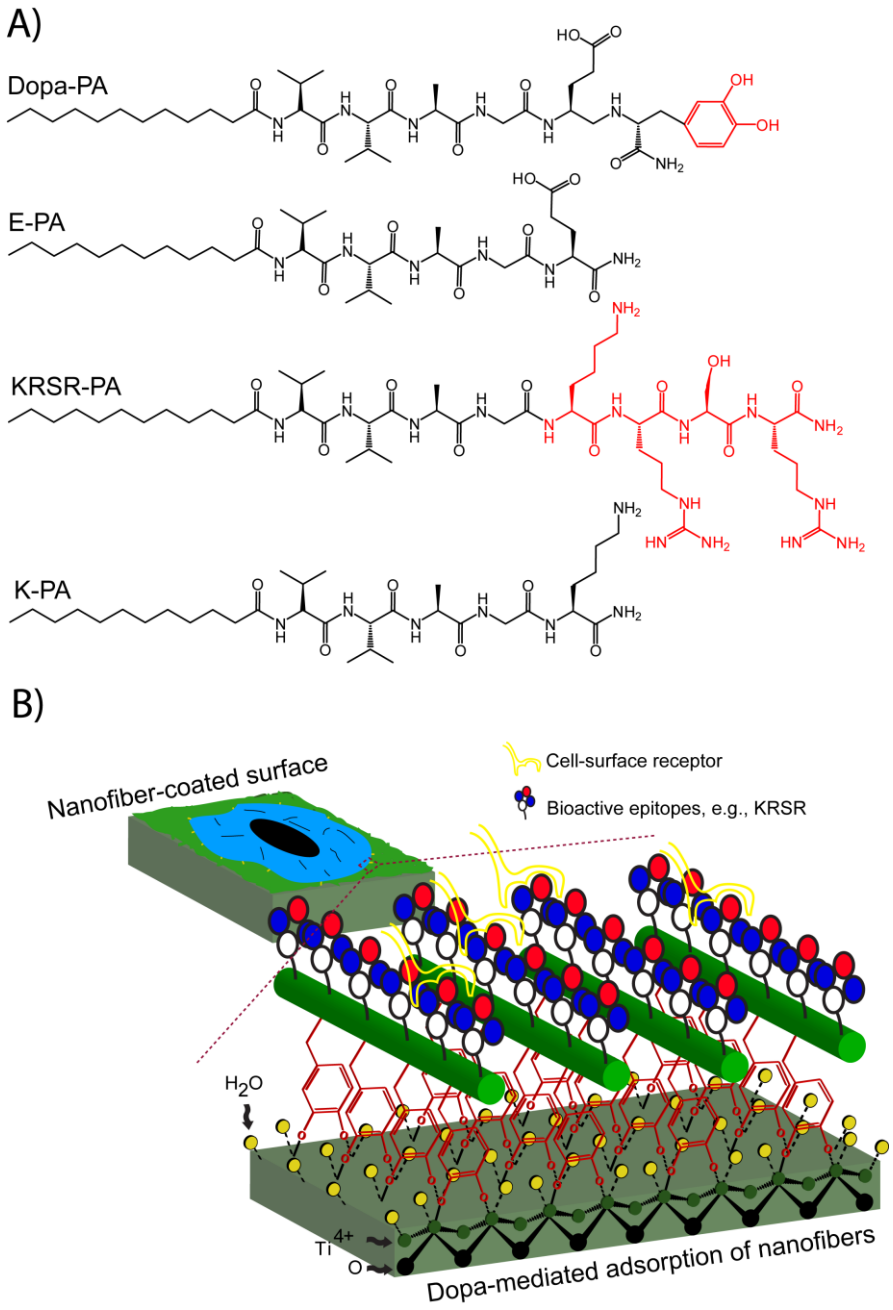

Figure 3.1 Schematic illustration of the immobilization strategy for osteogenic nanofibers on titanium surface based on the self-assembly of the KRSR-PA and Dopa-PA. (a) Chemical structures of the peptide amphiphile molecules designed for functionalization of titanium surfaces. (b) Dopa-mediated immobilization of the bioactive nanofibers on titanium surface in the presence of water is shown to occur through catechol–titanium coordination.

These nanofibers were readily washed away from the surface in the rinsing steps and hence did not form a peptide layer (Figure 3.3a) as shown by a dramatically lowered nitrogen photoelectron peak. Therefore, we concluded that Dopa incorporation is critical for immobilization of peptide nanofibers on the titanium surface. An SEM image of the KRSR-PA/Dopa-PA coated titanium surface after washing also revealed that the adsorbent species on the coated titanium surface were indeed peptide nanofibers (Figure 3.3b). To support this argument, we characterized KRSR-PA/Dopa-PA nanofibers adsorbed on the titanium surface with FT-IR, which revealed characteristic signals similar to previously reported Mefp-1 protein coating adsorbed on ZnSe surface (Figure 3.3c).[129] Mefp1 mainly consists of Dopa-containing repetitive sequences in its protein structure and constitutes one of the major proteins in the mussel adhesive system. The KRSR-PA/Dopa-PA FT-IR spectrum revealed amide I, amide II and Dopa-specific peaks (See Section 2.3.2 for FT-IR analyses). On the other hand, FT-IR analysis of the KRSR-PA/E-PA treated surface did not exhibit distinctive peptide signals after rinsing.

Investigation of surface properties is critical, since osteoblasts and fibroblasts, as many other cells do, respond to the chemistry, hydrophilicity and topography of the surface which altogether determine the success of the implant.[151] Since increased hydrophilicity and roughness are known to promote osteogenic activity, techniques such as titanium plasma spraying, oxide layer formation, acid etching and electrochemical anodization have previously been employed to roughen the surface and increase the surface hydrophilicity.[168] The titanium surfaces with KRSR-PA/Dopa-PA nanofibers showed more hydrophilic characteristics compared to bare titanium surface owing to the supramolecular nanostructures.

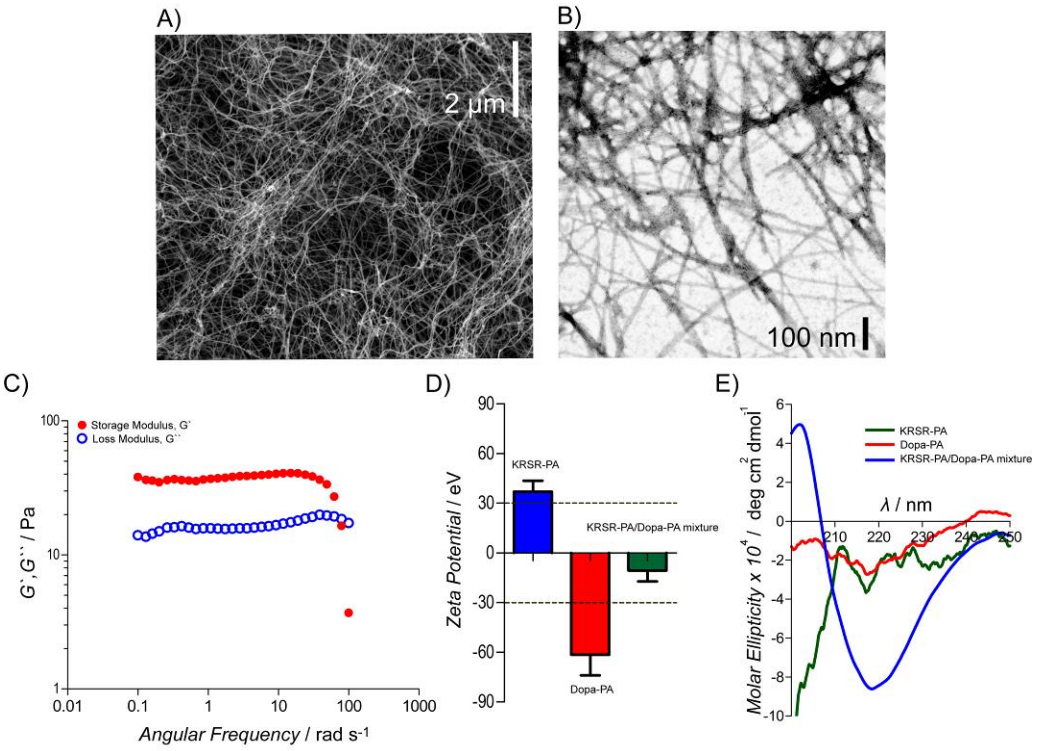

Figure 3.2 Characterization of the self-assembled peptide nanofibers and the mechanism of assembly. (a) SEM, (b) STEM images of the KRSR-PA/Dopa-PA nanofibers formed at pH 7.4. (c) Mechanical properties of the KRSR-PA/Dopa-PA gel under varying angular frequencies. (d) Zeta potential measurements of KRSR-PA, Dopa-PA and their mixture, KRSR-PA/Dopa-PA. (e) CD spectra of KRSR-PA, Dopa-PA and their mixture, KRSR-PA/Dopa-PA.

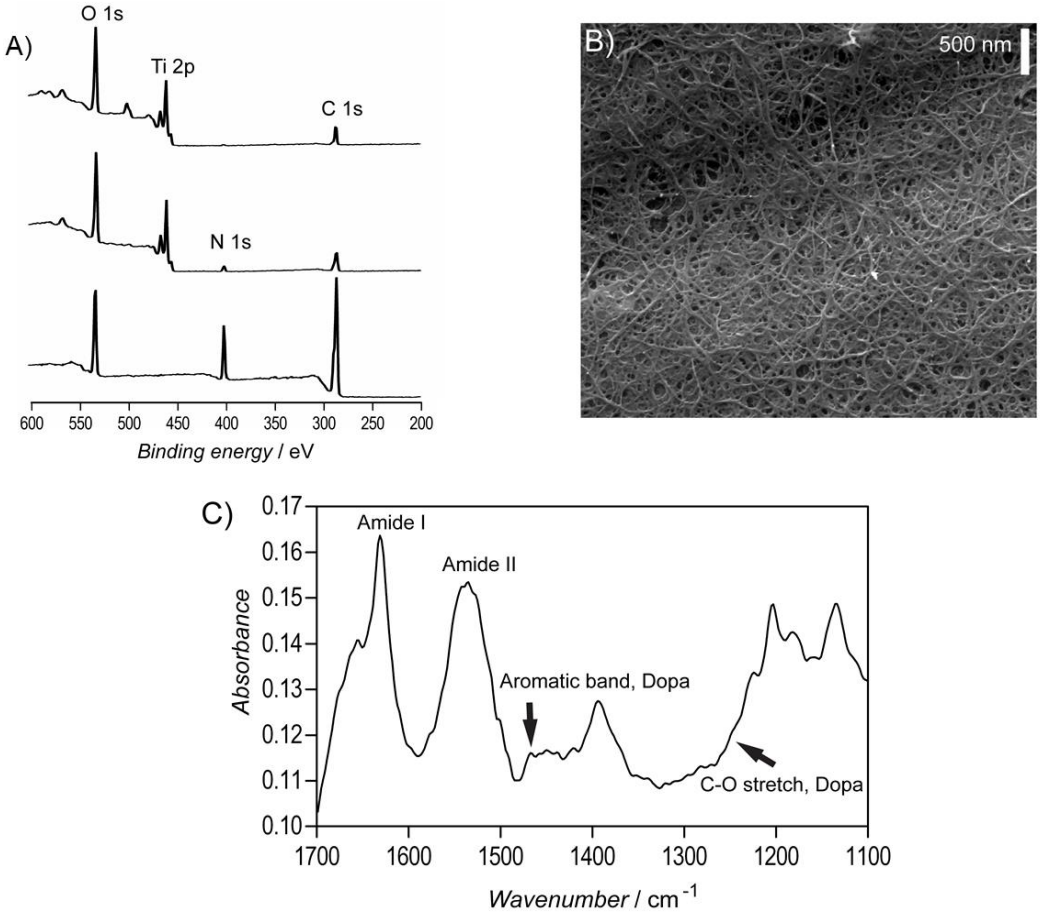

Figure 3.3 Specific immobilization of KRSR-PA/Dopa-PA nanofibers on titanium surface. (a) XPS spectra of (top to bottom) bare titanium, KRSR-PA/E-PA and KRSR-PA/Dopa-PA coated titanium surfaces. (b) SEM micrograph of immobilized KRSR-PA/Dopa-PA nanofibers on titanium surface. (c) ATR/FT-IR spectrum of KRSR-PA/Dopa-PA nanofibers adhered on titanium surface.

Mainly, the design of PA molecules dictates the hydrophilic ends of the PA molecules exposed to the aqueous environment, thereby significantly contributing to surface hydrophilicity. For this reason, the contact angle value of the modified surface decreased from 55.2° (bare titanium substrate) to below 17° (Figure 3.4a). For the same reason, a similar contact angle (<17°) decrease was observed on K-PA/Dopa-PA nanofiber modified titanium surface (Figure 3.4c). We also investigated the surface topography and the coating homogeneity of KRSR-PA/Dopa-PA modified titanium surface by using optical profilometer (Figure 3.4b). The surface roughness was found to increase on both KRSR-PA/Dopa-PA and K-PA/Dopa-PA coated titanium surfaces. We utilized the sensitivity of contact angle measurement technique to assess the retention of the KRSR-PA/Dopa-PA coating. Ultrasound sonication is a powerful technique to break apart noncovalent molecular interactions. After 1 h sonication treatment, the contact angle of the surface increased from <17 to 33.1°, indicating that despite some of the coating becoming detached, a significant portion of the nanofibers still remained strongly bound to the surface (Figure 3.4A) SEM images after sonication showed similar nanofibrous morphology as shown in Figure 3.3b. The relative increase in contact angle can be ascribed to removal of nanofibers that were not bound to the surface through Dopa-mediated titanium–catechol complexes; rather the nanofibers that were removed had originally bound to the surface by physical entanglement of nanofibers. On the other hand, the remaining nanofibers after sonication remained attached to the surface through the near-covalent strength of Dopa binding, which kept the contact angle below 55.2°. The long term stability of the coating was evident with visual observation.

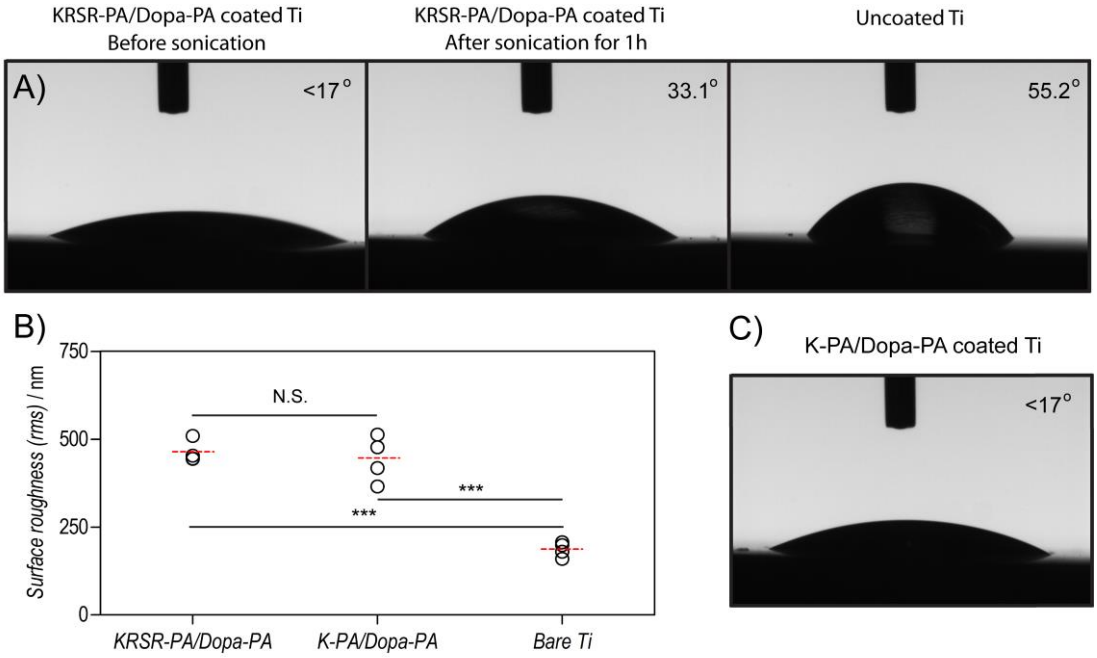

Figure 3.4 Dopa-mediated immobilization alters surface properties. (a) Contact angles of titanium substrates as bare, KRSR-PA/Dopa-PA coated and after 1 h sonication following KRSR-PA/Dopa-PA coating. (b) Surface roughness (in terms of root mean square, or rms) of PA nanofibers and bare titanium surface used in *in vitro* experiments.(c) Contact angle of K-PA/Dopa-PA coated titanium surface. *** $P < 0.0001$, NS: Non-significant.

The Dopa-PA/KRSR-PA coating remained on the titanium surface in various solvents, including water, acetone, PBS, 10% Fetal Bovine Serum containing PBS, ethanol and 2-propanol even after more than 2 months.

3.3.3 In vitro biocompatibility of preosteoblasts on osteoinductive nanofibers

Cellular behaviors at the bone-implant interface tightly dictate the long term success of the biomaterial and the fate of the regenerating tissue. Healing time, which is a measure of osteoblast adhesion, growth and mineral deposition on the implant, is critical as prolonged healing time causes the risk of tissue softening. For this reason, we first investigated the adhesion and spreading of the osteoblasts on titanium surface coated with KRSR-PA/Dopa-PA nanofibers. Adhesion and spreading of osteoblasts on the implant surface is crucial as an indication of implant bioactivity and the future behavior of cells on this surface. The *in vitro* results revealed that the number of osteoblastic Saos2 cells adhered on KRSR-PA/Dopa-PA coated titanium surface at 1 h was 2.96 ± 0.19-fold greater compared to the bare surface (Figure 3.5a unless otherwise specified all ± SEM values are quoted at $P < 0.0001$) while the number of Saos2 cells adhered on K-PA/Dopa-PA nanofibers was 2.51 ± 0.08-fold greater than the bare surface. Clearly the number of adhered Saos2 cells on KRSR-PA/Dopa-PA was significantly higher than on K-PA/Dopa-PA, highlighting the role of KRSR in mediating osteoblast adhesion.

The bioactivity provided by peptide nanofibers was further investigated by analyzing the adhesion behavior of MC3T3-E1 pre-osteoblasts. The results were found to be in parallel with Saos2 adhesion, where cells adhered significantly in greater numbers on KRSR-PA/Dopa-PA compared to both K-PA/Dopa-PA and the bare surface (Figure

3.6a). The increased adhesion of the osteoblasts and pre-osteoblasts on KRSR-lacking nanofibers compared to the bare metal surface can be explained by the altered surface properties due to peptide coating. It was previously reported that increased surface roughness and hydrophilicity promoted adhesion of osteoblasts.[141, 151, 168] We showed that surface roughness and hydrophilicity of K-PA/Dopa-PA coated titanium surface increased to a parallel level of the KRSR-PA/Dopa-PA coated surface, which may significantly contribute to our observation (Figure 3.4a). In addition, it is known that osteoblast adhesion, proliferation and alkaline phosphatase (ALP) activity are enhanced with nanostructures, and thus could further explain the observation made here.[169, 170] On the other hand, the number of human gingival fibroblasts (HGF) adhered on KRSR-PA/Dopa-PA coated titanium surface decreased to 0.74 ± 0.06-fold compared to K-PA/Dopa-PA and 0.46 ± 0.03-fold compared to bare titanium surface. The difference between KRSR-PA/Dopa-PA and K-PA/Dopa-PA shows the inhibitory role of KRSR toward fibroblast adhesion.[161] In addition, HGF adhesion on K-PA/Dopa-PA coated titanium surface was 0.61 ± 0.05-fold compared to the bare titanium surface. No other physical or chemical difference between these two coatings is expected. In addition, we observed that the fibroblast adhesion on K-PA/Dopa-PA decreased to 0.86 ± 0.06 ($P < 0.05$) of the bare surface. This finding is also supported by previous reports, which revealed that gingival fibroblasts favor hydrophobic and smoother surfaces, rather than rough and hydrophilic surfaces.[171] Therefore, our designed PA coatings could selectively favor osteoblast adhesion.

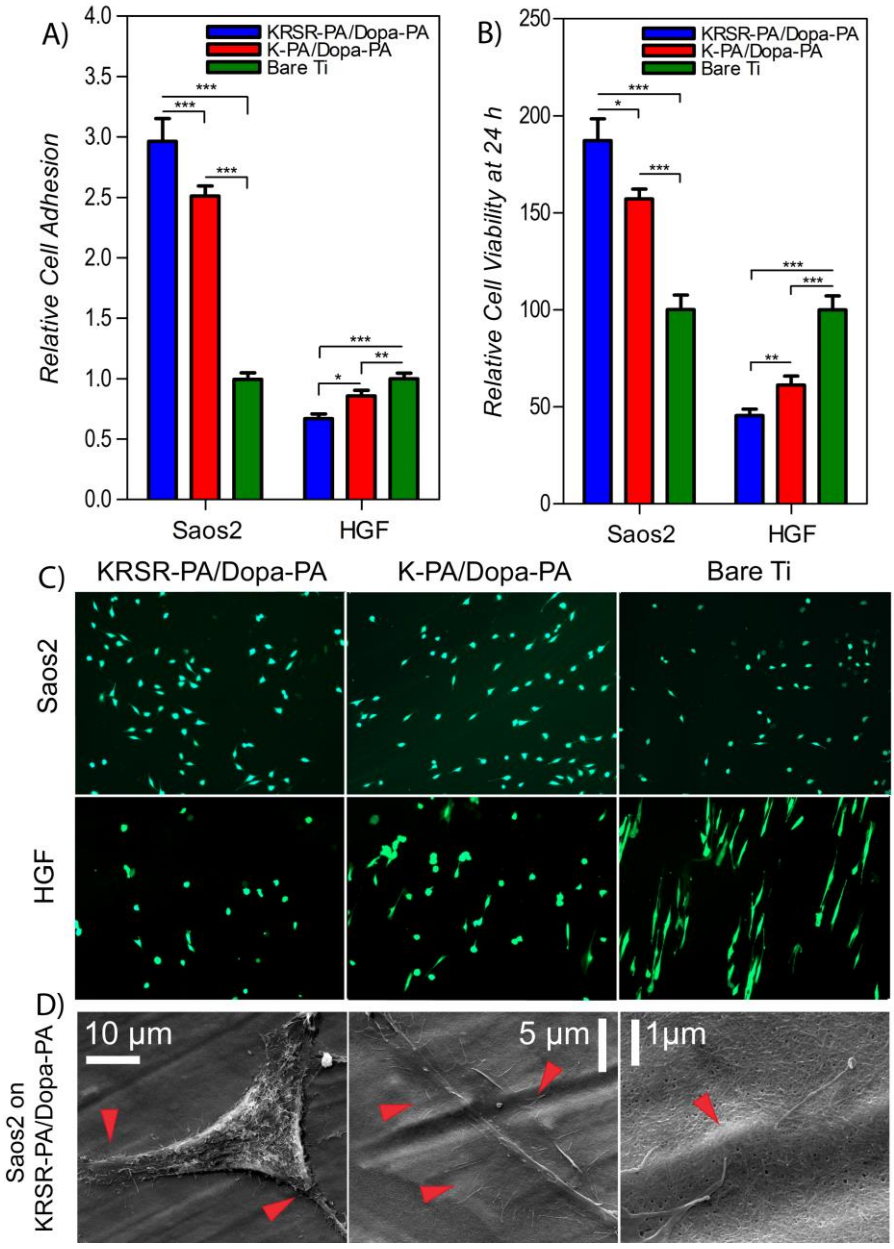

Figure 3.5 Adhesion, viability and morphology of cells on functionalized titanium surfaces. Adhesion (a) and viability (b) of Saos2 and HGF cells on functionalized titanium surfaces. (c) Representative calcein-AM stained micrographs (10X magnification) of Saos2 and HGF cells captured on functionalized titanium surfaces at 24 h. (d) Interactions between Saos2 and KRSR-PA/Dopa-PA coating captured using SEM at 24 h. Red arrows indicate the places at which cells make contact with the matrix. * $P < 0.05$, ** $P < 0.01$, *** $P < 0.0001$.

In order to see the effect of the surface properties on cell viability, we incubated osteoblasts and fibroblasts on KRSR-PA/Dopa-PA coated titanium surfaces for 24 h. We found that Saos2 cell viability gained a selective enhancement on KRSR-PA/Dopa-PA, whilst fibroblast viability decreased on that coating (Figure 3.5b, c). The number of viable Saos2 cells on the KRSR-PA/Dopa-PA coated titanium surface was 1.85 ± 0.19-fold greater compared to the cells on the bare surface and 1.17 ± 0.15 ($P < 0.05$) fold greater than on the K-PA/Dopa-PA coated surface. The viability of Saos2 cells was also favored 1.58 ± 0.15-fold on K-PA/Dopa-PA with respect to bare titanium surface at 24 h. These results revealed that even though surface characteristics, such as hydrophilicity and roughness are important factors in Saos2 adhesion and viability, the KRSR epitope also plays significant role as shown by the statistical analysis. A similar observation on the impact of surface hydrophilicity and roughness on cell viability was also reported previously.[163] We found that the viability of MC3T3-E1 cells was comparable on all tested surfaces (Figure 3.6b). In contrast, HGF viability dramatically decreased on PA coated surfaces. The viability of HGF decreased to almost 50% on KRSR-PA/Dopa-PA (0.55 ± 0.09-fold) and 75% on K-PA/Dopa-PA (0.75 ± 0.12-fold) compared to bare titanium surface. We noticed that KRSR plays a strong inhibitory role on fibroblast viability. The viability of HGF cells decreased 0.73 ± 0.12-fold on KRSR-PA/Dopa-PA with respect to K-PA/Dopa-PA. These cells attained round-like morphology on rougher and more hydrophilic PA coatings, which indicated an unfavorable microenvironment (Figure 3.5c). Actin filament-stained HGFs further showed the loss of their characteristic elongated shapes on both KRSR-PA/Dopa-PA and K-PA/Dopa-PA coatings at 24 h (Figure 3.5c and Figure 3.7). On the other hand, Saos2 cells attained their native

morphology on PA coated surfaces before they do on bare titanium substrate. Considering cell adhesion, viability and morphology of the cells, the KRSR-PA/Dopa-PA nanofibers provided a favorable microenvironment for osteoblast-like cells (Figure 3.5d), while creating an inhibitory microenvironment for fibroblast cells.

3.3.4 Osteoblastic maturation of preosteoblasts

As a long term marker for osteoblast adaptivity, we analyzed differentiation and mineral deposition of Saos2 cells on coated and bare surfaces. ALP activity is an early marker of osteoblast-specific phenotype that is significantly up-regulated during the early phases of osteogenic differentiation.[172] ALP activity of Saos2 cells on all the surfaces treated reached its peak value on day 3 and was doubled on KRSR-PA/Dopa-PA and K-PA/Dopa-PA coated surfaces compared to the bare surface (Figure 3.8a). On the following days, the ALP activity of Saos2 cells on coated surfaces remained significantly higher than those on the bare titanium. To test the mineral deposition of Saos-2 cells as a long term response to the titanium surface, Alizarin Red staining was performed on day 14 and 21 and calcium deposition was quantified by extracting Alizarin-Red bound calcium from the surface via cetylpyridinium chloride and measuring its absorbance at 562 nm. The results demonstrated significantly enhanced calcium deposition stained with Alizarin-Red on PA coated titanium surfaces compared to bare titanium surfaces (Figure 3.8) and the amount of Alizarin Red bound calcium was significantly higher on KRSR-PA/Dopa-PA (1.34 ± 0.1-fold, $P < 0.05$) and K-PA/Dopa-PA (1.29 ± 0.09-fold, $P < 0.05$) coatings compared to bare titanium surface (Figure 3.8c).

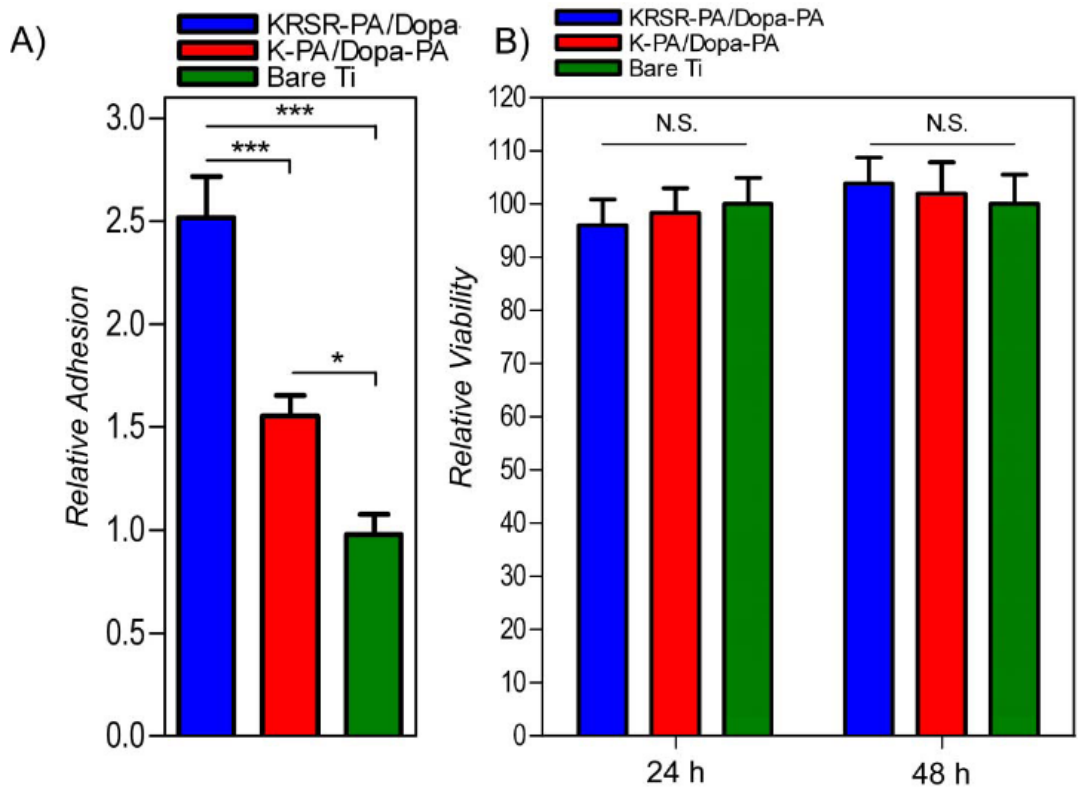

Figure 3.6 Adhesion (a) and viability (b) of MC3T3-E1 cells on functionalized titanium surfaces.* $P < 0.05$, *** $P < 0.0001$, NS: Non-significant.

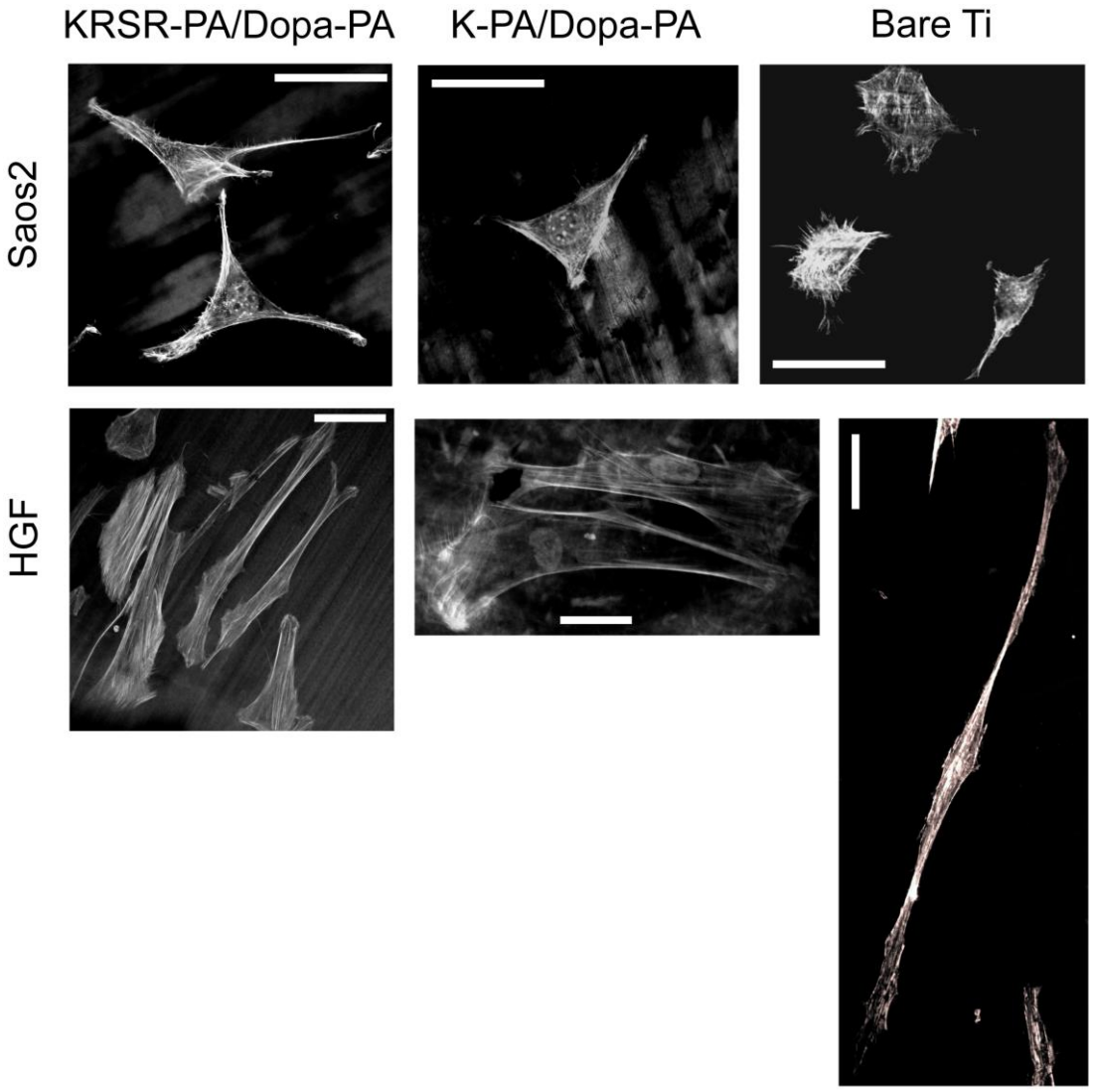

Figure 3.7 Representative high magnification confocal images of the cells at 24 h. Actin microfilaments and nuclei of cells were stained with TRITC-phalloidin and TOPRO®, respectively. Scale bars show 50 μm.

These results showed that the PA coated titanium surfaces exhibit highly enhanced capability of inducing differentiation into osteogenic lineage and mineralization of extracellular matrix. However, the KRSR epitope does not significantly contribute to ALP activity and mineral deposition.

3.4 Conclusion

Dopa-mediated immobilization of osteogenic peptide nanofibers on titanium surfaces created an osteoconductive interface between osteoblast-like cells and the titanium substrate. In addition, the bioactive surface coating inhibited adhesion and viability of soft tissue forming fibroblasts compared to the uncoated titanium surface. The bottom-up surface engineering strategy presented in this work consisted of gathering ECM-derived osteoblast-specific peptide (KRSR) and mussel-inspired adhesive residue (Dopa) into ECM-mimetic peptide nanofibers under physiological conditions. This hybrid material was securely and homogeneously immobilized onto the titanium surface while maintaining its bioactive properties. This strategy can be extended to other surface immobilization systems owing to the versatile adhesive properties of Dopa and the ease of ligand conjugation into peptide amphiphile molecules. By modifying the bioactive region of the peptide nanofiber system, a wide range of bioactive nanomaterials can be immobilized on various biomedical implants and devices. Therefore, our strategy offers a general route for biofunctionalization of biomedical material surfaces using bottom-up fabricated self-assembled peptide nanofibers that can be functionalized in accordance with the application of interest.

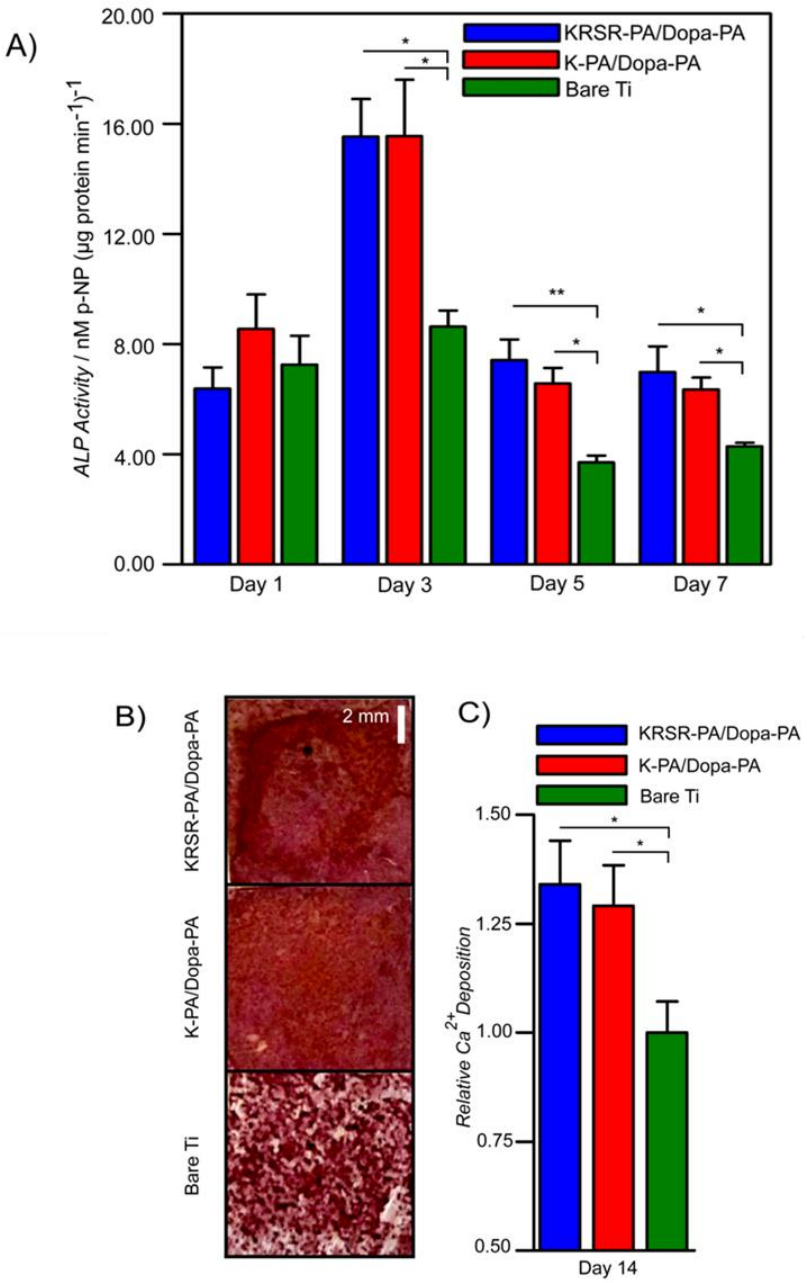

Figure 3.8 Effect of immobilized PA nanofibers on osteogenic activity. (a) ALP activity of Saos2 cells on days 1, 3, 5 and 7. (b) Deposition of calcium on peptide coated titanium substrates on day 14 as demonstrated by Alizarin Red staining. (c) Quantification of relative calcium deposition on the matrix on day 14. * $P < 0.05$, ** $P < 0.01$.

3.5 Experimental Section

3.5.1 Materials

All protected amino acids, lauric acid, [4-[α-(2′,4′-dimethoxyphenyl) Fmoc-aminomethylphenoxyacetomidonorleucyl-MBHA resin (Rink amide MBHA resin), 2-(1H-benzotriazol-1-yl)-1,1,3,3-tetramethyluroniumhexafluorophosphate (HBTU) and diisopropylethylamine (DIEA) were purchased from NovaBiochem, ABCR, or Sigma-Aldrich. Medical grade Ti6Al4V alloy was purchased from Goodfellow. All other chemicals and materials used in this study were analytical grade and purchased from Invitrogen, Fisher, Merck, Alfa Aesar, and/or Sigma–Aldrich.

3.5.2 Synthesis and characterization of peptide-amphiphile building blocks

Peptide amphiphile molecules were manually synthesized using a standard Fmoc-protected solid phase peptide synthesis method. Amino acid couplings were performed with 2 equivalents of amino acids activated with 1.95 equivalents of HBTU, and 3 equivalents of DIEA for 1 equivalent of starting resin. The coupling time for each amino acid was 2 h. Lauric acid addition was performed similarly to amino acid coupling except that the coupling time was 4 h. Fmoc removal was performed with 20% piperidine–dimethylformamide (DMF) solution for 20 min. 10% acetic anhydride–DMF solution was used to permanently acetylate the unreacted amine groups after each coupling step. DMF and dichloromethane (DCM) were used as washing solvents. Cleavage of protecting groups and peptide molecules from the resin was carried out by 95% trifluoroacetic acid-containing cleavage cocktail (95% TFA, 2.5% water, 2.5% triisopropylsilane) for 3 h. Excess TFA removal was carried out by rotary evaporation. PAs in the remaining solution were

precipitated in ice-cold diethyl ether overnight. The precipitate was collected the next day by centrifugation and dissolved in ultrapure water. This solution was frozen at −80 °C for 4 h and then lyophilized for one week. Synthesized batches were characterized by using a quadruple time of flight (Q-TOF) mass spectrometer with electrospray ionization (ESI) source equipped with a reverse-phase analytical high performance liquid chromatograph (HPLC). In order to remove residual TFA, positively-charged peptide amphiphiles were treated with 0.1 M HCl solution and lyophilized, negatively-charged PAs were purified with a preparative HPLC system (Agilent 1200 series). All peptide batches were freeze-dried and reconstituted in ultrapure water at pH 7.4 before use.

3.5.3 Formation of peptide nanofibers and their characterizations

KRSR-PA/Dopa-PA nanofibers were formed by mixing KRSR-PA and Dopa-PA at 1:3 ratios, respectively, which stabilizes all net charges at pH 7.4. For the same reason, KRSR-PA and E-PA were mixed at 2:3 ratios, respectively, to form KRSR-PA/E-PA, and K-PA and Dopa-PA were mixed at 1:1 ratios to form K-PA/Dopa-PA nanofibers. The samples for circular dichroism (Jasco J-815) were prepared by mixing KRSR-PA and Dopa-PA at 1 x 10^{-5} and 3 x 10^{-5} M concentrations, respectively. Zeta potential measurements (Malvern Zeta-ZS) of individual PA solutions or their mixtures were performed at the given ratios above at concentrations in the order of 10^{-4} M. Frequency sweep rheology measurements (Anton Paar Physica RM301) were performed using PA mixtures at 10^{-3} M concentration. SEM samples were prepared by mixing KRSR-PA/Dopa-PA at 1 mM and 3 mM concentrations, respectively, and then by critical-point drying following ethanol

exchange. The samples were coated with 4–5 nm Au-Pd before imaging. Scanning transmission electron microscopy (STEM) images at HAADF mode were acquired with FEI Tecnai G2 F30 TEM at 300 kV. This mode enables better contrast in comparison with the conventional TEM and hence better structural analysis can be done. Samples for STEM were prepared by mixing 1 mM KRSR-PA and Dopa-PA at 1:3 ratio, respectively, on a 200-mesh carbon TEM grid for 1 min followed by 2 wt% uranyl acetate staining for 30 s and drying immediately under nitrogen gas.

Surface binding and characterization of peptide amphiphile–titanium substrates

Medical grade Ti6Al4V titanium alloy (Goodfellow, UK) was used as titanium substrate. The substrate was truncated into 1 cm^2 pieces and used after polishing. The substrates were successively cleaned using acetone, ethanol and water wash coupled with ultrasound sonication for 1 h each and then dried in a high vacuum oven at 100 °C and 90 mbar for 6–7 h. The surface binding tests of nanofibers onto surfaces were carried out against water competition. 1 mM KRSR-PA and Dopa-PA solutions were mixed on a cleaned titanium surface at 1:3 ratios, respectively. The control of Dopa was designed using KRSR-PA and E-PA nanofibers, which were mixed at 1:1.5 ratios, respectively. The peptide nanofiber–titanium samples were kept in a humidified environment for 24–48 h in a Petri dish and were not allowed to dry. Then, the substrates were rinsed in water for 30 min and dried at 37 °C for a further 24 h. The physical properties of the peptide nanofiber-modified surface that are formed against water competition (without drying and washing after incubation in a humid Petri dish) were characterized using X-ray photoelectron spectroscopy (XPS) (Thermo Scientific), scanning electron microscopy (SEM), attenuated total internal reflectance Fourier transform infrared spectroscopy (ATR-FT-IR) (VORTEX 70),

contact angle measurements (OCA 30 Dataphysics), and optical profilometry (Zygo New view 7200). Samples for optical profilometer were coated with 5 nm Au-Pd before measurement. SEM samples were prepared by an ethanol gradient and critical point drying (Tourismis Autosamdri®-815B) followed by 4–5 nm Au-Pd coating.

3.5.4 Cell culturing and maintenance

Saos2 human osteosarcoma cells (ATCC® HTB-85™), MC3T3-E1 mouse preosteoblastic cells and primary human gingival fibroblast cells (HGF) were used in adhesion, spreading, viability and proliferation experiments on PA coated titanium surface. HGF cells were isolated and characterized as described and were kindly provided as a gift from Prof. Dr A. U. Ural of GATA, Ankara, Turkey.[173] All cells were cultured and propagated in 75 cm^2 cell culture flasks using Dulbecco's Modified Eagle Serum (DMEM) supplemented with 10% Fetal Bovine Serum (FBS), 1% penicillin/streptomycin and 2 mM L-glutamine. The cells were grown at 37 °C in a humidified chamber supplied with 5% CO_2. All cell experiments were carried out after 80–90% confluency was reached and cells were diluted 1:3 and 1:4 for sub culturing.

3.5.5 In vitro cell culture tests

All *in vitro* tests described in this study including with Saos2, MC3T3-E1 and HGF cells were carried out on KRSR-PA/Dopa-PA and K-PA/Dopa-PA coated and bare titanium surfaces. PA nanofibers were formed on cleaned titanium surface as described above and coated surfaces were allowed to dry in a chemical hood overnight. Further drying was done for 24 h at 37 °C. The mixing ratios of PAs were as described above. Before the experiments, the coatings were washed with PBS

prior to the experiments to remove unbound nanofibers, which otherwise could interfere with cellular behavior as a soluble factor. Adhesion and spreading tests were performed under serum-free conditions for 1 h. Before seeding cells for adhesion and spreading tests, they were incubated with serum-free DMEM medium, supplemented with 4 mg mL^{-1} BSA and 50 μg mL^{-1} cyclohexamide for 1 h at standard cell culture conditions. Cyclohexamide, which is a well-known translation inhibitor, was used to limit the interference of endogenous proteins in adhesion and spreading of cells. BSA served to non-specifically block cell adhesion receptors. After 1 h, cells were removed from tissue culture plate with trypsin/EDTA chemistry. Trypsin/EDTA was then removed by centrifugation and resuspension of cells in serum-free DMEM. The cells were then seeded on modified or unmodified titanium substrates (at density of 1.5×10^4 cells cm^{-2}) located in 24-well plates in a serum-free DMEM medium. After 1 h, the substrates were washed with PBS, and then were stained using calcein-AM for visualization. The viability experiments were carried out at 24 h in 10% FBS/DMEM. Cells seeded on substrates at a density of 1.0×10^4 cells cm^{-2} were washed with PBS after 24 h followed by calcein-AM staining. Relative cell adhesions and viability were quantified by directly counting the number of cells on different locations (at least five or six random locations were photographed per well, and at least six wells were used per independent experiment) as described previously.[57] The counts were then normalized to the bare titanium surface results. For probing the spreading and cellular morphology, cells were either fixed with 3.7% formaldehyde followed by 10 min Triton X-100 permeabilization and TRITC-conjugated phalloidin treatment (for confocal microscopy) or 2%

gluteraldehyde/PBS followed by post fixation with osmium tetroxide (for SEM imaging).

ALP activity of Saos2 cells was probed on day 1, 3, 5 and 7 by measuring the colorimetric product of p-nitrophenyl phosphate/endogenous ALP reaction. The ALP results were normalized to the total protein amount which was determined by BCA protein assay kit (Pierce) according to manufacturer's instructions. In brief, cells were lysed with M-PER Protein Extraction Kit (Pierce) containing 5% protease inhibitor for 20–25 min on shaker after discarding the culture medium and washing with PBS. Then, collected lysates were centrifuged for 15 min at 14,000 g to discard the cellular debris. Protein containing supernatant was taken and BCA protein assay was performed. 50 μL protein samples and 150 p-NP substrate were used together with p-NP standards to determine final ALP concentration after 30 min incubation.

Calcium deposition on the surface was measured on day 14 and day 21 using Alizarin Red staining as previously reported.42 Briefly, cells were fixed with ice-cold ethanol for 1 h and stained with 40 mM Alizarin-Red S for 15 min. After washing 4–5 times with double distilled water to get rid of non-specific Alizarin-Red binding, Alizarin Red bound Ca extraction was performed by using 10% (w/v) cetylpyridinium chloride in 10 mM sodium phosphate (pH 7) for 20 min at room temperature and the concentration of Alizarin-Red S was determined by measuring the absorbance at 562 nm. For ALP and Alizarin Red staining assays, Saos2 cells were seeded on titanium disks located in 24 well plates at a density of 1.5×10^4 cells cm^{-2} in 10% FBS/DMEM. Cells were kept growing in 10% FBS/DMEM until they reached 100% confluency, after which the medium was replaced with fresh osteogenic medium containing 10 mM β-glycerophosphate, 0.2 mM ascorbic acid

and 100 nM dexamethasone in 10% FBS/DMEM. This medium was replenished every 3-4 days in the course of experiments.

3.5.6 Statistical analyses

Unless otherwise indicated, all quantitative values were presented as mean ± SEM (standard error of means). All *in vitro* experiments were quantified with at least four replicates. All surface characterizations were performed on at least three different locations for each group of surface. Statistical analyses were performed using either one-way analysis of variance (ANOVA) or Student's t-test, wherever necessary. A *P* value of less than 0.05 was considered statistically significant.

CHAPTER 4

4 Bone-like Apatite Nucleating Nanofibers Induce Differentiation of Human Mesenchymal Stem Cells into Mature Osteoblasts

This work is partially described in the following publication:

Ceylan H., Kocabey S., Gulsuner H. U., Balcik O. S., Guler, M. O., Tekinay, A. B., *Biomacromolecules* DOI: 10.1021/bm500248r, 2014.

4.1 Objective

A bone implant should integrate to the tissue through a bone-like mineralized interface, which requires increased osteoblast activity at the implant-tissue boundary. Modification of the implant surface with synthetic bioinstructive cues facilitates on-site differentiation of progenitor stem cells to functional mature osteoblasts and results in subsequent mineralization. Inspired by the bioactive domains of the bone extracellular matrix proteins and the mussel adhesive proteins, we synthesized peptide nanofibers to promote bone-like mineralization on the implant surface. Nanofibers functionalized with osteoinductive collagen I derived Asp-Gly-Glu-Ala (DGEA) peptide sequence provide an advantage in initial adhesion, spreading, and early commitment to osteogenic differentiation for mesenchymal stem cells (hMSCs). In this study, we demonstrated that this early osteogenic commitment,

however, does not necessarily guarantee a priority for maturation into functional osteoblasts. Similar to natural biological cascades, early commitment should be further supported with additional signals to provide a long term effect on differentiation. In this chapter, we showed that peptide nanofibers functionalized with Glu-Glu-Glu (EEE) sequence enhanced mineralization abilities due to osteoinductive properties for late-stage differentiation of hMSCs. Mussel-inspired functionalization not only enables robust immobilization on metal surface, but also improves bone-like mineralization under physiologically-simulated conditions. The multifunctional osteoinductive peptide nanofiber biointerfaces presented here facilitate osseointegration for a long-term clinical stability.

4.2 Introduction

Understanding and controlling the complex interactions at the cell-material interface is important for developing more efficient treatment strategies in regenerative medicine. These cell-material interactions are especially important at the site of contact between the implants and tissues. Therapeutic success of bone implants relies on efficient tissue integration of the implant which is governed by formation of a tight, bone-like mineralized layer at the bone-implant interface.[174] Mineralization process is also under competitive pressure of fibrotic tissue development, which leads to softening of the surrounding bone tissue and hence failure of the implant.[151, 175-178] Particularly, in patients with impaired osteoblastogenesis, such as osteoporosis, mineralization process takes longer time and failure of the implant is more probable.[179] Thus, adequate osteoblast activity is necessary for rapid mineralization at the site of implantation.

Mature osteoblasts operate as the functional bone-forming cells by laying down mineralizable bone matrix called osteoid. The hMSCs are the ultimate progenitors of osteoblasts in the adult bone.[180] In the course of osteogenic differentiation, hMSCs follow a hierarchical pathway within the osteoblast lineage. An initial osteogenic commitment followed by a maturation step is regulated by a complex set of signaling factors, including intracellular, intercellular, and extracellular interactions, ending with mature osteoblasts. Because of the complexity of the biological processes, synthetic systems with a single function can fail to properly orchestrate this mechanism. In order to overcome this problem, bioinstructive molecules can be used in a multifunctional fashion for inducing maturation after initial differentiation, which is important for providing progenitor cells with clinically relevant competitive advantage.[181]

Recent studies have shown that modifying surfaces with short synthetic peptides derived from bone extracellular matrix proteins can promote survival and differentiation of osteoprogenitor cells with varying potency, including multipotent hMSCs and unipotent pre-osteoblasts. For example, Asp-Gly-Glu-Ala (DGEA) peptide sequence derived from collagen type I can induce osteogenic differentiation of hMSCs and mouse pre-osteoblast MC3T3 cells via binding to integrin receptor α2β1.[182-188] α2β1 is not only critical in the differentiation process, but also in adhesion, spreading, migration, and survival of hMSCs.[189] On the other hand, Arg-Gly-Asp (RGD) peptide sequence of fibronectin interacts with integrin α5β1. Blocking integrin α5β1 reduces adhesion and proliferation despite having any impact on osteogenic differentiation.[190]

In addition to receptor binding epitopes, the regulatory role of the acidic residues in nucleation and growth of hydroxyapatite crystals require a special attention since reconstitution of a synthetic process that can stimulate precipitation of carbonated biological apatite on the implanted material would be a useful platform for promoting adhesion, survival, and osteogenic differentiation of the progenitor cells.[176, 191, 192] Acidic residues in non-collagenous bone matrix proteins, such as bone sialoprotein, osteopontin, and osteocalcin, also exhibit appealing behavior due to their high hydroxyapatite affinity.[193] It has been shown that depending on the geometry and porosity, hydroxyapatite (HAp) grafts exhibit osteoinductivity in addition to its osteoconductive properties. This had been attributed to its ability to entrap and concentrate circulating bone morphogenetic proteins (BMPs).[176, 194] Moreover, by comparing osteoinductivity of porous hydroxyapatite with BMP-2, Lin et al. showed that mouse mesenchymal stem cell lines underwent osteogenic differentiation and the osteoinductivity of hydroxyapatite was found to be higher than of BMP-2 itself.[195] Very recently, Shih et al. proposed that calcium phosphate matrices can induce osteogenic differentiation of mesenchymal stem cells through phosphate-ATP-adenosine metabolic signaling.[192]

Supramolecular assemblies of biofunctional peptides provide well-defined molecular composition and architecture allowing high epitope density with optimal receptor binding geometry.[106, 182, 196] Chemical simplicity of the building blocks allows robust exploitation of the bioactive ligands in therapeutic applications.[57, 106, 185, 197-200] Peptide amphiphiles (PAs) is a class of self-assembling peptides containing an alkyl tail attached to the peptide part.[102] Because of the design flexibility, PA nanofibers can display bioinstructive ligands in a multivalent fashion to support adhesion,

proliferation, and differentiation of various cell types, including bone, cartilage, endothelial, and nerve cells as well as their progenitors.[109, 114-116]

In the present study, we demonstrated multifunctional osteoinductive nanofibers that induce differentiation of hMSCs into mature osteoblast. PA molecules that self assembles into these nanofibers, were synthesized inspired by the bioactive sequences of collagen type I (DGEA), non-collagenous matrix proteins (EEE), and the mussel-adhesive proteins (3,4-dihydroxy-L-phenyl alanine, or Dopa) (Figure 4.1). Dopa was used to provide immobilization of osteoinductive cues on biomaterial surface, since immobilization is a major drawback, which significantly limits the performance of the available surface modification technologies. Water molecules, dissolved ions and polyionic biomolecules in the biological environment compete with the implant surface and displace the immobilized molecules.[201] This challenge has been recently addressed by our group and others by exploiting mussel-inspired Dopa-mediated surface adhesion strategy.[57, 58, 69, 202] Under physiological conditions, these three bioactive PAs self-assembled into hybrid nanofibers, which were then applied as implant coatings on medical grade titanium substrate. We investigated the surface stability and osteoinductivity of these coatings. *In vivo* biointegration of these nanofibers was predicted by their ability of facilitating mineralization under biologically simulated conditions. Osteoinductivity of these artificial microenvironments was identified in detail by investigating cell-matrix interactions at molecular level.

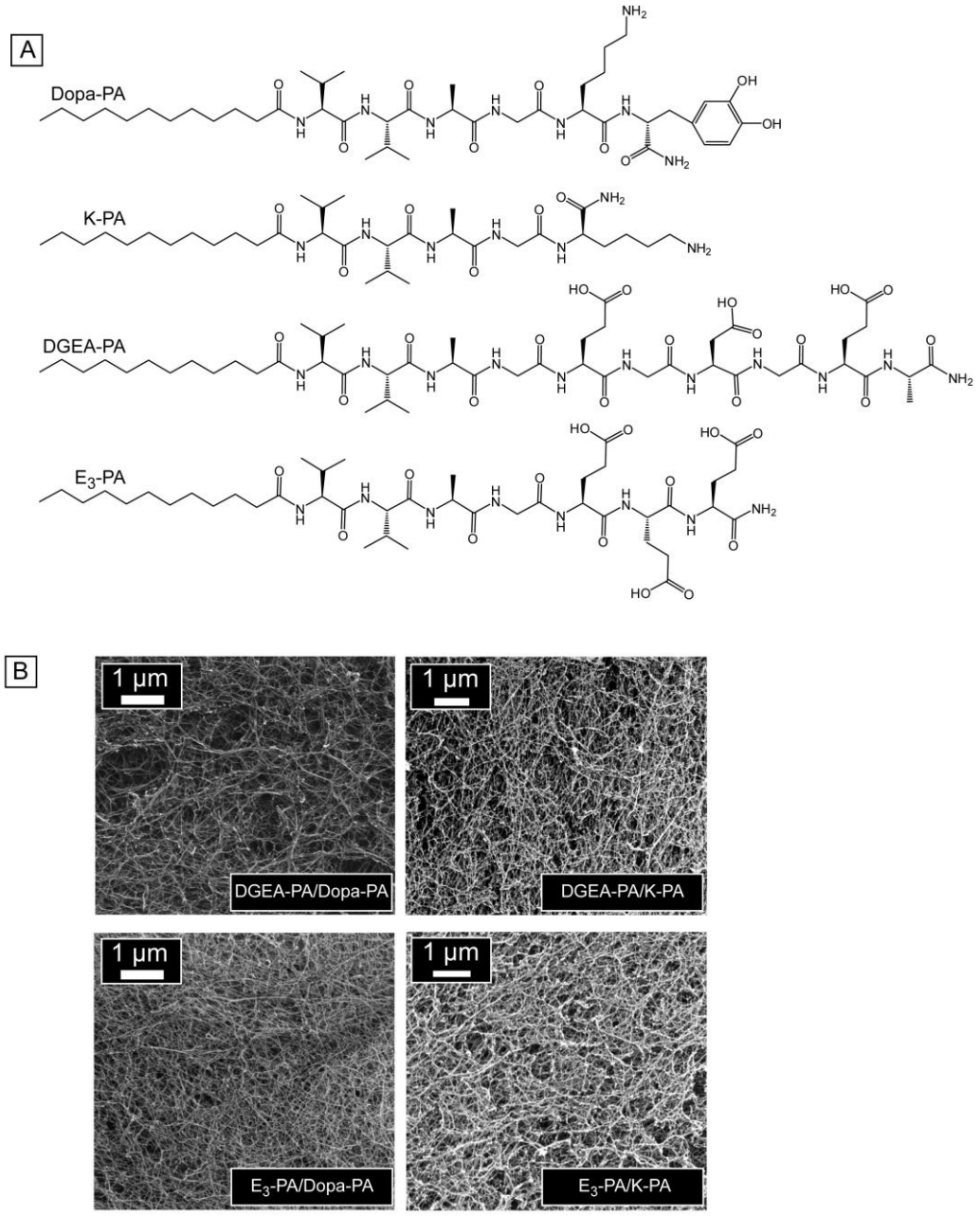

Figure 4.1 Self-assembly of PAs into multifunctional osteoinductive nanofibers. (a) Design and chemical representation of the building blocks: Lauryl-VVAGKDopa-NH_2 (Dopa-PA), Lauryl-VVAGK-NH_2 (K-PA), Lauryl-VVAGEGDGEA-NH_2 (DGEA-PA), Lauryl-VVAGEEE-NH_2 (E_3-PA). (b) SEM micrographs of nanofibrous matrices formed at pH 7.4.

4.3 Results and Discussion

4.3.1 Design of the building blocks and self-assembly into multifunctional nanofibers

DGEA-PA and E_3-PA were designed to have net charges of -3 while Dopa-PA and K-PA had +1 net charge at pH 7.4 (Figure 4.1a). Mixing oppositely charged DGEA-PA (or E_3-PA) with Dopa-PA (or K-PA) at 1:3 molar ratios drove the self-assembly into high-aspect-ratio nanofibers (Table 4.1, Figure 4.1b).[134] Modular parts of PAs concertedly act in the process of self-assembly as previously reported in detail.[102, 134] Briefly, hydrophobic collapse and van der Waals interactions at the hydrophobic module are accompanied by one-dimensional fibrillation through hydrogen bonding in the direction of fiber elongation.[102, 203] Buried hydrophobic domains inside the nanofibers result in a micellar structure, which allows for well-defined and high-density presentation of the functional moieties to the outer aqueous environment. Molecular presentation density of DGEA and E_3 were the same in all nanofiber combinations (Table 4.1). K-PA contained the same amino acid sequence of Dopa-PA, except for the Dopa residue, thereby serving as the control of the Dopa functionality. Densely interconnected nanofibers culminate in the formation of nanonetworks at a size scale similar to native extracellular matrix (Figure 4.1).[102, 204, 205] Beta-sheet-like organization was evident in all of the nanofiber constructs as demonstrated by circular dichroism (Figure 4.2a). When individual PAs are dissolved in water, their β-sheet forming capacity is limited as assessed from the magnitude of molar ellipticity. However, their combined capacity of β-sheet formation after mixing becomes much greater than the sum of the individual fibers.

Table 4.1 *Osteoinductive PA nanofiber compositions forming bone-mimetic cellular microenvironments*

Nanofiber composition	Monomeric stoichiometry[*]
DGEA-PA:Dopa-PA	1:3
E_3-PA:Dopa-PA	1:3
HAp (DGEA-PA:Dopa-PA)[**]	1:3
HAp (E_3-PA:Dopa-PA)[**]	1:3
DGEA-PA:K-PA	1:3
E_3-PA:K-PA	1:3

[*] Determined by the molar mixing ratio of the participating PAs.

[**] Immersed in simulated body fluid for hydroxyapatite (HAp) mineralization.

This showed emerging electrostatic interaction between the oppositely charged PA molecules stabilizes PAs to drive nanofiber formation.[203] Zeta potential measurements further supported the formation of self-assembly process, as mixing two oppositely charged PA molecules reduced the stability of the individual solutions, dropping in between ±30 mV, indicating aggregations due to self-assembly at pH 7.4 (Figure 4.2b).

4.3.2 Surface stability of the nanofibrous peptide coatings

As the model surface Ti6Al4V is abundantly used as orthopedic and dental support for its comparatively lower weight and corrosion properties, Dopa-mediated stability of the nanofibers on titanium (Ti6Al4V) surface was investigated against harsh chemical washing.

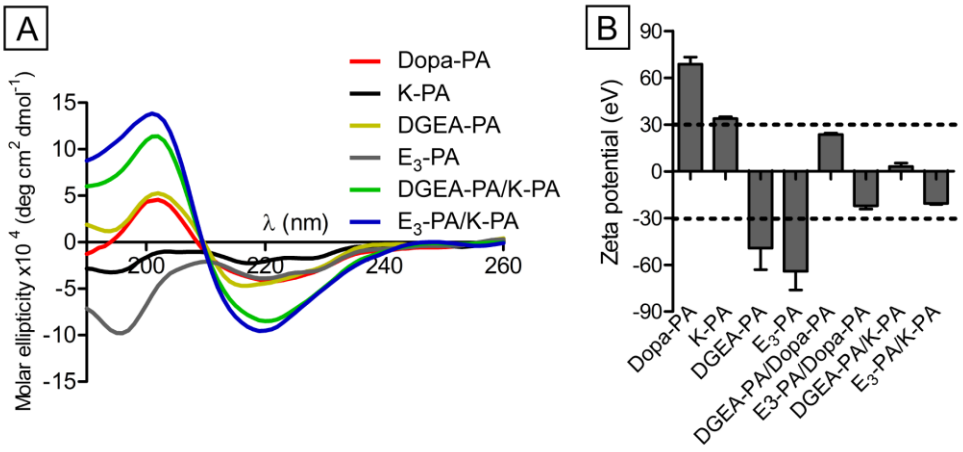

Figure 4.2 Biophysical analysis of PA self-assembly. (a) Circular dichroism spectra of the nanofibers undergoing β-sheet-like structural organization. (b) Zeta potentials of individual PAs and self-assembled nanofibers, revealing that the charge-screening drives the self-assembly process (pH 7.4).

Washing in a solution with high ionic strength (10X PBS) followed by surfactant treatment (10 wt% sodium dodecyl sulfate) under mechanical shearing creates a daunting environment where loosely attached ligands would be easily displaced. As a result, DGEA-PA/K-PA and E_3-PA/K-PA nanofibers were almost completely washed away after the treatment (Figure 4.3a). In sharp contrast, DGEA-PA/Dopa-PA and E_3-PA/Dopa-PA nanofibers remained on the titanium surface. This suggests that DGEA-PA/Dopa-PA and E_3-PA/Dopa-PA nanofibers were permanently, i.e., covalently, bonded to the titanium surface, which was attributable to the interaction of Dopa with the surface. Digitalized quantity of the coomassie dye following a standard destaining protocol showed that density of Dopa-containing nanofibers were in excess of 4 x 10^3 folds higher compared to DGEA-PA/K-PA and E_3-PA/K-PA (Figure 4.3b). Dense surface coverage of DGEA-PA/Dopa-PA and E_3-PA/Dopa-PA nanofibers on titanium surface was further vindicated by x-ray photoelectron spectroscopy (XPS). Complete suppression of titanium photoelectron signal with the appearance of intense nitrogen signals was indicative of the peptide bound to the surface (Figure 4.3c). However, the presence of titanium signal in addition to the much weaker nitrogen signal suggested removal of the large portion of the coating during the washing step. Altogether, Dopa residue on the nanofibers enabled robust surface biofunctionalization, which is essential for better restorative capacity and enhancing the biocompatibility of the underlying biomaterial.

4.3.3 Surface mineralization with biological apatite

A material that supports growth of bone-like HAp in simulated body fluid (SBF) is considered bioactive, and hence has the capacity of bone bonding. SBF contains

most of the ionic components of the blood plasma at comparable concentrations in an artificially prepared solution.[206] When the titanium substrates functionalized with DGEA-PA/Dopa-PA and E_3-PA/Dopa-PA nanofibers were transferred to SBF, the surfaces were found to be densely covered with spherical calcium phosphate minerals (Figure 4.4a-c). Detailed investigation showed that these minerals began to form within 6-12 h and become microscopically detectable after 24 h of incubation (Figure 4.5). As the incubation time increases, both the mineral density on the surface increases and the individual island sizes get bigger (Figure 4.5a). SAED and XRD patterns confirmed the minerals as HAp (Figure 4.4 and Figure 4.6c).[102, 207, 208] EDS showed the overwhelming presence of calcium and phosphorous in the minerals. Ca:P molar ratio was found to be 1.87, a close value to that of HAp (1.67) (Figure 4.4i).[209] Higher magnification SEM and TEM analyses showed characteristic flakes of HAp that form porous structure on the mineral islands (Figure 4.4d and Figure 4.6a, b). Raman spectrum showed specific fingerprints of crystalline HAp was bone-mimetic carbonated apatite due to the carbonate peak located at 1070 cm^{-1} (Figure 4.6d). Microscopic analyses showed that HAp formation follows island growth (Volmer-Weber) mode, which due to a large number of surface nuclei generation followed by the growth of separate and uniform islands homogenously distributed on the substrate (Figure 4.7).[210] However, we did not observe any mineralization on the nanofiber constructs of DGEA-PA/K-PA and E_3-PA/K-PA even after up to 9 days of treatment with SBF (Figure 4.4e, f and Figure 4.5). We also did not detect mineralization on bare Ti6Al4V (Figure 4.4g).

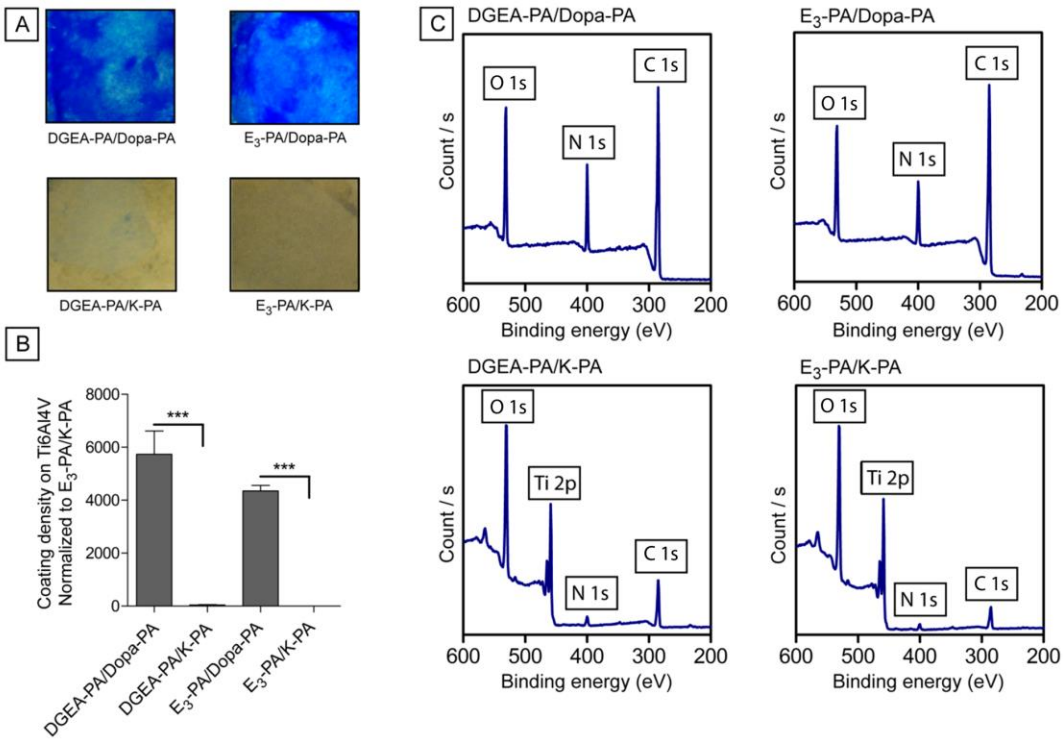

Figure 4.3 Dopa imparts surface stability to osteoinductive nanofibers. (a) Coomassie Blue staining shows the surface-bound peptide nanofibers. Coatings remained on Ti6Al4V substrates after washing sequentially in 10X PBS and 10 wt% SDS. (b) Digitalized spot density of the staining where the results were normalized to the spot density of E_3-PA/K-PA. (c) X-ray photoelectron spectra of the coatings after the washing procedure. *** $P < 0.0001$.

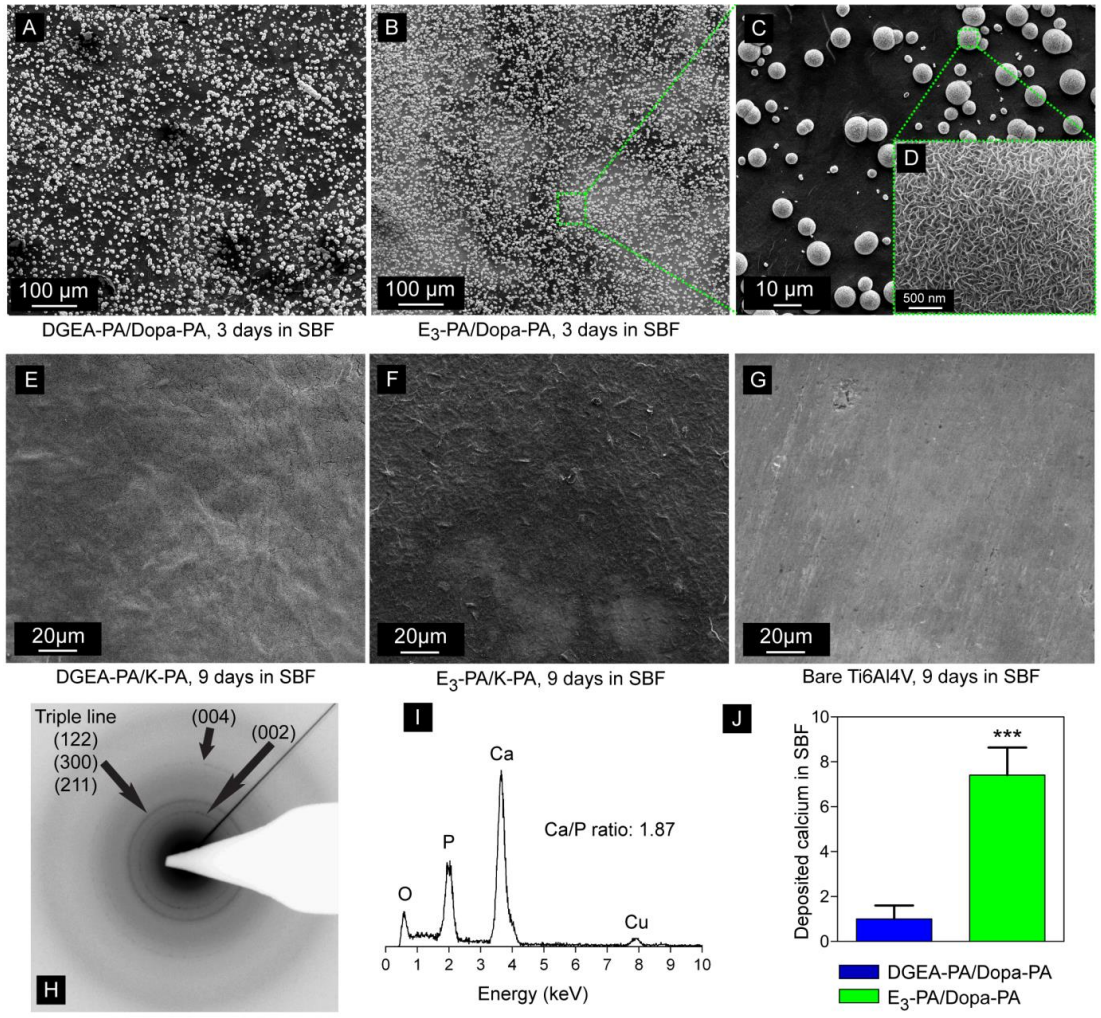

Figure 4.4 Hydroxyapatite formation on PA nanofibers in simulated body fluid. (a), (b), SEM micrographs of DGEA-PA/Dopa-PA and E_3-PA/Dopa-PA coated titanium surfaces on day 3. Hydroxyapatite islands nucleate from the surface of nanofibers, forming lath-like porous crystals (c), (d). Dopa residue has a predominant role in hydroxyapatite formation, as evidenced by the absence of the mineralization on DGEA-PA/K-PA and E_3-PA/K-PA up to 9 days in SBF (e), (f). Bare titanium also did not trigger mineralization (g). (h), (i) Diffraction patterns in SAED and Ca/P ratio in EDS identify the deposited mineral as hydroxyapatite. (j) On E_3-PA/Dopa-PA nanofibers, glutamic acid residues synergize with Dopa, leading to significantly higher amount (fold difference) of hydroxyapatite formation compared to DGEA-PA/Dopa-PA (Day 3). *** $P < 0.0001$.

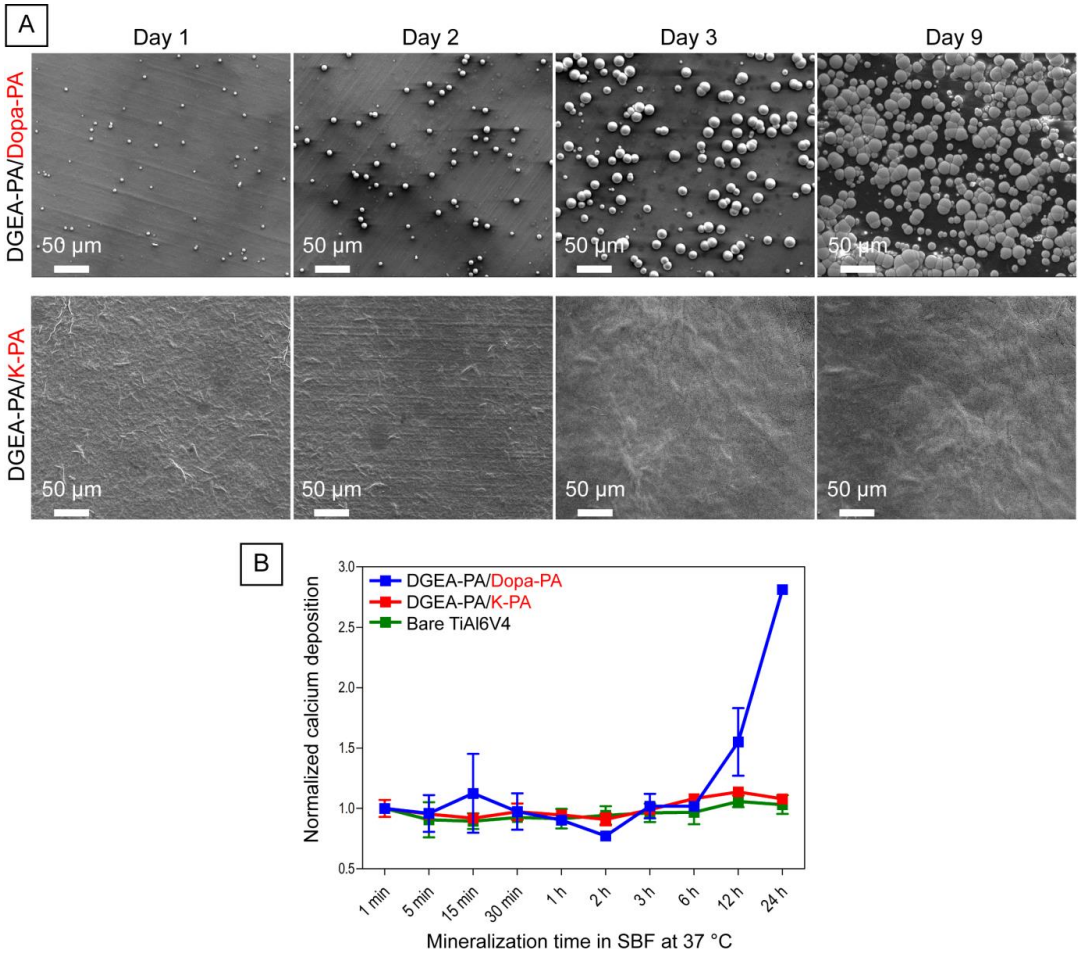

Figure 4.5 Dopa-functionalization is critical for HAp formation in SBF. (a) SEM images show deposition of HAp over the course of 9 days in SBF. The islands of HAp become evident on DGEA-PA/Dopa-PA even after 24 h. In the absence of Dopa, the control nanofibers of DGEA-PA/K-PA did not result in mineralization, highlighting the importance of this residue. (b) Kinetics of HAp formation on surface as probed by quantification of calcium over time showed that mineralization starts on DGEA-PA/Dopa-PA after 6 h in SBF. There is no detectable calcium on DGEA-PA/Dopa-PA and on bare Ti6Al4V over 24 h.

These results highlight the indispensible role of Dopa residue for hydroxyapatite formation on surface. Ryu et al. reported that poly dopamine-coating assists HAp formation by Ca^{2+} binding of catechol groups.[67] High negative charge density of oligo glutamic acid nanofibers can similarly induce hydroxyapatite formation in concentrated $CaCl_2$ solution supplemented with β-glycerophosphate and alkaline phosphatase enzyme.[211] On the other hand, analyzing mineralization in SBF is regarded as a more reliable strategy for understanding *in vivo* mineralization behavior of a biomaterial.[206] Indeed, higher concentration of poly glutamic acid inhibits HAp formation through strongly binding to calcium ion, and thereby inhibiting its supersaturation into crystalline phase.[212] Here, we combined the features of glutamic acid binding of calcium with that of catechol in the E_3-PA/Dopa-PA nanofibers. By doing so, we obtained much higher HAp on E_3-PA/Dopa-PA nanofibers compared to DGEA-PA/Dopa-PA in spite of the fact that both E_3-PA and DGEA-PA possess the same net charge at pH 7.4 (Figure 4.4j). Interestingly, SEM micrographs confirmed higher mineral density on E_3-PA/Dopa-PA with smaller individual island size (Figure 4.4a, b). Due to locally higher negative charge density of EEE, E_3-PA has a superior Ca-sequestering capacity compared to DGEA-PA, which had somewhat alternating negative residues in its primary sequence. This was thought to cause formation of higher number of prenucleation clusters on E_3-PA/Dopa-PA nanofibers, followed by Dopa-mediated crystallization into HAp.[213] Therefore, the bioactivity of E_3-PA/Dopa-PA in bone integration was predicted to be higher than DGEA-PA/Dopa-PA.

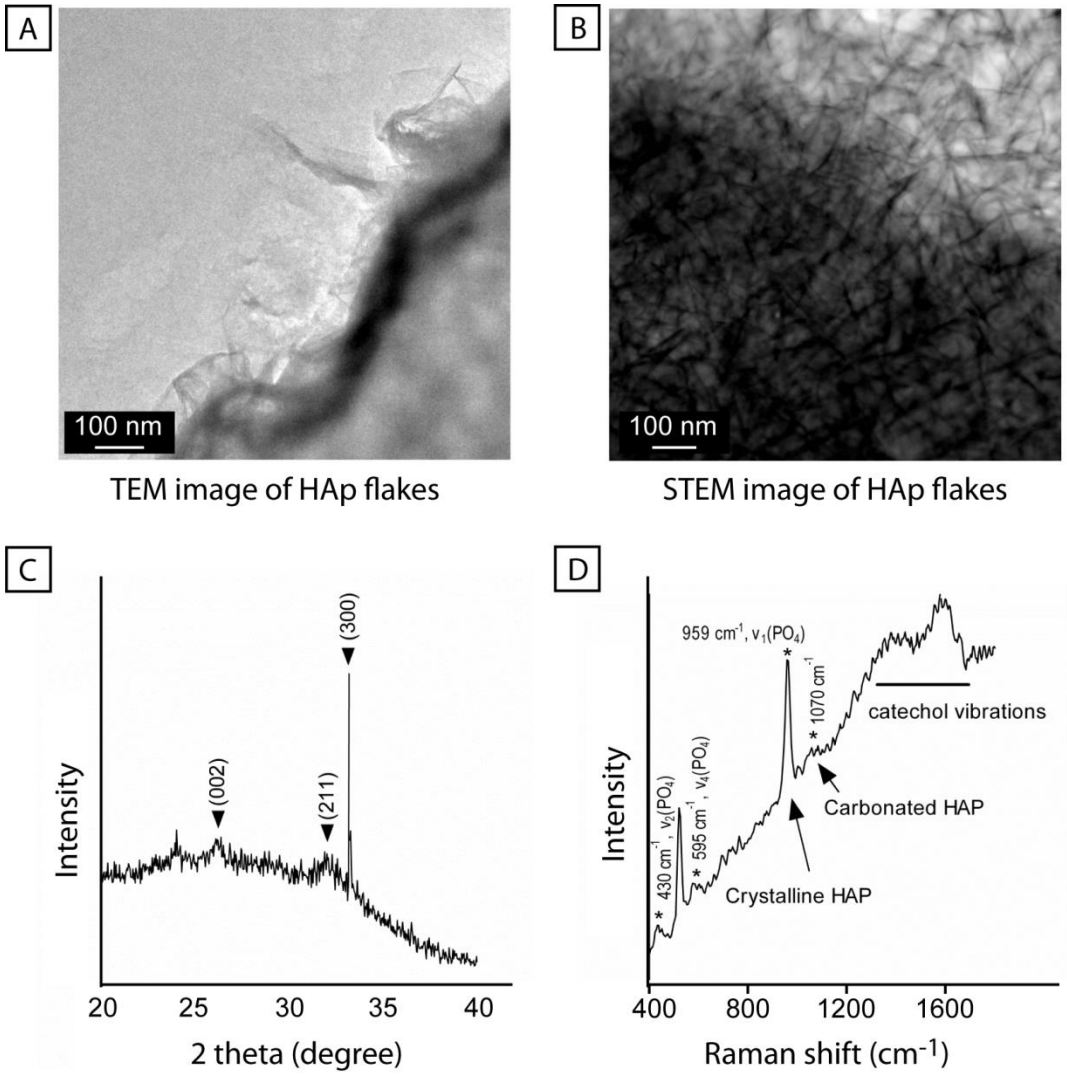

Figure 4.6 Characterization of HAp formation. (a) TEM, (b) STEM images showing characteristic flakes of HAp. (c) XRD patterns of HAp.[102, 207, 208] (d) Raman spectrum showing carbonated crystalline HAp similar to bone apatite.

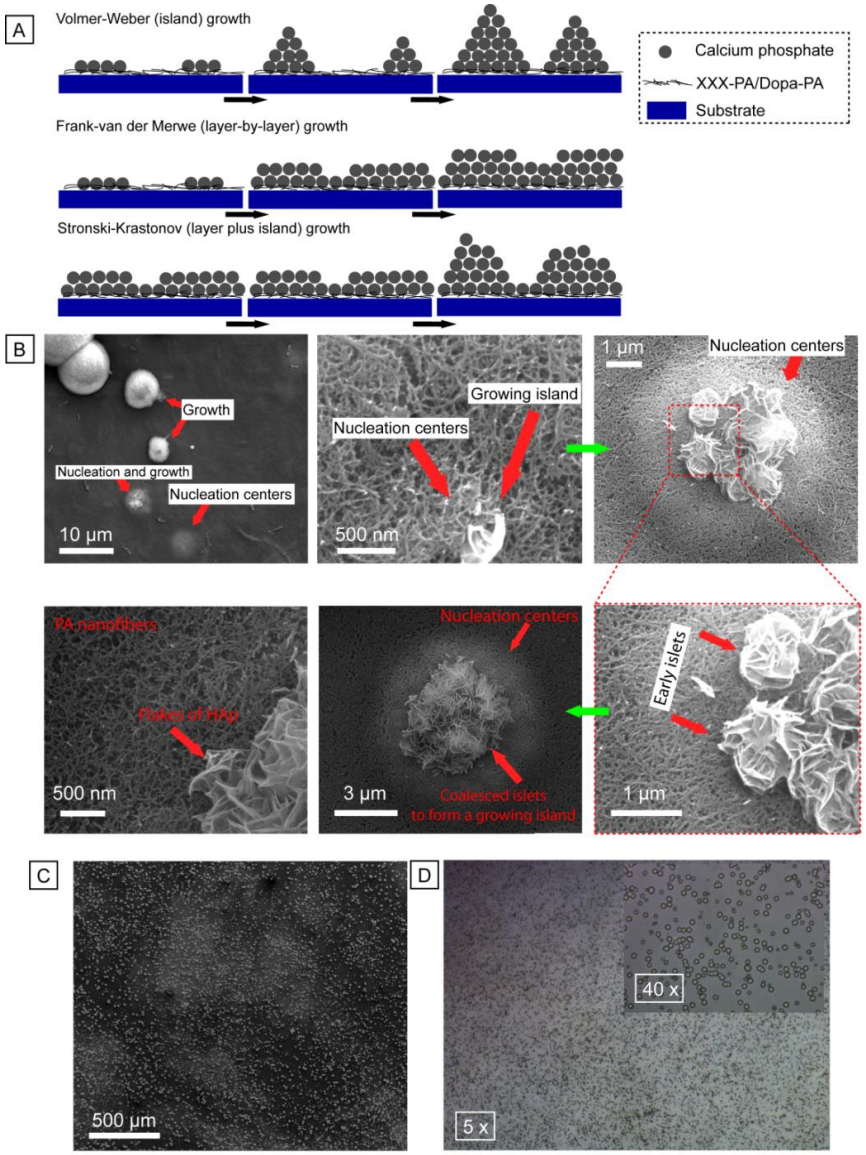

Figure 4.7 Three modes of thin film growth on a substrate. (a) HAp formation on Dopa-functionalized (DGEA-PA/Dopa-PA) nanofibers follow Volmer-Weber mode. In this island mode, first a large number of surface nuclei form across the substrate followed by the growth phase on these nuclei. (b) Representative SEM images showing nucleation and growth of HAp crystals at different phases. From nucleation centers form small (early) islets, which are then fused (coalesced) to form larger islands. This larger island then continues to grow until a spherical (mature) HAp is formed. (c) SEM and (d) light microscopy images indicating the homogeneity of HAp formation on Dopa-functionalized nanofibers coated tissue culture plate.

4.3.4 Adhesion, spreading, migration, survival, and proliferation of hMSCs

A bioinstructive microenvironment for bone tissue regeneration should support adhesion, spreading, and survival of hMSCs and induce their differentiation into mineral-depositing osteoblasts. Adhesion and spreading are first prerequisite events for the survival, proliferation, and phenotypic behaviors of most of the cells that come into contact with a biomaterial.[214-216] Moreover, analyses of these two parameters give direct evidence of specific cell-material contact. We investigated the adhesion and spreading of hMSCs on the nanofibers in serum-free medium supplemented with bovine serum albumin and cyclohexamide. Albumin acts to reduce non-specific interactions with the nanofibers whereby cyclohexamide inhibits the global translation process, which reduces the interference of endogenously synthesized proteins in the adhesion and spreading of the cells. By doing so, our emphasis was to enhance the signal pertaining to initial cell-nanomaterial interactions. After 2 h, the adhesion of hMSCs on DGEA-PA/Dopa-PA was found significantly higher than on E_3-PA/Dopa-PA and bare Ti6Al4V (Figure 4.8a). Adhesion on HAp (DGEA-PA/Dopa-PA) was also higher than HAp (E_3-PA/Dopa-PA), revealing the significance of DGEA that facilitates direct contact between the cells and surface-bound nanofibers. This behavior is in agreement with the previous studies, in which DGEA ligand facilitates cell binding through its integrin α2β1 receptor.[189] Interestingly, cell adhesion on both HAp (DGEA-PA/Dopa-PA) and HAp (E_3-PA/Dopa-PA) was higher compared to their non-mineralized counterparts. The enhanced total surface area on the mineralized substrates might be caused by the spherical HAp islands. Similar to the adhesion, the mean projection cell areas followed a trend where hMSCs spread the most on the pre-mineralized HAp (DGEA-

PA/Dopa-PA) and DGEA-PA/Dopa-PA coatings (Figure 4.8b). To further support this specific interaction, we investigated the cell motility of hMSCs on the nanofibers. Previously it was shown that cell motility and adhesion strength often show opposite trends.[215, 217, 218] This can allow empirical evaluation of the interaction between hMSCs and the nanofibers, such that cells should be slowest on the DGEA-presenting nanofibers as the interaction strength between DGEA ligands on the nanofibers and the surface receptors slows the overall cell motility. Indeed, on both DGEA-PA/Dopa-PA and HAp (DGEA-PA/Dopa-PA) coatings, cell locomotion was significantly slower than on bare surface (Figure 4.8c). In addition to these early-stage cell-matrix interactions, the nanofibers were also found to be biocompatible as evaluated by the comparable viability levels at 24 h (Figure 4.8d). Furthermore, hMSCs continued proliferation at comparable levels on DGEA-PA/Dopa-PA and E_3-PA/Dopa-PA. On the other hand, the proliferative cell numbers significantly decreased on the pre-mineralized coatings (Figure 4.8e). This could be due to the commitment of hMSCs for differentiation on the mineralized HAp (DGEA-PA/Dopa-PA) and HAp (E_3-PA/Dopa-PA) surfaces. Similar to our observation, adipose-derived mesenchymal stem cell proliferation was previously reported to be negatively correlated with the mineral content on a nanofibrous polymer scaffold.[219]

4.3.5 Osteogenic differentiation of hMSCs

Differentiation of hMSCs along the osteoblast lineage begins with commitment to osteoprogenitor cells followed by differentiation into pre-osteoblasts and finally maturation into functional osteoblasts.

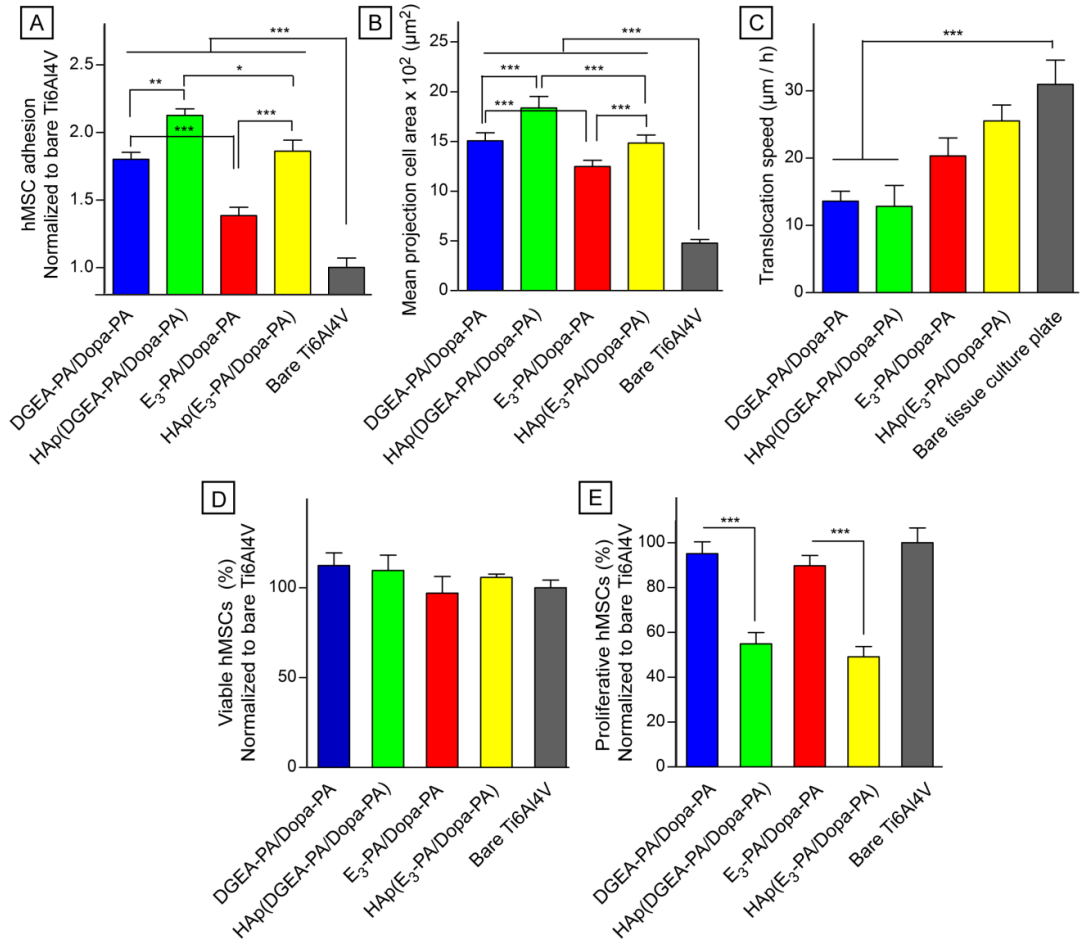

Figure 4.8 Early-stage interactions of hMSCs with the osteoinductive nanofibers. (a), (b) Adhesion and spreading of hMSCs on the nanofiber coatings in serum-free medium at 2 h 15 min. (c) Translocation speed of hMSCs. (d) Viability of hMSCs at 24 h. (e) Proliferative hMSCs over the course of 5 days. * $P < 0.05$, ** $P < 0.01$, *** $P < 0.0001$, Δ $P < 0.0001$; comparing day 1 with both day 3 and day 5.

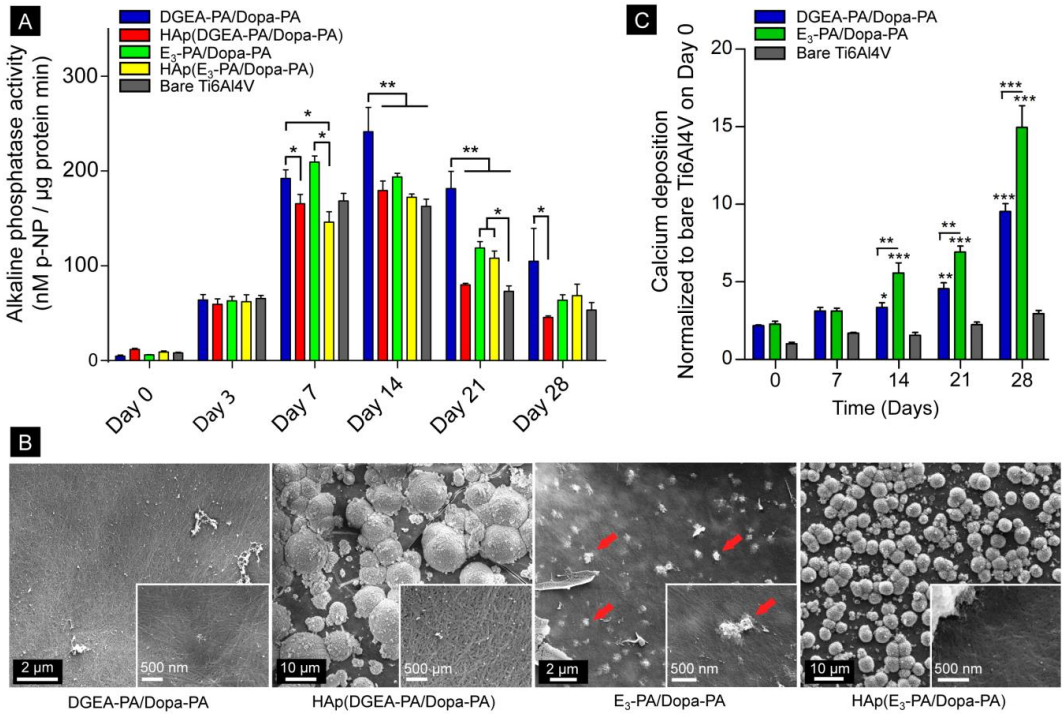

Figure 4.9 Osteoinductive effect of PA nanofibers on hMSCs. (a) Alkaline phosphatase activity of hMSCs over 4 weeks. (b) SEM micrographs of cell-seeded coatings, revealing the surface stability of the nanofibers against the cellular activity (day 28). Arrows point *de novo* calcium phosphate formation on E_3-PA/Dopa-PA as a result of osteoblast activity. (c) Calcium deposition (fold difference) on the PA nanofibers over 4 weeks. * $P < 0.05$, ** $P < 0.01$, *** $P < 0.0001$.

A biochemical marker for the initial commitment to osteoprogenitor cells is the elevated alkaline phosphatase (ALP) activity, which is a prerequisite for enriching bone formation site with inorganic phosphates. Over the course of 3 weeks, hMSCs cultured on DGEA-PA/Dopa-PA nanofibers exhibited the highest ALP activity after day 7 (Figure 4.9a). This was attributable to the initial osteoinductive signal provided by the DGEA sequence. This result is also in agreement with a previous study where DGEA ligand presented on a nanofibrous phage induced early differentiation of mouse pre-osteoblasts.[10] Interestingly, ALP activities stimulated by pre-mineralized HAp (DGEA-PA/Dopa-PA) and HAp (E_3-PA/Dopa-PA) nanofibers tended to remain lower (since day 7 up to day 21) than their non-mineralized nanofiber counterparts.

On both nanofiber systems, typical spindle-like morphology of hMSCs completely differentiated to osteoblast-like large cells over 28 days of differentiation (Figure 4.10). Some cells also contained multiple protrusions, with smaller cell body, reminiscent of osteocyte precursors. SEM micrographs of the surfaces acquired on day 28 confirmed the stability of the coatings against the biochemical activity of the cells, showing that osteoinductive signals of the nanofibers were be sustained over the course of the experiment (Figure 4.9b). Notably, on the E_3-PA/Dopa-PA nanofibers, we observed *de novo* agglomerates of calcium phosphate, which were attributed to the activity of mature osteoblasts (Figure 4.9 and Figure 4.11a). Since the alkaline phosphatase activity was higher on DGEA-PA/Dopa-PA, the resulting mineralization was expected to be higher as well. However, we did not observe similar aggregates on DGEA-PA/Dopa-PA coatings. It is also important to highlight that the flakes of HAp islands on HAp (DGEA-PA/Dopa-PA) and HAp (E_3-PA/Dopa-PA) got thickened after 28 days in culture with cells (Figure 4.11b).

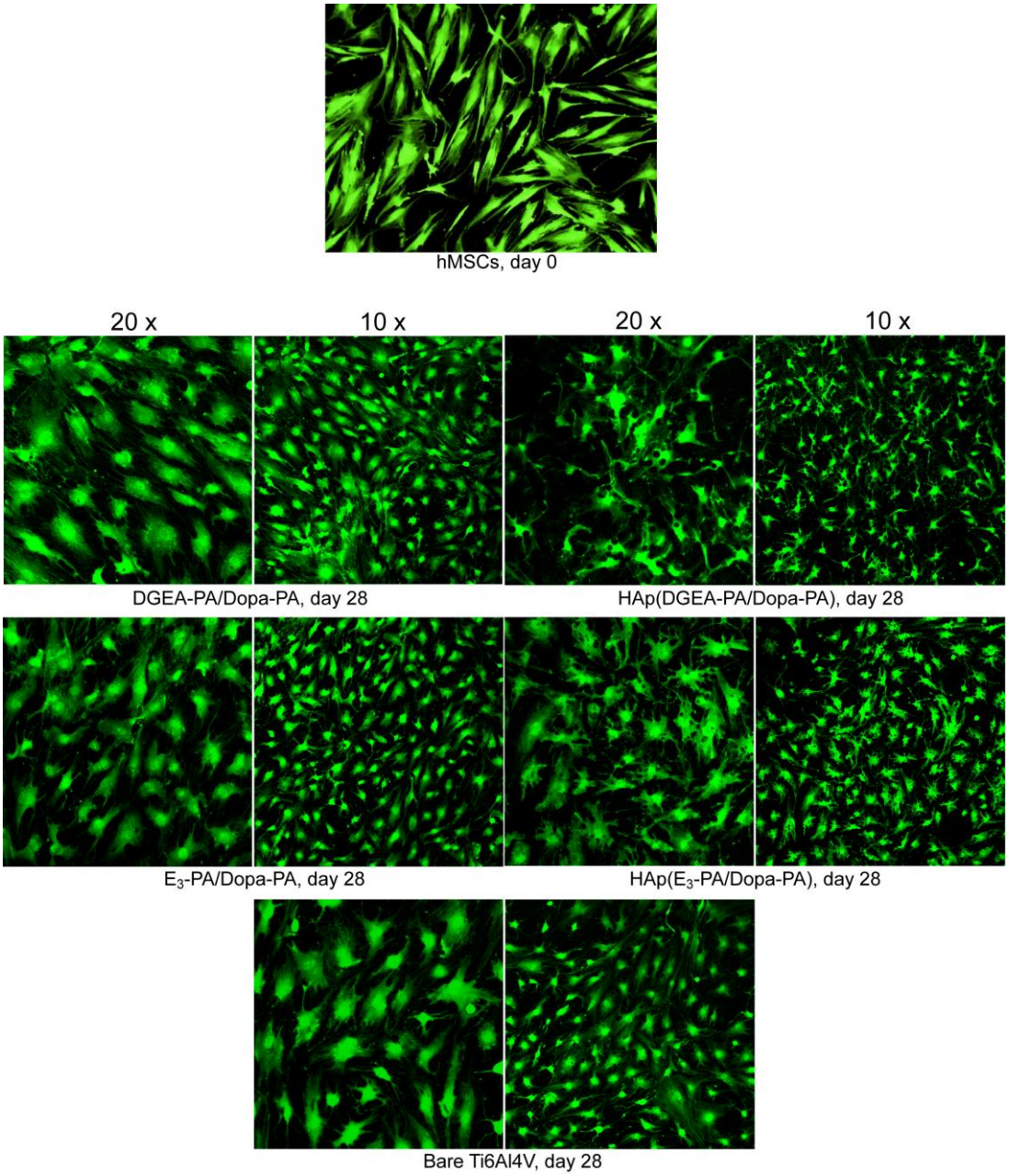

Figure 4.10 Morphology of hMSCs at day 0 and at day 28 after differentiation was induced. Cells were stained with calcein-AM.

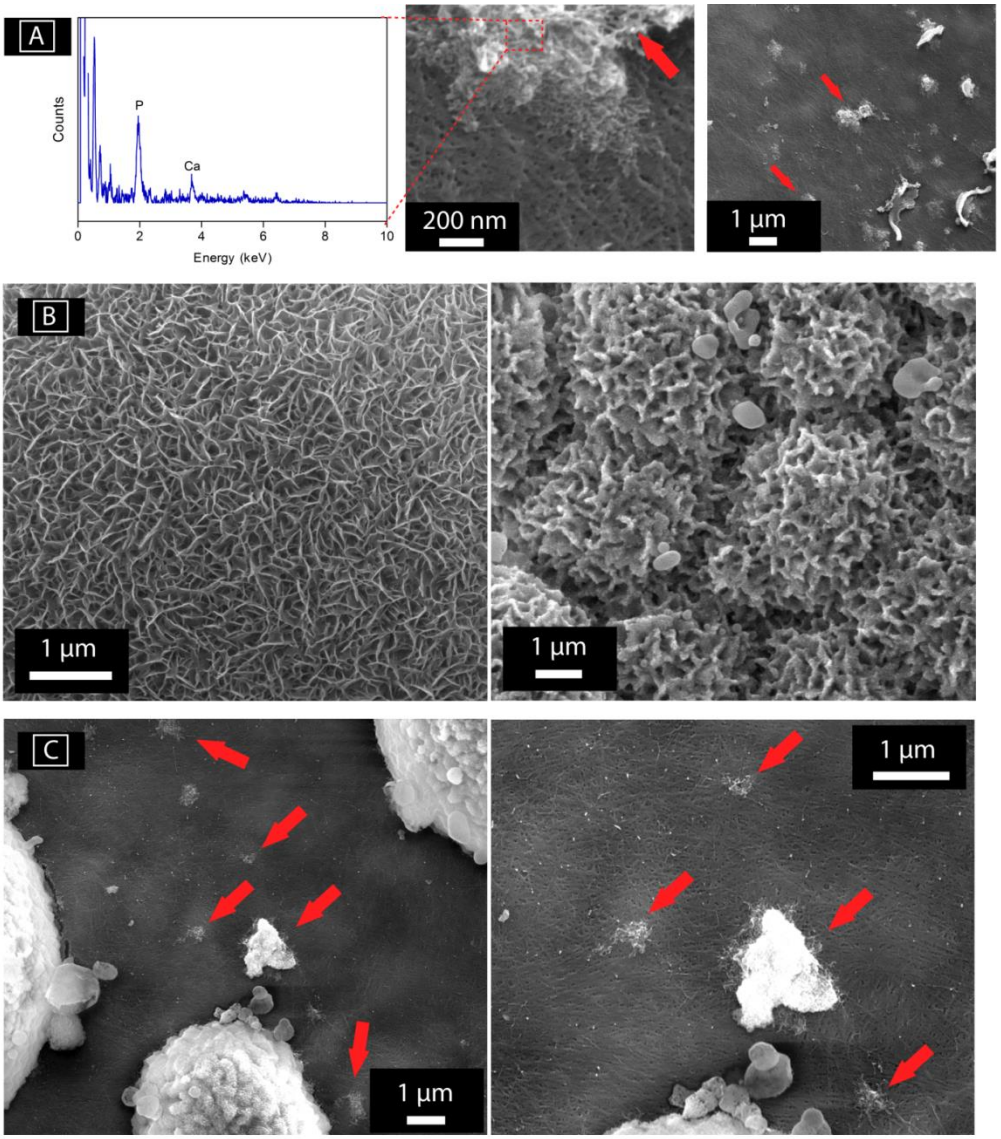

Figure 4.11 ***De novo*** **calcium phosphate formation on E_3-PA/Dopa-PA by differentiated osteoblast activity.** (A) EDAX spectrum on the left shows the presence of phosphorus and calcium. SEM micrographs on the right shows the mineral formed around a fibrous structure. The background nanofibrous surface is E_3-PA/Dopa-PA while the mineralized fibers remain elusive. (B) HAp morphology before (day 0, left) and after differentiation (day 28, right) of hMSCs. Thickening flakes were observed on both DGEA-PA/Dopa-PA and E_3-PA/Dopa-PA. (C) *De novo* calcium phosphate formation on HAp (DGEA-PA/Dopa-PA) by differentiated osteoblast activity. Arrows point the *de novo* mineral sites. Other large islands were formed in SBF prior to differentiation.

This was attributed to the activity of differentiated cells, so that *de novo* calcium phosphate continued to grow over the existing mineral. Nevertheless, newly nucleated calcium phosphate aggregates were also evident (Figure 4.11c). To further analyze the osteoinductive effect of DGEA-PA/Dopa-PA and E_3-PA/Dopa-PA on the osteogenic differentiation of hMSCs, we quantified deposited calcium as a result of cellular bioactivity of the maturated osteoblasts. We deduce that day 14 marks the emergence of mature osteoblasts, which is signified by the significantly higher amount of deposited calcium on both DGEA-PA/Dopa-PA and E_3-PA/Dopa-PA nanofibers in comparison with the bare titanium (Figure 4.9c). On day 14, the amount of calcium deposited on E_3-PA/Dopa-PA was also significantly higher than that of DGEA-PA/Dopa-PA. This difference continued to increase until day 28. Even though initial ALP activity was higher by the induction of DGEA-PA/Dopa-PA, E_3-PA/Dopa-PA induced mature osteoblast formation more efficiently. Taking into account of Figure 4.4j where HAp deposition on E_3-PA/Dopa-PA was greatly increased as a result of the synergistic interaction of poly glutamic acid groups with Dopa; we accounted this mainly to more favorable chemical properties of E_3-PA/Dopa-PA, which could better facilitate the mineralization by cellular activity. As a result, the overall mineral formation on the E_3-PA/Dopa-PA rapidly increased compared to DGEA-PA/Dopa-PA. In order to assess the impact of accelerated mineralization by E_3-PA/Dopa-PA on the differentiation of hMSCs, we explored the expression of genes associated with osteoblastogenesis. Runt-related transcription factor 2 (RUNX2) and collagen type I alpha 1 (COL1A1) are two cardinal marker proteins of this process, so their expression levels is informative about the differentiation stage of the cells.

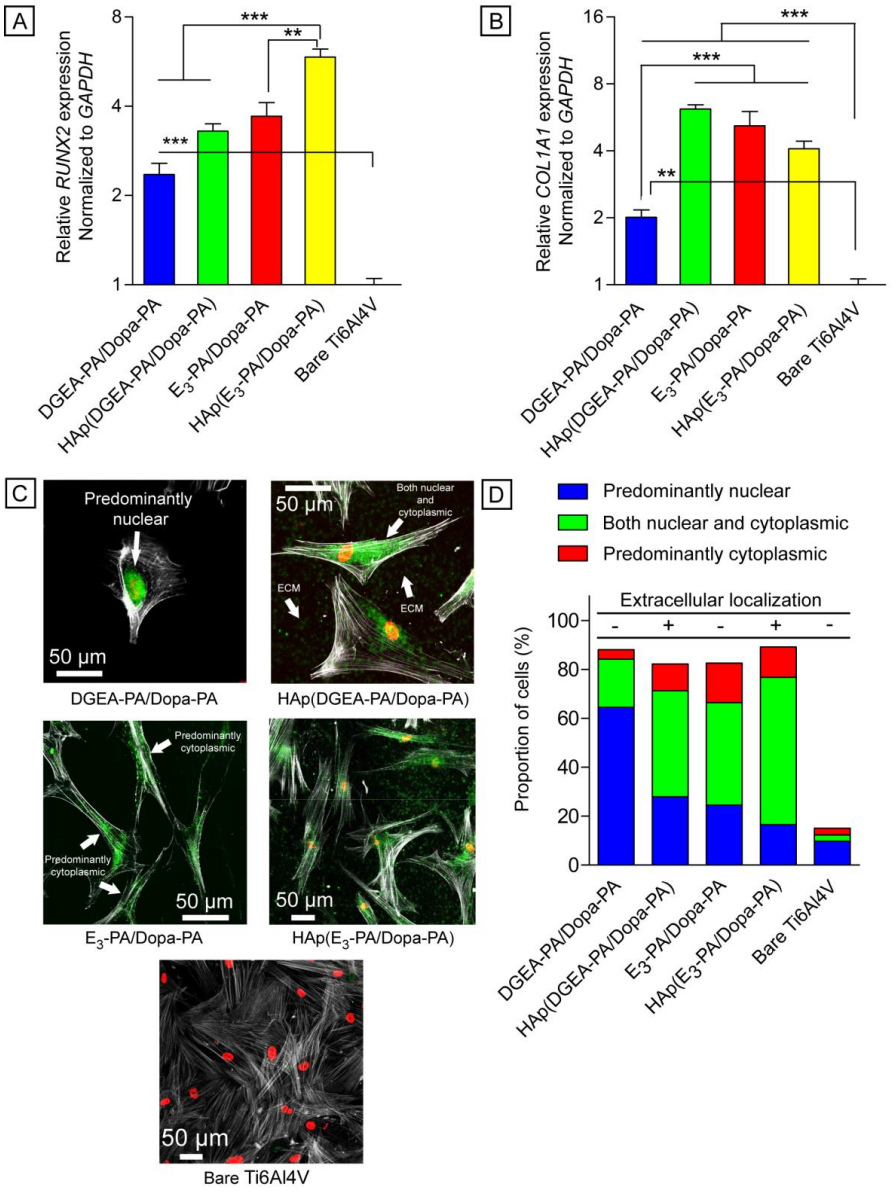

Figure 4.12 Differentiation of hMSCs into the osteoblast lineage cells by PA nanofibers. (a), (b) Expression levels of *RUNX2* and *COL1A1* genes confirm the osteogenic differentiation by day 28. Localization of DMP-1 protein inside the cell is informative about the differentiation stage of the cell within the osteoblast linage. (c) Confocal images of DMP-1 immunostaining. The arrows point the nuclear, cytoplasmic, or extracellular localization of DMP-1. Green shows DMP-1, grey shows filamentous actin, red shows the nucleus. (d) Distribution of DMP-1 localization in cell populations. ** $P < 0.01$, *** $P < 0.0001$.

Here, we also included pre-mineralized HAp (DGEA-PA/Dopa-PA) and HAp (E_3-PA/Dopa-PA) compositions to better evaluate the impact of mineralization on the differentiation in comparison with their non-mineralized nanofibers. On day 28, the highest *RUNX2* gene expression was observed on HAp (E_3-PA/Dopa-PA) and the lowest on the bare titanium (Figure 4.12a). Although statistically not significant, the expression of *RUNX2* on HAp (DGEA-PA/Dopa-PA) was found higher than that of DGEA-PA/Dopa-PA. A similar trend was also observed in the expression of *COL1A1* gene where the expression levels were comparable among HAp (DGEA-PA/Dopa-PA), HAp (E_3-PA/Dopa-PA), and E_3-PA/Dopa-PA (Figure 4.12b). However, the lower expressions of *COL1A1* and *RUNX2* on DGEA-PA/Dopa-PA compared to the other coatings show that maturation of cells was at a lesser stage on DGEA-PA/Dopa-PA. To further confirm this result, we investigated the intracellular and extracellular localization of dentin matrix protein-1 (DMP-1). DMP-1 belongs to the Small Integrin Binding Ligand N-Linked glycoprotein family (SIBLINGs) expressed in osteoblasts and osteocytes. [220] DMP-1 can be found in the nucleus, cytoplasm, or extracellular matrix depending on the maturation state of osteoblasts.[221] This protein has a dual role in the biomineralization process. In pre-osteoblasts, DMP-1 is predominantly localized in the nucleus where it acts as a transcriptional component for activation of osteoblast-specific genes, such as osteocalcin.[221] During the osteoblast maturation, phosphorylated DMP-1 is exported to the extracellular matrix where it regulates nucleation of hydroxyapatite. Therefore, localization of this protein is highly informative about the osteoinductivity of the

nanofibers. On day 28, on DGEA-PA/Dopa-PA, more than 60% of the cells showed predominant nuclear localization, showing that more than half of the cells differentiated on these nanofibers were at the pre-osteoblast stage (Figure 4.12c). On the other hand, on all HAp (DGEA-PA/Dopa-PA), HAp (E_3-PA/Dopa-PA), and E_3-PA/Dopa-PA coatings, predominant cytoplasmic localizations were evident. In addition, we observed extracellular localization of DMP-1, where phosphorylated DMP-1 proteins were attached to the HAp formed by the nanofibers on HAp (E_3-PA/Dopa-PA) and HAp (DGEA-PA/Dopa-PA).[222] As a result, we concluded that hMSC differentiation into mature osteoblasts was promoted in the highest degree by the pre-mineralized compositions. Although we did not notice extracellular DMP-1 localization on E_3-PA/Dopa-PA, its predominant localization in the cytoplasm shows that cells on these nanofibers were at a higher maturation stage compared to those on DGEA-PA/Dopa-PA. Conversely, even less than 20% of cells on the bare titanium showed positive DMP-1 staining, indicating that differentiation efficiency was much lower compared to the osteoinduction of nanofiber systems. Altogether, these results show that even though early osteogenic commitment was enhanced on DGEA-PA/Dopa-PA, the maturation of cells into functional osteoblasts was more efficient on E_3-PA/Dopa-PA, at almost comparable level to those of the pre-mineralized peptide nanofibers.

4.4 Conclusion

In this study, we developed bioinspired multifunctional nanofibers, which served as osteoinductive interfaces between hMSCs and titanium surface. All PA functionalized surfaces exhibited higher performance in terms of adhesion and

differentiation of hMSCs, compared to uncoated titanium. We demonstrated that Dopa residue has two critical functions: mediating robust immobilization of the nanofibers onto titanium surface and nucleating bone-like hydroxyapatite minerals on the nanofibers. Although DGEA-PA/Dopa-PA mediates early adhesion and differentiation into osteoprogenitor cells, E_3-PA/Dopa-PA efficiently directs mature osteoblast formation and subsequent mineralization. With that, we here showed that on the contrary to the common thinking [182, 185, 223-226], initial osteogenic commitment of the progenitor stem cells does not necessarily guarantee a priority for maturation into functional osteoblasts. Therefore, bone-like hydroxyapatite nucleating E_3-PA/Dopa-PA nanofibers exhibit an outstanding induction of osteogenesis, which, we suggest, is owing to the physical proximity of Dopa and glutamic acid residues on the nanofibers, boosting hydroxyapatite formation. Overall, this synthetic platform is a successful example of effective employment of the reductionist approach for eliciting strong regenerative response through molecular level cell-material interactions.

4.5 Experimental Section

4.5.1 Synthesis and characterization of peptide amphiphiles

Lauryl-VVAGKDopa-NH_2 (Dopa-PA), Lauryl-VVAGK-NH_2 (K-PA), Lauryl-VVAGEGDGEA-NH_2 (DGEA-PA), and Lauryl-VVAGEEE-NH_2 (E_3-PA) were synthesized using Fmoc solid phase peptide synthesis. Fmoc protection group on the N^{α}-amino group of the peptide was removed by 20% piperidine/dimethylformamide at each coupling step. Rink Amide MBHA resin (Novabiochem) was used as the solid support. Carboxylate group activation of 2 mole equivalents (equiv.) of amino

acids was achieved by 1.95 mole equiv. of N,N,N',N'-Tetramethyl-O-(1H-benzotriazole-1-yl) uranium hexafluorophosphate (HBTU), and 3 mole equiv. of diisopropylethylamine (DIEA) for 1 mole equiv. of N^{α}-amino sites attached on the resin. Coupling time at each step was limited to 2 h. For the removal of the protecting groups following the last coupling step, a cleavage cocktail containing 95% trifluoroacetic acid (TFA), 2.5% water, and 2.5% triisopropylsilane was used. Excess TFA was partly removed by rotary evaporation followed by precipitation in diethyl ether overnight. The precipitate was collected and dissolved in ultra-pure water. This solution was frozen at −80 °C followed by freeze-drying for one week. Residual TFA was removed from PAs with overall positive charge by dissolving the whole batch in dilute HCl solution with a subsequent dialysis procedure using cellulose ester dialysis membrane with molecular-weight-cut-off of 100–500 Da. For PAs with overall negative charge, a reverse-phase preparative HPLC purification was employed. Following the TFA removal procedure, PAs were once more freeze-dried and their purity was assessed using Agilent 6530 quadrupole time of flight (Q-TOF) mass spectrometry with electrospray ionization (ESI) source equipped with a reverse-phase analytical HPLC (Figure 4.13).

4.5.2 Formation of self-assembled peptide nanofibers

Aqueous solutions of all PAs were prepared at pH 7.4 using diluted HCl or NaOH. Self-assembly into hydrogels was rapid enough to allow monitoring by eye within a few minutes in the range of 1-10 mM monomer concentrations. The resulting nanonetwork was investigated using scanning electron microscopy (SEM).

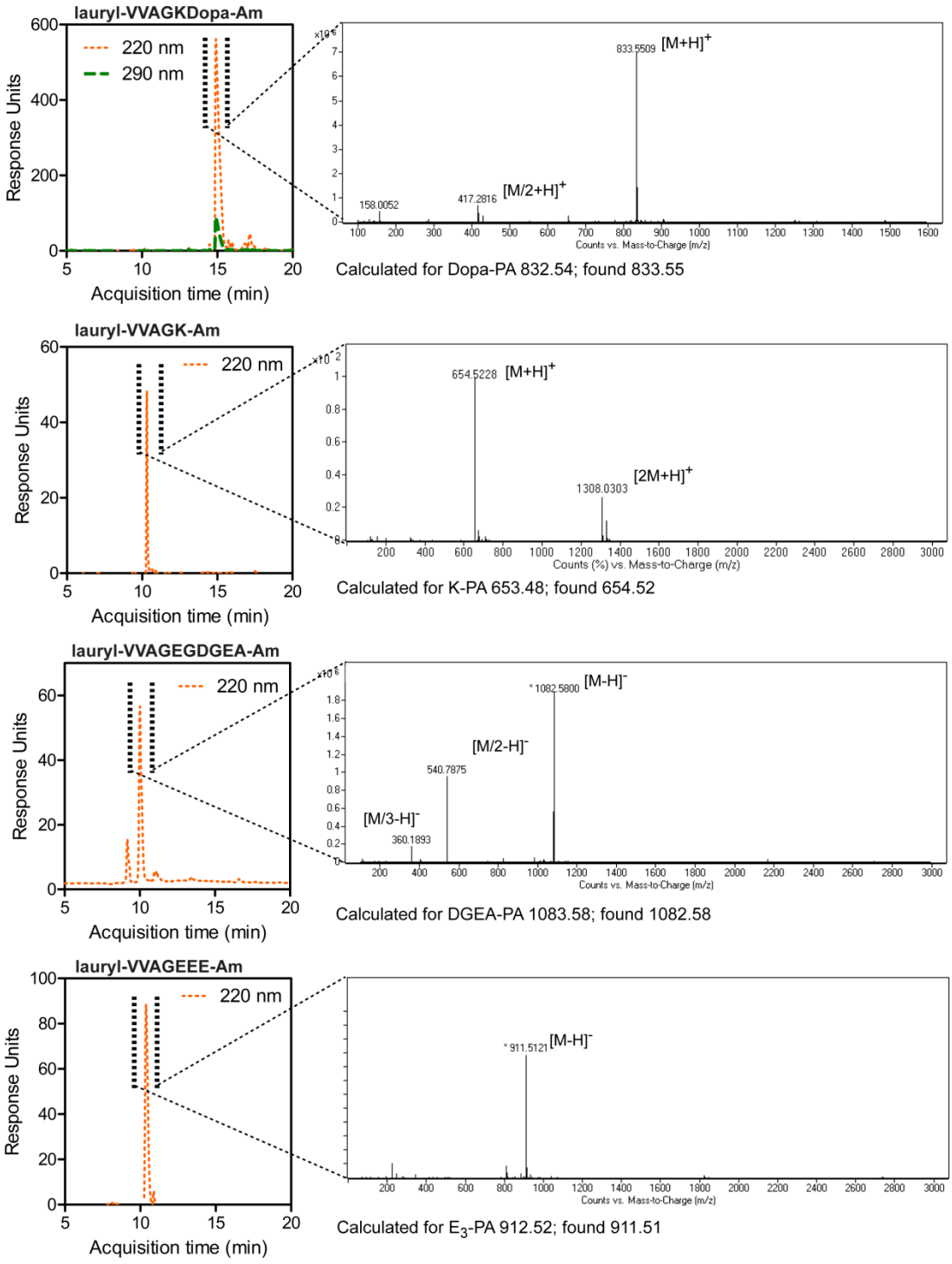

Figure 4.13 Liquid chromatography-mass spectrometry (LC-MS) analysis of the synthesized PAs. The purities of the crude products were analyzed according to the optical density at 220 nm.

Following 10 min of gelation on conductive stainless steel surfaces, hydrogels (formed by 10 mM monomer concentration) were dehydrated in gradually increasing concentrations of ethanol/water solutions. Dehydrated hydrogels were dried using a Tourismis Autosamdri®-815B critical point drier to preserve the network structure. The dried samples were coated with 3 nm Au/Pd and visualized under high vacuum with a FEI Quanta 200 FEG SEM equipped with an ETD detector. To investigate the secondary structure of PA nanofibers, circular dichroism (CD) (Jasco J-815) was used. 5 x 10^{-5} M DGEA-PA (or E_3-PA) was mixed with 5 x 10^{-5} M Dopa-PA (or K-PA) at 1:3 volume ratios. After 5 min, spectrometric measurement was acquired at room temperature from 260 nm to 190 nm with 0.1 nm data interval and 500 nm/min scanning speed. The results were converted to and represented as the molar ellipticity. Zeta potential measurements were performed with a Malvern Zeta-ZS Zetasizer at the same monomer concentrations used in CD.

4.5.3 Stability of peptide nanonetworks on titanium substrate

100 μm-thick plain medical grade Ti6Al4V (Good Fellow Inc.) substrates were cut into small pieces followed by ultrasonic cleaning sequentially in acetone, ethanol, and water for 1 h in each. Samples were then dried under vacuum at 50 °C for at least 6 h. DGEA-PA/Dopa-PA, E_3-PA/Dopa-PA, DGEA-PA/K-PA, and E_3-PA/K-PA coatings were formed *in situ* on Ti6Al4V surfaces. 25 μL of 1 mM DGEA-PA (or E_3-PA) solutions was mixed with 75 μL of 1 mM Dopa-PA (or K-PA) on per square centimeter of Ti6Al4V. The functional epitope concentrations on all nanofiber compositions were equal as shown in Table 4.1. The mixtures were then slowly dried in a humidified chamber at 37 °C for 48 h. K-PA served as the control of Dopa-PA.

After drying, the coatings were washed in 10X PBS for 2 days followed by washing in 10 wt% SDS for 1 h, all steps accompanied by vigorous shaking. To enhance visibility, the residual nanofibers were then stained with coomassie brilliant blue at room temperature for 1 h followed by a destaining solution containing water/methanol/acetic acid in a ratio of 50:40:10 for 3 h. To quantify the residual amount, the digital images were used to determine relative spot densities. The densities were normalized to that of E_3-PA/K-PA. Each bar represents the average of at least six measurements. A Thermo Scientific X-ray photoelectron spectrometer (XPS) with Al K_α micro-focused monochromatic X-ray source was utilized at ultra-high vacuum (~10^{-9} Torr). For XPS, the same sample preparation technique was employed as used in coomassie staining except that SDS washing step lasted 3 h. The spectra were acquired from at least three random locations on each substrate.

4.5.4 Mineralization of peptide nanonetworks in simulated body fluid

Titanium substrates coated with peptide nanofibers were prepared as described above. 1.5 x simulated body fluid (SBF) was prepared at pH 7.4 containing the following ion concentrations: Na^+ 213.0 mM, K^+ 7.5 mM, Mg^{2+} 2.3 mM, Ca^{2+} 3.8 mM, Cl^- 221.7 mM, HCO_3^- 6.3 mM, HPO_4^{3-} 1.5 mM, SO_4^{2-} 0.8 mM. Prior to immersing in SBF for mineralization, substrates were first washed with SBF to remove any residual particulates. Substrates were then immersed in 5 mL SBF per cm^2 peptide substrate. Unless otherwise is indicated, incubation period was set to 3 days at 37 °C and pH 7.4. For samples to be used in *in vitro* assays, the substrates were washed with water and PBS prior to cell seeding. For SEM imaging, samples were dehydrated in ethanol/water gradient. Then, samples were dried in critical point

drier as explained in Experimental Section 4.5.3. For the chemical analysis of the mineral, energy dispersive X-ray spectrometer (EDS), selected area electron diffraction (SAED) (both coupled to FEI Tecnai G2 F30 TEM), X-ray diffraction (PANalytical X'Pert Powder) and Raman spectrum (Witec) were employed. Minerals were investigated on day 3, following a thorough washing with deionized water and subsequent air drying.

4.5.5 Human mesenchymal stem cell culturing

hMSCs were isolated from the bone marrow of 31 years old healthy female donor (wt. 80 kg ht. 163 cm). Ethical committee approval was obtained from Turgut Ozal University School of Medicine. We adopted a previously published protocol for isolation of spindle-like colony-forming hMSCs, which exhibit culture plate adherence.[227] Isolated hMSCs were verified using four positive (CD44, CD90, CD105, integrin β1) and one negative (CD45) surface marker proteins, which were obtained from Abcam (Figure 4.14). hMSCs were used in passage numbers between 3 and 7. Cells were maintained in 225 cm^2 flasks in Dulbecco's Modified Eagle's Medium (DMEM) containing 20% fetal bovine serum and 1% penicillin/streptomycin. Cells were cultivated at standard humidified incubators with constant 5% CO_2 at 37 °C. Detachment of cells was done using trypsin/EDTA chemistry at *ca.* 75% confluency. At each passage, cell seeding density was determined to be 2 x 10^3 cells cm^{-1}.

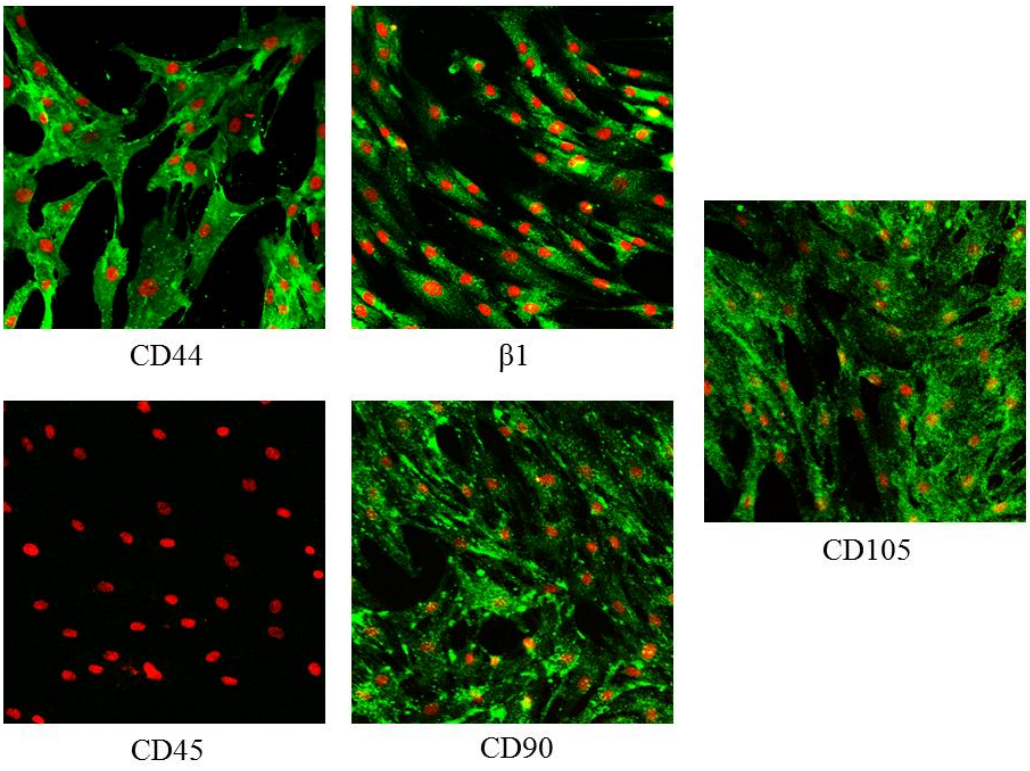

Figure 4.14 Characterization of surface markers of hMSCs isolated from the donor bone marrow. CD44, integrin beta 1, CD105, and CD90 are positive markers whereas CD 45 is a negative marker. Green shows positive staining and red shows nuclei. All images were acquired at 20X magnification.

4.5.6 Preparation of surfaces for in vitro assays

Titanium substrates coated with peptide nanofibers were prepared as described above. In order to remove any residual particulates, coated substrates were washed with PBS prior to cell seeding. Sterilization was achieved via UV irradiation for 2 h.

4.5.7 Cell adhesion, spreading and locomotion

Prior to seeding, hMSCs were incubated with serum-free DMEM supplemented with 3 wt% albumin (bovine serum) and 0.05 wt% cyclohexamide for 2 h. Following pre-incubation, cells were detached by brief trypsinization at room temperature (~30 s) in order not to chop off the cell surface receptors. Cell seeding density onto the coatings was 3 x 10^4 cells cm^{-1}. After 2 h 15 min, cells were gently washed with PBS on a rotatory shaker. To visualize cells, actin filaments were stained using TRITC-Phalloidin (Sigma-Aldrich). For this, specimens were fixed with 3.7 wt% formaldehyde followed by permeation with 0.1 vol% Triton-X. For counter staining, cell nuclei were stained with TO-PRO®-3 iodide (Molecular Probes). Adhesion and spreading were quantified based on the images of adhered cells acquired in randomized areas at each substrate. At least 5 random images were taken from a single replica at 10X magnification using a fluorescent microscope. For each independent assay, at least 4 technical replicas were included. Cellular locomotion was assessed based on the average displacement of hMSCs on peptide nanofibers in between a defined time period. hMSCs were seeded at a density of 1 x 10^3 cells cm^{-1}, with the aim of minimizing intercellular interactions to elucidate the impact of nanofibers on the movement. The consecutive images were acquired using a confocal microscope (Zeiss LSM 510) at every 30 min for 6 h in total.

4.5.8 Cell viability and proliferation

Cell viability was assessed using MTT assay. 24 h after seeding hMSCs on the nanofibers at a density of 5 x 10^3 cells cm^{-1}, cells were treated with (3-(4,5-dimethylthiazol-2-yl)-2,5-diphenyltetrazolium bromide (MTT) reagent (Sigma-Aldrich). Following a 3 h post-incubation period, the optical density of the purple color, as indicative of the number of the live cells, was quantified at 590 nm. Proliferative cells were determined using Click-iT™ EdU assay (Molecular Probes). hMSCs were incubated with a nucleoside analog of thymine, EdU (5-ethynyl-20-deoxyuridine), in the culture media. EdU incorporates in DNA during the synthesis phase (S phase) of the cell cycle, and hence enables direct quantification of proliferation. hMSCs were seeded on the substrates at a density of 2.5 x 10^3 cells cm^{-1}. Following the initial 8 h incubation after seeding, the medium was replaced with 10 mM EdU-containing fresh media supplemented with 20% FBS. Cells were post-incubated for 1, 3, and 5 days. Cells were then fixed with 4% formaldehyde, permeabilized with 5% Triton-X, and treated with Alexaflour-488 conjugated azide as recommended by the supplier. Proliferative cells were quantified by fluorescent microscope. The average counts of stained cell nuclei were used to evaluate the relative proliferative cell numbers. Both viability and proliferation results were normalized to that of bare titanium on day 1.

4.5.9 Osteogenic differentiation of hMSC

Osteogenic stimulatory media containing xeno-free serum was obtained from MesenCult™ (Catalog #05434), which was formulated for the *in vitro* differentiation of hMSCs into osteogenic progenitor cells. hMSCs were grown until reaching 100%

confluency. Then, FBS-containing medium was replaced with fresh MesenCult medium supplemented with 1% penicillin/streptomycin and 3.5 mM β-glycerophosphate. The differentiation medium was changed every 3-4 days for up to 28 days.

4.5.10 Alkaline phosphatase activity

Alkaline phosphatase activity of the cell extracts cultured on the modified surfaces was assessed by spectrophotometrically monitoring formation of the cleavage product, 4-nitrophenol, from 4-nitrophenyl phosphate (Sigma-Aldrich). Total protein from the cultured cells was extracted by 95% M-PER protein extraction kit (Thermo) with 5% protease inhibitor cocktail (Thermo). The enzymatic activities were normalized to the total protein content, which was determined by BCA protein assay kit (Pierce). The enzymatic activity was probed before (day 0) and after (day 3, 7, 14, 21, and 28) osteogenic induction.

4.5.11 Alizarin red staining

To detect calcium deposited by the cells, the substrates were stained with Alizarin red-S before (day 0) and after (day 7, 14, 21, and 28) osteogenic induction. First, the cells seeded on the substrates were fixed with ice-cold ethanol for 1 h. Then, the substrates were treated with 40 nM Alizarin red-S solution (pH 4.2) for 30 min followed by thorough washing with water. To quantify the amount of calcium, Alizarin-red-bound-calcium was extracted using 10 wt% cetylpyridinium chloride in 10 mM sodium phosphate (pH 7.0) for 20 min at room temperature. The concentration of calcium was indirectly determined by measuring the optical density at 562 nm.

4.5.12 Quantitative reverse transcription polymerase chain reaction (qRT-PCR)

Gene expression profiles for osteogenic differentiation (*RUNX2* and *COL1A1*) were assessed by quantitative reverse transcription polymerase chain reaction. Total RNA was isolated from the differentiated cells on day 28 using TRIzol® (Ambion) according to the manufacturer's instructions. Yield and purity of the extracted RNA were quantified by Nanodrop 2000 from Thermo Scientific. Primer sequences were designed using Primer 3 software (Table 4.2). SuperScript III Platinum SYBR Green One-Step qRT-PCR kit was used to carry out cDNA synthesis from RNA and qPCR sequentially within the same reaction tube. Temperature cycling for the overall reaction was as follows: 55 °C for 5 min, 95 °C for 5 min, 40 cycles of 95 °C for 15 s, T_m (58.3 °C, 60.0 °C, and 58.0 °C for *RUNX2*, *COL1A1*, and *GAPDH*, respectively) for 30 s, and 40 °C for 1 min, which was followed by a melting curve analysis. The reaction efficiency for each primer set was determined by a standard curve with 2-fold serial dilutions of the total RNA. Gene expressions were normalized to that of *GAPDH*, which served as the internal control gene. A comparative C_t method was used to analyze the results.

Table 4.2 *Primer list used in the qRT-PCR.*

	Forward Primer	Reverse Primer
RUNX2	TCTGGCCTTCCACTCTCAGT	GACTGGCGGGGTGTAAGTAA
COL1A1	AAGAGGAAGGCCAAGTCGAG	AGATCACGTCATCGCACAAC
GAPDH	TCGACAGTCAGCCGCATCTTCT	GTGACCAGGCGCCCAATACGAC

4.5.13 Immunofluorescence and DMP-1 localization

Differentiated cells (day 28) were first fixed with 4% formaldehyde for 15 min and then permeabilized with 0.5% Triton-X for 10 min at room temperature. For blocking, 3 wt% BSA/PBS was applied for 1 h. Rabbit-raised, anti-human, DMP-1 polyclonal primary and a goat-raised, anti-rabbit, IgG H&L DyLight® 488 conjugated secondary antibodies (ab82351 and ab96899, respectively) were obtained from Abcam. Filamentous actin was stained with TRITC-conjugated phalloidin and the cell nuclei were stained with TO-PRO®-3 iodide. The samples were analyzed with a Zeiss LSM 510 confocal microscope. DMP-1 localization was quantified based on the cellular images acquired in randomized areas at each group. In each group, min. 80, max. 210 cells were analyzed. Each cell was investigated to observe whether DMP-1 expression was positive, and if so, whether it is predominantly nuclear, predominantly cytoplasmic, nuclear and cytoplasmic, and/or extracellular matrix positive.

4.5.14 Statistical analysis

All experiments were independently repeated at least twice with at least four replica for each experimental or control group in each independent assay. All quantitative results are expressed as mean ± standard error of means (SEM). Statistical analyses were carried out by one-way analysis of variance (ANOVA) or Student's t-test, whichever applicable. A *P* value of less than 0.05 was considered statistically significant.

CHAPTER 5

5 Mussel Inspired Dynamic Cross-Linking of Self-Healing Peptide Nanofiber Network

This work is partially described in the following publication:

Ceylan H., Urel M., Turan, S. E., Tekinay, A. B., Dana, A., Guler, M. O., *Advanced Functional Materials* 23(16), 2081-2090, 2013.

5.1 Objective

A general drawback of supramolecular peptide networks is their weak mechanical properties. In order to overcome a similar challenge, mussels have adapted to a pH-dependent iron complexation strategy for adhesion and curing. This strategy also provides successful stiffening and self-healing properties. The present study is inspired by the mussel curing strategy to establish iron cross-link points in self-assembled peptide networks. The impact of peptide-iron complexation on the morphology and secondary structure of the supramolecular nanofibers is characterized by scanning electron microscopy, circular dichroism and Fourier transform infrared spectroscopy. Mechanical properties of the cross-linked network are probed by small angle oscillatory rheology and nanoindentation by atomic force microscopy. It is shown that iron complexation has no influence on self-assembly and β-sheet-driven elongation of the nanofibers. On the other hand, the organic-inorganic hybrid network of iron cross-linked nanofibers demonstrates strong

mechanical properties comparable to that of covalently cross-linked network. Strikingly, iron cross-linking does not inhibit intrinsic reversibility of supramolecular peptide polymers into disassembled building blocks and the self-healing ability upon high shear load. The strategy described here could be extended to improve mechanical properties of a wide range of supramolecular polymer networks.

5.2 Introduction

Supramolecular polymers have become an attractive class of soft materials because their self-assembly is stimuli-responsive and reversible, and they possess self-healing properties.[97, 228-231] An unrivaled advantage of supramolecular polymer networks compared to traditional polymers is that many small-size building blocks could be synthesized with well-defined chemistry and organized into a particular architecture through noncovalent linkages.[97, 232, 233] Due to their chemical versatility, short peptide sequences have emerged as one of the most referred building blocks within the context of supramolecular polymers.[97, 231] Although they are largely designed to be utilized in tissue engineering and drug delivery, potential use of peptide based supramolecular polymers have extended into mechanical, electronic, and optical applications.[97, 234]

Despite the chemical and biological utilities of self-assembled peptide polymers, weak mechanical properties and limited control over these properties constitute a concern regarding their suitability in applications of a wider scope.[235, 236] To improve and tune mechanical properties, several independent strategies have been explored. An emerging approach is to form reversible cross-link points between supramolecular polymer chains, thereby keeping original advantages of the

noncovalent assembly. Previously, Aulisa et al. explored contribution of dynamic Mg^{2+} and PO_4^{3-} linkers on bulk elastic modulus of peptide hydrogels with various peptide sequences, compared to covalently cross-linked hydrogel control.[237] However, storage moduli of the physical hydrogels (~250 Pa on average) remained an order of magnitude lower than storage moduli of the covalently cross-linked system (~6000 Pa). Using a similar approach, Stendahl et al. tuned Ca^{2+} ion concentration for gelation and modulation of mechanical properties of peptide amphiphile gels through interfiber cross-linking.[238] This strategy enabled controlling storage modulus over three orders of magnitude. Nonetheless, using Ca^{2+} ions as both gelator and cross-linker brought additional issues regarding the degree of self-assembly. Since lowering Ca^{2+} concentration is not sufficient to screen all charges at neutral pH, a significant portion of the peptide building blocks could not participate in nanofiber formation. Therefore, a main drawback of mechanical tunability in this system is that the elastic modulus was strictly coupled to the degree of self-assembly. In another strategy, Paramonov et al., and Pashuck et al. proposed that manipulation of peptide sequence dictating the secondary structure could provide control over bulk viscoelastic properties.[113, 239] Although some remarkable conclusions were drawn regarding the impacts of amphiphilic packing and orientation of building blocks on bulk elasticity, tunability range remained less than an order of magnitude. Taken altogether, alternative approaches for improving and controlling mechanical properties of supramolecular peptide networks, while retaining intrinsic reversibility and self-healing ability, are required.

Marine organisms have unique properties that enable them to survive the destructive conditions of ocean. These characteristics provide a plethora of inspiration to

surmount challenges for development of advanced functional materials. A remarkable example is the adaptation of common blue mussel, *Mytulis edulis*, to remain sessile, i.e., nonmotile, under the highly unstable conditions of intertidal zones where irregularities in salinity, ceaseless wearing of the ocean waves, and sharp fluctuations of temperature and pH create an environment of harsh extremes. In order to overcome these, mussels produce a special adhesive containing hierarchically organized mussel adhesive proteins with a high content of 3,4-dihydroxy-L-phenylalanine (Dopa) residues (Figure 5.1a). Catecholic units of Dopa are regarded as vital for adhesion onto a wide range of organic and inorganic substrates and for cross-linking reactions of the cohesive curing.[19, 26, 38, 240, 241] Because of the simplicity of conjugation of Dopa molecule onto synthetic materials and versatility of the substrates it could bind to, mussel mimetic adhesion has become an established strategy for developing biomimetic adhesion systems.[19, 26, 57, 58, 69] In contrast, there are only a few examples that recapitulate the chemistry of mussel cuticle in synthetic materials towards materials science applications.[38, 242, 243] *Ex vivo* studies showed that mussel adhesive proteins could be cross-linked through metal-ion-complexation or oxidation mediated covalent reactions (Figure 5.1c).[24] At alkaline pH, Dopa is easily oxidized to highly reactive quinone and semiquinone species that further react with each other to form covalent cross-link points.[19, 25] However, the main organization of mussel cuticle is formed by coordination complexes between Dopa and metal ions, predominantly by ferric iron ions. Under basic conditions (pH ~8.5), Dopa and iron ions form bis $Fe(Dopa)_2$ and tris $Fe(Dopa)_3$ complexes. Shafiq *et al.* reported that conjugation of a nitro group to dopamine could reduce pKa of the catechol hydroxyl groups to ~6.5, revealing that

iron mediated cross-linking could be controlled through chemical modifications on the catechol and hence widening the scope of utility of this material.[243] While reversible, Dopa-iron bis- and tris-complexes have one of the highest known stability constants (log Ks ~37–40) of metal-ligand chelates and cross-links provide the cuticle both hardness and self-healing ability after fracture.[20, 244] This unique strategy has inspired us to apply metal-ligand coordination as a mechanical reinforcing strategy for self-assembled peptide networks.

Herein, we show that reversible cross-linking of self-assembled peptide network with iron is a promising method to improve mechanical properties while retaining intrinsic self-healing properties. For this purpose, we designed a mussel-inspired peptide amphiphile, Lauryl-Val-Val-Ala-Gly-Lys-Dopa-NH_2 (DopaK-PA) (Figure 5.1b). Similar to mussel adhesive proteins, self-assembled DopaK-PA network can be cross-linked either with iron incorporation or oxidative pathway. As a control of chemical cross-linking, we synthesized another mussel-inspired peptide amphiphile, Lauryl-Val-Val-Ala-Gly-Lys-NH_2 (K-PA). K-PA has the same sequence of DopaK-PA; however, it lacks Dopa (Figure 5.1b). As it takes place in mussels, pH dependent complexation of iron ions enabled formation of tris $Fe(Dopa)_3$ complexes in DopaK-PA network without destructing the supramolecular order. In the absence of iron, catecholic units in the self-assembled network underwent oxidation followed by covalently cross-linking of nanofibers. Since K-PA lacked Dopa, its nanofibers were physically entangled and hence demonstrated weak mechanical properties. We revealed that the mechanical properties of the iron cross-linked DopaK-PA network matched the properties of covalently cross-linked DopaK-PA network. Strikingly, iron cross-linking had a dynamic nature; it retained its pH dependent reversibility

and demonstrated self-healing properties similar to uncross-linked K-PA network. On the other hand, covalent cross-linking inhibited pH response and self-healing properties of the self-assembled DopaK-PA network. Both cross-linking strategies were entirely orthogonal to the self-assembly mechanism. These results highlighted the significance of metal coordination in a supramolecular network to improve mechanical properties without causing mineralization or interfering with the self-assembly mechanism. Because Dopa incorporation into synthetic molecules is relatively simple, this strategy can be extended into other systems operating under neutral or basic pH.

5.3 Results and Discussion

5.3.1 Self-Assembly of Mussel-Mimetic Peptide Building Blocks

A peptide amphiphile molecule is composed of several functional modules carrying the necessary information to self-assemble into nanofibers and to manifest its desired chemical or biological functionality (Figure 5.1b). Our amphiphile design included a hydrophobic lauryl group attached to the N-terminus of the peptide segment to force packing the building blocks into micellar assemblies. In favor of entropic gain, the hydrophobic segment was buried into the nanofibers to expose hydrophilic peptide sequence to the aqueous environment. The lauryl group was attached to Val-Val-Ala-Gly peptide sequence, whose amide backbone facilitated the secondary structure through hydrogen bonds in the direction of nanofiber elongation. Lys residue was incorporated as a switch for the self-assembly.

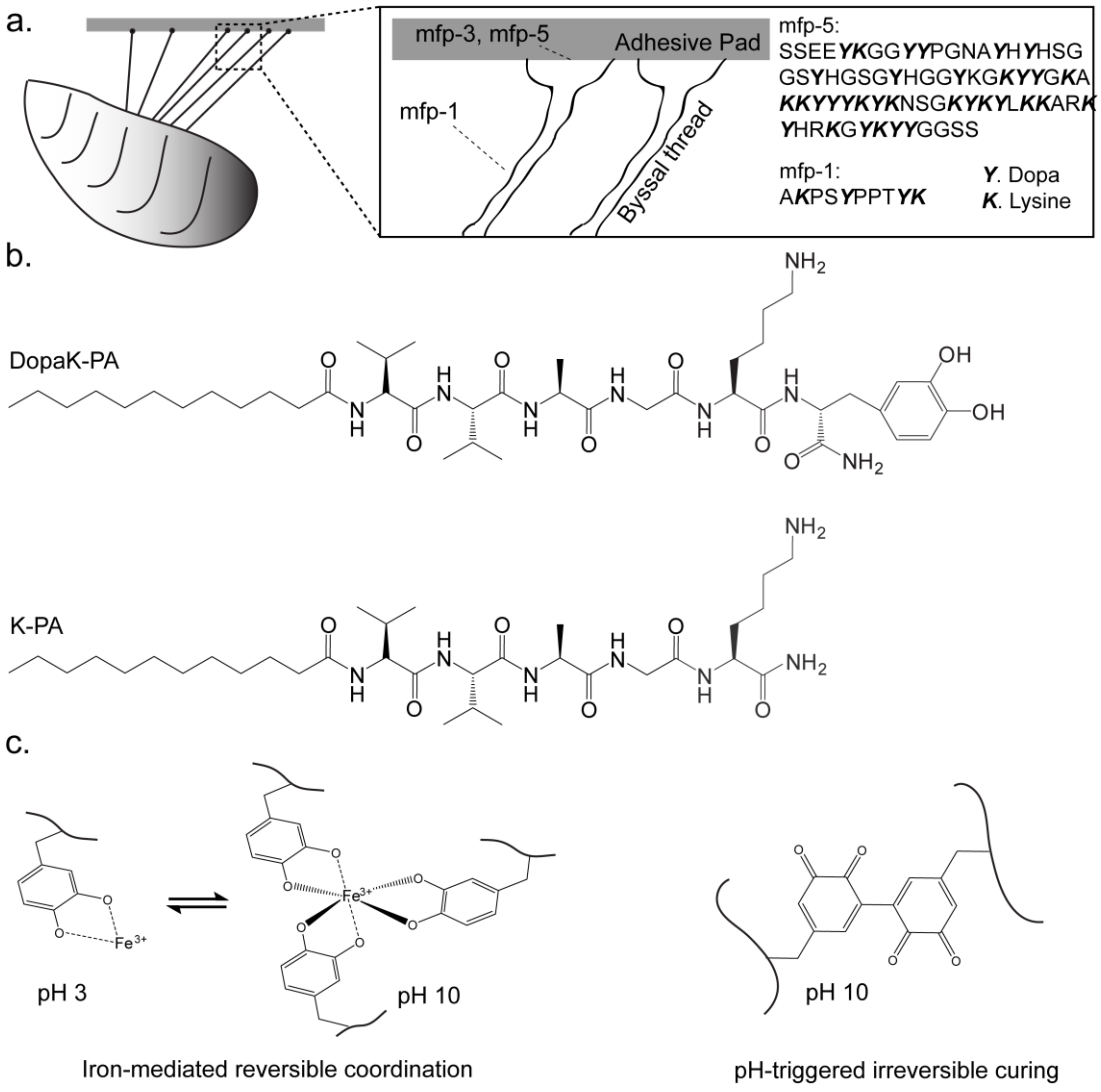

Figure 5.1 Mussel-inspired mechanical enhancement strategy for supramolecular peptide network. (a) Schematic of a marine mussel affixing to a surface. Dopa and lysine are the two key residues in mussel adhesive proteins (here only mfp-1, mfp-3, and mfp-5 are shown) for mussel adhesion and curing.[8, 33] (b) Chemical representation of DopaK-PA and K-PA building blocks of supramolecular peptide networks introduced in this study. **c.** In the presence of iron, tris Fe(Dopa)$_3$ complexes form dynamic cross-link points in mussel adhesive proteins of the byssus while basic pH triggers oxidation mediated covalent cross-linking of the proteins.

Supramolecular ordering of the peptide amphiphile molecules is robustly promoted upon neutralization where strong repelling forces of the same charged species are deactivated and hydrophobic interactions dominate.[102, 245] Therefore, deprotonation of positively charged side chains on both DopaK-PA and K-PA acted as a switch for the self-assembly into nanofibers. Further, Lys residue is known to play a distinct role in mussel adhesion and curing chemistry. Positively charged Lys residue is abundantly found in major mussel adhesive proteins, mfp-1, mfp-3, and mfp-5, imparting a cationic nature to the mussel adhesive proteins.[19, 44, 241] Titration of DopaK-PA and K-PA solutions with NaOH revealed their isoelectric points to be 8.9 and 9.9, respectively, which are very close to the pIs of mfp-1 (pH ~10), mfp-3 (pH ~8-10), and mfp-5 (pH ~9-10) (Figure 5.2).[241] Even though its particular role is still unknown, recent attempts to imitate mussel adhesion mechanism in synthetic materials have focused on utilizing Dopa and Lys residues together.[19, 26, 44, 57] It is currently considered that the excess positive charge forms columbic interactions with surfaces that mussels adhere in their native environment, such as rocks that are highly rich in negatively charged silicates and aluminates.[44] In fact, Dopa and Lys are utilized not only in mussel adhesives but also in natural adhesives of other organisms including sandcastle worm, *Phragmatopoma californica*.[240] The commonality of this system indicates that an exclusive interaction and/or cooperation between Dopa and Lys may have provided a universal solution for adhesion of marine animals. Fe(III) has low solubility at neutral or basic pH at room temperature as it readily precipitates in hydroxylated form. In order to form iron cross-linked peptide gels, $FeCl_3$ solution was initially mixed with DopaK-PA solution at pH ~3 with a final stoichiometric ratio of 3:1 [Dopa:Fe].

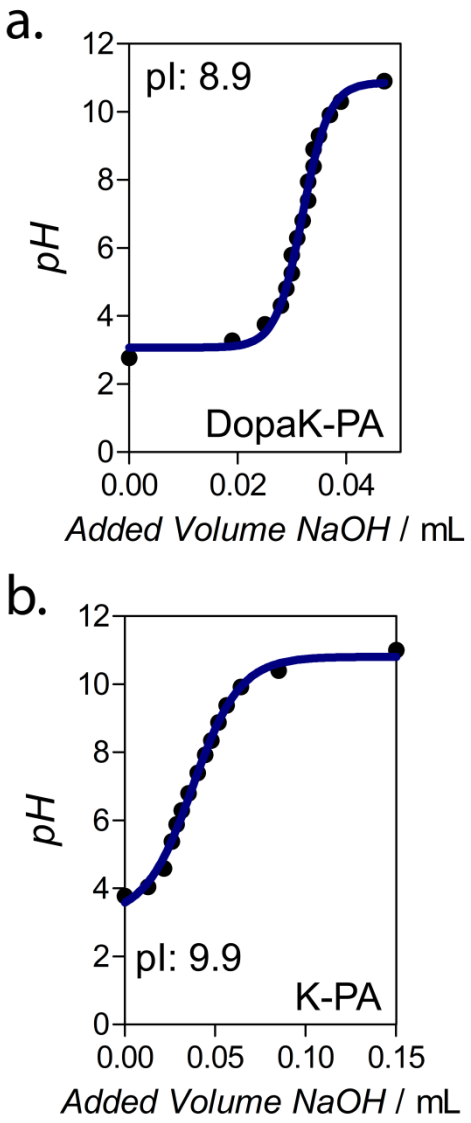

Figure 5.2 **Titration of mussel inspired peptide amphiphiles with NaOH.**

Within seconds after mixing, the color of the mixture turned to dark green indicating formation of mono Fe(Dopa) complex (Figure 5.3).[25, 38] Incorporation of ferric ions by themselves did not induce self-assembly, as determined from circular dichroism spectrum, and the mixture remained dissolved in the solution. To induce self-assembly, pH of the solution was increased to ~10 (to deprotonate ϵ-amine of lysine residue) by adding NaOH. Immediate color change from dark green to wine red accompanied the self-assembly process. Color change indicated a transition from mono Fe(Dopa) complex to tris $Fe(Dopa)_3$ complex.[25, 38] The pH dependent absorbance shifts were identical to the color changes of catechol-Fe(III) coordination status reported previously (Figure 5.4).[25] This strategy is analogous to mussels that integrate Fe(III) into densely cross-linked granules inside the cuticle layer of byssal threads.[20, 244] Inside acidic (pH ~5) intracellular granules of byssal gland cells, a proteinaceous precursor of glue cocktail is produced. At acidic pH, catechol units of Dopa are not oxidized spontaneously and coordinates with Fe(III) as a mono complex. Once released into the ocean, the alkaline environment (pH ~8.5) directs bis- and tris-$Fe(Dopa)_3$ complexation.[38] In our system, since the initial mono complexation of Fe(III) to DopaK-PA took place in the solution phase (at acidic pH) homogeneously, $Fe(Dopa)_3$ cross-link points were dispersed highly uniformly inside the gel after pH increase. In the absence of iron, DopaK-PA followed a totally different reaction pathway at pH ~10 (Figure 5.3 and Figure 5.4).[25] Catechol units of Dopa are not stable at basic pH and are rapidly oxidized to quinone and semiquinone, which further react with each other to form covalent linkages.[19, 25]

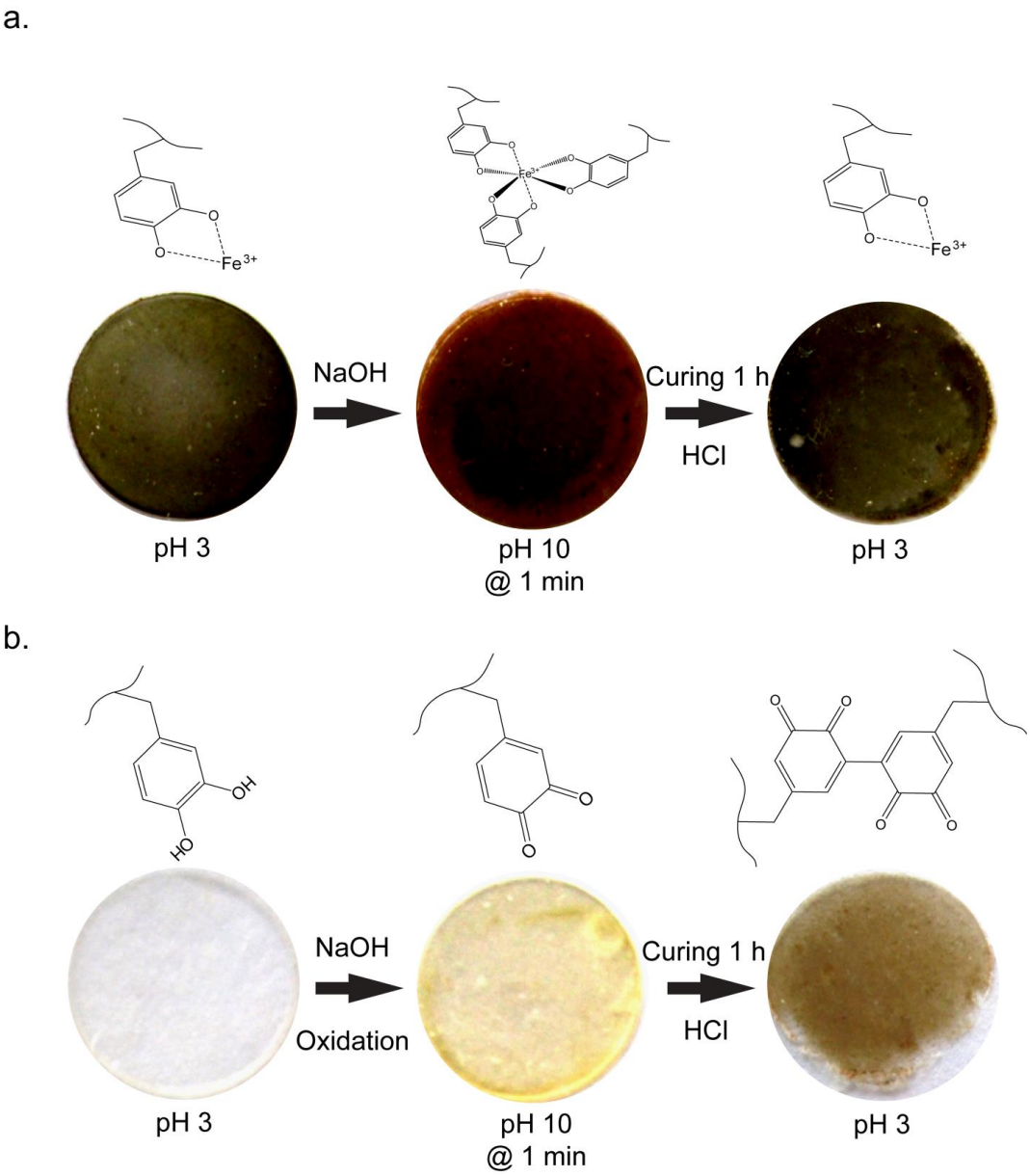

Figure 5.3 pH dependent reactions of mussel inspired peptide nanofibers. Reaction schemes (a) in the presence, (b) in the absence of ferric iron ion.

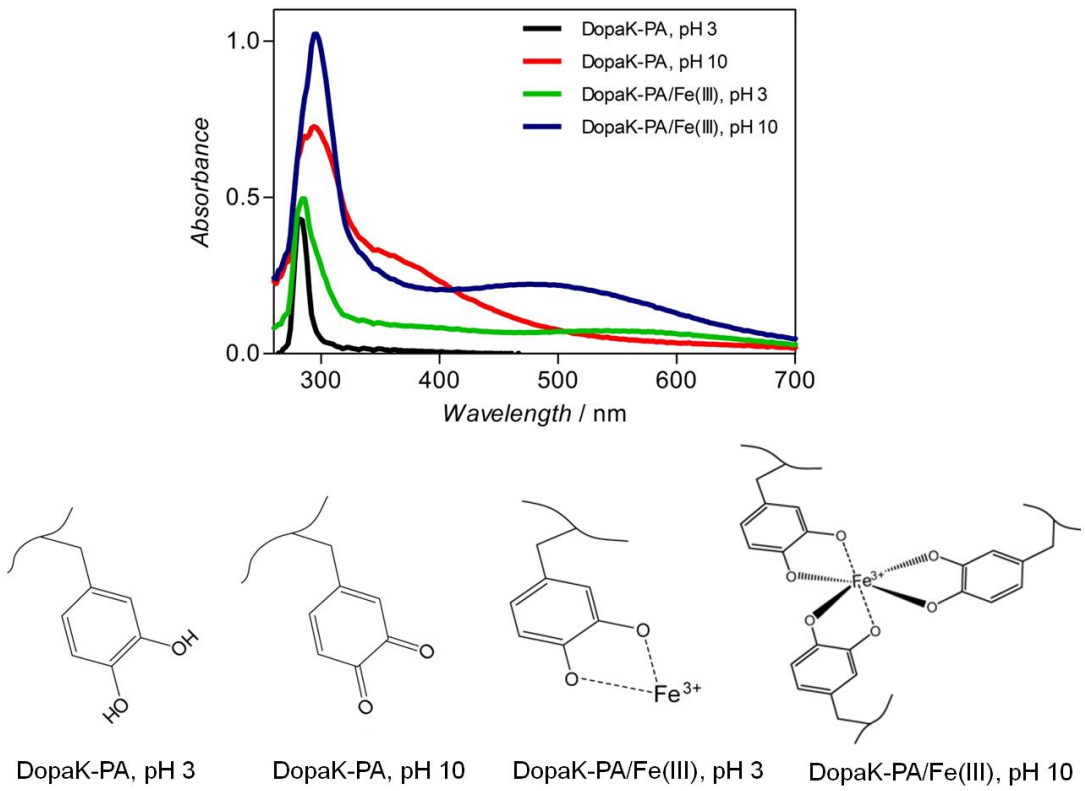

Figure 5.4 pH and Fe(III) dependent UV-Vis spectra of DopaK-PA. Oxidation of catechol to quinone through pH shift causes a new peak to appear around 386 nm.[25] This peak was not observed in the presence of iron, indicating that iron did not cause oxidation of Dopa. In the presence of iron at pH 3 a peak appears at around 520 nm, indicating monocatecholate Fe(Dopa) formation.[25, 37] Upon increasing pH to ~10, this peak shifts to 520 nm corresponding to triscatecholate $Fe(Dopa)_3$ formation.[28,37]

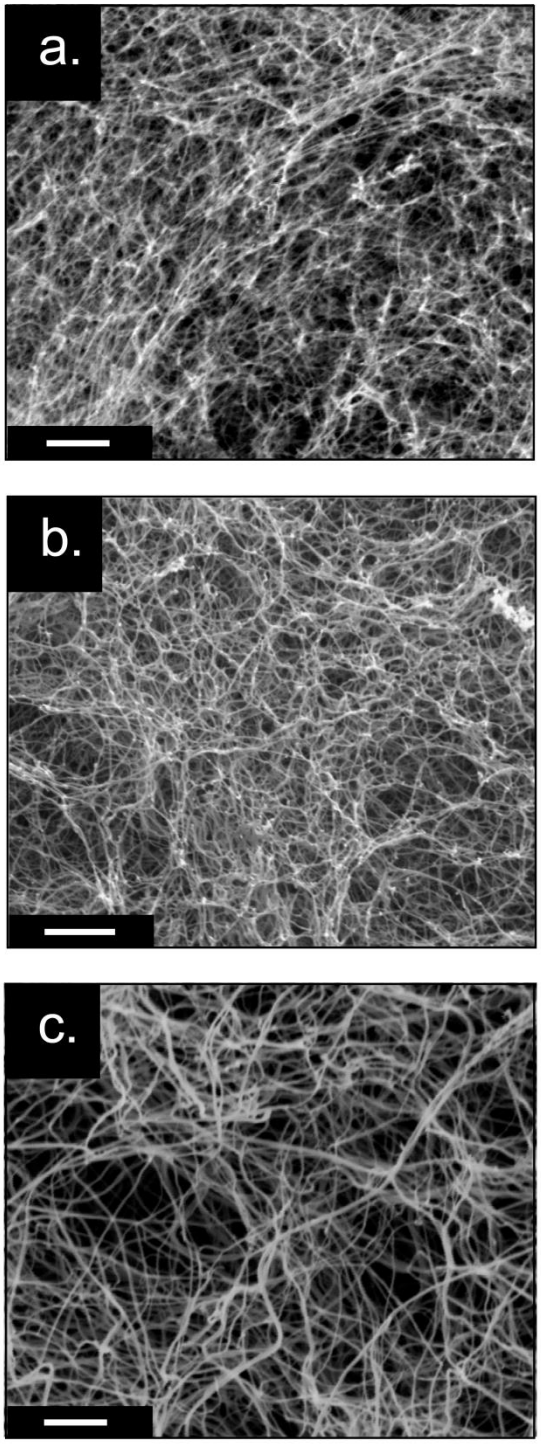

Figure 5.5 SEM images of the mussel inspired, self-assembled peptide nanofibers. (a) Iron-cross-linked DopaK-PA/Fe(III) network. (b) Covalently cross-linked DopaK-PA network. (c) Physically entangled nanofibers of K-PA network. Scale bar: 500 nm.

Addition of NaOH to DopaK-PA at pH ~3 caused a color change to yellow that gradually developed into pale yellow, indicating oxidation-driven covalent cross-linking of the network (Figure 5.3). Because basic pH is required for both self-assembly of the building blocks and cross-linking of the network (either iron-coordinated or covalent cross-linking), there was a competition between the two reactions that occur concomitantly. However, SEM images show that the supramolecular order of the nanofibrous networks were preserved in both cross-linking schemes, indicating that self-assembly had a faster rate of reaction (Figure 5.5a, b). Likewise, self-assembly of K-PA was induced at pH 10 resulting in a nanofibrous network (Figure 5.5c). The network of K-PA was held intact through weak noncovalent interfiber interactions, such as van der Waals, dipole-dipole, hydrogen bonding, and columbic interactions.

5.3.2 Secondary Structure Characterization of the Peptide Nanofibers

In order to probe the secondary structure of peptide nanofibers, circular dichroism (CD) and FT-IR spectroscopy were employed. Circular dichroism spectra revealed a maximum at 203 nm and minimum at 220 nm, which shows that the predominant organization of building blocks at pH ~10 was β-sheet in all three groups (Figure 5.6a).[237] In FT-IR analysis, amide I vibration mainly originates from the carbonyl stretching aligned with hydrogen bonding direction in the backbone of polypeptides; and therefore contains information regarding the secondary structure. In all three peptide nanofibers, amide I peaks were located between 1630–1640 cm^{-1}, revealing β-sheet organization as shown in CD analysis (Figure 5.6b).[239] These results show that chemical cross-linking inside the network did not change the supramolecular

organization of the constituent building blocks of the nanofibers. Thus, mussel inspired protocol for iron cross-linking is a safe method to form interfiber cross-links and can be applied to similar self-assembly-based structures without harming the supramolecular order.

5.3.3 Bulk Rheological Analyses of Cross-Linked Supramolecular Network

Gelation kinetics and viscoelastic properties at equilibrium are critical material properties for a gel, which dictates its suitability for the desired use.[246] Gelation kinetics was monitored through time-sweep analysis in linear viscoelastic range. In rheological terms, gelation occurs at a time point at which the storage modulus, i.e., energy stored during deformation, exceeds loss modulus, i.e., energy dissipated during deformation. Within 1 h, the storage and loss moduli of all three groups almost reached plateau (Figure 5.7a). Therefore, the rest of the rheological tests were carried out after 1 h equilibration period. The storage modulus of iron cross-linked network (DopaK-PA/Fe(III)) was greater than storage modulus of covalently cross-linked DopaK-PA network during the first 30 min, after which there was no significant difference between them. This indicates iron cross-linking takes place at a faster rate than covalent cross-linking whilst the storage moduli are comparable at equilibrium. A more elaborative way to interpret kinetics of gelation and to elucidate the impact of cross-linking on the mechanical properties of networks is to convey the phase angle as a function of time.[247] The storage (G') and loss (G'') moduli are related by $\tan(\delta) = G''/G'$, where δ is the phase angle and $\tan(\delta)$ is the loss (damping) factor. Gelation takes place if δ falls below 90°, or $G''/G' < 1$.

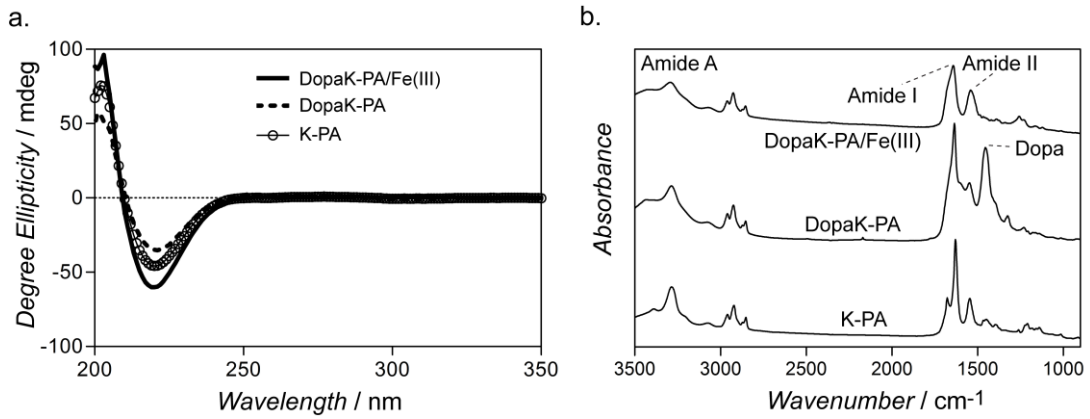

Figure 5.6 Secondary structure analyses of the mussel-inspired peptide nanofibers. (a) Circular dichroism, (b) FT-IR spectra.

In other words, as δ approaches from 90° to 0°, the network gains an elastic character and loses its viscous character, and vice versa. From t_0 to t_{1h}, δ remained lower than 90° with a logarithmical decrease over time in all three networks (Figure 5.7b). Although rheological test was started immediately upon pH increase to ~10, we were not able to catch the sol-gel transition point (where δ was greater than 90°), as the rate of self-assembly was exceedingly high (probably in the time scale around or lower than milliseconds). Regarding gelation kinetics, K-PA gel reached plateau at a faster rate than both DopaK-PA/Fe(III) and DopaK-PA (Figure 5.7b). The value δ of K-PA almost reached plateau within as fast as 3 min while it took 8 min for DopaK-PA/Fe(III) and 11 min for DopaK-PA revealing that self-assembly was a faster process than cross-linking. This explains the preservation of supramolecular architecture upon cross-linking, which concomitantly took place with self-assembly at pH 10. The faster reaction rate of iron coordination compared to oxidative cross-linking is a significant phenomenon for marine organisms as well, because formation of highly organized and dense granules of iron cross-links on the cuticle of mussel byssal threads needs to be competitive against the oxidation. Previous reports about peptide amphiphiles showed that physically entangled (noncovalent cross-linking) supramolecular peptide gels had a loss factor in the range of 0.20–0.10 at equilibrium.[239, 248] This value was in agreement with the loss factor of K-PA (0.170). As expected, chemical cross-linking caused a sharp (~5-fold) decrease of this value although the values were comparable for DopaK-PA/Fe(III) (0.038) and covalently cross-linked DopaK-PA network (0.036). Similarly, the phase angles of covalently cross-linked DopaK-PA, iron coordinated DopaK-PA/Fe(III), and K-PA networks at the end of 1 h were 1.96° ± 0.03°, 2.22° ± 0.02°, and 9.78° ± 0.03°, respectively.

This pronounced difference in the loss factor and δ between chemically cross-linked and physically cross-linked networks were because of the decrease in dissipated energy (loss modulus) and increase in stored energy (storage modulus). During cross-linking, shrinking mesh size causes some portion of water to be excluded from the gel (decreased average distances in interfiber interaction points), thereby diminishing the viscous character. SEM images revealed shrinking in average mesh size (Figure 5.5). As a result, more energy was stored compared to that dissipated. On the contrary, the increase in loss factor and phase angle was due to the relative increase in dissipated energy which was the result of partial breaks within and between the nanofibers in the network. Accordingly, iron coordination or covalent bonding could act as bridges to link such breaks inside the network. After 1 h of equilibration, average bulk storage moduli (G′) of 1 wt% DopaK-PA/Fe(III) and DopaK-PA gels were found to be comparable ($1.28 \times 10^4 \pm 3.81 \times 10^3$ Pa and $1.05 \times 10^4 \pm 0.91 \times 10^3$ Pa, respectively) (Figure 5.7). There was no statistical difference between these magnitudes. On the other hand, storage modulus of K-PA gel was less than an order of magnitude ($(1.18 \pm 0.84) \times 10^3$ Pa) of either of the cross-linked gels ($P < 0.05$), signifying the impact of chemical cross-linking on bulk viscoelasticity of self-assembled peptide network.

After 1 h of equilibration, storage moduli of all gels demonstrated a frequency-independent behavior and no crossover was observed at lower frequencies, indicating that gelation was completed and nanofibers were linked through dense interaction points (either physical interactions or chemical cross-linking) (Figure 5.7d).[249]

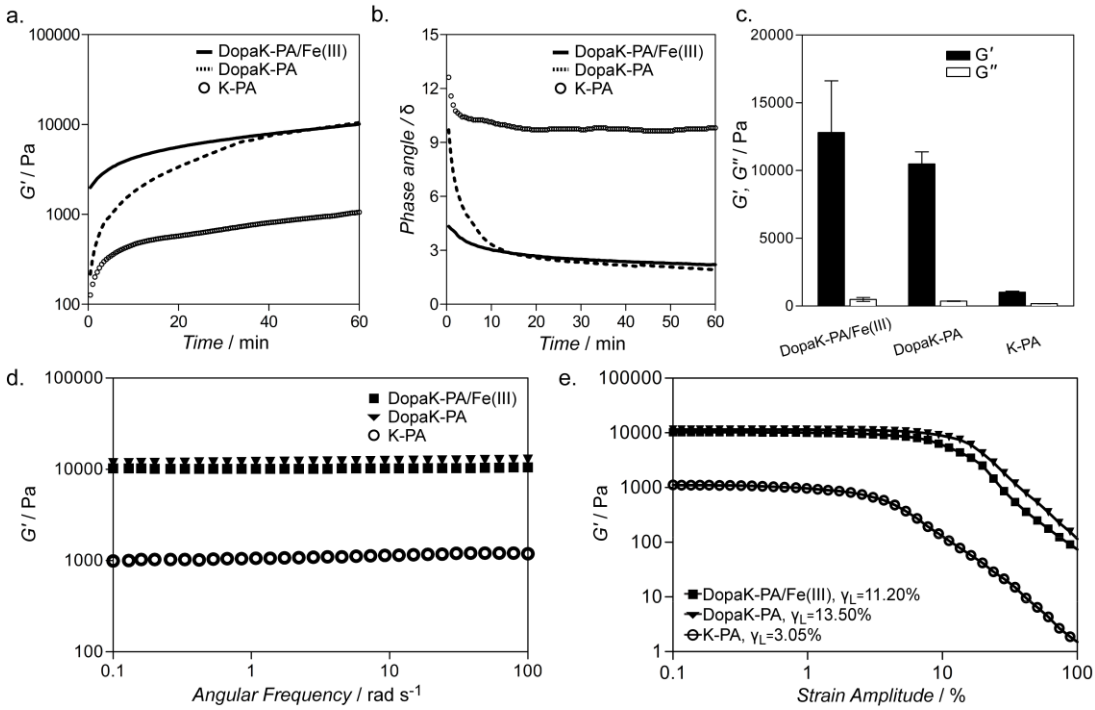

Figure 5.7 Rheological characterizations of mussel inspired peptide gels at 1 wt% concentration. (a) Gelation kinetics, (b) Phase angle as a function of time, (c) Equilibrium moduli at 1 h, d. Frequency sweep test, e. Amplitude sweep test.

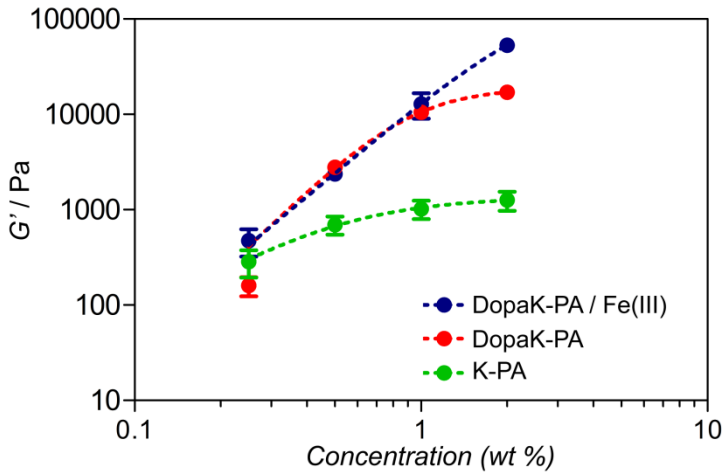

Figure 5.8 Relationship between equilibrium storage modulus and initial peptide amphiphile concentration.

To investigate the relationship between storage modulus and strain amplitudes, we performed a amplitude sweep test. Beyond certain strain amplitude, called the limiting strain amplitude, or γL, the network showed a transition from linear to nonlinear viscoelastic behavior. Below γL, the storage modulus is independent of the strain amplitude and constitutes the linear viscoelastic range. Limiting strain amplitudes of the DopaK-PA/Fe(III), DopaK-PA, and K-PA were 11.20%, 13.50%, and 3.05%, respectively (Figure 5.7e). This difference in γL shows that compared to K-PA, DopaK-PA/Fe(III) could withstand more than three times higher shear strain, while, for DopaK-PA, plastic deformation occurred after approximately four times higher strain. In other words, chemical cross-linking inside the network imparted resistance to deformation until intrafiber interactions were broken at γL. As initial monomer concentration increased, the difference of equilibrium storage moduli between chemically cross-linked DopaK-PA/Fe(III) and uncross-linked K-PA increased due to the increase in the total number of cross-link points inside the network and increased number of elastically active chains (Figure 5.8).

5.3.4 Influence of Temperature on the Curing of Mussel Inspired Cross-Linking in the Supramolecular Networks

In order to investigate the curing effect of temperature on mussel-inspired networks and the constituent nanofibers, the system was heated to 80 °C followed by cooling back down to room temperature (Figure 5.9). Noncovalent interactions of adjacent monomers within the nanofibers and between the fiber chains are sensitive to even small temperature changes and network tends to collapse during heating.[248] Both iron cross-linked and covalently cross-linked networks first showed (up to ~40 °C) a

tendency to break apart assessed by the collapsing storage modulus. Above this temperature and up to 80 °C, the storage modulus suddenly increased linearly to recover the initial storage moduli. This indicated that heating provided a dynamic platform that caused formation of new cross-link points within the network. As cooling back to room temperature, storage moduli of both networks further increased up to three folds of the equilibrium moduli (kinetic equilibrium). During cooling, monomer packing into the nanofibers and nanofiber organization within the network allows more efficient organization culminating in higher network stiffness. Further heating and cooling both iron and covalently cross-linked networks followed the previous cooling path and the system reached to its thermodynamic equilibrium.[250]

5.3.5 pH Dependent Reversibility of the Mussel Inspired Supramolecular Network

Due to the ionic nature of the molecule, pH is an essential stimuli to trigger reversible assembly of peptide amphiphile molecules into supramolecular polymer networks.[102, 245] As disassembly of the network is strongly coupled with the viscoelastic behaviors of the networks, decrease in the storage modulus upon lowering pH into acidic zone is attributable to the degree of reversibility of the assembly. After 1 h of equilibration at pH ~10, pH was decreased back to ~3 by addition of HCl solution. Physically entangled K-PA nanofibers rapidly disassembled at pH ~3, with ~90% decline in storage modulus within 10 min (Figure 5.10a). Similarly, DopaK-PA/Fe(III) network disorganized into mono Fe(Dopa) complex building blocks, as the color change from wine red into dark green indicated (Figure 5.3).

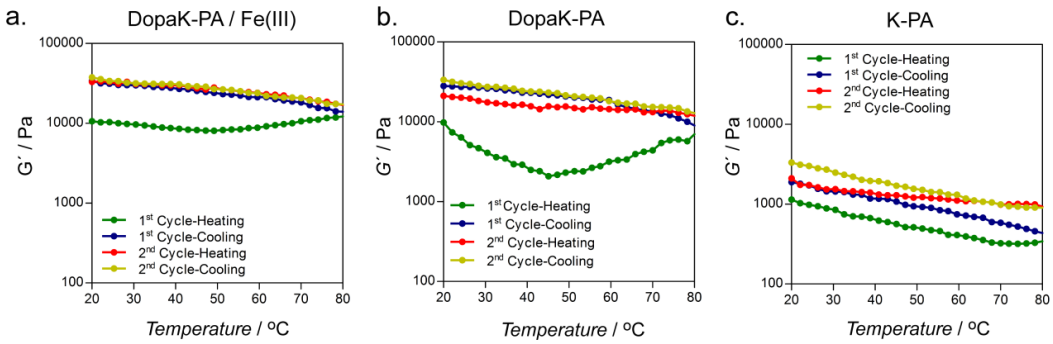

Figure 5.9 Impact of temperature on the mechanical properties of peptide networks. Bulk rheological analyses of the iron cross-linked DopaK-PA/Fe(III), covalently cross-linked DopaK-PA, and noncovalent network of K-PA as a function of temperature.

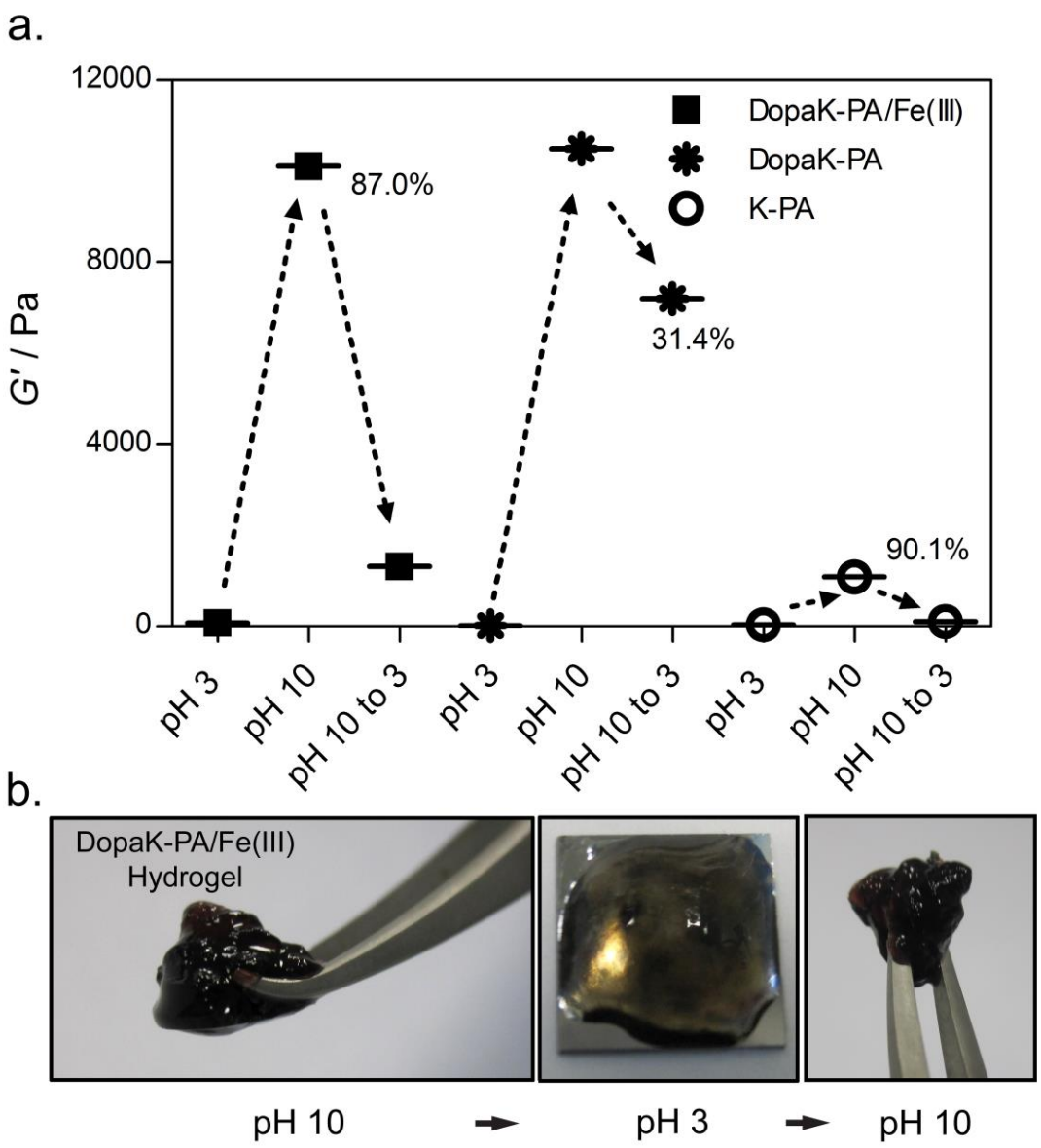

Figure 5.10 pH dependent reversibility of the peptide networks. (a) Disassembly of the iron cross-linked DopaK-PA/Fe(III) network monitored as the loss of the storage modulus upon pH lowering to ~3. (b) Images of iron cross-linked DopaK-PA/Fe(III) network and its pH dependent reversibility.

Decrease in storage modulus of tris $Fe(Dopa)_3$ cross-linked gel was 87%, comparable to that of K-PA. This indicates that $Fe(Dopa)_3$ complex is fully reversible into mono Fe(Dopa) complex with pH. DopaK-PA/Fe(III) gel lost all of its mechanical strength upon lowering pH while it rapidly recovered its mechanical properties after increasing pH (Figure 5.10b). A few past studies reported oxidation of catechol and reduction of Fe(III) because of their similar redox potential (~0.75 V).[251] Based on the degree of decrease in mechanical properties of DopaK-PA/Fe(III) and colorimetric analysis, we did not notice iron mediated oxidation within the time scale of these experiments. In contrast, decrease in storage modulus in DopaK-PA was only 31.4% and no apparent color reversibility was observed, demonstrating that covalent cross-linking irreversibly locked the network.

5.3.6 Self-Healing Properties of the Networks

To test the self-healing ability upon high shear load far beyond linear viscoelastic behavior (1000%), we performed thixotropic test. Under such high deformation, both covalent and noncovalent bonds within and between the nanofibers are broken; therefore, noncovalent bonds are expected to recover rapidly after the load is removed. Within 10 min after load was applied, DopaK-PA/Fe(III) recovered 77.6% (8.85 × 103 Pa) of its original storage modulus at 1 h (Figure 5.11). Comparably, the recovery of K-PA was 80.7% (8.98×10^2 Pa). Following deformation at 1000% shear strain, noncovalent interactions that drive self-assembly of the peptide amphiphiles were mostly restored rapidly in both K-PA and iron cross-linked DopaK-PA/Fe(III). Fe(III) ions diffused in and rebound to the network in a highly reversible fashion.

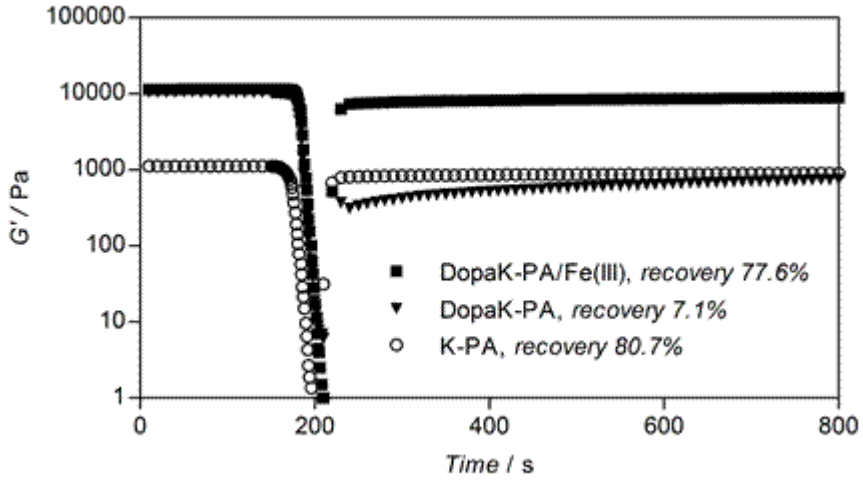

Figure 5.11 Self-healing of the mussel inspired peptide gels. Recovery after high shear load monitored via storage modulus as a function of time.

In contrast, covalently cross-linked DopaK-PA recovered by only 7.1% (7.51×10^2 Pa), because covalent bonds inside the nanonetwork could not be recovered after structural deformation. This shows that DopaK-PA could withstand slightly larger strains before plastic deformation (with γL 13.50% compared to 11.20% of iron-cross-linked network), while showing severely diminished recovery compared to DopaK-PA/Fe(III).

5.4 Conclusion

Metal complexation has emerged as a promising cross-linking strategy for mechanical reinforcement of synthetic polymeric materials while its promise has not yet been recognized for supramolecular polymers. In the present study, we showed that mussel inspired iron coordination into supramolecular networks formed by peptides could improve mechanical properties while remaining orthogonal to the self-assembly process. We showed that enhancement of elasticity in iron cross-linked DopaK-PA/Fe(III) was one order of magnitude greater compared to physically entangled network of K-PA. We further showed pH-dependent reversibility of DopaK-PA/Fe(III) was at a comparable level to that of K-PA while covalently cross-linked DopaK-PA showed very limited reversibility after lowering pH to acidic levels. Likewise, recovery after high-shear load in iron coordinated peptide gel was comparable to K-PA gel. On the other hand, recovery of DopaK-PA gel was very limited, since covalent cross-linking inhibited reestablishment of the bonds. Overall, DopaK-PA/Fe(III) network showed improved mechanical properties, characteristic of chemically cross-linked networks, while retaining its original features of pH response and self-healing. Using a similar strategy, Dopa-mediated cross-linking can

further be applied to a broad range of supramolecular systems, through which mechanical properties can be reversibly controlled. Considering underwater adhesion capacity, self-healing, and reversible bonding scheme, this work reveals important results in development of high performance hydrogels, adhesives, and coatings that can remain mechanically stable under abrasive conditions while retaining surface versatility and environmentally friendliness.

5.5 Experimental Section

5.5.1 Materials

All reagents used in this study were purchased from commercially available sources as analytical grade and were used as received.

5.5.2 Synthesis and Characterization of Peptide Amphiphiles

Fmoc solid phase peptide synthesis method was employed to manually synthesize Lauryl-Val-Val-Ala-Gly-Lys-Dopa-NH_2 (DopaK-PA), and Lauryl-Val-Val-Ala-Gly-Lys-NH_2 (K-PA). Rink amide MBHA resin (Novabiochem) served as the solid support. Carboxylate group activation of 2 mole equivalents of amino acid was succeeded by 1.95 mole equivalents of N,N,N′,N′-Tetramethyl-O-(1H-benzotriazole-1-yl) uronium hexafluorophosphate (HBTU), and 3 mole equivalents of diisopropylethylamine (DIEA) for 1 mole equivalent of functional sites on the solid resin. Fmoc groups were removed at each coupling step with 20% piperidine/dimethylformamide for 20 min. Amino acid coupling time was set to be 2 h at each cycle. Lauric acid served as the source of lauryl group and its coupling mechanism was similar to amino acid coupling. After synthesis, all protecting groups were removed using trifluoroacetic acid (TFA) (95%) cleavage cocktail containing

water (2.5%) and triisopropylsilane (2.5%). Excess TFA was removed by rotary evaporation. Peptides were then precipitated in diethyl ether overnight. The precipitate was collected and dissolved in ultra-pure water. This solution was frozen at −80 °C followed by freeze-drying for one week. Residual TFA was removed by dissolving the whole batch in dilute HCl solution and freeze-drying. Small contaminants and salts were removed through dialysis using a cellulose ester dialysis membrane with molecular-weight-cut-off of 100–500 Da. After dialysis, DopaK-PA and K-PA were once more freeze-dried and their purity was assessed using Agilent 6530 quadrupole time of flight (Q-TOF) mass spectrometry with electrospray ionization (ESI) source equipped with reverse-phase analytical high performance liquid chromatography (HPLC). DopaK-PA and K-PA were synthesized and used with >95% purity (Figure 5.12). UV-Vis spectrum of DopaK-PA at pH ~3 showed that catechol side chain of Dopa remained unoxidized during the synthesis and purification steps (Figure 5.12c). Samples for analyses were prepared by dissolving freeze-dried products in ultrapure water and adjusting pH using sufficient amount of HCl or NaOH. The pH of DopaK-PA solution was prepared at pH ~3 and used immediately after it is dissolved in order to prevent spontaneous oxidation.

5.5.3 Cross-linked Gel Preparations

Fe(III) coordination to Dopa at basic pH was performed as previously described.17 Unless otherwise is indicated, 20 volume units of DopaK-PA (1.25 wt%) solution in water was mixed with 2 volume units 53.3 mm $FeCl_3$ solution at pH ~3. Dopa:Fe ratio in DopaK-PA/Fe(III) gels was 3:1. The blend was thoroughly mixed through a micro pipette.

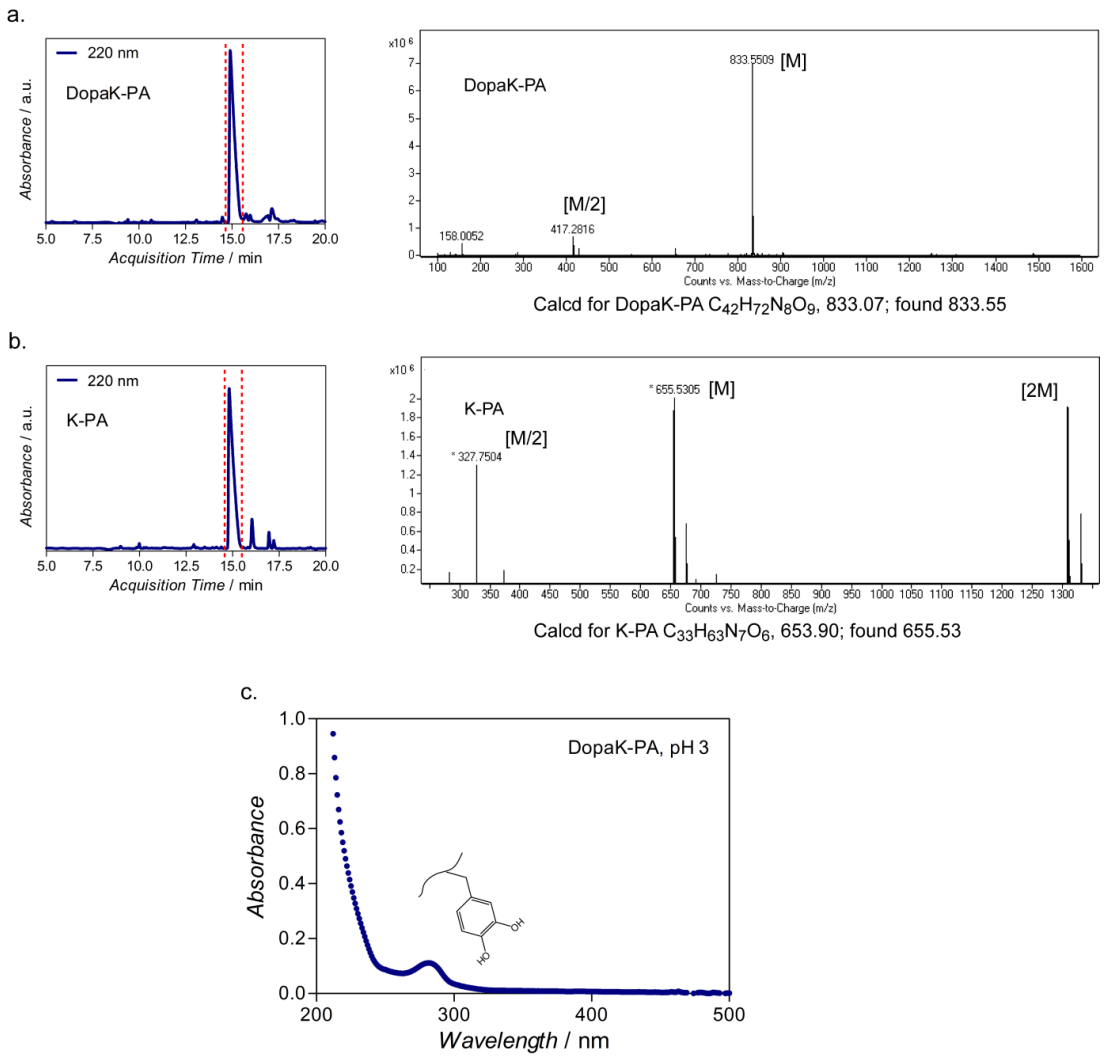

Figure 5.12 Characterization of the purity and functionality of the mussel-inspired peptide amphiphiles. (a, b) Liquid chromatograms and mass spectra of DopaK-PA and K-PA. (c) UV-Vis spectrum of DopaK-PA after synthesis to show catechol groups are functional.

After a homogenous solution was prepared, pH was increased to ~10 using 3 volume units of 150 mm NaOH. Immediate color shift to wine-red was assessed as $Fe(Dopa)_3$ tris-complexation (Figure 5.3 and Figure 5.4).[38] Covalent cross-linking of DopaK-PA gel was done in the absence of iron at pH 10. Unless otherwise indicated, 20 volume units of 1.25 wt% (16 mm) DopaK-PA solution in water was mixed with 2 volume units of ultra-pure water at pH ~3. The blend was thoroughly mixed through a micro pipette. After a homogenous solution was prepared, pH was increased to ~10 using 3 volume units of 150 mm NaOH. Immediate color change to pale yellow indicated formation of o-quinone (Figure 5.3 and Figure 5.4). Over time, color of the gel turned from pale yellow to brown (Figure 5.3), indicating formation of covalently cross-linked species of oxidized Dopa residues.[25]

5.5.4 Scanning Electron Microscopy (SEM)

Samples for SEM imaging were prepared from 1 wt% gels. Following gradual exchange with ethanol, samples were dried at the critical point of carbon dioxide. A FEI Quanta 200 FEG scanning electron microscope with an ETD detector was used for visualization of peptide networks. Samples were sputter coated with 5 nm gold/palladium prior to imaging.

5.5.5 Circular Dichroism (CD)

CD measurements were carried out at 2×10^{-4} m peptide concentration in a 1-mm path length quartz cuvette. In Fe(III) cross-linked nanofibers, Dopa:Fe ratio was 3:1. A Jasco J-815 spectropolarimeter was employed with a band width of 1.0 nm, and scanning speed of 100 nm min^{-1}. The 190–350 nm spectral region was monitored for the analysis of secondary structure of peptide nanostructures.

5.5.6 Fourier Transform Infrared Spectroscopy (FT-IR)

A Bruker VERTEX 70 was utilized to probe the secondary structure of peptide nanostructures. After 1 h equilibration under humid and ambient conditions, 1 wt% gels were instantaneously frozen in liquid nitrogen followed by freeze-drying to remove all water content. The remaining peptide network was used to form pellet with KBr. The spectral region of 400–4000 cm^{-1} was scanned with 128 scan number and 4 cm^{-1} resolution.

5.5.7 Oscillatory Rheology

An Anton Paar Physica RM301 Rheometer with a 25-mm parallel-plate configuration was used to probe the viscoelastic properties of DopaK-PA, DopaK-PA/Fe(III), and K-PA gels at pH 10. Gels were formed in situ on the lower plate of the rheometer. The final peptide concentration after gelation was set to be 1 wt%. Shear gap distance was 500 μm and total loading volume was 250 μL in the measurement gap. Unless otherwise noted, all measurements were carried out at room temperature. Kinetics of gelation was probed with time-dependent rheology until the system reached a plateau, during which angular frequency (ω) and strain (γ) were held constant at 10 rad s^{-1} and 0.01%, respectively, within the linear viscoelastic range (LVR). Frequency sweep test was performed at equilibrium after 1 h gelation under constant strain, 0.01%, with logarithmic ramping from 0.1 to 100 rad s^{-1}. Amplitude sweep test was performed to determine the linear viscoelastic range of the supramolecular networks. The test was done for equilibrated samples at constant angular frequency of 10 rad s^{-1} with logarithmically ramping strain amplitude from 0.01 to 100%. The pH-dependent reversibility of self-assembled

peptide networks was tested after gels were equilibrated for 1 h at pH 10. After 1 h sufficient amount of HCl was dropped onto the gels. After 10 min of equilibration, rheological parameters were monitored at 0.01% strain and 10 rad s^{-1} angular frequency. Thixotropic behavior was investigated as time-dependent recovery after high shear load. In the first part of the experiment, gels at equilibrium modulus were deformed in LVR, 0.01% for 3 min. Then, strain was logarithmically ramped to 1000% within 1 min followed by recovery of deformation back again in the LVR, at 0.01% for 10 min. During thixotropic analyses, angular frequency was held constant at 10 rad s^{-1}. Thermal properties of the gels were investigated between 20–80 °C, at 10 rad s^{-1} angular frequency and 0.01% shear strain. Heating and cooling rates were set to 10 °C min^{-1} with linear ramping. In order to maintain the hydration level of the gels during measurements, a solvent trap supported with a humidified environment was used during temperature-sweep tests. This system has no direct contact with the measurement system and hence does not influence the mechanical measurements. Concentration dependent analyses of the gels were presented at their equilibrium for each concentration point. Each measurement in concentration sweep was carried out under constant 10 rad s^{-1} angular frequency, and 0.01% strain.

CHAPTER 6

6 Size-controlled conformal nanofabrication of biotemplated three-dimensional TiO_2 and ZnO nanonetworks

This work is partially described in the following publication:

Ceylan H., Akgun C. O., Erkal, T. S., Donmez I., Garifullin R., Tekinay, A. B., Usta H., Biyikli N., Guler, M. O. *Scientific Reports* 3:2306, 2013.

6.1 Objective

A solvent-free fabrication of TiO_2 and ZnO nanonetworks is demonstrated by using supramolecular nanotemplates with high coating conformity, uniformity, and atomic scale size control. Deposition of TiO_2 and ZnO on three-dimensional nanofibrous network template is accomplished. Ultrafine control over nanotube diameter allows robust and systematic evaluation of the electrochemical properties of TiO_2 and ZnO nanonetworks in terms of size-function relationship. We observe hypsochromic shift in UV absorbance maxima correlated with decrease in wall thickness of the nanotubes. Photocatalytic activities of anatase TiO_2 and hexagonal wurtzite ZnO nanonetworks are found to be dependent on both the wall thickness and total surface area per unit of mass. Wall thickness has effect on photoexcitation properties of both TiO_2 and ZnO due to band gap energies and total surface area per unit of mass. The

present work is a successful example that concentrates on nanofabrication of intact three-dimensional semiconductor nanonetworks with controlled band gap energies.

6.2 Introduction

Interest in developing novel fabrication strategies at the nanometer scale has continued to rise over the last decade. The main motivations behind crafting materials at smaller dimensions have been to increase the surface-to-volume ratio and to reduce diffusion path length. Nano-crafted materials can also manifest emergent electronic and optical properties.[252] Superior control over the size, shape, and uniformity of the materials constitute the principal parameters within the context of nanofabrication. Materials in different size and architectures, such as, zero-dimensional nanoparticles; one-dimensional nanowires, nanotubes; two-dimensional nanosheets; and three-dimensional mesoporous structures, and nanonetworks have been fabricated and their properties in desired applications have been closely investigated.[253-261] Among these, nanonetwork architecture, which can be defined as isotropically distributed, three-dimensional interconnected nanowires, draws particular attention for its high surface area and porosity, which allow robust interaction with the solvent and solute molecules. Interconnected intact structure of the nanonetwork, extending millimeter-to-centimeter scales, provides practical applicability in device designs. Various materials fabricated in the structure of nanonetwork exhibited superior performance in energy, sustainability, and biomedical applications.[253, 262-266]

Template-directed mineralization is regarded as a promising nanofabrication strategy, because both physical and chemical cues presented by the template allow

control over the size and structure of the resulting materials. As opposed to hard (inorganic) templates, soft (organic) templates are particularly attractive due to relative ease of modification over the chemical functionality, architecture diversity, and physical properties of the template.[255, 259] However, low chemical stability at high temperature, liability to organic solvents, and fast chemical degradation remain as the major challenges with organic templates.[267] Incomplete template coverage and thickness control are the further challenges in organic templates. Maintaining structural conformity and uniformity of the deposit is another unresolved issue on macroscopic three-dimensional templates (mm-to-cm scale) having nanoscale architecture with ultra-high-aspect-ratio components.

TiO_2 and ZnO nanostructures have been widely used in photocatalytic self-cleaning surfaces, piezoelectric devices, chemical sensing, and dye-sensitized solar cell applications mainly due to their suitable electrochemical properties, excellent solution stability, and relatively low toxicity.[254, 266, 268-270] Having relatively high band gap energies (3.00–3.30 eV), TiO_2 and ZnO can generate excited-state conduction-band electrons and valence-band holes with large redox potential differences upon photoexcitation in the ultraviolet domain of the spectrum. This property has been utilized for a variety of photocatalytic applications in aqueous environment, such as artificial photosynthesis, decomposition of potentially toxic organic materials, cancer treatment, and hydrogen gas production for clean, renewable energy.[271] A convenient, template-based manufacturing of these materials in nanoscale is of particular significance.

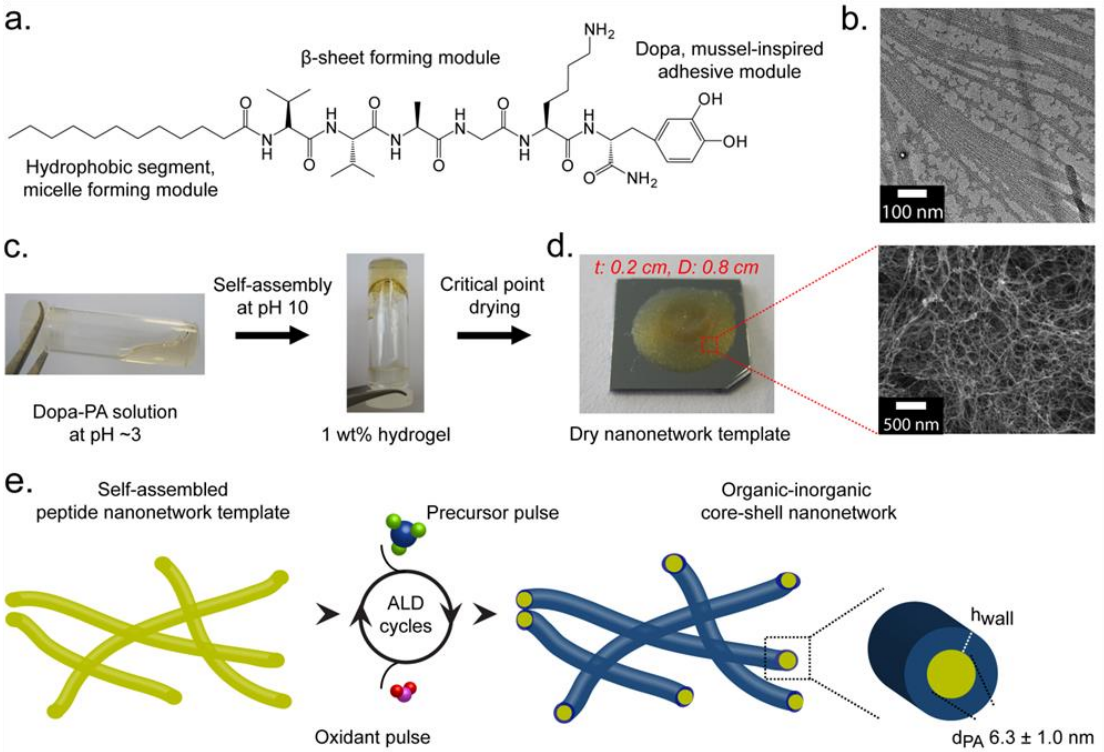

Figure 6.1 Strategy for three-dimensional nanofabrication of TiO_2 and ZnO nanonetworks on supramolecular nanofibers of peptide amphiphile nanonetwork. (a) Chemical sketch of Dopa-PA, the building block of the self-assembled network. (b) TEM micrograph showing self-assembled nanofibers at pH 10. (c) The pH-dependent gelation of Dopa-PA network in water and controlled removal of the solvent through critical point drying. (d) Three-dimensional macrostructure (left) of the nanofibrous template (SEM image, right) after drying. t is the thickness, D is the diameter of the template used for ALD. (e) A schematic representation of TiO_2 and ZnO organic-inorganic core-shell nanonetwork formation through ALD.

Motivated by our recent work on bioinspired supramolecular template directed nanostructure fabrications, bioinspired peptide nanofiber templates (5–7 nm in diameter) combined with an atomic-layer controlled thin-film deposition technique can form a nanofabrication platform to efficiently fabricate transition metal compounds on a nanonetwork template.[255, 259, 272] Here, we describe utilization of bioinspired self-assembled peptide nanonetwork as template for fabrication of TiO_2 and ZnO nanonetwork semiconductors (Figure 6.1). For this purpose, we designed and synthesized a mussel-inspired peptide amphiphile molecule, Dopa-PA, which efficiently self-assembles into mechanically intact nanofibrous network with thin fiber diameter (6.3 ± 1.0 nm) having good adhesive properties to the solid support.[57, 58, 273] These three-dimensional nanofibrous peptide nanonetworks can reach to the length scales of millimeter and centimeter in all three dimensions. We demonstrate that TiO_2 and ZnO nanonetworks can be reliably deposited on dried self-assembled peptide nanonetwork template with significant uniformity and exceptionally high conformity via atomic layer deposition (ALD) technique.[274] Due to separate dosing of reactive gaseous precursors and limited number of surface reaction sites, ALD is intrinsically self-limiting. This unique reaction property leads to uniform and highly conformal deposition on ultra-high-aspect-ratio surfaces (> 1000) where conventional sol-gel, chemical and physical vapor deposition techniques fall short.[274] In a typical ALD process, growth per cycle (GPC) is constant and in the order of angstrom level. Furthermore, gaseous precursor molecules could directly penetrate inside the porous structures without mechanically destroying, or dissolving, relatively weak organic architecture at comparatively lower temperatures.[275]

The TiO_2 and ZnO nanonetworks produced by peptide nanofibrous network templates and ALD technique were characterized by XRD, XPS, TGA, SEM, TEM, and EDX. Since deposition occurs at the atomic scale, we systematically evaluated the electrochemical properties of TiO_2 and ZnO nanonetworks and studied size-function relationship.

6.3 Results and Discussion

6.3.1 Synthesis and preparation of the peptide template for ALD

Self-assembly of bioinspired peptide molecules forms isotropically distributed nanofibers providing a highly porous and homogenous three-dimensional nanonetwork as described in Figure 6.1. The self-assembly process was triggered by increase of the pH of the peptide solution to ~10 (Figure 6.1). The catechol groups on the peptide nanofibers undergo covalent cross-linking above pH 8.5, which strengthens the network against destabilizing factors during sample preparation and relatively high temperatures at ALD.[273] Well-preserved network structure showed Dopa-PA nanofibrous template can withstand temperatures up to 150°C without any structural damage on the supramolecular architecture.[276] The dimensions of the gel can be expanded to couple of centimeters in both height and diameter without destructing its homogeneity and forming macroscale cracks in the template network. In order to obtain a dry peptide network, solvent in the gel was removed by critical point drying, which had been proposed to be a reliable route to obtain undamaged dry peptide network of the gel.[277] It is imperative to maintain the porosity of the network without any degree of collapse, because our fabrication strategy depends on

the delivery of gaseous precursors across the whole template through such nanoscale meshes to maximize the specific surface area.

Individual nanofibers forming the hydrogel network were determined to be 6.3 ± 1.0 nm in diameter and several tens of micrometers in length by TEM. Nevertheless, few bundles of nanofibers, in the range of 10.6-28.3 nm in diameter, were also observed. SEM images showed that the drying procedure did not cause any noticeable damage on the structure of the network (Figure 6.1d). The majority of the previously reported template thicknesses for fibrous self-assembled peptide or polymer templates for mineral deposition are in the range of 20–100 nm.[255, 259, 272, 276, 278-280] Nanofibrous materials with a diameter of less than 10 nm, is rare (particularly for three-dimensional networks). In addition, there were no macro level cracks and no shrinkage in the dimensions of the network upon drying.

6.3.2 Characterization of TiO_2 and ZnO nanonetworks

Dopa-PA nanonetworks were coated with TiO_2 and ZnO separately, forming organic-inorganic core-shell nanostructures, as schematically shown in Figure 6.1e. SEM images revealed nanofibrous networks of TiO_2 and ZnO deposited with 350 and 100 ALD cycles, respectively (Figure 6.2a–b, e–f). The inorganic nanofibers are interconnected to each other forming continuous three-dimensional network structures. The whole inorganic network was true replica of the core peptide network. Both TiO_2 and ZnO core-shell nanonetworks remained intact after atomic layer deposition, resulting in one whole nanonetwork in mm to cm scale. Both energy dispersive X-ray spectroscopy (EDX) (Figure 6.2c, g) and X-ray photoelectron spectroscopy (XPS) (Figure 6.3a–b) independently confirmed the TiO_2

and ZnO deposition. High resolution XPS scans of Ti 2p3/2 and Ti 2p1/2 peaks located at 459.2 and 465.2 eV, respectively, and Zn 2p3/2 and Zn 2p1/2 peaks located at 1044.8 and 1021.8 eV, respectively, were in agreement with the previously reported data for TiO_2 and ZnO.[281-284] Thermogravimetric analyses (TGA) revealed that 68.74% of the organic-inorganic composite structure consisted of TiO_2 and 85.51% was ZnO (Figure 6.3c). In terms of surface morphology, TiO_2 shell was smooth along the length of the nanofibers while ZnO shell was more irregular depending on the crystal structure of the nanotubes. Brunauer–Emmett–Teller (BET) surface areas for these nanonetworks were estimated to be 34.54 $m^2 g^{-1}$ for as-synthesized (without calcination) TiO_2 and 93.99 $m^2 g^{-1}$ for as-synthesized ZnO. X-ray diffraction (XRD) analysis showed that as-synthesized TiO_2 nanonetwork was amorphous (Figure 6.2d). Anatase phase of TiO_2 is known to be the most efficient morphology with a band gap energy of 3.2 eV and suitable band-edge positions to split water into highly oxidative hydroxyl radicals and peroxides.[257] A common strategy for the phase transition is to anneal the amorphous TiO_2 at sufficiently high temperatures. Anatase phase can be obtained by calcination at 300-500 °C, while > 550 °C is required for rutile phase transformation at ambient conditions. Accordingly, we calcined TiO_2 nanonetwork at 450 °C. An amorphous-to-anatase phase transition took place while the nanofibrous network was thoroughly preserved (Figure 6.5a–d).[285] On the other hand, as-synthesized ZnO nanonetwork exhibited hexagonal wurtzite crystal structure (Figure 6.2h). This is thermodynamically the most stable phase of ZnO at ambient conditions having the same band gap energy of anatase TiO_2 (3.2 eV).[268]

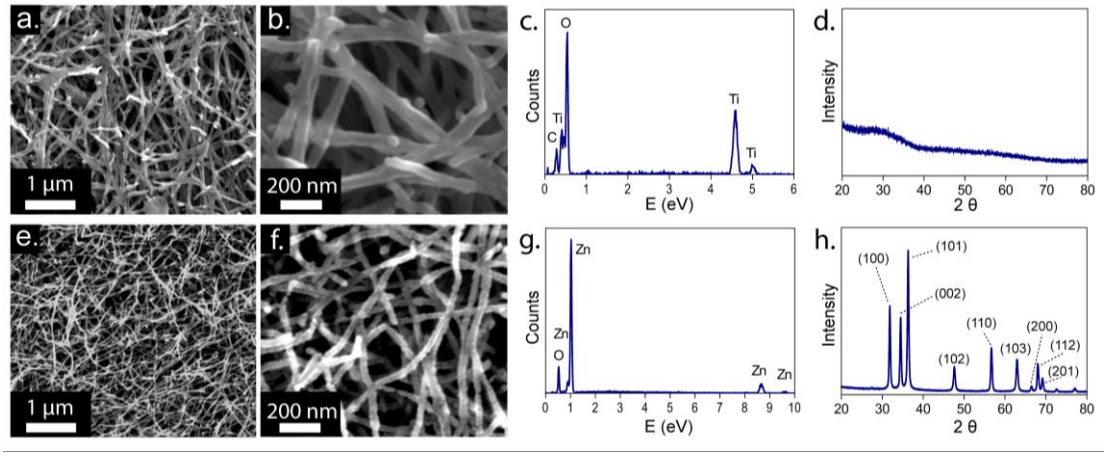

Figure 6.2 Characterization of as-synthesized TiO_2 and ZnO nanonetworks deposited with 350 and 100 ALD cycles, respectively. (a, b) SEM images, (c) EDX spectrum, and (d) XRD pattern of TiO_2 nanonetworks. (e, f) SEM images, (g) EDX spectrum, and (h) XRD pattern of ZnO nanonetworks.

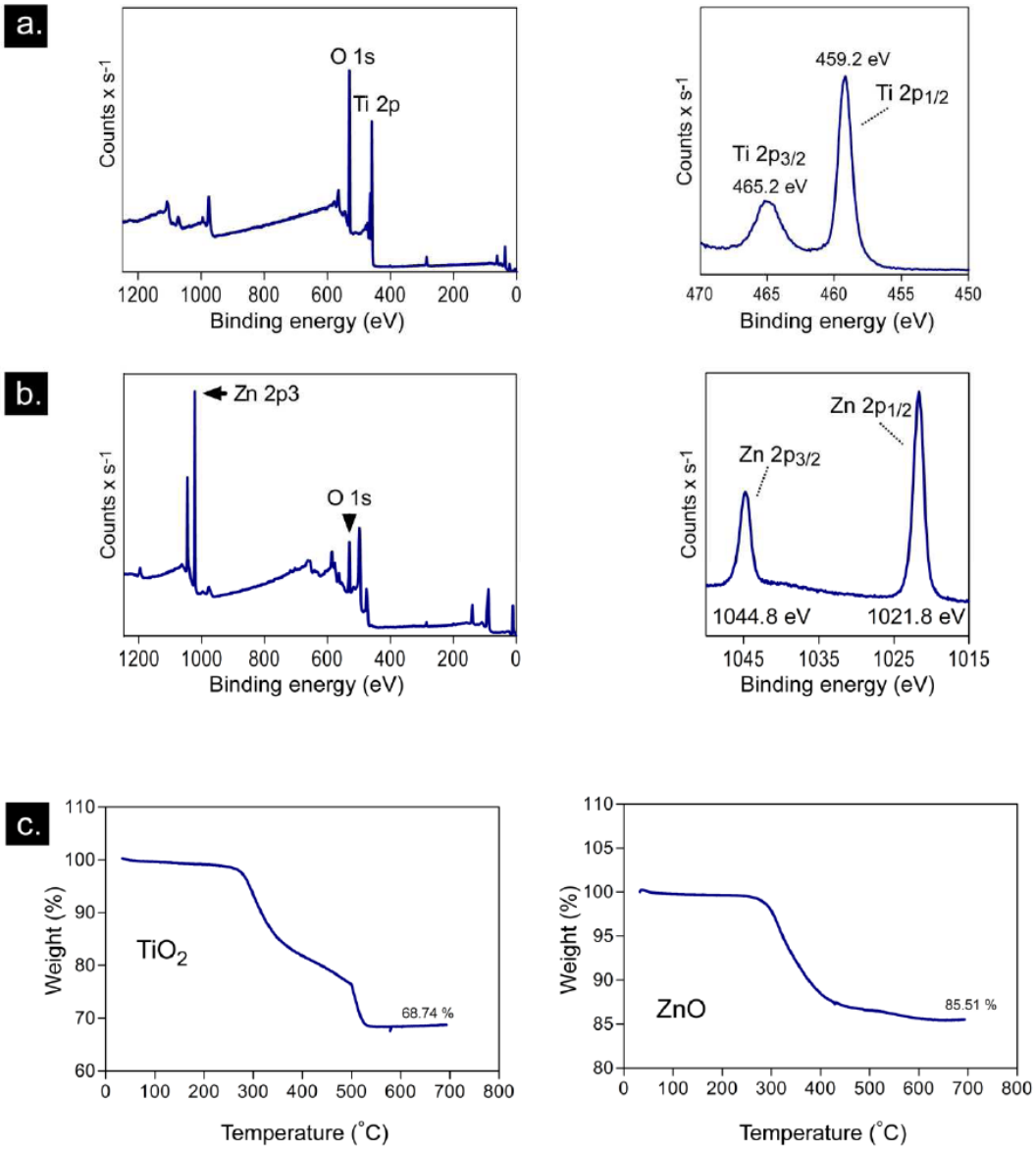

Figure 6.3 Characterization of inorganic nanofabrication on peptide network. XPS survey (left) and high resolution scans of as-synthesized (a) TiO_2, (b) ZnO. (c) TGA of TiO_2 and ZnO organic-inorganic core-shell composite structures.

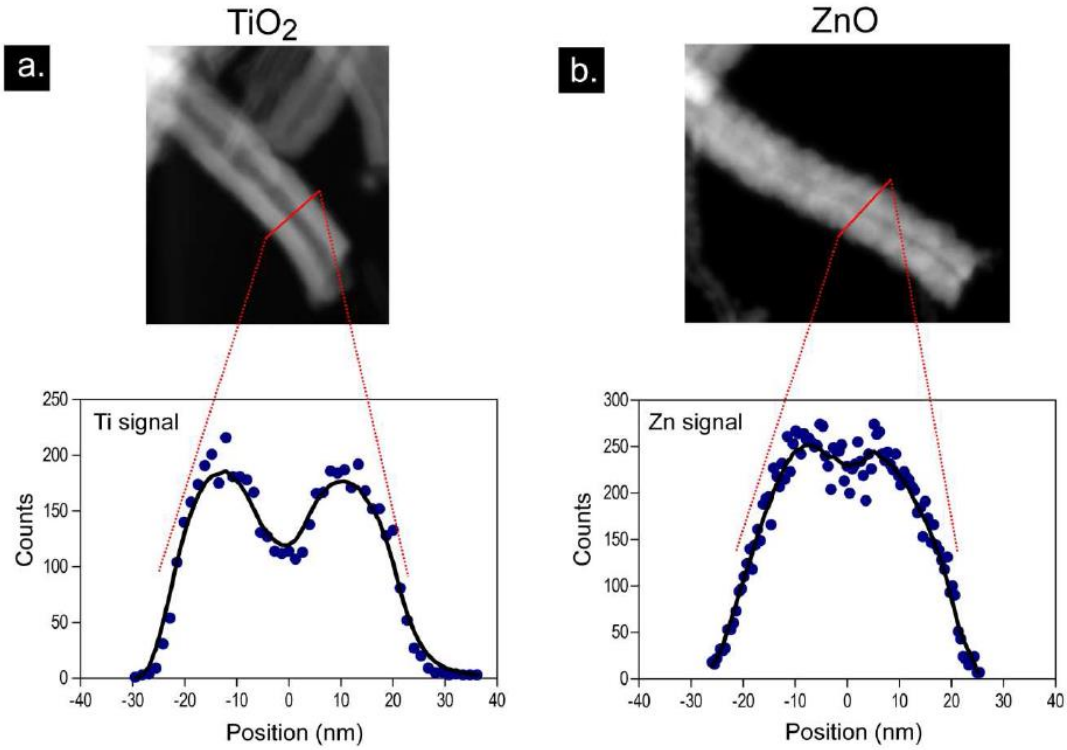

Figure 6.4 EDX mappings of Ti (a) and Zn (b) along transverse section.

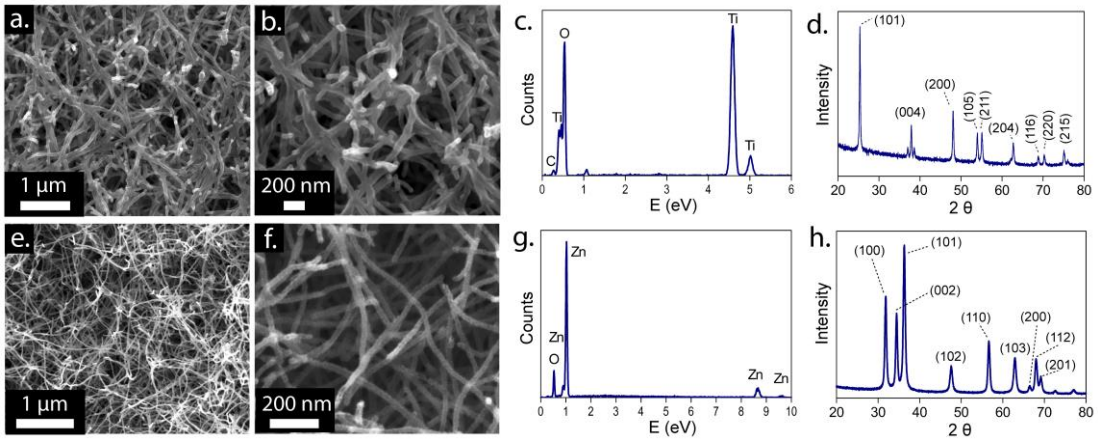

Figure 6.5 Characterization of calcined TiO_2 and ZnO nanonetworks prepared by the deposition of 350 and 100 ALD cycles, respectively. (a, b) SEM images, (c) EDX spectrum, and (d) XRD pattern of TiO_2 nanonetwork corresponding to anatase phase. (e, f) SEM images, (g) EDX spectrum, and (h) XRD pattern of ZnO nanonetwork corresponding to a wurtzite structure.

Calcination of this network at 450 °C did not alter the nanonetwork architecture and its crystal structure (Figure 6.5e–h).

6.3.3 Atomic layer size control of the semiconductor nanotubes

The diameter of TiO_2 nanotubes linearly decreased from 52.0 ± 5.0 to 13.4 ± 1.8 nm with decreased ALD cycles from 350 to 50. In the same trend, the diameter of ZnO nanotubes linearly decreased from 37.4 ± 5.6 (100 cycles) to 13.9 ± 2.4 nm (25 cycles) (Figure 6.6). Growth per cycle (GPC) was found to be 0.56 Å for TiO_2 and 1.55 Å for ZnO (Figure 6.7). The growth rates on three-dimensional networks were in good agreement with spectroscopic ellipsometry measurements acquired on flat silicon surfaces coated with TiO_2 and ZnO by using the same ALD method (*See* Section 7.5.4). After calcination, the diameter of TiO_2 and ZnO nanotubes negligibly changed (Figure 6.8). In ZnO nanotubes, we observed morphological differences in TEM images. The peptide cores were filled with ZnO crystals while the total diameter remained same as before calcination. ZnO nanotubes formed a necklace-like structure at 20 nm and smaller nanotube diameters. On the other hand, the network underwent sintering at 10 nm and the integrity of the fibrous architecture was largely lost. The diameters of both TiO_2 and ZnO nanonetworks were uniformly and precisely modulated by simply altering the total number of ALD cycles. The linear relationship was due to the constant deposition rate at each cycle. Angstrom level precision in each deposition cycle brings about powerful tunability over the nanotube diameter.

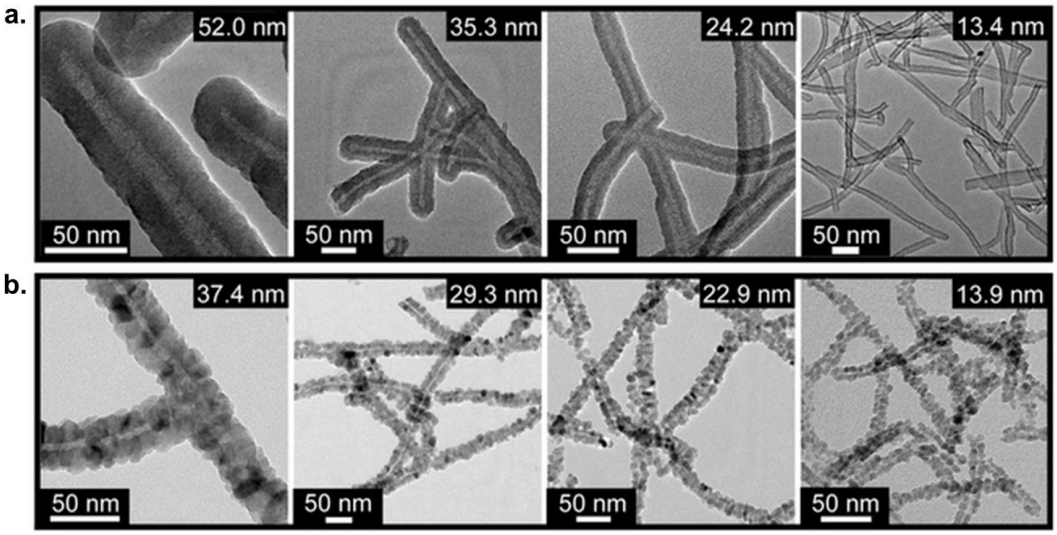

Figure 6.6 Size-controlled deposition of TiO_2 and ZnO on peptide nanonetwork template through ALD cycle number. Representative TEM images of as-synthesized (a) TiO_2, (b) ZnO nanotubes at varying ALD cycle numbers, which facilitate fabrication of the core-shell nanotubes at desired diameters. Images also show high levels of coating conformality on peptide nanofibers.

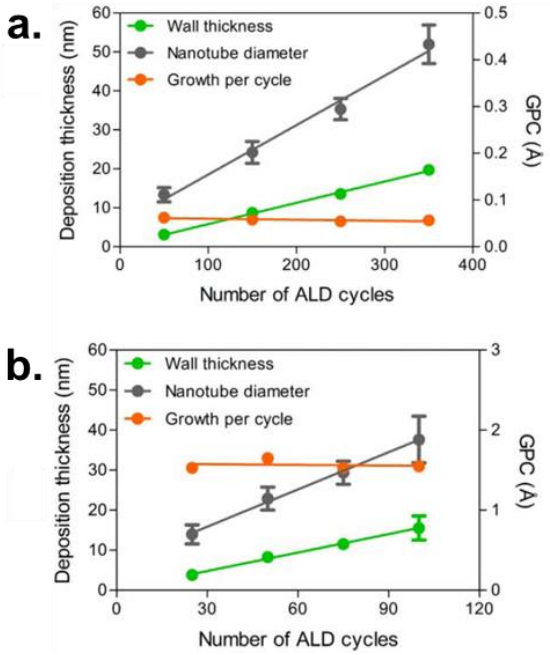

Figure 6.7 Atomic layer deposition parameters. Change in wall thicknesses, nanotube diameters, and growth per cycle (GPC) as a function of the number of ALD cycles for (a) TiO_2, (b) ZnO. Error bars indicate standard deviation.

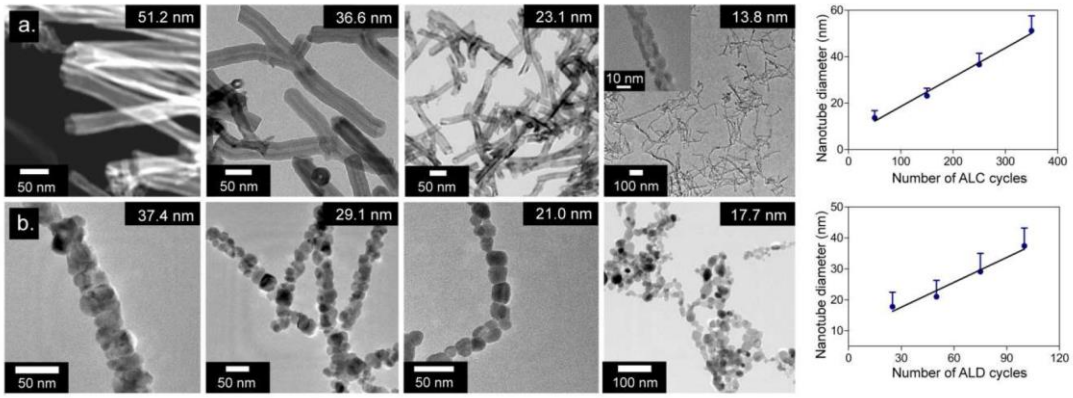

Figure 6.8 Representative TEM images of TiO_2 and ZnO nanonetworks after calcination at 450 °C. (a) Anatase TiO_2 and (b) wurtzite ZnO nanotubes at varying ALD cycles. Images also show high level of coating conformality on peptide nanofibers. Graphs in the right show the linear relation of nanotube diameter and number of ALD cycles deposited. Error bars indicate standard deviation.

TEM images of both TiO_2 and ZnO nanotubes showed complete template coverage with homogenous deposition and high degree of coating conformity revealing the superiority of ALD for the fabrication of ultra-high-surface-area materials with three-dimensional structure. Slight deviation (10–15%) in the nanotube diameters of both TiO_2 and ZnO was observed, possibly due to the formation of few Dopa-PA nanofiber bundles, which increased the core size of the inorganic nanotube. Less efficient diffusion of the precursor molecules into the centimeter scale network could contribute to the deviation. The growing inorganic thickness narrows the mesh size, and hence the deviation from the average wall thickness increases. Nonetheless, to best of our knowledge, this uniformity is far superior to any wet-chemistry-involved protocol reported and thus represents a better alternative to the current methods.

6.3.4 Size-function relationship

As TiO_2 and ZnO nanonetworks with tuned thicknesses (from ~13 nm to ~50 nm diameters with ~3 nm to ~20 nm wall thicknesses) were easily prepared by simply altering the number of ALD cycles, we safely explored the relationship between band gap energy and wall thickness (or nanotube diameter). Photoexcitation of TiO_2 and ZnO semiconductor nanonetworks were characterized by monitoring decomposition of a model organic dye methylene blue under UV irradiation. The specific surface area of the nanonetwork is inversely proportional to the wall thickness (or diameter of the nanotube) per unit mass. Therefore, decreasing the wall thickness is expected to increase the photoexcitation efficiency since higher number of hot spots per unit of mass becomes available for the reaction.

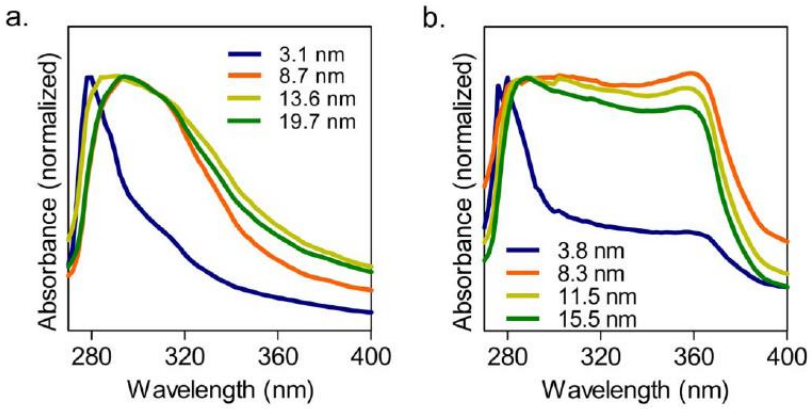

Figure 6.9 UV-Vis spectra of (a) anatase TiO_2, (b) wurtzite ZnO nanonetworks (after calcination).

In the UV-Vis absorption spectra of the nanonetworks, significant hypsochromic shifts ($\Delta\lambda$ = 10–20 nm) were observed for both anatase TiO_2 and wurtzite ZnO as the wall thicknesses decreased below approximately 8 nm (Figure 6.9), indicating an increase in energy gap between valence band and conduction band states. In parallel, we also noted a dramatic decrease of the relative absorbance at the photoexcitation wavelength (365 nm) when the wall thicknesses are below 8 nm. The photocatalytic activities of both semiconductors exhibited considerable decrease below the wall thicknesses ~8 nm. For TiO_2 nanonetworks, methylene blue degradation rate increased as the wall thickness decreased from 19.7 nm to 8.7 nm (Figure 6.10). For ZnO nanonetworks, methylene blue degradation rate remained almost the same (with barely detectable increase) as the wall thickness decreased from 15.5 nm to 8.3 nm. However, this trend sharply deviated at 3.1 nm and 3.8 nm for TiO_2 and ZnO, respectively. The reduction in absorbance at photoexcitation wavelength decreases the number of photons absorbed by the nanotubes, which results in a reduction in the number of photogenerated electron-hole pairs formed for the same amount of photocatalyst. Therefore, for the present TiO_2 and ZnO nanonetworks, we conclude that the observed optical changes play a major role in decreased photoexcitation efficiency below ~8 nm nanotube wall thickness, even though the total surface area per unit mass was increased. Consistent with our present findings, it was previously demonstrated that band gap energy of TiO_2 and ZnO nanoparticles increases with decreasing nanoparticle size due to the physical confinement of electrons and holes.[286-288] Through nanostructuring, excited-state electron-hole pairs' bulk recombination process becomes less dominant, and redox potential difference between conduction-band electrons and valence-band holes increases due to the

quantum confinement effect, which overall enhances the photocatalytic activity. However, when the nanostructure dimension is lowered below a certain limit, surface charge recombination process may become dominant and most of the electron-hole pairs generated sufficiently in the proximity of the surface undergo rapid quenching before the interfacial charge transfer process happens.[289] Additionally, due to quantum confinement effect at smaller nanometer dimensions, energy gap between valence band and conduction band states increases and only sufficiently high energy portion of the photons can initiate the catalytic activity.[287] Overall, these effects may significantly lower the photocatalytic performance of the nanostructures below a certain size limit. Based on the comparison with the nanoparticle-based semiconductor materials, we conclude that the optimal size in TiO_2 and ZnO nanonetworks for photocatalytic efficiency may be caused by the wall thickness rather than the diameter of the nanotube.[290, 291]

6.3.5 Photoexcitation of surface-immobilized TiO_2 and ZnO nanonetworks

Semiconductor nanonetworks were further prepared on solid supports by using peptide nanofiber templates as shown in Figure 1. As a control, flat inorganic substrates without peptide nanofiber template were also prepared by ALD with the same average wall thickness of the constituent nanotubes. Under UV irradiation, 69% and 63% of methylene blue was degraded by the end of 7 h by using peptide nanofiber templated TiO_2 and ZnO networks, respectively (Figure 6.11). Methylene blue degradation by non-templated TiO_2 and ZnO catalysts, however, remained only at 7% and 9%, respectively.

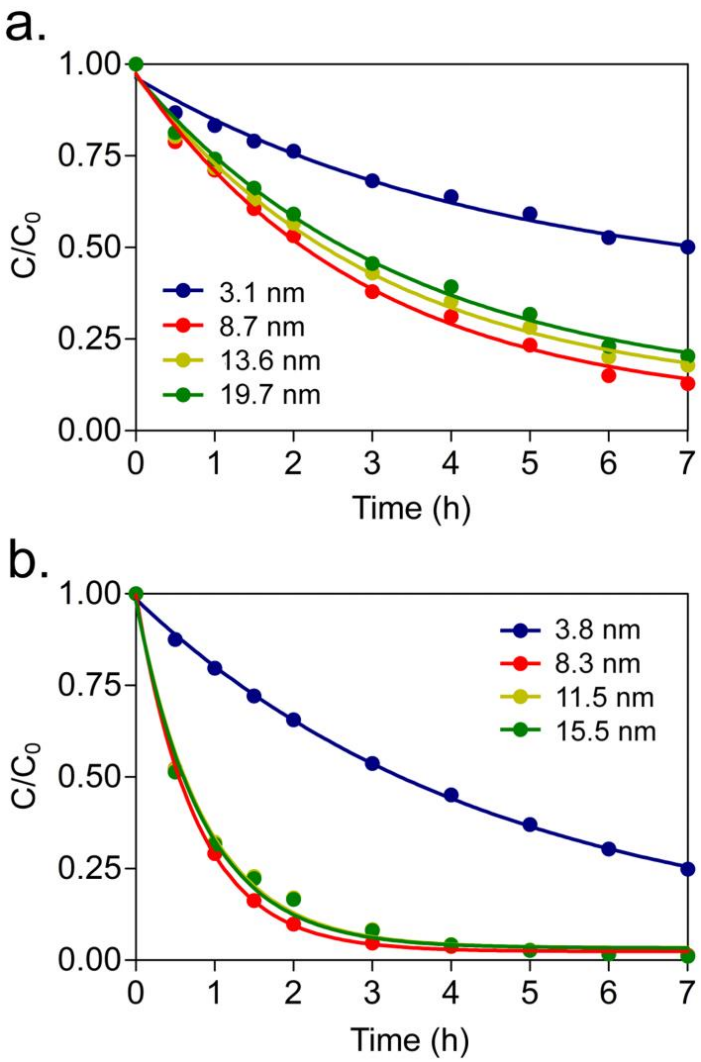

Figure 6.10 Photoexcitation of TiO_2 and ZnO nanonetworks as a function of nanotube wall thicknesses. Degradation of methylene blue through the photocatalytic activity of (a) TiO_2, (b) ZnO nanonetworks.

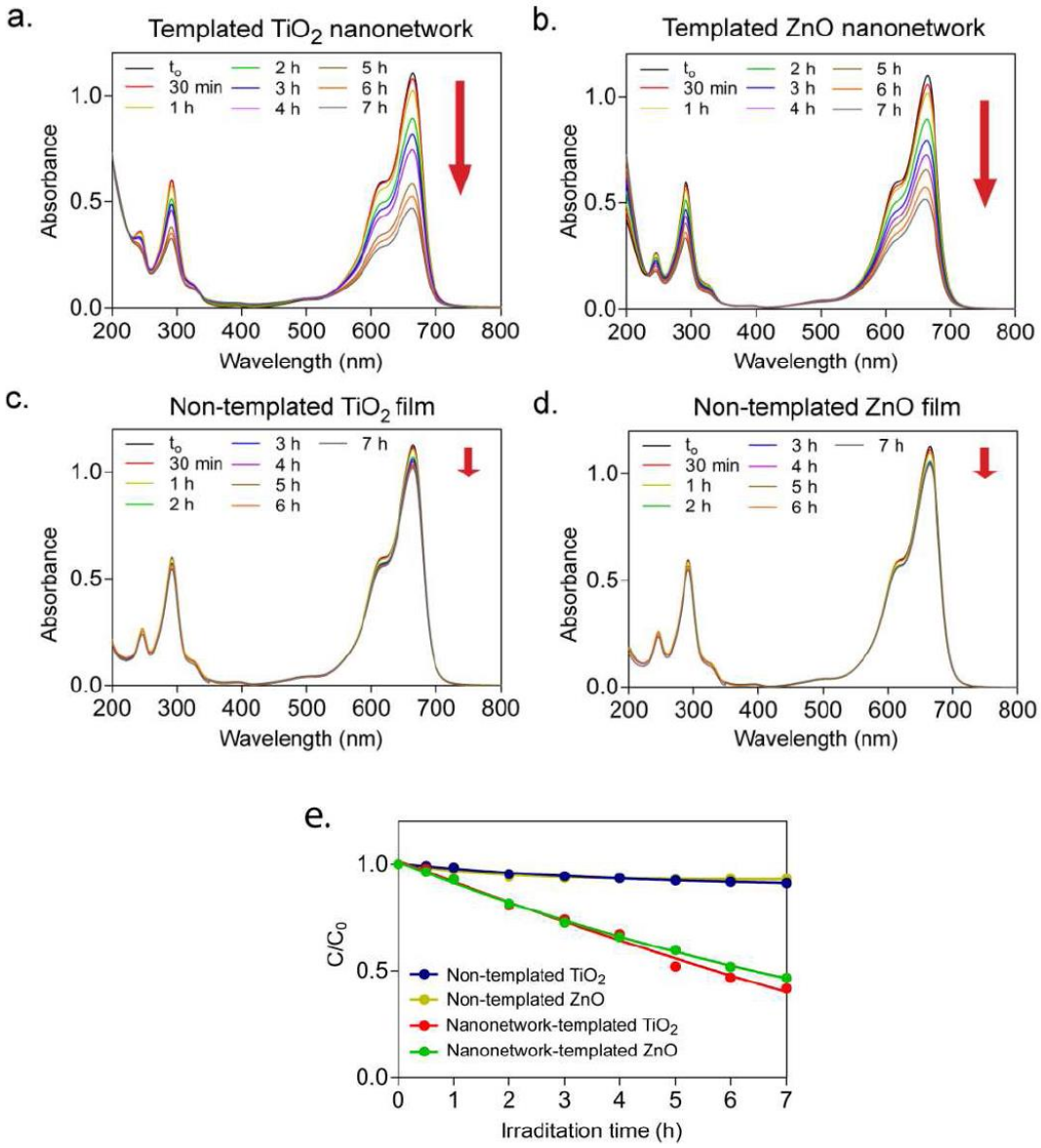

Figure 6.11 UV-Vis spectra of methylene blue solutions to show degradation of methylene blue. (a) peptide-templated TiO_2 nanonetwork deposited with 350 cycles, (b) peptide-templated ZnO nanonetwork deposited for 100 cycles, (c) non-templated TiO_2 flat film, (d) non-templated ZnO flat film. Photoactive surfaces were prepared on silicon wafer supports. (e) Kinetics of methylene blue degradation conveyed via λ_{max} (663 nm).

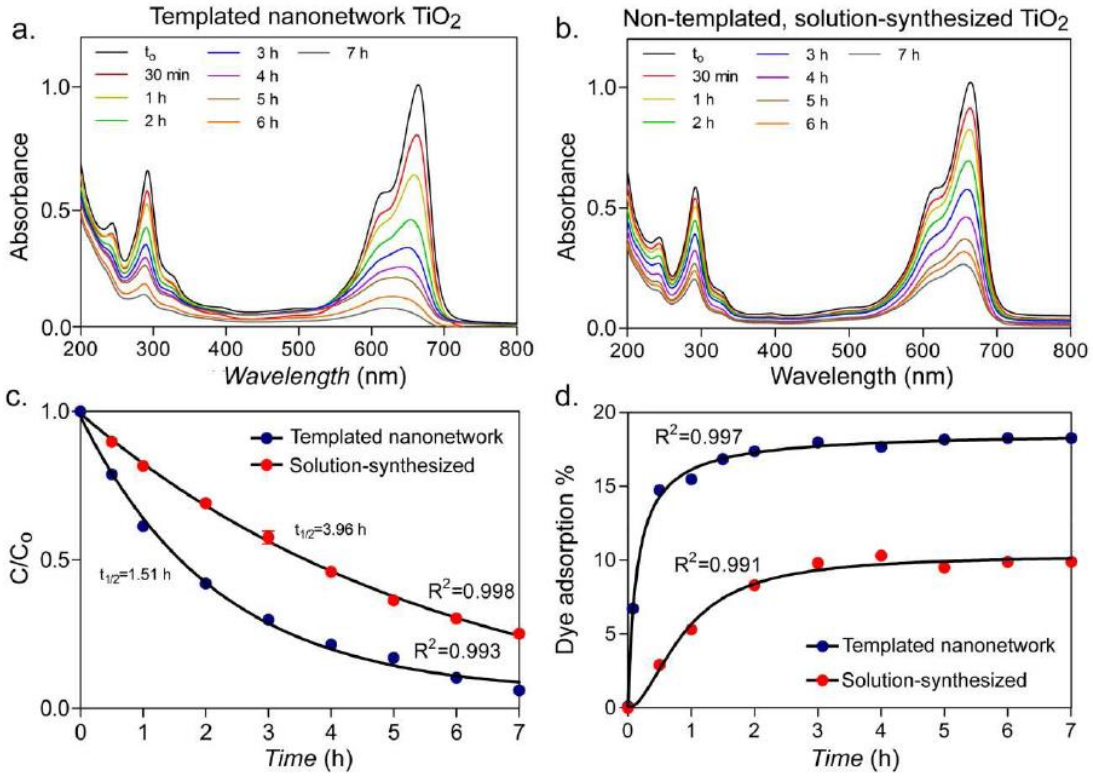

Figure 6.12 Comparison of the photoexcitation activities of templated anatase TiO_2 and non-templated, solution synthesized anatase. (a, b) UV-Vis spectra of methylene blue during degradation. (c) Kinetics of degradation conveyed via λ_{max} (663 nm). (d) Physical adsorption of the dye onto photoactive surfaces.

The photoexcitation efficiency of templated TiO_2 nanonetwork was 2.62 folds (calculated based on the $t_{1/2}$ templated/$t_{1/2}$ non-templated ratio) greater than that of non-templated solution-synthesized anatase TiO_2 (Figure 6.12a-c). The rate of methylene blue adsorption on nanonetwork TiO_2 was higher than that of non-templated (Figure 6.12d). The sharp difference in photoexcitation properties of surface immobilized nanostructures and the flat surface was due to gained specific surface area through nanostructuring. Both TiO_2 and ZnO nanonetworks remained intact after the photoexcitation experiments. Surface-immobilized intact nanonetworks of TiO_2 and ZnO ensured reusability of the photoactive surface, as well. In order to further study the advantage of nanostructuring on the photoexcitation efficiency, we next compared peptide nanofiber template-based synthesized anatase TiO_2 nanonetwork to template-free solution-synthesized anatase TiO_2. The accessible surface area was strikingly different between templated and non-templated anatase materials confirmed by higher physical adsorption kinetics and total adsorption of methylene blue on templated anatase TiO_2 network (Figure 6.12d).

6.4 Conclusion

Overall, we demonstrate a facile and reliable fabrication method for TiO_2 and ZnO semiconductor nanonetworks by using self-assembled peptide amphiphile nanofiber network as templates. Apart from the traditional organic templates in wet chemistry, we used a fully dried, three-dimensional (cm scale), highly interconnected supramolecular nanofibrous network template, which enabled ALD precursors to be homogenously deposited with exceptional conformity. The wall thickness of the

inorganic nanotubes can be precisely controlled by simply altering the number of ALD cycles. Decrease in the wall thickness of both TiO_2 and ZnO caused hypsochromic shift in UV absorbance. TiO_2 and ZnO nanonetworks demonstrated superior photoexcitation properties compared to the unstructured TiO_2 and ZnO substrates because of the enhanced surface area with nanostructured morphology. On the other hand, anatase TiO_2 and hexagonal wurtzite ZnO nanonetworks are found to be dependent on both the wall thickness and total surface area per unit of mass. Importantly, immobilization of the semiconductor materials on a solid support enables recycling of the photoactive surface. Further studies can be extended to other transition metals and their compounds, such as oxides, nitrides, and sulfides. As a result of the rapid and convenient scaling of the peptide nanofibers into macro-size networks, new opportunities could be available for fabrication of nanonetworks for a wider range of inorganic materials.

6.5 Experimental Section

6.5.1 Materials

All reagents used in this study were purchased from Sigma-Aldrich, Merck, Fisher Scientific, ABCR, or Alfa-Aesar as analytical grade and were used without any further purification.

6.5.2 Synthesis and characterization of peptide amphiphile molecule

Fmoc solid phase peptide synthesis method was employed to synthesize Lauryl-Val-Val-Ala-Gly-Lys-Dopa-Am (Dopa-PA). Rink Amide MBHA resin (Novabiochem®) was used as the solid support. Carboxylate group activation of 2 mole equivalents (equiv.) of amino acids was succeeded by 1.95 mole equiv. of N,N,N',N'-

Tetramethyl-O-(1H-benzotriazole-1-yl) uronium hexafluorophosphate (HBTU), and 3 mole equiv. of diisopropylethylamine (DIEA) for 1 mole equiv. of functional sites on the solid resin. Fmoc groups were removed prior to each coupling step with 20% piperidine/dimethylformamide for 20 min. Amino acid coupling time was set to be 2 h at each cycle. Lauric acid was used as the source of lauryl group and its coupling mechanism was similar to amino acid coupling. After synthesis, all protecting groups were removed using a cleavage cocktail containing 95% trifluoroacetic acid (TFA), 2.5% water, and 2.5% triisopropylsilane. Excess TFA was removed by rotary evaporation followed by precipitation in diethyl ether overnight. The precipitate was collected and dissolved in ultra-pure water. This solution was frozen at −80°C followed by freeze-drying for one week. Residual TFA was removed by dissolving the whole batch in dilute HCl solution and freeze-drying. Small molecular contaminants and the remaining salts were removed through dialysis using a cellulose ester dialysis membrane with molecular-weight-cut-off of 100–500 Da. After dialysis, Dopa-PA molecules were once more freeze-dried and their purity was assessed using Agilent 6530 quadrupole time of flight (Q-TOF) mass spectrometry with electrospray ionization (ESI) source equipped with reverse-phase HPLC. Dopa-PA as synthesized and used with > 95% purity.

6.5.3 Template preparation

Template preparation procedure is schematically illustrated in Figure 6.1. To induce self-assembly, 1 wt% Dopa-PA solution (pH ~3) was casted onto the silicon wafer, which served as a solid support. The pH was then shifted to ~10, which triggered rapid gelation followed by covalent cross-linking of the peptide network (Figure

6.1c). In order to prepare the ALD template, 1 wt% Dopa-PA hydrogel was formed in situ on a solid support (*ca.* 2 mm in height and *ca.* 0.8 cm in diameter). After 10–15 min incubation in a humidified environment, hydrogels were dehydrated with ethanol for critical point drying (Tourismis Autosamdri®-815B). Dried samples immobilized on the solid substrates were used for ALD.

6.5.4 Atomic layer deposition of TiO_2 and ZnO

TiO_2 and ZnO layers were deposited by ALD using $Ti(NMe_2)_4$, Et_2Zn, and H_2O as titanium, zinc, and oxygen precursors, respectively. $Ti(NMe_2)_4$ was preheated to 75°C and stabilized at this temperature prior to depositions. Depositions were carried out at 150°C in Savannah S100 ALD reactor (Cambridge Nanotech Inc.) using N_2 as the carrier and purge gas. Exposure mode (a trademark of Cambridge Nanotech Inc.) was applied, in which dynamic vacuum was switched to static vacuum just before the precursor and oxidant pulses, and switched back to dynamic vacuum before the purging periods after waiting for some time, i.e., exposure time. This special mode allowed time for precursor and oxidant molecules to diffuse into the highly porous, three-dimensional network of Dopa-PA nanofibers. N_2 flow rate, which is normally 20 standard cubic centimeters per minute (sccm), was set to 10 sccm just before dynamic vacuum was switched to static vacuum. One growth cycle of TiO_2 consisted of $Ti(NMe_2)_4$ pulse (0.1 s) and exposure (10 s), N_2 purge (20 s), H_2O pulse (0.015 s) and exposure (10 s), and N_2 purge (20 s). TiO_2 depositions were also carried out using tripled exposure and purge times, i.e., 30 s and 60 s, respectively. One growth cycle of ZnO consisted of Et_2Zn pulse (0.015 s) and exposure (20 s), N_2 purge (30 s), H_2O pulse (0.015 s) and exposure (20 s), and N_2 purge (30 s). Another set of ZnO

depositions was carried out using tripled exposure and purge times, i.e., 60 s and 90 s, respectively, with no N_2 flow after the first 30 s of exposure. For comparative purposes, TiO_2 and ZnO films were deposited on solvent-cleaned, 5% HF-dipped Si wafers. Standard ALD mode was applied with the same precursor pulse and purge times used for the exposure mode. Growth rates of TiO_2 and ZnO films at 150°C were measured by spectroscopic ellipsometry (V-VASE, J.A. Woollam Co.) as 0.51 Å/cycle and 1.53 Å/cycle, respectively.

6.5.5 Characterization of TiO_2 and ZnO nanonetwork

The morphology and chemical composition of TiO_2 and ZnO nanonetworks were characterized using a field emission scanning electron microscope (FEI Quanta 200 FEG) coupled with an energy dispersive X-ray spectrometer. Bare peptide networks were sputter coated with 5 nm gold/palladium prior to SEM imaging. TiO_2 and ZnO deposited networks were investigated without any further coating. TEM and STEM images were acquired by using a FEI Tecnai G2 F30 TEM operating at 300 kV. To visualize Dopa-PA nanofibers, negative staining with uranyl acetate was performed. TiO_2 and ZnO deposited nanofibers were visualized without any staining procedure. Nitrogen adsorption–desorption isotherms at 77 K were measured on an Autosorb-iQwin™ automated gas sorption analyzer from Quantachrome® Instruments was employed. A PANalytical X'Pert Powder Diffractometer was used to reveal the crystal structure of TiO_2 and ZnO nanonetworks. All data were recorded by using Cu Kα radiation in the range of $2\theta = 20°\text{-}100°$ and with the spinning rate of 16 rpm in order to achieve homogenous data acquisition from samples. A thermogravimetric analyzer (TGA) (Q500, TA Instruments) was used to quantify the organic-inorganic

composition of the ALD deposits. The temperature was ramped from 25 to 500 with 20°C min^{-1} heating rate in the presence N_2. After 500°C, N_2 was switched to O_2 and heating was continued to 700°C with the same rate. A Thermo Scientific X-ray photoelectron spectrometer with Al Kα micro-focused monochromatic X-ray source and with ultra-high vacuum (~10^{-9}) was utilized. The pH of Dopa-PA solution was prepared at pH ~3 and used immediately after it is dissolved in order to prevent spontaneous oxidation.

6.5.6 Photoexcitation reactions

Amorphous TiO_2 was calcined to obtain anatase phase. For this, a gradient heating protocol (250 °C for 1 h, 350 °C for 30 min and 450 °C for 30 min, sequentially) was applied, through which agglomeration of the nanostructures was prevented. To remove the peptide core, ZnO samples were calcined with the same protocol applied to the TiO_2 samples. Photocatalytic reactions in Figure 6.12 were carried out by immobilizing photocatalysts on silicon supports. Network-templated TiO_2 and ZnO samples were prepared as shown in Figure 7.1 with 350 and 100 cycles, respectively. As a control of nanostructured material, silicon surfaces with the same projection area were coated with TiO_2 and ZnO using ALD with 350 and 100 cycles, respectively. The photocatalyst surfaces were dipped into 2 x 10^{-5} M aqueous methylene blue solutions and irradiated by 365 nm light source. UV-Vis spectrum of the dye was collected for 7 h with one or half-an-hour intervals using a spectrophotometer (Cary 5000, Varian). The reactions in Figure 6 were carried out using 0.87 mg templated anatase TiO_2 and 0.87 mg non-templated, solution-synthesized anatase in 2 x 10^{-5} M of methylene blue aqueous solution. For this

purpose 39.3 μL of 95% $Ti(O\text{-}i\text{-}Pr)_4$ was added to 5 mL of pure ethanol and agitated by magnetic stirrer for 3 h. Solvent was removed and sample was calcined as described above. The photocatalysts used in this experiment were powdered in a mortar to obtain fine-grained particles. TEM images of the powdered nanonetworks were similar to Figure 6.6. In order to test dye adsorption, samples were prepared similarly to photocatalytic experiment, only the test was carried out in the absence UV. As a result, decrease in the absorbance signal was attributed to physical adsorption of the dye molecules onto the photocatalyst surfaces. Samples of the photocatalytic reactions in Figure 6.12 were prepared similar to shown in Figure 7.1 followed by calcination and powdering in a mortar prior to obtaining fine grained particles. 0.5 mg TiO_2 and 1.1 mg ZnO were used in 2 x 10^{-5} M aqueous methylene blue solution irradiated by 365 nm light source.

CHAPTER 7

7 Modular Short Peptides for Coupled Synthesis and Biofunctionalization of Gold Nanoparticles for Integrin-Targeted Cell Uptake

A partial content of this work is under preparation for a publication with the following authors:

Ceylan H., Gulsuner H. U., Guler, M. O., Tekinay, A. B.

7.1 Objective

Engineered gold nanoparticles (AuNPs) find numerous applications in the fields of biomedicine, chemical synthesis, and energy conversion. However, the conventional ligand exchange reaction, which utilizes sulfur affinity to surface gold atoms, is not an efficient process as it causes spontaneous aggregation as well as incomplete ligand exchange. Here, we demonstrate a short, modular peptide design that allows for a reaction cascade coupling the synthesis, stabilization and surface functionalization steps. The synthesis is achieved via simple mixing of the aqueous solutions of auric acid and modular peptides at room temperature. This method allows facile control over the nanoparticle size in between ~2-15 nm, which opens a practical window for biomedical applications. Peptide-mediated synthesis and stabilization, in contrast to the conventional citrate-mediated Turkevich method, provide AuNPs with an increased colloidal stability. Importantly, synthesis of small-

size gold nanoparticles (D < 10 nm) using our modular design does not require any toxic surfactant stabilizer, thereby eliminating potential biosafety concerns. As proof of the concept, we designed a biofunctional peptide of Arg-Gly-Asp (RGD), which targets cell-surface integrin receptors. Active targeting of such biofunctional AuNPs to a human breast adenocarcinoma cell line (MCF7) was demonstrated. Cytotoxicity experiment showed that RGD peptide capped AuNPs does not affect cell viability. Overall, we present a green approach for the synthesis and functionalization of gold nanoparticles in a single-step in a size-controlled manner. The chemical versatility of the modular peptide design is expected to broaden the applicability of this strategy, rendering it a successful alternative to the currently available nanoparticle preparation technology.

7.2 Introduction

Engineered gold nanoparticles (AuNPs) have drawn substantial attention for their unique optoelectronic and physicochemical properties. Their exceptionally low cytotoxicity and high stability in the biological media have enabled an extensive range of biomedical applications including drug or gene delivery, photo-thermal therapy, colorimetric sensing and imaging.[292-298] As targeting and delivery agents, engineered AuNPs have even reached early-phase clinical trials.[299] As a result, preparation of such nanoparticles require a special attention in respect to control over the engineering parameters; i.e., size, shape and surface coating, and purification of the final construct from toxic reactants.

Functionalized gold nanoparticles are usually prepared by two successive reactions. In the first step, Au(III) ions are reduced into Au(0), which is followed by

aggregation of gold atoms for the growth of the AuNPs. Particle growth is terminated through a stabilizer, which surrounds the nanoparticle surface, creating electrostatically or sterically hindered surface for insertion of any further gold atom. In classical Turkevich method, citrate ions are used for both reduction and stabilization. By varying Au(III):citrate ratio in the reaction, size control is achieved over the nanoparticle in the range of 10-20 nm.[300, 301] To obtain smaller particles, Brust method is of general preference as it allows particles as small as 2-5 nm.[301, 302] For this method, a stronger reducing agent, sodium borohydride, and more effective stabilizers, alkanethiols, tetraoctylammonium bromide, cetyl trimethylammonium bromide (CTABr) and Tween-20, are used.[302, 303] In the second step, functional (bio)organic molecules containing a sulfhydryl group are expected to displace the stabilizer via a ligand exchange reaction. One major drawback of the ligand exchange reaction is that partially destabilized gold nanoparticles can irreversibly fuse to form larger aggregates.[304] In addition, this reaction does not always go to completion, which can significantly dilute ligand amount on the nanoparticle surface, and thereby reducing the expected effectiveness of the construct. Moreover, toxic surfactants like CTABr and tetraoctylammonium bromide are difficult to completely remove.[303] Altogether, a greener and practical method that couples the synthesis and bio-functionalization steps in one reaction would significantly improve the usefulness of the nanoparticle-based applications.

Here, we describe modular design of a short peptide for single-step, size-controlled synthesis of bio-functionalized gold nanoparticles. Modular design enables concerted reduction, stabilization and functionalization all by the same molecule at one-pot whereby no additional reagent or reaction is needed. Furthermore, modular design

provides geometrically flexible space for presentation of the biofunctional ligand to the outer environment. In contrast to the existing methods, inherent biocompatibility of the peptide provides a greener route towards the synthesis of a broad range (~2-15 nm in diameter), bio-functional nanoparticles. This strategy is also free of inefficiencies that might arise during ligand exchange reaction as stabilization and bio-functionalization are accomplished by the same molecule. As a result, these NPs exhibit remarkable stability in high ionic strength. As proof of the concept, we synthesized AuNPs functionalized with a targeting moiety, Arg-Gly-Asp, which is known to bind to integrin $\alpha_v\beta_3$ upregulated on cancer cell surface.[305] Synthesized AuNPs were exposed to MCF7 cells and uptake was confirmed by ICP-MS analysis. Overall, the strategy here provides a practical and toxic-free alternative to the currently established methods for preparation of functionalized AuNPs.

7.3 Results and Discussion

7.3.1 Design and Synthesis of Modular Peptides

The use of bioconjugated AuNPs have emerged as a powerful tool for both diagnosis and therapeutic applications. The major drawbacks in the design and synthesis of these nanobioconjugates are their requirement of the use of toxic chemicals, their reaction times ranging from hours to days, and unstable AuNPs after functionalization. In this study, we used RGD peptides to synthesize improved AuNPs, free of these drawbacks. This multi-tasking RGD peptide is able to display three functional domains (Figure 7.1a): (1) Catechol molecules have outstanding binding affinities to most of the organic and inorganic materials, and their unique reductive properties make them suitable to form metal nanoparticles.[306]

Hydroxyphenols can rapidly oxidize into their quinone forms due to their high reduction potential by releasing electrons for the reduction of metal precursors. In this design, 3,4-dihydroxy-L-phenylalanine (Dopa) serves as a reducing and stabilizing agent. Lys residues help to stabilize AuNPs. (2) Linker domain forms an interface between AuNP and the following functionalization domain. We used Gly in this study for a simple proof of concept design. This domain can further be functionalized according to various applications. For example, Gly can be replaced with positively charged residues to serve as carriers for nucleotides in gene delivery applications. Additionally, amino groups with a pKa ~5-7 (e.g. His) that absorb protons in response to the acidic environment of endosomes might be used for endosomal escape via "proton sponge" effect.[307, 308] (3) For effective nanoparticle delivery to take place, not only transportation of the therapeutic materials but also transportation to specific molecular targets are needed. In order to achieve this, we designed a targeting domain containing Arg-Gly-Asp sequence for integrin mediated cell uptake.

7.3.2 Development and Characterization of RGD peptide conjugated Gold Nanoparticles

Gold nanoparticles were synthesized by the route outlined in Figure 7.1b. In order to synthesize gold nanoparticles, RGD peptide solution (0.6 mM) was allowed to react with equal volume of $H[AuCl_4]$ solution (19.2 mM). Synthesis was performed at room temperature in order to achieve simultaneous and homogeneous nucleation. Upon addition of peptide solution into gold salt solution at pH 10.0, the yellow color of the solution rapidly turned into red which darkened by time (Figure 7.2a, inset).

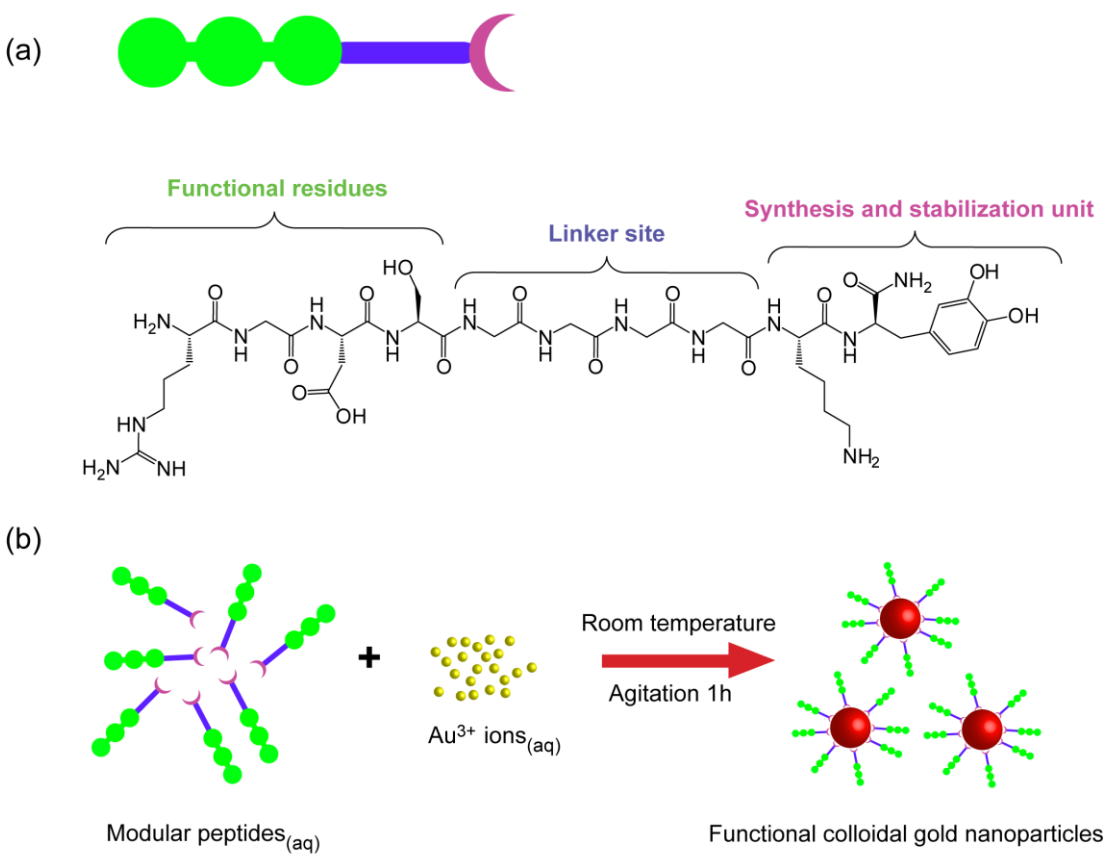

Figure 7.1 Schematic illustration of the modular peptide design. (a) Chemical sketch of a model RGD-functionalized peptide, $RGDSG_4KDopa\text{-}NH_2$, where Dopa and Lys serve as synthesis and stabilization units, Gly_4 functions as a steric linker to Arg-Gly-Asp, the integrin-targeting domain. (b) Proposed functionalization (capping) of AuNPs with the peptides.

This color change was attributable to the reduction of Au^{3+} to Au^{0} which is characterized by optical spectroscopy, and a peak at 518 nm was detected (Figure 7.2a). This indicated the formation of gold nanoparticles. To confirm the formation of nanoparticles, samples were imaged with TEM, which showed moderately-dispersed spherical nanoparticle formation with an average core size of 11.0 ± 1.9 nm (Figure 7.2b, c). The hydrodynamic size was found to be 14.5 ± 0.8 nm. Higher hydrodynamic size indicated the solvation effect and the presence of peptide cap. Furthermore, DLS measurements confirmed that there was no aggregation during the nanoparticle formation. Energy dispersive X-ray spectroscopy (EDX) imaging verified that the nanoparticles consist of gold (Figure 7.3). Selected-area electron diffraction (SAED) performed on a single nanoparticle specifies the polycrystalline features of the synthesized AuNPs (Figure 7.3, inset). Monitoring the formation of AuNPs kinetically by following the appearance of SPR band at 518 nm indicated that AuNP formation starts within seconds after the addition of reactants; and the reaction comes to equilibrium within 1 h (Figure 7.2d). Overall, these results imply that the reaction of RGD peptides with gold metal solutions culminated in well-dispersed, poly-crystalline gold nanoparticles (RGD-AuNPs). Nanoparticles represent the lowest end of the colloid range (1 nm to 1 μm) and their colloidal properties affect their characteristics and further applications.[309] In order to investigate the colloidal stability of RGD-AuNPs, they were incubated in increasing concentrations of NaCl (Figure 7.2e). Optical spectroscopy (UV-Vis) was used to characterize the stability of nanoparticles in different ionic strength conditions. RGD-AuNP dispersions were relatively stable up to 100 mM salt solution.

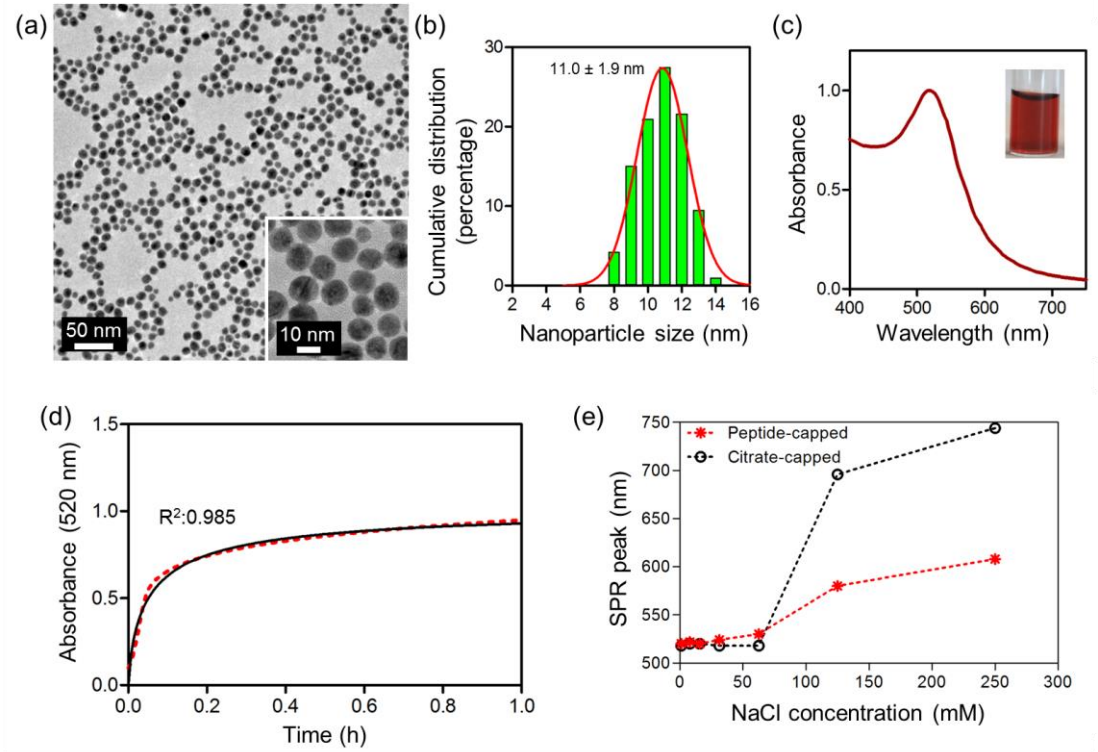

Figure 7.2 One-pot synthesis, kinetics and colloidal stability of AuNPs. (a) Transmission electron micrograph and (b) particle size distribution of AuNPs. (c) UV-Vis spectra of the peptide-gold solution (1:32 molar ratio) mixture at 1 h. The inset shows the reaction tube developing a typical wine red color of AuNPs. (d) Kinetics of AuNP formation monitored by the light absorption of surface plasmons at 520 nm. (e) Colloidal stability of peptide-functionalized AuNPs as compared to citrate-capped AuNPs with same size.

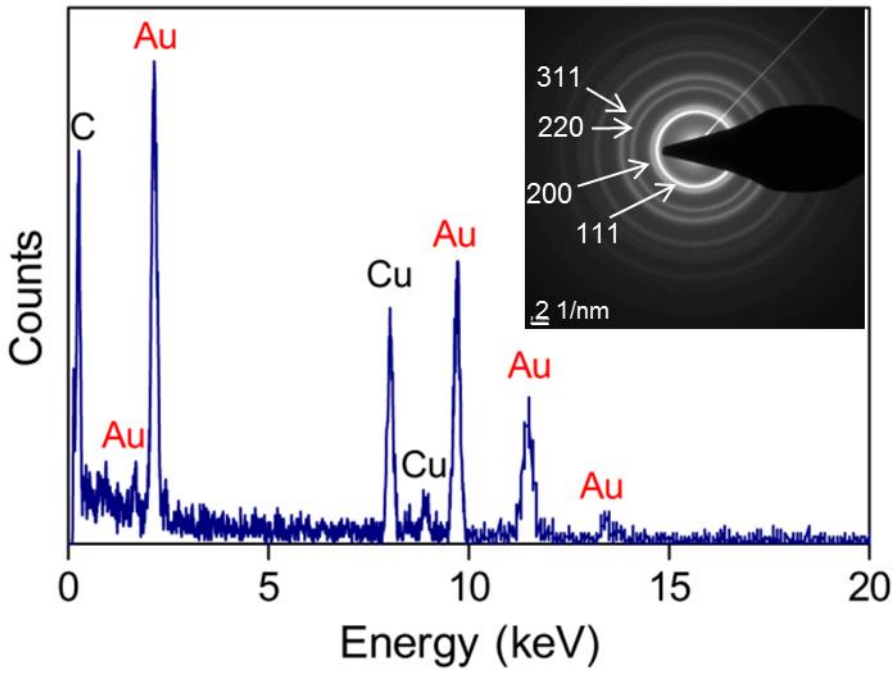

Figure 7.3 Energy-dispersive X-ray spectrum. The inset shows the selected area electron diffraction of AuNPs.

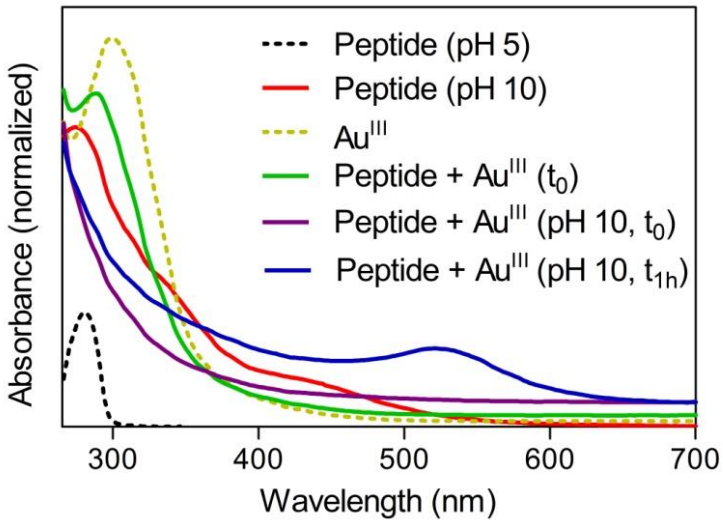

Figure 7.4 Synthesis mechanism of AuNPs by a model RGD-functionalized modular peptide. UV-Vis spectra of the model peptide and auric acid solution before and after mixing, indicating that oxidation of the peptide couples with the reduction of gold.

On the other hand citrate capped AuNPs started to coagulate after 62 mM salt addition with further red shifting in SPR bands in increasing NaCl concentrations. Moreover, RGD-AuNPs remained stable for months when stored at room temperature in distilled water. Therefore, RGD peptide coating enhances the stability of gold nanoparticles, a result that can be ascribed to the efficient binding of the RGD peptides on the surface of the nanoparticles and strong binding capacity of Dopa to metals.[19]

Mechanism of gold nanoparticle formation was analyzed by UV-Vis spectroscopy (Figure 7.4). Before the addition of gold salt into the RGD peptide solution at pH 5, Dopa adsorption peak at 280 nm was detected. When the pH of the peptide solution was increased to 10, a broad shoulder ranging from 300 to 500 nm indicating the oxidized quinone formation was observed. Aqueous $H[AuCl_4]$ solution shows an intense band around 320 nm due to charge transfer between the metal and chloride ions.[310] As soon as mixing aqueous $H[AuCl_4]$ with RGD peptide solution at pH 10, this peak vanished corresponding to the complete reduction of Au(III). This is because of the high reduction potential of Dopa (E^0-Dopa = -745 mV), so that Dopa residues electrons to Au(III) ions (E^0-Au(III) = +1.52V) to instantly generate gold nanoparticles, and convert themselves into quinones.[311, 312] After 1 hour of incubation, gold nanoparticle peak at 518 nm stabilized which indicates the colloidal gold formation.

7.3.3 Size Control on Synthesized Gold Nanoparticles

The ability to synthesize nanoparticles in a controlled size with a narrow distribution is highly important because their physicochemical and optoelectronic properties

depend on their size. We varied the fraction of gold salt in the solution as a means of controlling the size of resulting RGD-AuNPs. 600 μM peptide solution in water was added to serially diluted (76.8 mM to 1.2 mM) equal volume of $H[AuCl_4]$ solution. The color of the solution changed according to the peptide fraction inside the solution ranging from wine-red to light-red (Figure 7.5a). RGD-AuNPs synthesized with 1:128 molar ratio had a golden-brown color. Concomitant with the color change, SPR bands of synthesized AuNPs shifted to longer wavelengths with decreasing amounts of gold salt in the initial solution (Figure 7.5b). Similarly, core size analysis by TEM revealed that particle size increases progressively with decreasing amounts of gold salt in the initial solution (Figure 7.6). The average diameters extracted from TEM images along with their Au-to-peptide ratios are listed in Table 7.1. The size distributions were concordant with the prediction made by Howard Reiss that decreasing the monomer concentration increases the critical size and results in the formation of larger nanoparticles.[313, 314] We were able to synthesize RGD-AuNPs ranging from 2.3 nm to 15.5 nm in diameter with uniform dispersions. RGD-AuNPs had an average of ~20% polydispersity in their individual size ranges which is better than the polydispersity of AuNPs synthesized with single-step methods.[315, 316] Because of their small size (2.3 nm), particles with 1:128 molar ratio did not exhibit SPR band.[301, 317] In summary, RGD peptide controls the nanoparticle nucleation and growth and finely tunes the size of the nanoparticles with a narrow distribution.

The modular peptide approach was further investigated by additional peptides with altered or cleaved sequences (Figure 7.7). AuNP syntheses with same one-pot technique were completed within 1 h (Figure 7.7a). For consistent comparison,

similar sized nanoparticles were used. In terms of colloidal stability, all peptide-capped AuNPs showed better stability than citrate capped AuNPs in increasing ionic strength conditions (Figure 7.7b). This result also verifies the presence of a peptide coated layer on AuNPs. TEM was employed to investigate AuNPs formed by each modular peptide. We were able to synthesize P2-AuNPs from 2.3 nm to 26.1 nm with an average polydispersity of 22.5%. P3-AuNPs have a smaller size range from 9.8 nm to 13.3 nm with an average polydispersity of 17.8%. Due to the short peptide sequence of P3, nanoparticles smaller than 10 nm were prone to aggregation.

7.3.4 Biocompatibility and Cellular Uptake of Gold Nanoparticles

Nanoparticle toxicity has gained an increasing interest during the past years as the nanotechnology based drugs entered the phase of approval in clinical trials.[318, 319] Cytotoxicity of RGD-AuNPs was investigated with a dose response colorimetric cellular viability assay. MCF7 cells were incubated with serially increasing concentrations of 11 nm RGD-AuNPs (12.5 μg mL^{-1}, 25 μg mL^{-1}, and 50 μg mL^{-1}). After 3 h of incubation, RGD-AuNPs did not elicit any significant loss in cell viability. This result designates the biocompatibility of the RGD peptide coated gold nanoparticles within the concentration range of 50 μg mL^{-1}. Understanding mechanisms of internalization is critical to design nanoparticles precisely for specific purposes. In order to obtain a deep understanding of RGD-AuNP uptake, their internalization mechanisms and pathways were analyzed in MCF7. MCF7 cells have previously been used in RGD based targeting strategies due to its expression of $\alpha_v\beta_3$ integrins on their surface.[320-322] Protein agglomeration on nanoparticle surfaces introduces new epitopes for cellular uptake and therefore enhances endocytosis.[323]

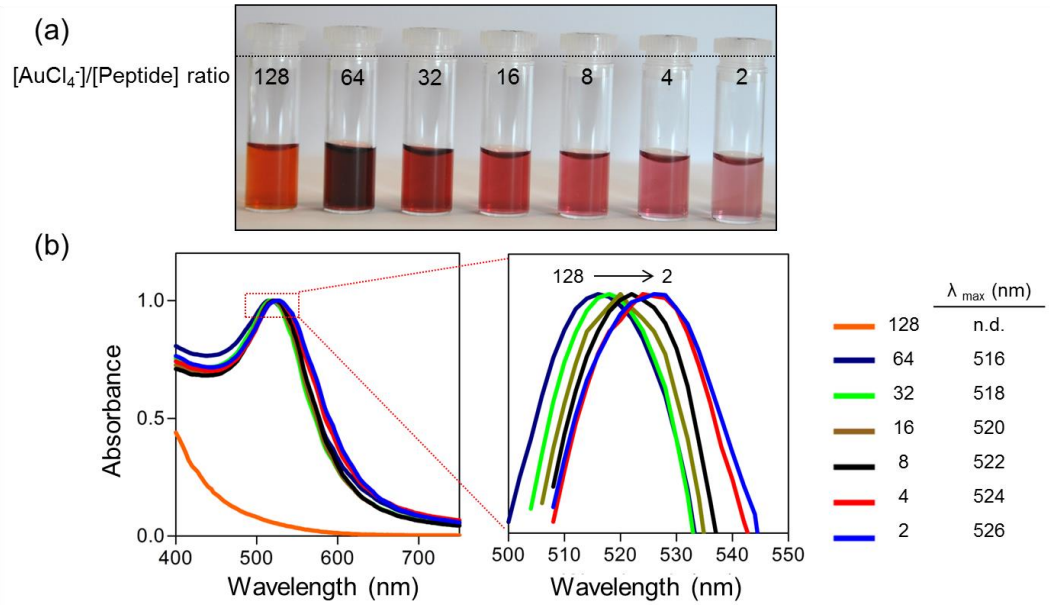

Figure 7.5 Size-controlled one-pot synthesis of RGD-functionalized AuNPs. (a) Size-dependent color development in the reaction tubes. (b) Normalized UV-Vis spectra of RGD-AuNPs showing a consistent red-shift as the particle size increases.

Table 7.1 *Size and surface characteristics of AuNPs: core size, estimated number of gold atoms per nanoparticles, and the number of RGD ligands on each nanoparticle.*

[Au][a] : [RGD peptide]	Core size[b] (nm)	N[c] Au atoms/NP	Ligand/NP[d]
128	2.3 ± 0.7	376	n.a.
64	7.0 ± 1.3	10597	191
32	11.0 ± 1.9	41123	627
16	12.8 ± 2.1	64642	755
8	14.3 ± 3.1	90726	1741
4	15.5 ± 2.9	115053	2115
2	15.0 ± 2.2	105951	2150

[a]Molar ratios of RGD peptide solution and gold solution used to synthesize various sized RGD-AuNPs. [b]Core size was determined by >300 particle counts in each group from TEM images. [c]The average number (N) of gold atoms per nanoparticle was calculated assuming that AuNPs are spherical with a uniform fcc structure with the following equation.[324] $N = 30.89602D^3$. [d]Ligand number per nanoparticle was estimated by the colorimetric staining of peptides.

In order to prevent non-specific enhancement of endocytosis, uptake experiments were performed in serum-free media. Although internalization mechanisms are really diverse, they generally are classified into three main groups: clathrin mediated, lipid raft/caveolae mediated, and macropinocytosis/phagocytosis.[325] Chemical inhibition of these pathways are regularly used in biology.[326] Amilioride, which blocks macropinocytosis; chlorpromazine, which prevents the formation of clathrin coated pits; and filipin III, which inhibits caveole mediated uptake, were incubated with the cells for 1 h.[327] Then solutions containing RGD-AuNPs (25 μg mL^{-1}) and each inhibitor were added to the culture media and incubated for an additional 4 hours.

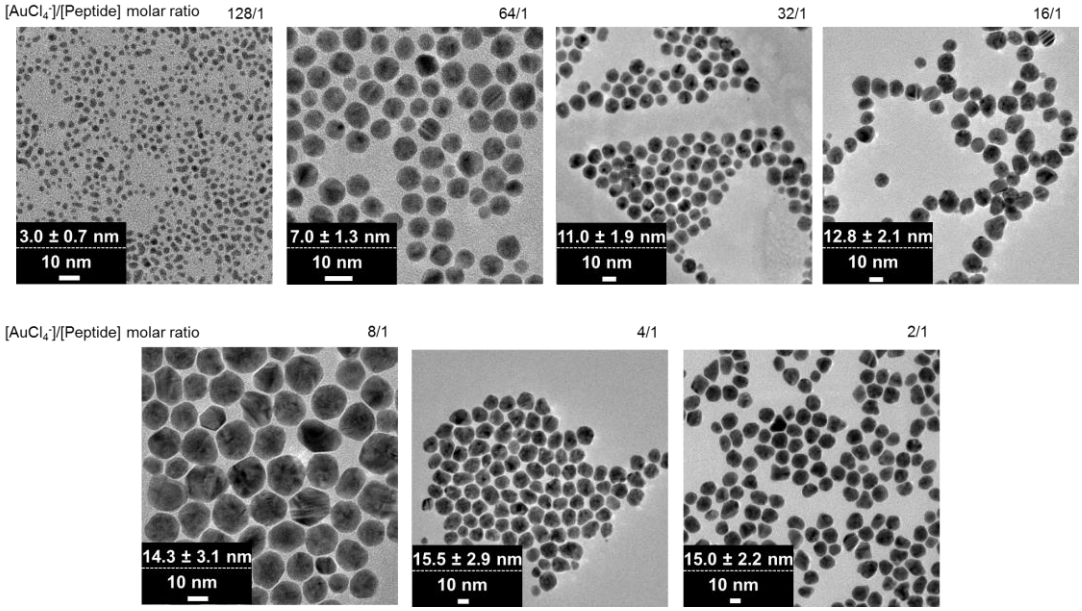

Figure 7.6 TEM images of AuNPs synthesized-stabilized with the RGD peptide. Average size and standard deviations are represented for each image along with their $[AuCl_4^-]$/[Peptide] molar ratios.

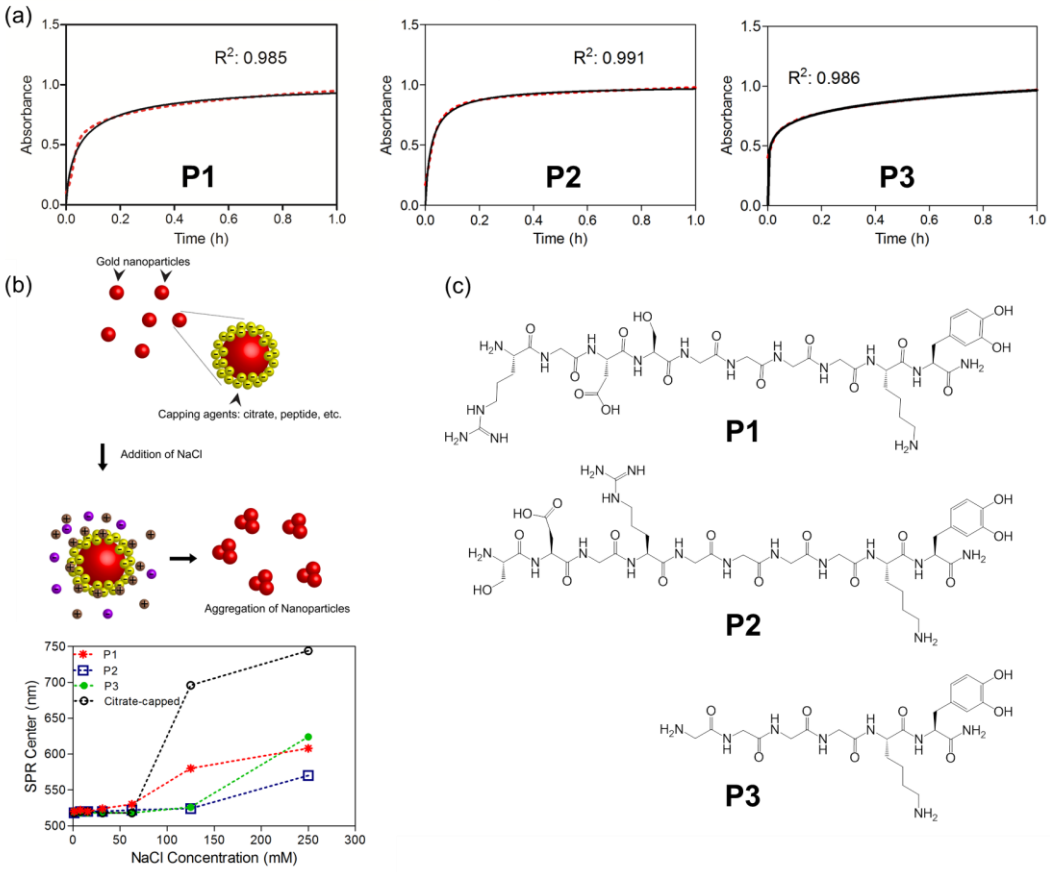

Figure 7.7 (a) Kinetics of AuNP formation with capped with P1 (RGDSG$_4$KDopa-NH$_2$), P2 (SDGRG$_4$KDopa-NH$_2$) and P3 (G$_4$KDopa-NH$_2$) monitored by absorbance at 520 nm. (b) Colloidal stability of peptide-capped nanoparticles under high salt concentrations. (c) Chemical sketches of P1, P2 and P3.

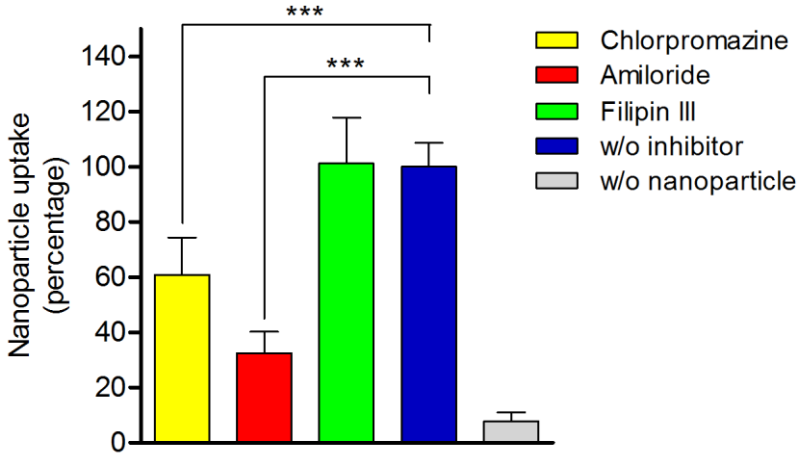

Figure 7.8 Cellular uptake of RGD-AuNPs. ICP-MS analysis of MCF7 cells treated with chemical inhibitors of endocytosis and incubated with 25 µg mL^{-1} of RGD-AuNPs. Cell numbers were normalized to untreated MCF7 cells (n=4). Error bars indicate standard error of the mean (n = 4). Statistical significance was determined using one-way ANOVA with Tukey's Multiple Comparison Test, *** $P < 0.0001$.

The resulting cells were lysed and subjected to ICP-MS for the detection of gold content. Cells that were not exposed to nanoparticles were used as negative control and cells that were not exposed to inhibitors were used as positive control. The quantitative gold analysis revealed that RGD-AuNPs enter into MCF7 cells by several pathways (Figure 7.8). Amilioride and chlorpromazine significantly inhibited 68% and 39% of the nanoparticles uptaken by cells, respectively. This indicates the role of macropinocytosis and clathrin-mediated endocytosis (CME) in RGD-AuNP uptake. filipin III; on the other hand, had no effect on uptake suggesting that cavole-mediated uptake might not be involved in endocytosis of RGD-AuNPs. Collectively these results support the strong involvement of CME and macropinocytosis in the uptake of RGD-AuNPs by MCF7 cells.

7.4 Conclusion

This study describes a simple, effective, and greener way to synthesize gold nanoparticles to circumvent the major obstacles of standard nanoparticle synthesis procedures such as toxic byproducts, extended synthesis times, instability and lack of size control. The synthesis of AuNPs is simplified with the use of Dopa containing multi-tasking RGD peptide structures in a way that no additional stabilizer, toxic surfactant, photo-irradiation or further functionalization is needed. RGD-AuNPs were prepared in an efficient way that the synthesis process is completed within 1 h. Moreover, this synthesis methodology is highly reproducible. These nanoparticles have excellent long-term and high salt concentration stabilities. Controlled synthesis of AuNPs with RGD peptides enables the stable formation of AuNPs in the range of 2 nm to 15 nm. This is within the therapeutic range of AuNPs which have the

potential to be utilized as drug and gene carriers, and in photothermal therapy and screening applications. RGD-AuNPs showed excellent biocompatibility. In conclusion, one can optimize the design of AuNPs for aforementioned applications using modular peptide sequences.

7.5 Experimental Section

7.5.1 Materials

All chemicals used in this study were purchased from Sigma-Aldrich, Invitrogen and Millipore.

7.5.2 Synthesis and Characterization of Modular Peptides

The peptide used in this study was manually synthesized using the fluorenylmethyloxycarbonyl (Fmoc) solid phase peptide synthesis strategy on Rink amide resin. 2 equivalents of aminoacids were activated with 1.95 equivalents of *N,N,N′,N′*-Tetramethyl-*O*-(1*H*-benzotriazol-1-yl)uronium hexafluorophosphate (HBTU), and 3 equivalents of *N*,*N*-Diisopropylethylamine (DIAE) for 1 equivalent of resin were used during aminoacid coupling. For Fmoc removal 20% piperidine/dimethylformamide (DMF) solution was used for 20 min. After each coupling step, 10% acetic anhydride/DMF solution was used to permanently acetylate the unreacted amine groups. A cleavage cocktail containing 95% trifluoroacetic acid (TFA), 2.5% water, and 2.5% triisopropylsilane was used to cleave the protecting groups after the final coupling step. Excess TFA removal was performed by rotary evaporator followed by diethyl ether precipitation overnight. The precipitate was dissolved in ultra-pure water, frozen at -80ºC and lyophilized for 1 week. Synthesized peptides were characterized using Agilent 6530 quadrupole time

of flight (Q-TOF) mass spectrometry with electrospray ionization (ESI) source equipped with reverse-phase HPLC (Figure 7.1).

7.5.3 Synthesis of Gold Nanoparticles

For the synthesis of gold nanoparticles, 600 μM of RGD peptide solution in ultrapure deionized water was added to serially diluted (76.8 mM to 1.2 mM) equal volume of $H[AuCl_4]$ solution. The pH of the solution was adjusted to 10.0 with the addition of 2 M NaOH, vortexed briefly and incubated at 40 ºC for 1 h. Finally the AuNP solutions were filtered through 10,000 Da filter for further characterization and cell culture experiments.

7.5.4 Nanoparticle Characterization

Spectral and kinetic analyses of AuNPs were performed with SpectraMax M5 Multi-Mode Microplate Reader and compared to water blank. Spectral scanning of AuNPs was done in a 250-750 nm range with 2 nm increments using freshly prepared AuNP solutions. Kinetic studies were started as soon as the reaction components were mixed and scanning was performed in 3 min increments at 518 nm until the curve had reached equilibrium. Hydrodynamic diameters of gold nanoparticles were measured with Malvern NanoZS Zeta sizer at room temperature. Auto correction was done as the average of three runs of 10 s each. Transmission electron microscopy (TEM) images of AuNPs were obtained with FEI Tecnai G2 F30 series at 300 kV. The samples were prepared by drop casting AuNP solutions in water on a carbon-coated cupper grid and drying the samples before imaging.

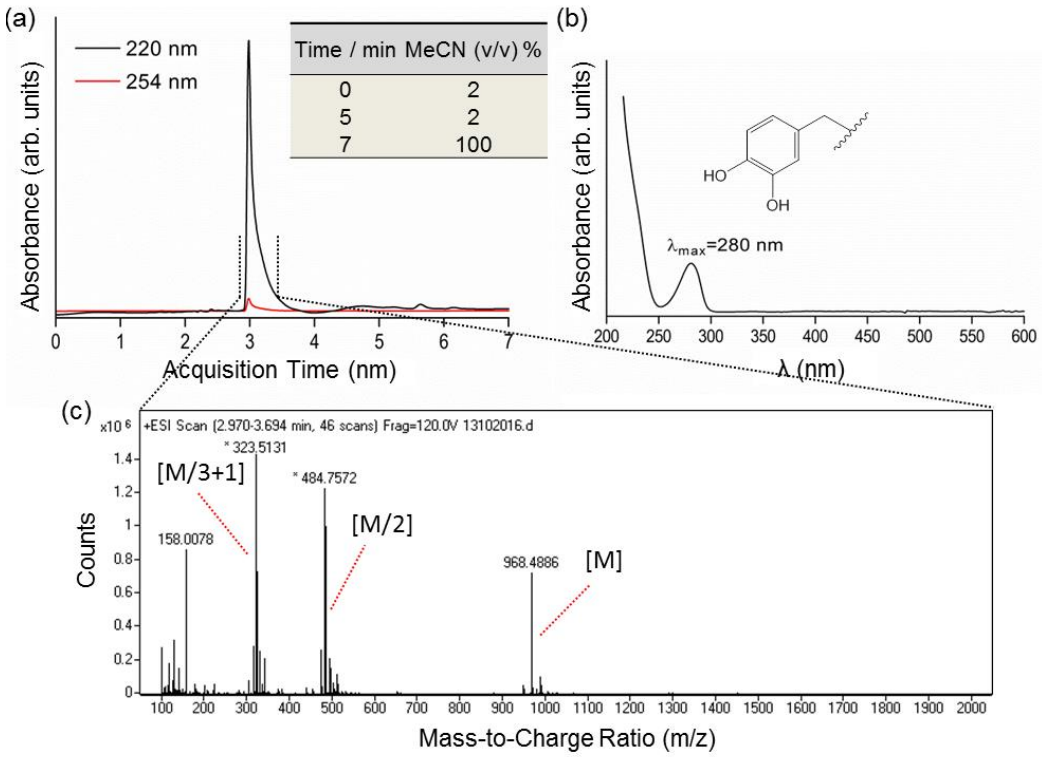

Figure 7.9 (a) Liquid chromatogram, (b) mass spectrum, and (c) UV-Vis analyses of the modular peptide.

7.5.5 Colloidal Stability of Gold Nanoparticles

Citrate capped AuNPs and RGD peptide capped AuNPs in same concentrations were incubated in a series of increasing sodium chloride (NaCl) concentrations (0 to 250 mM). The mixtures were allowed to stabilize for 1 h. Stability of AuNPs was assessed by monitoring the surface plasmon resonance (SPR) bands using SpectraMax M5 Multi-Mode Microplate Reader.

7.5.6 Ligand Density on Gold Nanoparticles

Ligand densities on various sized RGD peptide capped gold nanoparticles were determined by Bio-Rad Protein Assay Kit. It uses a colorimetric reaction where one Cu(II) complexes with four to six peptide bonds and reduces to Cu(I) producing a faint blue-violet color which was detected at 540 nm. Standard curves for peptides were prepared.

7.5.7 Cell Culture

MCF7 cells were maintained in DMEM supplemented with 10% FBS and 1% penicilin/streptomycin in standard cell culture conditions (37 ºC, 5% CO_2, 95% humidity). For AuNP uptake experiments DMEM containing 1% penicilin/streptomycin was used without serum.

7.5.8 Cytotoxicity of Gold Nanoparticles

MCF7 cells were seeded on 24-well plates in complete growth medium until cells reached 80-90% confluency. Cells were treated with varying concentrations of RGD-AuNPs (50 μg mL^{-1}, 25 μg mL^{-1}, 12.5 μg mL^{-1}). Viability experiments of cells after 3 h of incubation with nanoparticles were performed by using *in vitro* toxicity assay kit MTT (Sigma) according to manufacturer's protocol. Cell numbers were

normalized to untreated MCF7 cells. Absorbance of dye was measured at a wavelength of 570 nm with background subtraction at 690 nm by SpectraMax M5 Multi-Mode Microplate Reader.

7.5.9 Cellular Uptake of Gold Nanoparticles

Effect of Endocytosis Inhibitors: MCF7 cells were grown on 96-well plate in standard cell culture conditions until they became 80-90% confluent. The medium was replaced with fresh medium containing either one of the following inhibitors and incubated for 1 h amiloride (5 mM), chlorpromazine (5 μg mL^{-1}), or Filipin III (50 nM). MCF7 cells were incubated for an additional 4 hours with 25 μg mL^{-1} AuNPs in the presence of one of the inhibitors. Uptake was terminated by removing the medium and washing the cells with phosphate buffered saline (PBS, pH 7.4). The cells were then prepared for ICP-MS. MCF7 cells were digested and gold was dissolved in aqua regia overnight. Each sample was diluted to 10 mL with 2% nitric acid. Gold standard solutions (12.5, 6.25, 3.125, 1.56, 0.78 ppb) were prepared and used to obtain a calibration line in order to determine the gold amount in each solution. Gold measurements were performed with Thermo Scientific X Series 2 ICP-MS.

7.5.10 Statistical Analysis

Cell viability experiments were analyzed in triplicates (n = 3) and cellular uptake experiments in quadruplicates (n = 4), with at least two independent repeats. Error bars represent standard error of the mean (SEM). Statistical significance was determined using one-way ANOVA with a confidence interval of $P < 0.05$.

8 CHAPTER 8

CONCLUSION & FUTURE PROSPECTS

Biological materials that can confront environmental constraints inspire developing more efficient strategies to overcome analogous challenges faced in industry and medicine. Therefore, the research activity on bioinspired materials is expected to escalate in the coming years. As the complexity of material demands increase, bioinspired strategies gain more importance for next generation hybrid materials that combine functional moieties from multiple sources. For example, we here proposed that mussel-inspired surface attachment and the extracellular matrix-inspired bioactivity can be integrated in one supramolecular design for developing bioactive cardiovascular stent coatings.

Regarding underwater adhesion, Dopa or catechol-modification has proven to be a very minimalist and practical approach for functionalization of both bulk and nanoparticle surfaces. However, these biomimetic adhesives are far from reaching the exceptional adhesive and mechanical performance of the original glue. In mussels, the hierarchical organization of a number of different types of proteins, including collagens with silk- and elastin-like domains, mfps with varying Dopa and other amino acid contents, determine the overall performance of the final glue. Consequently, it is imperative to elucidate the functional roles of other chemical groups and conditions under which Dopa adhesion is the optimal. For instance, lysine and arginine are abundant residues in major mfps, mfp-1, mfp-3, and mfp-5, imparting a cationic character to the mussel glue.[17, 19, 33, 44, 328] This is not unique to mussels. The sandcastle worm, *Phragmatopoma californica*, lives in a protective

tubular shelter, formed by gluing inorganic particles together with a special glue, which is rich in Dopa and lysine.[240, 329] Although the particular role of having lysine and Dopa together is still unclear, the commonality of this system among natural underwater adhesion systems indicates that an exclusive interaction and/or cooperation between Dopa and lysine may provide a universal solution for surviving the challenging conditions of the seashores. For this reason, many synthetic materials mimicking the mussel adhesion mechanism have focused on utilizing Dopa and Lys (or its positively charged amine side chain) residues together.[19, 26, 44, 57, 273, 330, 331] On the other hand, high positive charge density was shown to be detrimental for surface adhesion.[27] Consequently, designing a novel material should take positive charge density into account for achieving the most efficient adhesion strength.

Phosphate is another intriguing group that is found in the underwater adhesive of sandcastle worm.[35] This group imparts a water-resistant character to sandcastle worm adhesive through interaction with amine, Mg^{2+} and Ca^{2+} cations forming a complex coacervate.[332] Increasing pH rapidly hardens this coacervate within seconds followed by slower covalent curing through catechol oxidation. Therefore, grafting phosphate residues in addition to lysine and Dopa with optimized density and backbone design can develop a new generation of biomimetic adhesives.

Despite their state-of-art organization and functional superiority, operation limits of biological materials are always bounded by the natural selection barrier. In other words, biological materials are just to be good enough to surmount selection barrier. Therefore, there is always room for man-made materials with much superior performance than provided by the biological materials. Nonetheless, the way to reach

this complexity and dynamic organization is through better understanding of the available biological systems.

BIBLIOGRAPHY

1. Sanchez, C., Arribart, H. & Guille, M.M. Biomimetism and bioinspiration as tools for the design of innovative materials and systems. *Nat Mater* **4**, 277-288 (2005).
2. Wang, C.S. & Stewart, R.J. Localization of the bioadhesive precursors of the sandcastle worm, Phragmatopoma californica (Fewkes). *The Journal of Experimental Biology* **215**, 351-361 (2012).
3. Kaur, S., Weerasekare, G.M. & Stewart, R.J. Multiphase Adhesive Coacervates Inspired by the Sandcastle Worm. *ACS Applied Materials & Interfaces* **3**, 941-944 (2011).
4. Winslow, B.D., Shao, H., Stewart, R.J. & Tresco, P.A. Biocompatibility of adhesive complex coacervates modeled after the sandcastle glue of Phragmatopoma californica for craniofacial reconstruction. *Biomaterials* **31**, 9373-9381 (2010).
5. Sun, C., Fantner, G.E., Adams, J., Hansma, P.K. & Waite, J.H. The role of calcium and magnesium in the concrete tubes of the sandcastle worm. *Journal of Experimental Biology* **210**, 1481-1488 (2007).
6. Waite, J.H. Adhesion à la Moule. *Integrative and Comparative Biology* **42**, 1172-1180 (2002).
7. Waite, J.H. & Broomell, C.C. Changing environments and structure–property relationships in marine biomaterials. *The Journal of Experimental Biology* **215**, 873-883 (2012).
8. Waite, J.H. & Qin, X. Polyphosphoprotein from the Adhesive Pads of Mytilus edulis†. *Biochemistry* **40**, 2887-2893 (2001).
9. Jonker, J.-L., von Byern, J., Flammang, P., Klepal, W. & Power, A.M. Unusual adhesive production system in the barnacle Lepas anatifera: An ultrastructural and histochemical investigation. *Journal of Morphology*, **273**, 1377-1391 (2012).
10. Burden, D.K. *et al.* Barnacle Balanus amphitrite Adheres by a Stepwise Cementing Process. *Langmuir* (2012).
11. Phang, I.Y., Aldred, N., Clare, A.S. & Vancso, G.J. Towards a nanomechanical basis for temporary adhesion in barnacle cyprids (Semibalanus balanoides). *Journal of The Royal Society Interface* **5**, 397-402 (2008).
12. Stewart, R.J., Ransom, T.C. & Hlady, V. Natural underwater adhesives. *Journal of Polymer Science Part B: Polymer Physics* **49**, 757-771 (2011).
13. Richards, R.G., Moriarty, T.F., Miclau, T., McClellan, R.T. & Grainger, D.W. Advances in Biomaterials and Surface Technologies. *Journal of Orthopaedic Trauma* **26**, 703-707 (2012).
14. Avila, G., Misch, K., Galindo-Moreno, P. & Wang, H.-L. Implant Surface Treatment Using Biomimetic Agents. *Implant Dentistry* **18**, 17-26 (2009).
15. Liu, Y., Li, J.P., Hunziker, E.B. & de Groot, K. Incorporation of growth factors into medical devices via biomimetic coatings. *Philosophical*

Transactions of the Royal Society A: Mathematical, Physical and Engineering Sciences **364**, 233-248 (2006).
16. Waite, J.H., Andersen, N.H., Jewhurst, S. & Sun, C. Mussel Adhesion: Finding the Tricks Worth Mimicking. *The Journal of Adhesion* **81**, 297-317 (2005).
17. Lee, B.P., Messersmith, P.B., Israelachvili, J.N. & Waite, J.H. Mussel-Inspired Adhesives and Coatings. *Annual Review of Materials Research* **41**, 99-132 (2011).
18. Crisp, D.J., Walker, G., Young, G.A. & Yule, A.B. Adhesion and substrate choice in mussels and barnacles. *Journal of Colloid and Interface Science* **104**, 40-50 (1985).
19. Lee, H., Dellatore, S.M., Miller, W.M. & Messersmith, P.B. Mussel-Inspired Surface Chemistry for Multifunctional Coatings. *Science* **318**, 426-430 (2007).
20. Harrington, M.J., Masic, A., Holten-Andersen, N., Waite, J.H. & Fratzl, P. Iron-Clad Fibers: A Metal-Based Biological Strategy for Hard Flexible Coatings. *Science* **328**, 216-220 (2010).
21. Lee, H., Scherer, N.F. & Messersmith, P.B. Single-molecule mechanics of mussel adhesion. *Proceedings of the National Academy of Sciences* **103**, 12999-13003 (2006).
22. Hamming, L.M., Fan, X.W., Messersmith, P.B. & Brinson, L.C. Mimicking mussel adhesion to improve interfacial properties in composites. *Composites Science and Technology* **68**, 2042-2048 (2008).
23. Rief, M., Clausen-Schaumann, H. & Gaub, H.E. Sequence-dependent mechanics of single DNA molecules. *Nat Struct Mol Biol* **6**, 346-349 (1999).
24. Monahan, J. & Wilker, J.J. Cross-Linking the Protein Precursor of Marine Mussel Adhesives: Bulk Measurements and Reagents for Curing. *Langmuir* **20**, 3724-3729 (2004).
25. Xu, H. *et al.* Competition between Oxidation and Coordination in Cross-Linking of Polystyrene Copolymer Containing Catechol Groups. *ACS Macro Letters* **1**, 457-460 (2012).
26. Lee, H., Rho, J. & Messersmith, P.B. Facile Conjugation of Biomolecules onto Surfaces via Mussel Adhesive Protein Inspired Coatings. *Advanced Materials* **21**, 431-434 (2009).
27. Holten-Andersen, N. & Waite, J.H. Mussel-designed Protective Coatings for Compliant Substrates. *Journal of Dental Research* **87**, 701-709 (2008).
28. Carrington, E. The Ecomechanics of Mussel Attachment: From Molecules to Ecosystems1. *Integrative and Comparative Biology* **42**, 846-852 (2002).
29. Gosline, J. *et al.* Elastic proteins: biological roles and mechanical properties. *Philosophical Transactions of the Royal Society of London. Series B: Biological Sciences* **357**, 121-132 (2002).
30. Waite, J.H., Lichtenegger, H.C., Stucky, G.D. & Hansma, P. Exploring Molecular and Mechanical Gradients in Structural Bioscaffolds†. *Biochemistry* **43**, 7653-7662 (2004).
31. Waite, J.H., Vaccaro, E., Sun, C. & Lucas, J.M. Elastomeric Gradients: A Hedge against Stress Concentration in Marine Holdfasts? *Philosophical Transactions: Biological Sciences* **357**, 143-153 (2002).

32. Waite, J.H. Evidence for a repeating 3,4-dihydroxyphenylalanine- and hydroxyproline-containing decapeptide in the adhesive protein of the mussel, Mytilus edulis L. *Journal of Biological Chemistry* **258**, 2911-2915 (1983).
33. Papov, V.V., Diamond, T.V., Biemann, K. & Waite, J.H. Hydroxyarginine-containing Polyphenolic Proteins in the Adhesive Plaques of the Marine Mussel Mytilus edulis. *Journal of Biological Chemistry* **270**, 20183-20192 (1995).
34. Cha, H.J., Hwang, D.S. & Lim, S. Development of bioadhesives from marine mussels. *Biotechnology Journal* **3**, 631-638 (2008).
35. Zhao, H. & Waite, J.H. Linking Adhesive and Structural Proteins in the Attachment Plaque of Mytilus californianus. *Journal of Biological Chemistry* **281**, 26150-26158 (2006).
36. Zhao, H. & Waite, J.H. Proteins in load-bearing junctions: the histidine-rich metal-binding protein of mussel byssus. *Biochemistry* **45**, 14223-14231 (2006).
37. Avdeef, A., Sofen, S.R., Bregante, T.L. & Raymond, K.N. Coordination chemistry of microbial iron transport compounds. 9. Stability constants for catechol models of enterobactin. *Journal of the American Chemical Society* **100**, 5362-5370 (1978).
38. Holten-Andersen, N. *et al.* pH-induced metal-ligand cross-links inspired by mussel yield self-healing polymer networks with near-covalent elastic moduli. *Proceedings of the National Academy of Sciences* **108**, 2651-2655 (2011).
39. Holten-Andersen, N., Fantner, G.E., Hohlbauch, S., Waite, J.H. & Zok, F.W. Protective coatings on extensible biofibres. *Nat Mater* **6**, 669-672 (2007).
40. Inoue, K., Takeuchi, Y., Miki, D. & Odo, S. Mussel Adhesive Plaque Protein Gene Is a Novel Member of Epidermal Growth Factor-like Gene Family. *Journal of Biological Chemistry* **270**, 6698-6701 (1995).
41. Wilker, J.J. Biomaterials: Redox and adhesion on the rocks. *Nat Chem Biol* **7**, 579-580 (2011).
42. Burzio, L.A. & Waite, J.H. Reactivity of peptidyl-tyrosine to hydroxylation and cross-linking. *Protein Science* **10**, 735-740 (2001).
43. Burzio, L.A. & Waite, J.H. Cross-Linking in Adhesive Quinoproteins: Studies with Model Decapeptides†. *Biochemistry* **39**, 11147-11153 (2000).
44. White, J.D. & Wilker, J.J. Underwater Bonding with Charged Polymer Mimics of Marine Mussel Adhesive Proteins. *Macromolecules* **44**, 5085-5088 (2011).
45. Parks, G.A. The Isoelectric Points of Solid Oxides, Solid Hydroxides, and Aqueous Hydroxo Complex Systems. *Chemical Reviews* **65**, 177-198 (1965).
46. Schramm, L.L., Mannhardt, K. & Novosad, J.J. Electrokinetic properties of reservoir rock particles. *Colloids and Surfaces* **55**, 309-331 (1991).
47. Warner, S.C. & Waite, J.H. Expression of multiple forms of an adhesive plaque protein in an individual mussel, Mytilus edulis. *Marine Biology* **134**, 729-734 (1999).
48. Zhao, H. & Waite, J.H. Proteins in Load-Bearing Junctions: The Histidine-Rich Metal-Binding Protein of Mussel Byssus†,‡. *Biochemistry* **45**, 14223-14231 (2006).

49. Yu, J. *et al.* Mussel protein adhesion depends on interprotein thiol-mediated redox modulation. *Nat Chem Biol* **7**, 588-590 (2011).
50. Yu, J., Wei, W., Danner, E., Israelachvili, J.N. & Waite, J.H. Effects of Interfacial Redox in Mussel Adhesive Protein Films on Mica. *Advanced Materials* **23**, 2362-2366 (2011).
51. Silverman, H. & Roberto, F. Understanding Marine Mussel Adhesion. *Marine Biotechnology* **9**, 661-681 (2007).
52. Hwang, D.S., Yoo, H.J., Jun, J.H., Moon, W.K. & Cha, H.J. Expression of Functional Recombinant Mussel Adhesive Protein Mgfp-5 in Escherichia coli. *Applied and Environmental Microbiology* **70**, 3352-3359 (2004).
53. Filpula, D.R., Lee, S.-M., Link, R.P., Strausberg, S.L. & Strausberg, R.L. Structural and Functional Repetition in a Marine Mussel Adhesive Protein. *Biotechnology Progress* **6**, 171-177 (1990).
54. Salerno, A.J. & Goldberg, I. Cloning, expression, and characterization of a synthetic analog to the bioadhesive precursor protein of the sea mussel <i>Mytilus edulis</i&gt. *Applied Microbiology and Biotechnology* **39**, 221-226 (1993).
55. Kitamura, M. *et al.* Expression of a model peptide of a marine mussel adhesive protein in Escherichia coli and characterization of its structural and functional properties. *Journal of Polymer Science Part A: Polymer Chemistry* **37**, 729-736 (1999).
56. Choi, B.-H. *et al.* Cell behavior on extracellular matrix mimic materials based on mussel adhesive protein fused with functional peptides. *Biomaterials* **31**, 8980-8988 (2010).
57. Ceylan, H., Tekinay, A.B. & Guler, M.O. Selective adhesion and growth of vascular endothelial cells on bioactive peptide nanofiber functionalized stainless steel surface. *Biomaterials* **32**, 8797-8805 (2011).
58. Ceylan, H., Kocabey, S., Tekinay, A.B. & Guler, M.O. Surface-adhesive and osteogenic self-assembled peptide nanofibers for bioinspired functionalization of titanium surfaces. *Soft Matter* **8**, 3929-3937 (2012).
59. Dalsin, J.L. & Messersmith, P.B. Bioinspired antifouling polymers. *Materials Today* **8**, 38-46 (2005).
60. Dalsin, J.L. *et al.* Protein Resistance of Titanium Oxide Surfaces Modified by Biologically Inspired mPEG−DOPA. *Langmuir* **21**, 640-646 (2004).
61. Wach, J.-Y. *et al.* Protein-Resistant Surfaces through Mild Dopamine Surface Functionalization. *Chemistry – A European Journal* **14**, 10579-10584 (2008).
62. Ryu, J.H. *et al.* Catechol-Functionalized Chitosan/Pluronic Hydrogels for Tissue Adhesives and Hemostatic Materials. *Biomacromolecules* **12**, 2653-2659 (2011).
63. Lee, H., Lee, B.P. & Messersmith, P.B. A reversible wet/dry adhesive inspired by mussels and geckos. *Nature* **448**, 338-341 (2007).
64. Ling, D. *et al.* Multiple-Interaction Ligands Inspired by Mussel Adhesive Protein: Synthesis of Highly Stable and Biocompatible Nanoparticles. *Angewandte Chemie International Edition* **50**, 11360-11365 (2011).
65. Kim, E. *et al.* Biomimetic Approach to Confer Redox Activity to Thin Chitosan Films. *Advanced Functional Materials* **20**, 2683-2694 (2010).

66. Hong, S. *et al.* Non-Covalent Self-Assembly and Covalent Polymerization Co-Contribute to Polydopamine Formation. *Advanced Functional Materials*, DOI: 10.1002/adfm.201201156 (2012).
67. Ryu, J., Ku, S.H., Lee, H. & Park, C.B. Mussel-Inspired Polydopamine Coating as a Universal Route to Hydroxyapatite Crystallization. *Advanced Functional Materials* **20**, 2132-2139 (2010).
68. Wei, H. *et al.* Compact Zwitterion-Coated Iron Oxide Nanoparticles for Biological Applications. *Nano Letters* **12**, 22-25 (2011).
69. Kang, S.M. *et al.* One-Step Multipurpose Surface Functionalization by Adhesive Catecholamine. *Advanced Functional Materials* **22**, 2949-2955 (2012).
70. Oliveira Martins, J., Gonand, F., Antolín, P., De la Maisonneuve, C. & Yoo, K.-Y. (Paris Dauphine University, 2005).
71. Hynes, R.O. The extracellular matrix: Not just pretty fibrils. *Science* **326**, 1216-1219 (2009).
72. Watt, F.M. & Huck, W.T.S. Role of the extracellular matrix in regulating stem cell fate. *Nat Rev Mol Cell Biol* **14**, 467-473 (2013).
73. Dvir, T., Timko, B.P., Kohane, D.S. & Langer, R. Nanotechnological strategies for engineering complex tissues. *Nat Nanotechnol* **6**, 13-22 (2011).
74. Frantz, C., Stewart, K.M. & Weaver, V.M. The extracellular matrix at a glance. *Journal of Cell Science* **123**, 4195-4200 (2010).
75. Gordon, M. & Hahn, R. Collagens. *Cell and Tissue Research* **339**, 247-257 (2010).
76. Walters, B.D. & Stegemann, J.P. Strategies for directing the structure and function of three-dimensional collagen biomaterials across length scales. *Acta Biomater* **10**, 1488-1501 (2014).
77. Myllyharju, J. & Kivirikko, K.I. Collagens, modifying enzymes and their mutations in humans, flies and worms. *Trends Genet* **20**, 33-43 (2004).
78. Chowdhury, F. *et al.* Material properties of the cell dictate stress-induced spreading and differentiation in embryonic stem cells. *Nat Mater* **9**, 82-88 (2010).
79. Engler, A.J., Sen, S., Sweeney, H.L. & Discher, D.E. Matrix Elasticity Directs Stem Cell Lineage Specification. *Cell* **126**, 677-689 (2006).
80. Ouasti, S. *et al.* Network connectivity, mechanical properties and cell adhesion for hyaluronic acid/PEG hydrogels. *Biomaterials* **32**, 6456-6470 (2011).
81. Taubenberger, A.V., Woodruff, M.A., Bai, H., Muller, D.J. & Hutmacher, D.W. The effect of unlocking RGD-motifs in collagen I on pre-osteoblast adhesion and differentiation. *Biomaterials* **31**, 2827-2835 (2010).
82. Pierschbacher, M.D. & Ruoslahti, E. Variants of the cell recognition site of fibronectin that retain attachment-promoting activity. *Proceedings of the National Academy of Sciences* **81**, 5985-5988 (1984).
83. Puklin-Faucher, E. & Sheetz, M.P. The mechanical integrin cycle. *Journal of Cell Science* **122**, 179-186 (2009).
84. Grashoff, C. *et al.* Measuring mechanical tension across vinculin reveals regulation of focal adhesion dynamics. *Nature* **466**, 263-266 (2010).

85. Hynes, R.O. Integrins: Bidirectional, Allosteric Signaling Machines. *Cell* **110**, 673-687 (2002).
86. Legate, K.R., Wickström, S.A. & Fässler, R. Genetic and cell biological analysis of integrin outside-in signaling. *Genes & Development* **23**, 397-418 (2009).
87. Heino, J. The collagen receptor integrins have distinct ligand recognition and signaling functions. *Matrix Biology* **19**, 319-323 (2000).
88. Miller, T., Goude, M.C., McDevitt, T.C. & Temenoff, J.S. Molecular engineering of glycosaminoglycan chemistry for biomolecule delivery. *Acta Biomater* **10**, 1705-1719 (2014).
89. Bishop, J.R., Schuksz, M. & Esko, J.D. Heparan sulphate proteoglycans fine-tune mammalian physiology. *Nature* **446**, 1030-1037 (2007).
90. Seyrek, E. & Dubin, P. Glycosaminoglycans as polyelectrolytes. *Adv Colloid Interface Sci* **158**, 119-129 (2010).
91. Jean-Marie, L. Supramolecular chemistry: from molecular information towards self-organization and complex matter. *Reports on Progress in Physics* **67**, 249 (2004).
92. Antzutkin, O.N. *et al.* Hydrogen bonding in Alzheimer's amyloid-beta fibrils probed by 15N{17O} REAPDOR solid-state NMR spectroscopy. *Angew Chem Int Ed Engl* **51**, 10289-10292 (2012).
93. Toksöz, S. & Guler, M.O. Self-assembled peptidic nanostructures. *Nano Today* **4**, 458-469 (2009).
94. Ke, Y., Ong, L.L., Shih, W.M. & Yin, P. Three-Dimensional Structures Self-Assembled from DNA Bricks. *Science* **338**, 1177-1183 (2012).
95. Whitesides, G.M. *et al.* Noncovalent Synthesis: Using Physical-Organic Chemistry To Make Aggregates. *Accounts of Chemical Research* **28**, 37-44 (1995).
96. Genot, A.J., Bath, J. & Turberfield, A.J. Combinatorial Displacement of DNA Strands: Application to Matrix Multiplication and Weighted Sums. *Angewandte Chemie* **125**, 1227-1230 (2013).
97. Aida, T., Meijer, E.W. & Stupp, S.I. Functional Supramolecular Polymers. *Science* **335**, 813-817 (2012).
98. Zhang, S. Fabrication of novel biomaterials through molecular self-assembly. *Nat Biotech* **21**, 1171-1178 (2003).
99. Cui, H., Webber, M.J. & Stupp, S.I. Self-assembly of peptide amphiphiles: From molecules to nanostructures to biomaterials. *Peptide Science* **94**, 1-18 (2010).
100. Lin, B.F., Missirlis, D., Krogstad, D.V. & Tirrell, M. Structural effects and lipid membrane interactions of the pH-responsive GALA peptide with fatty acid acylation. *Biochemistry* **51**, 4658-4668 (2012).
101. Newcomb, C.J. *et al.* Cell death versus cell survival instructed by supramolecular cohesion of nanostructures. *Nat Commun* **5** (2014).
102. Hartgerink, J.D., Beniash, E. & Stupp, S.I. Self-Assembly and Mineralization of Peptide-Amphiphile Nanofibers. *Science* **294**, 1684-1688 (2001).
103. Guler, M.O. & Stupp, S.I. A Self-Assembled Nanofiber Catalyst for Ester Hydrolysis. *Journal of the American Chemical Society* **129**, 12082-12083 (2007).

104. Dvir, T., Timko, B.P., Kohane, D.S. & Langer, R. Nanotechnological strategies for engineering complex tissues. *Nat Nano* **6**, 13-22 (2011).
105. Sargeant, T.D., Oppenheimer, S.M., Dunand, D.C. & Stupp, S.I. Titanium foam-bioactive nanofiber hybrids for bone regeneration. *Journal of Tissue Engineering and Regenerative Medicine* **2**, 455-462 (2008).
106. Silva, G.A. *et al.* Selective Differentiation of Neural Progenitor Cells by High-Epitope Density Nanofibers. *Science* **303**, 1352-1355 (2004).
107. Aggeli, A. *et al.* Hierarchical self-assembly of chiral rod-like molecules as a model for peptide beta -sheet tapes, ribbons, fibrils, and fibers. *Proc Natl Acad Sci U S A* **98**, 11857-11862 (2001).
108. Collier, J.H. & Messersmith, P.B. Self-Assembling Polymer–Peptide Conjugates: Nanostructural Tailoring. *Advanced Materials* **16**, 907-910 (2004).
109. Mammadov, B., Mammadov, R., Guler, M.O. & Tekinay, A.B. Cooperative effect of heparan sulfate and laminin mimetic peptide nanofibers on the promotion of neurite outgrowth. *Acta Biomaterialia* **8**, 2077-2086 (2012).
110. Ceylan, H. *et al.* Size-controlled conformal nanofabrication of biotemplated three-dimensional TiO_2 and ZnO nanonetworks. *Sci. Rep.* **3** (2013).
111. Cui, H., Muraoka, T., Cheetham, A.G. & Stupp, S.I. Self-Assembly of Giant Peptide Nanobelts. *Nano Letters* **9**, 945-951 (2009).
112. Dong, H., Paramonov, S.E., Aulisa, L., Bakota, E.L. & Hartgerink, J.D. Self-Assembly of Multidomain Peptides: Balancing Molecular Frustration Controls Conformation and Nanostructure. *Journal of the American Chemical Society* **129**, 12468-12472 (2007).
113. Paramonov, S.E., Jun, H.-W. & Hartgerink, J.D. Self-Assembly of Peptide−Amphiphile Nanofibers: The Roles of Hydrogen Bonding and Amphiphilic Packing. *Journal of the American Chemical Society* **128**, 7291-7298 (2006).
114. Kocabey, S., Ceylan, H., Tekinay, A.B. & Guler, M.O. Glycosaminoglycan mimetic peptide nanofibers promote mineralization by osteogenic cells. *Acta Biomaterialia* **9**, 9075-9085 (2013).
115. Ustun, S., Tombuloglu, A., Kilinc, M., Guler, M.O. & Tekinay, A.B. Growth and Differentiation of Prechondrogenic Cells on Bioactive Self-Assembled Peptide Nanofibers. *Biomacromolecules* **14**, 17-26 (2012).
116. Mammadov, R. *et al.* Heparin Mimetic Peptide Nanofibers Promote Angiogenesis. *Biomacromolecules* **12**, 3508-3519 (2011).
117. Garg, S. & Serruys, P.W. Coronary Stents: Current Status. *Journal of the American College of Cardiology* **56**, S1-S42 (2010).
118. Serruys, P.W. *et al.* Angiographic Follow-up after Placement of a Self-Expanding Coronary-Artery Stent. *New England Journal of Medicine* **324**, 13-17 (1991).
119. van Domburg, R.T. *et al.* Long term outcome after coronary stent implantation: a 10 year single centre experience of 1000 patients. *Heart* **82 Suppl 2**, Ii27-34 (1999).
120. Hoffmann, R. *et al.* Patterns and mechanisms of in-stent restenosis. A serial intravascular ultrasound study. *Circulation* **94**, 1247-1254 (1996).

121. Karas, S.P. *et al.* Coronary intimal proliferation after balloon injury and stenting in swing: An animal model of restenosis. *Journal of the American College of Cardiology* **20**, 467-474 (1992).
122. Moses, J.W. *et al.* Sirolimus-eluting stents versus standard stents in patients with stenosis in a native coronary artery. *N Engl J Med* **349**, 1315-1323 (2003).
123. Daemen, J. *et al.* Three-Year Clinical Follow-Up of the Unrestricted Use of Sirolimus-Eluting Stents as Part of the Rapamycin-Eluting Stent Evaluated at Rotterdam Cardiology Hospital (RESEARCH) Registry. *The American Journal of Cardiology* **98**, 895-901 (2006).
124. McFadden, E.P. *et al.* Late thrombosis in drug-eluting coronary stents after discontinuation of antiplatelet therapy. *The Lancet* **364**, 1519-1521.
125. Finn, A.V. *et al.* Pathological correlates of late drug-eluting stent thrombosis: strut coverage as a marker of endothelialization. *Circulation* **115**, 2435-2441 (2007).
126. Awata, M. *et al.* Serial angioscopic evidence of incomplete neointimal coverage after sirolimus-eluting stent implantation: comparison with bare-metal stents. *Circulation* **116**, 910-916 (2007).
127. Hubbell, J.A., Massia, S.P., Desai, N.P. & Drumheller, P.D. Endothelial Cell-Selective Materials for Tissue Engineering in the Vascular Graft Via a New Receptor. *Nat Biotech* **9**, 568-572 (1991).
128. Massia, S.P. & Hubbell, J.A. Vascular endothelial cell adhesion and spreading promoted by the peptide REDV of the IIICS region of plasma fibronectin is mediated by integrin alpha 4 beta 1. *J Biol Chem* **267**, 14019-14026 (1992).
129. Fant, C. *et al.* Investigation of Adsorption and Cross-Linking of a Mussel Adhesive Protein Using Attenuated Total Internal Reflection Fourier Transform Infrared Spectroscopy (ATR-FTIR). *The Journal of Adhesion* **86**, 25-38 (2010).
130. Fant, C., Sott, K., Elwing, H. & Hook, F. Adsorption behavior and enzymatically or chemically induced cross-linking of a mussel adhesive protein. *Biofouling* **16**, 119-132 (2000).
131. Kushwaha, M. *et al.* A nitric oxide releasing, self assembled peptide amphiphile matrix that mimics native endothelium for coating implantable cardiovascular devices. *Biomaterials* **31**, 1502-1508 (2010).
132. Tysseling-Mattiace, V.M. *et al.* Self-Assembling Nanofibers Inhibit Glial Scar Formation and Promote Axon Elongation after Spinal Cord Injury. *The Journal of Neuroscience* **28**, 3814-3823 (2008).
133. Srinivasan, R., Marchant, R.E. & Gupta, A.S. In vitro and *in vivo* platelet targeting by cyclic RGD-modified liposomes. *J Biomed Mater Res A* **93**, 1004-1015 (2010).
134. Niece, K.L., Hartgerink, J.D., Donners, J.J.J.M. & Stupp, S.I. Self-Assembly Combining Two Bioactive Peptide-Amphiphile Molecules into Nanofibers by Electrostatic Attraction. *Journal of the American Chemical Society* **125**, 7146-7147 (2003).
135. Fischell, T.A. Polymer coatings for stents. Can we judge a stent by its cover? *Circulation* **94**, 1494-1495 (1996).

136. Suci, P.A. & Geesey, G.G. Comparison of adsorption behavior of two Mytilus edulis foot proteins on three surfaces. *Colloids Surf B Biointerfaces* **22**, 159-168 (2001).
137. Suci, P.A. & Geesey, G.G. Influence of Sodium Periodate and Tyrosinase on Binding of Alginate to Adlayers of Mytilus edulis Foot Protein 1. *J Colloid Interface Sci* **230**, 340-348 (2000).
138. Olivieri, M.P., Loomis, R.E., Meyer, A.E. & Baier, R.E. Surface characterization of mussel adhesive protein films. *Journal of Adhesion Science and Technology* **4**, 197-204 (1990).
139. Olivieri, M.P., Rittle, K.H., Tweden, K.S. & Loomis, R.E. Comparative biophysical study of adsorbed calf serum, fetal bovine serum and mussel adhesive protein films. *Biomaterials* **13**, 201-208 (1992).
140. Chung, T.-W., Liu, D.-Z., Wang, S.-Y. & Wang, S.-S. Enhancement of the growth of human endothelial cells by surface roughness at nanometer scale. *Biomaterials* **24**, 4655-4661 (2003).
141. Wu, Y., Zitelli, J.P., TenHuisen, K.S., Yu, X. & Libera, M.R. Differential response of Staphylococci and osteoblasts to varying titanium surface roughness. *Biomaterials* **32**, 951-960 (2011).
142. Ranjan, A. & Webster, T.J. Increased endothelial cell adhesion and elongation on micron-patterned nano-rough poly(dimethylsiloxane) films. *Nanotechnology* **20**, 305102 (2009).
143. Salloum, D.S., Olenych, S.G., Keller, T.C. & Schlenoff, J.B. Vascular smooth muscle cells on polyelectrolyte multilayers: hydrophobicity-directed adhesion and growth. *Biomacromolecules* **6**, 161-167 (2005).
144. Joner, M. *et al.* Pathology of Drug-Eluting Stents in Humans: Delayed Healing and Late Thrombotic Risk. *Journal of the American College of Cardiology* **48**, 193-202 (2006).
145. Baudin, B., Bruneel, A., Bosselut, N. & Vaubourdolle, M. A protocol for isolation and culture of human umbilical vein endothelial cells. *Nat Protoc* **2**, 481-485 (2007).
146. Laing, P.G., Ferguson, A.B., Jr. & Hodge, E.S. Tissue reaction in rabbit muscle exposed to metallic implants. *J Biomed Mater Res* **1**, 135-149 (1967).
147. Hayashi, K., Uenoyama, K., Matsuguchi, N. & Sugioka, Y. Quantitative analysis of *in vivo* tissue responses to titanium-oxide- and hydroxyapatite-coated titanium alloy. *J Biomed Mater Res* **25**, 515-523 (1991).
148. Spoerke, E.D. *et al.* A bioactive titanium foam scaffold for bone repair. *Acta Biomater* **1**, 523-533 (2005).
149. Spoerke, E.D. & Stupp, S.I. Synthesis of a poly(L-lysine)-calcium phosphate hybrid on titanium surfaces for enhanced bioactivity. *Biomaterials* **26**, 5120-5129 (2005).
150. Hayashi, K., Inadome, T., Tsumura, H., Nakashima, Y. & Sugioka, Y. Effect of surface roughness of hydroxyapatite-coated titanium on the bone-implant interface shear strength. *Biomaterials* **15**, 1187-1191 (1994).
151. Lavenus, S., Louarn, G. & Layrolle, P. Nanotechnology and Dental Implants. *International Journal of Biomaterials* **2010** (2010).

152. Schliephake, H. *et al.* Functionalization of dental implant surfaces using adhesion molecules. *Journal of Biomedical Materials Research Part B: Applied Biomaterials* **73B**, 88-96 (2005).
153. Morra, M. Biochemical modification of titanium surfaces: peptides and ECM proteins. *Eur Cell Mater* **12**, 1-15 (2006).
154. Sargeant, T.D. *et al.* Hybrid bone implants: self-assembly of peptide amphiphile nanofibers within porous titanium. *Biomaterials* **29**, 161-171 (2008).
155. Petrie, T.A. *et al.* Multivalent integrin-specific ligands enhance tissue healing and biomaterial integration. *Sci Transl Med* **2**, 45ra60 (2010).
156. Mata, A. *et al.* Bone regeneration mediated by biomimetic mineralization of a nanofiber matrix. *Biomaterials* **31**, 6004-6012 (2010).
157. Kraai, T., Brown, C., Neeff, M. & Fisher, K. Complications of bone-anchored hearing aids in pediatric patients. *Int J Pediatr Otorhinolaryngol* **75**, 749-753 (2011).
158. Vale, F.M. *et al.* Acrylic bone cement induces the production of free radicals by cultured human fibroblasts. *Biomaterials* **18**, 1133-1135 (1997).
159. Mostardi, R.A., Meerbaum, S.O., Kovacik, M.W. & Gradisar, I.A., Jr. In vitro response of human fibroblasts to commercially pure titanium. *J Biomed Mater Res* **47**, 60-64 (1999).
160. Pap, T. *et al.* Osteoclast-independent bone resorption by fibroblast-like cells. *Arthritis Res Ther* **5**, R163-173 (2003).
161. Dee, K.C., Andersen, T.T. & Bizios, R. Design and function of novel osteoblast-adhesive peptides for chemical modification of biomaterials. *J Biomed Mater Res* **40**, 371-377 (1998).
162. Shin, H., Jo, S. & Mikos, A.G. Biomimetic materials for tissue engineering. *Biomaterials* **24**, 4353-4364 (2003).
163. Balasundaram, G. & Webster, T.J. Increased osteoblast adhesion on nanograined Ti modified with KRSR. *Journal of Biomedical Materials Research Part A* **80A**, 602-611 (2007).
164. Martin, S.M., Schwartz, J.L., Giachelli, C.M. & Ratner, B.D. Enhancing the biological activity of immobilized osteopontin using a type-1 collagen affinity coating. *Journal of Biomedical Materials Research Part A* **70A**, 10-19 (2004).
165. Xiao, S.J. *et al.* Immobilization of the cell-adhesive peptide Arg–Gly–Asp–Cys (RGDC) on titanium surfaces by covalent chemical attachment. *Journal of Materials Science: Materials in Medicine* **8**, 867-872 (1997).
166. Lee, H., Scherer, N.F. & Messersmith, P.B. Single-molecule mechanics of mussel adhesion. *Proc Natl Acad Sci U S A* **103**, 12999-13003 (2006).
167. Belibasakis, G.N. *et al.* Cytokine responses of human gingival fibroblasts to Actinobacillus actinomycetemcomitans cytolethal distending toxin. *Cytokine* **30**, 56-63 (2005).
168. Novaes, A.B., Jr. *et al.* Influence of implant surfaces on osseointegration. *Braz Dent J* **21**, 471-481 (2010).
169. Price, R.L., Waid, M.C., Haberstroh, K.M. & Webster, T.J. Selective bone cell adhesion on formulations containing carbon nanofibers. *Biomaterials* **24**, 1877-1887 (2003).

170. Elias, K.L., Price, R.L. & Webster, T.J. Enhanced functions of osteoblasts on nanometer diameter carbon fibers. *Biomaterials* **23**, 3279-3287 (2002).
171. Kunzler, T.P., Drobek, T., Schuler, M. & Spencer, N.D. Systematic study of osteoblast and fibroblast response to roughness by means of surface-morphology gradients. *Biomaterials* **28**, 2175-2182 (2007).
172. Quarles, L.D., Yohay, D.A., Lever, L.W., Caton, R. & Wenstrup, R.J. Distinct proliferative and differentiated stages of murine MC3T3-E1 cells in culture: An in vitro model of osteoblast development. *Journal of Bone and Mineral Research* **7**, 683-692 (1992).
173. Zeldich, E., Koren, R., Nemcovsky, C. & Weinreb, M. Enamel matrix derivative stimulates human gingival fibroblast proliferation via ERK. *J Dent Res* **86**, 41-46 (2007).
174. Gittens, R.A., Olivares-Navarrete, R., Schwartz, Z. & Boyan, B.D. Implant osseointegration and the role of microroughness and nanostructures: Lessons for spine implants. *Acta Biomaterialia*.
175. Osborn, J.F. & Newesely, H. The material science of calcium phosphate ceramics. *Biomaterials* **1**, 108-111 (1980).
176. LeGeros, R.Z. Calcium Phosphate-Based Osteoinductive Materials. *Chemical Reviews* **108**, 4742-4753 (2008).
177. Daculsi, G. *et al.* Macroporous calcium phosphate ceramic for long bone surgery in humans and dogs. Clinical and histological study. *Journal of Biomedical Materials Research* **24**, 379-396 (1990).
178. Yuan, H. *et al.* Osteoinductive ceramics as a synthetic alternative to autologous bone grafting. *Proceedings of the National Academy of Sciences* (2010).
179. Alghamdi, H.S., Bosco, R., van den Beucken, J.J.J.P., Walboomers, X.F. & Jansen, J.A. Osteogenicity of titanium implants coated with calcium phosphate or collagen type-I in osteoporotic rats. *Biomaterials* **34**, 3747-3757 (2013).
180. Dominici, M. *et al.* Minimal criteria for defining multipotent mesenchymal stromal cells. The International Society for Cellular Therapy position statement. *Cytotherapy* **8**, 315-317 (2006).
181. Pashuck, E.T. & Stevens, M.M. Designing Regenerative Biomaterial Therapies for the Clinic. *Science Translational Medicine* **4**, 160sr164-160sr164 (2012).
182. Yoo, S.Y., Kobayashi, M., Lee, P.P. & Lee, S.-W. Early Osteogenic Differentiation of Mouse Preosteoblasts Induced by Collagen-Derived DGEA-Peptide on Nanofibrous Phage Tissue Matrices. *Biomacromolecules* **12**, 987-996 (2011).
183. Mizuno, M., Fujisawa, R. & Kuboki, Y. Type I collagen-induced osteoblastic differentiation of bone-marrow cells mediated by collagen-α2β1 integrin interaction. *Journal of Cellular Physiology* **184**, 207-213 (2000).
184. Staatz, W.D. *et al.* Identification of a tetrapeptide recognition sequence for the alpha 2 beta 1 integrin in collagen. *Journal of Biological Chemistry* **266**, 7363-7367 (1991).
185. Anderson, J.M. *et al.* Osteogenic Differentiation of Human Mesenchymal Stem Cells Directed by Extracellular Matrix-Mimicking Ligands in a

Biomimetic Self-Assembled Peptide Amphiphile Nanomatrix. *Biomacromolecules* **10**, 2935-2944 (2009).
186. Hennessy, K.M. *et al.* The effect of collagen I mimetic peptides on mesenchymal stem cell adhesion and differentiation, and on bone formation at hydroxyapatite surfaces. *Biomaterials* **30**, 1898-1909 (2009).
187. Mizuno, M. & Kuboki, Y. Osteoblast-related gene expression of bone marrow cells during the osteoblastic differentiation induced by type I collagen. *J Biochem* **129**, 133-138 (2001).
188. Olivares-Navarrete, R. *et al.* Integrin α2β1 Plays a Critical Role in Osteoblast Response to Micron-Scale Surface Structure and Surface Energy of Titanium Substrates. *Proceedings of the National Academy of Sciences of the United States of America* **105**, 15767-15772 (2008).
189. Popov, C. *et al.* Integrins [alpha]2[beta]1 and [alpha]11[beta]1 regulate the survival of mesenchymal stem cells on collagen I. *Cell Death and Dis* **2**, e186 (2011).
190. Keselowsky, B.G., Wang, L., Schwartz, Z., Garcia, A.J. & Boyan, B.D. Integrin α5 controls osteoblastic proliferation and differentiation responses to titanium substrates presenting different roughness characteristics in a roughness independent manner. *Journal of Biomedical Materials Research Part A* **80A**, 700-710 (2007).
191. Layrolle, P. 1.112 - Calcium Phosphate Coatings, in *Comprehensive Biomaterials*. (ed. P. Ducheyne) 223-229 (Elsevier, Oxford; 2011).
192. Shih, Y.-R.V. *et al.* Calcium phosphate-bearing matrices induce osteogenic differentiation of stem cells through adenosine signaling. *Proceedings of the National Academy of Sciences* (2014).
193. Tye, C.E. *et al.* Delineation of the Hydroxyapatite-nucleating Domains of Bone Sialoprotein. *Journal of Biological Chemistry* **278**, 7949-7955 (2003).
194. Chien, C.-Y. & Tsai, W.-B. Poly(dopamine)-Assisted Immobilization of Arg-Gly-Asp Peptides, Hydroxyapatite, and Bone Morphogenic Protein-2 on Titanium to Improve the Osteogenesis of Bone Marrow Stem Cells. *ACS Applied Materials & Interfaces* **5**, 6975-6983 (2013).
195. Lin, L., Chow, K.L. & Leng, Y. Study of hydroxyapatite osteoinductivity with an osteogenic differentiation of mesenchymal stem cells. *Journal of Biomedical Materials Research Part A* **89A**, 326-335 (2009).
196. Englund, E.A. *et al.* Programmable multivalent display of receptor ligands using peptide nucleic acid nanoscaffolds. *Nat Commun* **3**, 614 (2012).
197. Tejeda-Montes, E. *et al.* Bioactive membranes for bone regeneration applications: Effect of physical and biomolecular signals on mesenchymal stem cell behavior. *Acta Biomaterialia* **10**, 134-141 (2014).
198. Sargeant, T.D., Rao, M.S., Koh, C.-Y. & Stupp, S.I. Covalent functionalization of NiTi surfaces with bioactive peptide amphiphile nanofibers. *Biomaterials* **29**, 1085-1098 (2008).
199. Mata, A. *et al.* Bone regeneration mediated by biomimetic mineralization of a nanofiber matrix. *Biomaterials* **31**, 6004-6012 (2010).
200. Lim, Y.-b., Moon, K.-S. & Lee, M. Recent advances in functional supramolecular nanostructures assembled from bioactive building blocks. *Chemical Society Reviews* **38**, 925-934 (2009).

201. Ceylan, H., Tekinay, A.B. & Guler, M.O. Mussel-inspired Adhesive Interfaces for Biomedical Applications, in *Biological and Biomimetic Adhesives: Challenges and Opportunities* 103-116 (The Royal Society of Chemistry, 2013).
202. Meredith, H.J., Jenkins, C.L. & Wilker, J.J. Enhancing the Adhesion of a Biomimetic Polymer Yields Performance Rivaling Commercial Glues. *Advanced Functional Materials*, DOI: 10.1002/adfm.201303536 (2014).
203. Behanna, H.A., Donners, J.J.J.M., Gordon, A.C. & Stupp, S.I. Coassembly of Amphiphiles with Opposite Peptide Polarities into Nanofibers. *Journal of the American Chemical Society* **127**, 1193-1200 (2005).
204. Raspanti, M. *et al.* The extracellular matrix of the human aortic wall: ultrastructural observations by FEG-SEM and by tapping-mode AFM. *Micron* **37**, 81-86 (2006).
205. Muthusubramaniam, L. *et al.* Collagen fibril diameter and alignment promote the quiescent keratocyte phenotype. *Journal of Biomedical Materials Research Part A* **100A**, 613-621 (2012).
206. Kokubo, T. & Takadama, H. Simulated Body Fluid (SBF) as a Standard Tool to Test the Bioactivity of Implants, in *Handbook of Biomineralization* 97-109 (Wiley-VCH Verlag GmbH, 2007).
207. Song, J., Saiz, E. & Bertozzi, C.R. A New Approach to Mineralization of Biocompatible Hydrogel Scaffolds: An Efficient Process toward 3-Dimensional Bonelike Composites. *Journal of the American Chemical Society* **125**, 1236-1243 (2003).
208. Spoerke, E.D., Anthony, S.G. & Stupp, S.I. Enzyme Directed Templating of Artificial Bone Mineral. *Advanced Materials* **21**, 425-430 (2009).
209. Ishikawa, K., Ducheyne, P. & Radin, S. Determination of the Ca/P ratio in calcium-deficient hydroxyapatite using X-ray diffraction analysis. *Journal of Materials Science: Materials in Medicine* **4**, 165-168 (1993).
210. Volmer M., W.A. Keimbildung in übersättigten Gebilden (Nucleation of supersaturated structures). *Zeitschrift für Physikalische Chemie* **119**, 277-301 (1926).
211. Newcomb, C.J., Bitton, R., Velichko, Y.S., Snead, M.L. & Stupp, S.I. The Role of Nanoscale Architecture in Supramolecular Templating of Biomimetic Hydroxyapatite Mineralization. *Small* **8**, 2195-2202 (2012).
212. Li, L. *et al.* Bio-Inspired Enamel Repair via Glu-Directed Assembly of Apatite Nanoparticles: an Approach to Biomaterials with Optimal Characteristics. *Advanced Materials* **23**, 4695-4701 (2011).
213. Dey, A. *et al.* The role of prenucleation clusters in surface-induced calcium phosphate crystallization. *Nat Mater* **9**, 1010-1014 (2010).
214. Frisch, S.M., Vuori, K., Ruoslahti, E. & Chan-Hui, P.Y. Control of adhesion-dependent cell survival by focal adhesion kinase. *The Journal of Cell Biology* **134**, 793-799 (1996).
215. Mann, B.K. & West, J.L. Cell adhesion peptides alter smooth muscle cell adhesion, proliferation, migration, and matrix protein synthesis on modified surfaces and in polymer scaffolds. *Journal of Biomedical Materials Research* **60**, 86-93 (2002).

216. Schwartz, M.A. & Assoian, R.K. Integrins and cell proliferation: regulation of cyclin-dependent kinases via cytoplasmic signaling pathways. *Journal of Cell Science* **114**, 2553-2560 (2001).
217. Wilson, C.J., Clegg, R.E., Leavesley, D.I. & Pearcy, M.J. Mediation of biomaterial-cell interactions by adsorbed proteins: a review. *Tissue Eng* **11**, 1-18 (2005).
218. Sagnella, S.M. *et al.* Human microvascular endothelial cell growth and migration on biomimetic surfactant polymers. *Biomaterials* **25**, 1249-1259 (2004).
219. Liu, W. *et al.* Nanofiber scaffolds with gradients in mineral content for spatial control of osteogenesis. *ACS Appl Mater Interfaces* **6**, 2842-2849 (2014).
220. D'Souza, R.N. *et al.* Gene expression patterns of murine dentin matrix protein 1 (Dmp1) and dentin sialophosphoprotein (DSPP) suggest distinct developmental functions *in vivo*. *J Bone Miner Res* **12**, 2040-2049 (1997).
221. Narayanan, K. *et al.* Dual functional roles of dentin matrix protein 1. Implications in biomineralization and gene transcription by activation of intracellular Ca2+ store. *J Biol Chem* **278**, 17500-17508 (2003).
222. He, G., Dahl, T., Veis, A. & George, A. Nucleation of apatite crystals in vitro by self-assembled dentin matrix protein 1. *Nat Mater* **2**, 552-558 (2003).
223. Anderson, J.M. *et al.* Osteogenic differentiation of human mesenchymal stem cells synergistically enhanced by biomimetic peptide amphiphiles combined with conditioned medium. *Acta Biomater* **7**, 675-682 (2011).
224. You, M.H. *et al.* Synergistically enhanced osteogenic differentiation of human mesenchymal stem cells by culture on nanostructured surfaces with induction media. *Biomacromolecules* **11**, 1856-1862 (2010).
225. Costa-Pinto, A.R. *et al.* Osteogenic Differentiation of Human Bone Marrow Mesenchymal Stem Cells Seeded on Melt Based Chitosan Scaffolds for Bone Tissue Engineering Applications. *Biomacromolecules* **10**, 2067-2073 (2009).
226. Liao, S. *et al.* Biomimetic Nanocomposites to Control Osteogenic Differentiation of Human Mesenchymal Stem Cells. *Advanced Healthcare Materials* **3**, 737-751 (2014).
227. Penfornis, P. & Pochampally, R. Isolation and Expansion of Mesenchymal Stem Cells/Multipotential Stromal Cells from Human Bone Marrow, in *Mesenchymal Stem Cell Assays and Applications*, Vol. 698. (eds. M. Vemuri, L.G. Chase & M.S. Rao) 11-21 (Humana Press, 2011).
228. Dexter, A.F., Malcolm, A.S. & Middelberg, A.P.J. Reversible active switching of the mechanical properties of a peptide film at a fluid-fluid interface. *Nat Mater* **5**, 502-506 (2006).
229. de Loos, M., Feringa, B.L. & van Esch, J.H. Design and Application of Self-Assembled Low Molecular Weight Hydrogels. *European Journal of Organic Chemistry* **2005**, 3615-3631 (2005).
230. Yan, X. *et al.* A Multiresponsive, Shape-Persistent, and Elastic Supramolecular Polymer Network Gel Constructed by Orthogonal Self-Assembly. *Advanced Materials* **24**, 362-369 (2012).
231. Ikeda, M., Tanida, T., Yoshii, T. & Hamachi, I. Rational Molecular Design of Stimulus-Responsive Supramolecular Hydrogels Based on Dipeptides. *Advanced Materials* **23**, 2819-2822 (2011).

232. Rothemund, P.W.K. Folding DNA to create nanoscale shapes and patterns. *Nature* **440**, 297-302 (2006).
233. Tsai, W.-W., Li, L.-s., Cui, H., Jiang, H. & Stupp, S.I. Self-assembly of amphiphiles with terthiophene and tripeptide segments into helical nanostructures. *Tetrahedron* **64**, 8504-8514 (2008).
234. Roy, S. & Banerjee, A. Amino acid based smart hydrogel: formation, characterization and fluorescence properties of silver nanoclusters within the hydrogel matrix. *Soft Matter* **7**, 5300-5308 (2011).
235. Shi, N.E., Dong, H., Yin, G., Xu, Z. & Li, S.H. A Smart Supramolecular Hydrogel Exhibiting pH-Modulated Viscoelastic Properties. *Advanced Functional Materials* **17**, 1837-1843 (2007).
236. Jung, J.P., Jones, J.L., Cronier, S.A. & Collier, J.H. Modulating the mechanical properties of self-assembled peptide hydrogels via native chemical ligation. *Biomaterials* **29**, 2143-2151 (2008).
237. Aulisa, L., Dong, H. & Hartgerink, J.D. Self-Assembly of Multidomain Peptides: Sequence Variation Allows Control over Cross-Linking and Viscoelasticity. *Biomacromolecules* **10**, 2694-2698 (2009).
238. Stendahl, J.C., Rao, M.S., Guler, M.O. & Stupp, S.I. Intermolecular Forces in the Self-Assembly of Peptide Amphiphile Nanofibers. *Advanced Functional Materials* **16**, 499-508 (2006).
239. Pashuck, E.T., Cui, H. & Stupp, S.I. Tuning Supramolecular Rigidity of Peptide Fibers through Molecular Structure. *Journal of the American Chemical Society* **132**, 6041-6046 (2010).
240. Brubaker, C.E. & Messersmith, P.B. The Present and Future of Biologically Inspired Adhesive Interfaces and Materials. *Langmuir* **28**, 2200-2205 (2012).
241. Lin, Q. *et al.* Adhesion mechanisms of the mussel foot proteins mfp-1 and mfp-3. *Proceedings of the National Academy of Sciences* **104**, 3782-3786 (2007).
242. Zeng, H., Hwang, D.S., Israelachvili, J.N. & Waite, J.H. Strong reversible Fe3+-mediated bridging between dopa-containing protein films in water. *Proceedings of the National Academy of Sciences* **107**, 12850-12853 (2010).
243. Shafiq, Z. *et al.* Bioinspired Underwater Bonding and Debonding on Demand. *Angewandte Chemie International Edition* **51**, 4332-4335 (2012).
244. Taylor, S.W., Chase, D.B., Emptage, M.H., Nelson, M.J. & Waite, J.H. Ferric Ion Complexes of a DOPA-Containing Adhesive Protein from Mytilus edulis. *Inorganic Chemistry* **35**, 7572-7577 (1996).
245. Hartgerink, J.D., Beniash, E. & Stupp, S.I. Peptide-amphiphile nanofibers: A versatile scaffold for the preparation of self-assembling materials. *Proceedings of the National Academy of Sciences* **99**, 5133-5138 (2002).
246. Yan, C. & Pochan, D.J. Rheological properties of peptide-based hydrogels for biomedical and other applications. *Chemical Society Reviews* **39**, 3528-3540 (2010).
247. Kurniawan, N.A., Wong, L.H. & Rajagopalan, R. Early Stiffening and Softening of Collagen: Interplay of Deformation Mechanisms in Biopolymer Networks. *Biomacromolecules* **13**, 691-698 (2012).

248. Dagdas, Y.S., Tombuloglu, A., Tekinay, A.B., Dana, A. & Guler, M.O. Interfiber interactions alter the stiffness of gels formed by supramolecular self-assembled nanofibers. *Soft Matter* **7**, 3524-3532 (2011).
249. Greenfield, M.A., Hoffman, J.R., Olvera de la Cruz, M. & Stupp, S.I. Tunable Mechanics of Peptide Nanofiber Gels. *Langmuir* **26**, 3641-3647 (2009).
250. Zhang, S. *et al.* A self-assembly pathway to aligned monodomain gels. *Nat Mater* **9**, 594-601 (2010).
251. Wilker, J.J. Marine bioinorganic materials: mussels pumping iron. *Current Opinion in Chemical Biology* **14**, 276-283 (2010).
252. Hwang, H.Y. *et al.* Emergent phenomena at oxide interfaces. *Nat Mater* **11**, 103-113 (2012).
253. Luo, S.-C. *et al.* Polydioxythiophene Nanodots, Nonowires, Nano-Networks, and Tubular Structures: The Effect of Functional Groups and Temperature in Template-Free Electropolymerization. *ACS Nano* **6**, 3018-3026 (2012).
254. Roy, P., Berger, S. & Schmuki, P. TiO_2 Nanotubes: Synthesis and Applications. *Angewandte Chemie International Edition* **50**, 2904-2939 (2011).
255. Acar, H., Garifullin, R. & Guler, M.O. Self-Assembled Template-Directed Synthesis of One-Dimensional Silica and Titania Nanostructures. *Langmuir* **27**, 1079-1084 (2011).
256. Mahmoudi, M., Sant, S., Wang, B., Laurent, S. & Sen, T. Superparamagnetic iron oxide nanoparticles (SPIONs): Development, surface modification and applications in chemotherapy. *Advanced Drug Delivery Reviews* **63**, 24-46 (2011).
257. Lee, K. *et al.* Anodic Formation of Thick Anatase TiO_2 Mesosponge Layers for High-Efficiency Photocatalysis. *Journal of the American Chemical Society* **132**, 1478-1479 (2010).
258. Park, J.-H., Choi, H.-J., Choi, Y.-J., Sohn, S.-H. & Park, J.-G. Ultrawide ZnO nanosheets. *Journal of Materials Chemistry* **14**, 35-36 (2004).
259. Khalily, M.A., Ustahuseyin, O., Garifullin, R., Genc, R. & Guler, M.O. A supramolecular peptide nanofiber templated Pd nanocatalyst for efficient Suzuki coupling reactions under aqueous conditions. *Chemical Communications* **48**, 11358-11360 (2012).
260. Herle, P.S., Ellis, B., Coombs, N. & Nazar, L.F. Nano-network electronic conduction in iron and nickel olivine phosphates. *Nat Mater* **3**, 147-152 (2004).
261. Adachi, M.M., Anantram, M.P. & Karim, K.S. Core-shell silicon nanowire solar cells. *Sci. Rep.* **3** (2013).
262. Zhao, Y. & Gruner, G. Nanonet as a scaffold with targeted functionalities. *Journal of Materials Chemistry* **22**, 24983-24991 (2012).
263. Zhuang, J. *et al.* Hierarchical porous TiO_2@C hollow microspheres: one-pot synthesis and enhanced visible-light photocatalysis. *Journal of Materials Chemistry* **22**, 7036-7042 (2012).
264. Kim, S.-W. *et al.* Fabrication and Electrochemical Characterization of TiO_2 Three-Dimensional Nanonetwork Based on Peptide Assembly. *ACS Nano* **3**, 1085-1090 (2009).

265. Wang, X. *et al.* Effects of structural properties of electrospun TiO_2 nanofiber meshes on their osteogenic potential. *Acta Biomaterialia* **8**, 878-885 (2012).
266. Chiang, C.-Y. *et al.* Formation of TiO_2 nano-network on titanium surface increases the human cell growth. *Dental Materials* **25**, 1022-1029 (2009).
267. Müllner, M., Lunkenbein, T., Miyajima, N., Breu, J. & Müller, A.H.E. A Facile Polymer Templating Route Toward High-Aspect-Ratio Crystalline Titania Nanostructures. *Small* **8**, 2636-2640 (2012).
268. Zhang, Q., Dandeneau, C.S., Zhou, X. & Cao, G. ZnO Nanostructures for Dye-Sensitized Solar Cells. *Advanced Materials* **21**, 4087-4108 (2009).
269. Kamegawa, T., Shimizu, Y. & Yamashita, H. Superhydrophobic Surfaces with Photocatalytic Self-Cleaning Properties by Nanocomposite Coating of TiO_2 and Polytetrafluoroethylene. *Advanced Materials* **24**, 3697-3700 (2012).
270. Bjursten, L.M. *et al.* Titanium dioxide nanotubes enhance bone bonding *in vivo*. *J Biomed Mater Res A* **92**, 1218-1224 (2010).
271. Tong, H. *et al.* Nano-photocatalytic Materials: Possibilities and Challenges. *Advanced Materials* **24**, 229-251 (2012).
272. Acar, H. *et al.* Self-Assembled Peptide Nanofiber Templated One-Dimensional Gold Nanostructures Exhibiting Resistive Switching. *Langmuir* **28**, 16347-16354 (2012).
273. Ceylan, H. *et al.* Mussel Inspired Dynamic Cross-Linking of Self-Healing Peptide Nanofiber Network. *Advanced Functional Materials* **23**, 2081-2090 (2013).
274. George, S.M. Atomic Layer Deposition: An Overview. *Chemical Reviews* **110**, 111-131 (2009).
275. Knez, M., Nielsch, K. & Niinistö, L. Synthesis and Surface Engineering of Complex Nanostructures by Atomic Layer Deposition. *Advanced Materials* **19**, 3425-3438 (2007).
276. Knez, M. *et al.* Atomic Layer Deposition on Biological Macromolecules: Metal Oxide Coating of Tobacco Mosaic Virus and Ferritin. *Nano Letters* **6**, 1172-1177 (2006).
277. Scanlon, S. *et al.* Peptide aerogels comprising self-assembling nanofibrils. *Micro & Nano Letters, IET* **2**, 24-29 (2007).
278. Korhonen, J.T. *et al.* Inorganic Hollow Nanotube Aerogels by Atomic Layer Deposition onto Native Nanocellulose Templates. *ACS Nano* **5**, 1967-1974 (2011).
279. Han, T.H. *et al.* Highly entangled hollow TiO_2 nanoribbons templating diphenylalanine assembly. *Journal of Materials Chemistry* **19**, 3512-3516 (2009).
280. Sone, E.D., Zubarev, E.R. & Stupp, S.I. Semiconductor Nanohelices Templated by Supramolecular Ribbons. *Angewandte Chemie International Edition* **41**, 1705-1709 (2002).
281. Greenlief, C.M., White, J.M., Ko, C.S. & Gorte, R.J. An XPS investigation of titanium dioxide thin films on polycrystalline platinum. *The Journal of Physical Chemistry* **89**, 5025-5028 (1985).
282. Kharlampieva, E. *et al.* Bioenabled Surface-Mediated Growth of Titania Nanoparticles. *Advanced Materials* **20**, 3274-3279 (2008).

283. Mulligan, R.F., Iliadis, A.A. & Kofinas, P. Synthesis and characterization of ZnO nanostructures templated using diblock copolymers. *Journal of Applied Polymer Science* **89**, 1058-1061 (2003).
284. Wu, K., Sun, Z. & Cui, J. Unique Approach toward ZnO Growth with Tunable Properties: Influence of Methanol in an Electrochemical Process. *Crystal Growth & Design* **12**, 2864-2871 (2012).
285. Chen, X. & Mao, S.S. Titanium Dioxide Nanomaterials: Synthesis, Properties, Modifications, and Applications. *Chemical Reviews* **107**, 2891-2959 (2007).
286. Lin, K.-F., Cheng, H.-M., Hsu, H.-C., Lin, L.-J. & Hsieh, W.-F. Band gap variation of size-controlled ZnO quantum dots synthesized by sol–gel method. *Chemical Physics Letters* **409**, 208-211 (2005).
287. Zhang, Z., Wang, C.-C., Zakaria, R. & Ying, J.Y. Role of Particle Size in Nanocrystalline TiO_2-Based Photocatalysts. *The Journal of Physical Chemistry B* **102**, 10871-10878 (1998).
288. Almquist, C.B. & Biswas, P. Role of Synthesis Method and Particle Size of Nanostructured TiO_2 on Its Photoactivity. *Journal of Catalysis* **212**, 145-156 (2002).
289. Liu, J. *et al.* Self-Assembling TiO_2 Nanorods on Large Graphene Oxide Sheets at a Two-Phase Interface and Their Anti-Recombination in Photocatalytic Applications. *Advanced Functional Materials* **20**, 4175-4181 (2010).
290. Ishibashi, K.-i., Fujishima, A., Watanabe, T. & Hashimoto, K. Quantum yields of active oxidative species formed on TiO_2 photocatalyst. *Journal of Photochemistry and Photobiology A: Chemistry* **134**, 139-142 (2000).
291. Xiang, Q., Yu, J. & Wong, P.K. Quantitative characterization of hydroxyl radicals produced by various photocatalysts. *Journal of Colloid and Interface Science* **357**, 163-167 (2011).
292. Webb, J.A. & Bardhan, R. Emerging advances in nanomedicine with engineered gold nanostructures. *Nanoscale* **6**, 2502-2530 (2014).
293. Brown, S.D. *et al.* Gold Nanoparticles for the Improved Anticancer Drug Delivery of the Active Component of Oxaliplatin. *Journal of the American Chemical Society* **132**, 4678-4684 (2010).
294. Muroski, M.E., Kogot, J.M. & Strouse, G.F. Bimodal Gold Nanoparticle Therapeutics for Manipulating Exogenous and Endogenous Protein Levels in Mammalian Cells. *Journal of the American Chemical Society* **134**, 19722-19730 (2012).
295. Kennedy, L.C. *et al.* A New Era for Cancer Treatment: Gold-Nanoparticle-Mediated Thermal Therapies. *Small* **7**, 169-183 (2011).
296. Huang, X., El-Sayed, I.H., Qian, W. & El-Sayed, M.A. Cancer Cell Imaging and Photothermal Therapy in the Near-Infrared Region by Using Gold Nanorods. *Journal of the American Chemical Society* **128**, 2115-2120 (2006).
297. Curry, T., Kopelman, R., Shilo, M. & Popovtzer, R. Multifunctional theranostic gold nanoparticles for targeted CT imaging and photothermal therapy. *Contrast Media & Molecular Imaging* **9**, 53-61 (2014).

298. Valentini, P. *et al.* Gold-Nanoparticle-Based Colorimetric Discrimination of Cancer-Related Point Mutations with Picomolar Sensitivity. *ACS Nano* **7**, 5530-5538 (2013).
299. Libutti, S.K. *et al.* Results of a completed phase I clinical trial of CYT-6091: A pegylated colloidal gold-TNF nanomedicine. (2009)
300. Turkevich, J., Stevenson, P.C. & Hillier, J. A study of the nucleation and growth processes in the synthesis of colloidal gold. *Discussions of the Faraday Society* **11**, 55-75 (1951).
301. Daniel, M.-C. & Astruc, D. Gold Nanoparticles: Assembly, Supramolecular Chemistry, Quantum-Size-Related Properties, and Applications toward Biology, Catalysis, and Nanotechnology. *Chemical Reviews* **104**, 293-346 (2003).
302. Brust, M., Walker, M., Bethell, D., Schiffrin, D.J. & Whyman, R. Synthesis of thiol-derivatised gold nanoparticles in a two-phase Liquid-Liquid system. *Journal of the Chemical Society, Chemical Communications*, 801-802 (1994).
303. Aslan, K. & Pérez-Luna, V.H. Surface Modification of Colloidal Gold by Chemisorption of Alkanethiols in the Presence of a Nonionic Surfactant. *Langmuir* **18**, 6059-6065 (2002).
304. Takahashi, H. *et al.* Modification of Gold Nanorods Using Phosphatidylcholine to Reduce Cytotoxicity. *Langmuir* **22**, 2-5 (2005).
305. Pierschbacher, M.D. & Ruoslahti, E. Cell attachment activity of fibronectin can be duplicated by small synthetic fragments of the molecule. *Nature* **309**, 30-33 (1984).
306. Waite, J.H. Nature's underwater adhesive specialist. *International Journal of Adhesion and Adhesives* **7**, 9-14 (1987).
307. Shi, J. *et al.* Influence of Histidine Incorporation on Buffer Capacity and Gene Transfection Efficiency of HPMA-co-oligolysine Brush Polymers. *Biomacromolecules* **14**, 1961-1970 (2013).
308. Bennevault-Celton, V. *et al.* Supramolecular Assemblies of Histidinylated α-Cyclodextrin in the Presence of DNA Scaffold during CDplexes Formation. *Bioconjugate Chemistry* **22**, 2404-2414 (2011).
309. Gao, J., Huang, X., Liu, H., Zan, F. & Ren, J. Colloidal Stability of Gold Nanoparticles Modified with Thiol Compounds: Bioconjugation and Application in Cancer Cell Imaging. *Langmuir* **28**, 4464-4471 (2012).
310. Qin, X. *et al.* Novel synthesis of Au nanoparticles using fluorescent carbon nitride dots as photocatalyst. *Gold Bull* **45**, 61-67 (2012).
311. Eslami, M., Zare, H.R. & Namazian, M. Thermodynamic Parameters of Electrochemical Oxidation of l-DOPA: Experimental and Theoretical Studies. *The Journal of Physical Chemistry B* **116**, 12552-12557 (2012).
312. Lee, Y. & Park, T.G. Facile Fabrication of Branched Gold Nanoparticles by Reductive Hydroxyphenol Derivatives. *Langmuir* **27**, 2965-2971 (2011).
313. Reiss, H. The Growth of Uniform Colloidal Dispersions. *The Journal of Chemical Physics* **19**, 482-487 (1951).
314. Yin, Y. & Alivisatos, A.P. Colloidal nanocrystal synthesis and the organic-inorganic interface. *Nature* **437**, 664-670 (2005).

315. Black, K.C.L., Liu, Z. & Messersmith, P.B. Catechol Redox Induced Formation of Metal Core−Polymer Shell Nanoparticles. *Chemistry of Materials* **23**, 1130-1135 (2011).
316. Huang, X., Wu, H., Liao, X. & Shi, B. One-step, size-controlled synthesis of gold nanoparticles at room temperature using plant tannin. *Green Chemistry* **12**, 395-399 (2010).
317. Yeh, Y.-C., Creran, B. & Rotello, V.M. Gold nanoparticles: preparation, properties, and applications in bionanotechnology. *Nanoscale* **4**, 1871-1880 (2012).
318. Dobrovolskaia, M.A. & McNeil, S.E. Immunological properties of engineered nanomaterials. *Nat Nano* **2**, 469-478 (2007).
319. Khlebtsov, N. & Dykman, L. Biodistribution and toxicity of engineered gold nanoparticles: a review of in vitro and *in vivo* studies. *Chemical Society Reviews* **40**, 1647-1671 (2011).
320. Kim, J. *et al.* Active targeting of RGD-conjugated bioreducible polymer for delivery of oncolytic adenovirus expressing shRNA against IL-8 mRNA. *Biomaterials* **32**, 5158-5166 (2011).
321. Lin, R.-Y. *et al.* Targeted RGD nanoparticles for highly sensitive *in vivo* integrin receptor imaging. *Contrast Media & Molecular Imaging* **7**, 7-18 (2012).
322. Jiang, J. *et al.* Sequential treatment of drug-resistant tumors with RGD-modified liposomes containing siRNA or doxorubicin. *European Journal of Pharmaceutics and Biopharmaceutics* **76**, 170-178 (2010).
323. Nel, A.E. *et al.* Understanding biophysicochemical interactions at the nano-bio interface. *Nat Mater* **8**, 543-557 (2009).
324. Liu, X., Atwater, M., Wang, J. & Huo, Q. Extinction coefficient of gold nanoparticles with different sizes and different capping ligands. *Colloids and Surfaces B: Biointerfaces* **58**, 3-7 (2007).
325. Doherty, G.J. & McMahon, H.T. Mechanisms of Endocytosis. *Annual Review of Biochemistry* **78**, 857-902 (2009).
326. Thompson, David B., Villaseñor, R., Dorr, Brent M., Zerial, M. & Liu, David R. Cellular Uptake Mechanisms and Endosomal Trafficking of Supercharged Proteins. *Chemistry & Biology* **19**, 831-843 (2012).
327. Iversen, T.-G., Skotland, T. & Sandvig, K. Endocytosis and intracellular transport of nanoparticles: Present knowledge and need for future studies. *Nano Today* **6**, 176-185 (2011).
328. Waite, J.H. EVIDENCE FOR A repeating 3,4-dihydroxyphenylalanine-containing and hydroxyproline-containing decapeptide in the adhesive protein of the mussel, mytilus-edulis-l. *J. Biol. Chem.* **258**, 2911-2915 (1983).
329. Waite, J.H., Jensen, R.A. & Morse, D.E. Cement precursor proteins of the reef-building polychaete Phragmatopoma californica (Fewkes). *Biochemistry* **31**, 5733-5738 (1992).
330. Yu, M. & Deming, T.J. Synthetic Polypeptide Mimics of Marine Adhesives. *Macromolecules* **31**, 4739-4745 (1998).
331. Podsiadlo, P., Liu, Z., Paterson, D., Messersmith, P.B. & Kotov, N.A. Fusion of Seashell Nacre and Marine Bioadhesive Analogs: High-Strength

Nanocomposite by Layer-by-Layer Assembly of Clay and L-3,4-Dihydroxyphenylalanine Polymer. *Advanced Materials* **19**, 949-955 (2007).
332. Shao, H. & Stewart, R.J. Biomimetic Underwater Adhesives with Environmentally Triggered Setting Mechanisms. *Advanced Materials* **22**, 729-733 (2010).

APPENDIX

Copyright Clearance Agreements†

Reference Number	License Supplier	License Number
17	Royal Society of Chemistry	Permission not required
41	Nature Publishing Group	3455000786420
57	Elsevier	3454860596533
58	Royal Society of Chemistry	Permission not required
73	Nature Publishing Group	3415981178953
76	Elsevier	3455001148197
82	National Academy of Sciences of the U.S.A.	Permission not required
86	Cold Spring Harbor Laboratory Press	Permission not required
88	Elsevier	3455010583577
89	Nature Publishing Group	3455211348092
95	The American Association for the Advancement of Science	3455211492076
201	Royal Society of Chemistry	Permission not required
273	John Wiley and Sons	3415990176931

† All license agreements between Hakan Ceylan and the License Suppliers are made by means of Copyright Clearance Center (CCC).